Astrophysics and Space Science Library 451

Guillermo M. Muñoz Caro
Rafael Escribano *Editors*

Laboratory Astrophysics

ASSL

Springer

Laboratory Astrophysics

Astrophysics and Space Science Library

Guillermo M. Muñoz Caro • Rafael Escribano
Editors

Laboratory Astrophysics

Springer

Editors
Guillermo M. Muñoz Caro
Centro de Astrobiología
INTA-CSIC
Torrejón de Ardoz
Madrid, Spain

Rafael Escribano
Inst. de Estructura de la Materia
IEM-CSIC
Madrid, Spain

ISSN 0067-0057 ISSN 2214-7985 (electronic)
Astrophysics and Space Science Library
ISBN 978-3-319-90019-3 ISBN 978-3-319-90020-9 (eBook)
https://doi.org/10.1007/978-3-319-90020-9

Library of Congress Control Number: 2018950457

Cover illustration: Artist's composition of the absorption spectrum of icy dust with the Pleiades star cluster in the background. Credit: Ángel González Valdenebro

This Springer imprint is published by the registered company Springer Nature Switzerland AG
The registered company address is: Gewerbestrasse 11, 6330 Cham, Switzerland

Preface

Astrochemistry is the science devoted to the study of the chemical processes at work in astrophysical environments, including the interstellar medium, comets, and circumstellar and circumplanetary regions, according to M. De Becker. It may be distinguished from astrophysics, which focuses on the study, formation, and evolution of astronomical objects based on physical principles, but clearly both disciplines go hand in hand. Astrochemistry has evolved tremendously in the last fifty years, coinciding with the detection of the first molecules in the interstellar medium. The science of astrochemistry has preceded astrobiology and occasionally deals with related topics, in particular the reactions leading to prebiotic molecules in space and their delivery to habitable planets like our primitive Earth. Laboratory astrophysics is nowadays a well-established multidisciplinary field. The true scope of these studies lies between physics and chemistry, since the gas, ice, and dust physical properties are explored, in addition to chemical reactions occurring in the gas phase, in the bare dust surface, or in the ice bulk and its surface. Since the 1970s, there is a growing worldwide community dedicated to this area of research that publishes regularly in astrophysical journals and is represented in the main symposia dedicated to astrochemistry in general. Our deep gratitude goes to all of them, who have often sacrificed their spare time to contribute to this book.

The aim of this book is to introduce laboratory astrophysics to PhD students working in this field. It can also be used as a manual for observers and modelers who are searching for information on ice and dust processes. The ultimate goal of the experimental astrophysicist is that the knowledge gained in the laboratory simulations is used to interpret the observations, or incorporated in computer models of astrophysical environments. The first two chapters are an introduction to dust grains, sometimes covered by ice mantles, in the interstellar medium and the solar system, respectively. Although icy moons and the transneptunian objects known to contain ice in the solar system were not discussed, the astronomers dedicated to their study may also use this volume for consultation. Chapter 3 is an introduction to spectroscopy and astronomical observations, since most of our knowledge on ice and dust in space is based on spectroscopic observations. Chapters 4, 5, 6 and 7 are dedicated to the ice properties: density, optical constants, quantum-chemical

description, and Monte Carlo simulations of porosity and accretion. Chapters 8, 9 and 10 are devoted to the ice processes: temperature programmed desorption, photon-induced desorption, and thermal reactivity. Chapter 11 deals with carbonaceous dust. Since the early years of astrophysics, the absorption and scattering of radiation by dust particles has been taken into consideration due to its undesirable effects on optical images. But the perspective of astronomers dedicated to study the interstellar medium is radically different, since the polarization and scattering properties of the medium trace the particle shape and their alignment with magnetic fields, among other dust grain parameters, as it will be discussed in Chap. 12. Most of the observations of molecules in space target species in the gas phase with the use of radiotelescopes. Chapter 13 is dedicated to laboratory simulations of ion processes, of interest for observations in the gas phase. There is, however, compelling evidence for the important role played by dust in the physics and chemistry of various astrophysical environments. As an example, many of the observed molecular abundances cannot be explained solely by reactions in the gas phase. Chapter 14 presents the recent astrophysical models which, in addition to the gas-phase processes, also include the dust grains.

January 2018

Guillermo M. Muñoz Caro
Rafael Escribano

Synopsis

Laboratory astrophysics is nowadays a well-established multidisciplinary field. Focused on astrophysical environments, which include asteroids, comets, the interstellar medium, and circumstellar and circumplanetary regions, its scope lies between physics and chemistry, since it explores physical properties of the gas, ice, and dust present in those systems, as well as chemical reactions occurring in the gas phase, in the bare dust surface, or in the ice bulk and its surface. There is a growing worldwide community dedicated to this area of research that publishes regularly in astrophysical journals and is represented in the main symposia dedicated to astrophysics and astrochemistry in general.

The ultimate goal of the experimental astrophysicist is that the knowledge gained in laboratory simulations is used to interpret the observations, or incorporated in computer models of astrophysical environments. This volume is designed to provide adequate material to help in such task. The aim of this book is thus to introduce and describe the use of spectroscopic tools for laboratory astrophysics and, in addition, the techniques and theoretical methods that serve to characterize the physical properties of ice: density, optical constants, morphology, and porosity. The book is addressed mainly to PhD graduates working in this field. It can also be used as a manual for observers and modelers who are searching for information on ice and dust processes.

Acknowledgements

The Spanish Ministry of Economy (MINECO) financially supported the “Cosmic Dust” network, which allowed fruitful interactions among many of the contributors to this book. Our gratitude goes to all of them.

Contents

Part I
Introduction

Chapter 1
Dust and Ice in the Interstellar Medium

Guillermo M. Muñoz Caro

Abstract This chapter presents an introduction to the bare dust grains and grains covered by ice mantles in diffuse and dense interstellar clouds. It follows the life-cycle of dust from its formation in evolved stellar atmospheres to its incorporation in bodies of the solar system. Dust particles play an important role in the physics and chemistry of numerous space environments. Regarding the dust composition, two different populations are commonly observed: silicate and carbonaceous dust. The energetic processing of ice mantles by UV, X-rays, or cosmic rays, followed by heating leads to the formation of complex organic molecules; some of them are of prebiotic interest. Delivery of this organic fraction to the primitive Earth via comets and asteroids might have contributed to the origin of life.

1.1 Introduction

The Sun is a main sequence star, a period characterized by the fusion of hydrogen in the core of the star into helium. Like any other star with a mass no greater than eight solar masses, after about 5×10^9 years, the hydrogen in the core is depleted and hydrogen fusion of the upper layers (red giant phase) is initiated, followed by helium burning in the core (horizontal branch) and the combustion of hydrogen and helium in the upper layers (asymptotic giant branch or AGB, in which the star loses much of its mass). When the mass loss stops, star contraction begins and the temperature increases (post-asymptotic giant phase). This contraction continues until the temperature is high enough to emit in the UV (planetary nebula), and nuclear fusion finishes when the star ends its days as a white dwarf.

G. M. Muñoz Caro (✉)
Centro de Astrobiología, INTA-CSIC, Torrejón de Ardoz, Madrid, Spain
e-mail: munozcg@cab.inta-csic.es

G. M. Muñoz Caro, R. Escribano (eds.), *Laboratory Astrophysics*,
Astrophysics and Space Science Library 451,
https://doi.org/10.1007/978-3-319-90020-9_1

The origin of silicate grains occurs in the atmospheres of AGB stars that eject dust grains (silicates and carbonaceous particles) into the interstellar medium. The birth of dust particles in space is, therefore, linked to the death of stars. Gas and dust in the interstellar medium constitute the so-called diffuse and dense clouds. Throughout their stay in the interstellar medium, a dust grain moves from the diffuse to the dense medium, and vice versa, until it is destroyed by shock waves during, e.g. a supernova explosion. Silicate grains are processed in the interstellar medium. In dense clouds, dust grains participate in star formation absorbing the excess energy generated during the gravitational collapse of a region in the cloud, and emit this energy in the IR range where the cloud is optically thin, allowing the release of energy. Conservation of angular momentum favors the formation of a disk around the protostar, which often evolves leading to planets, comets and asteroids. Dust grains are thus originated during the stellar death and their life ends when a new star is born. This lifecycle of dust is depicted in Fig. 1.1.

The interstellar medium, namely the space between stars, was thought to be empty but is now known to contain gas and dust. The number of interstellar molecules detected in the solid and gas phase is continuously increasing. To date, about 200 different species have been identified. The interstellar medium is, however, a harsh environment, where the high radiation field destroys the existing molecules and hinders the accretion of ice mantles onto dust grains because the temperatures are not sufficiently low. This environment is called the diffuse interstellar medium. On the other hand, the interiors of dense interstellar clouds, with densities above 10^4 particles cm^{-3}, are preserved from the external ultraviolet (UV) radiation emitted by massive stars, and the typical temperatures below 20 K permit the accretion of volatiles onto dust grains, thus forming ice mantles. Dense clouds are exposed to secondary UV-photons generated by cosmic-ray excitation of molecular hydrogen, which is expected to be no higher than 10^4 photons cm^{-2} s^{-1} (Cecchi-Pestellini and Aiello 1992; Shen et al. 2004). This weak UV-field is, however, expected to trigger photochemistry in the ice mantles, thus enriching their composition with more complex molecules. If the radiation dose is too high, the molecules desorbing to the gas phase will also be destroyed, as it often occurs in diffuse clouds. During the early stages of stellar evolution, the outer parts of circumstellar regions offer a new scenario for ice mantle processing, where the main radiation sources are the central object and the surrounding interstellar field. The coagulation of grains leading to planetesimals and cometesimals protects the photoproducts from subsequent irradiation (Muñoz Caro et al. 2006). In those environments, radiation is driven by cosmic rays (protons and heavier ions covering a wide energy range), UV photons, and X-rays; the later are expected to dominate the photon processing during the first 300 Myr of solar type stars (Ribas et al. 2005).

Space missions to comets and asteroids enrich our understanding of the formation of our solar system and also serve to characterize the most primitive matter preserved in these small bodies. The delivery of these materials via comets, (micro-) meteorites, and interplanetary dust particles to Earth enables their investigation in the laboratory. In this chapter, the dust and ice present in the interstellar medium are introduced.

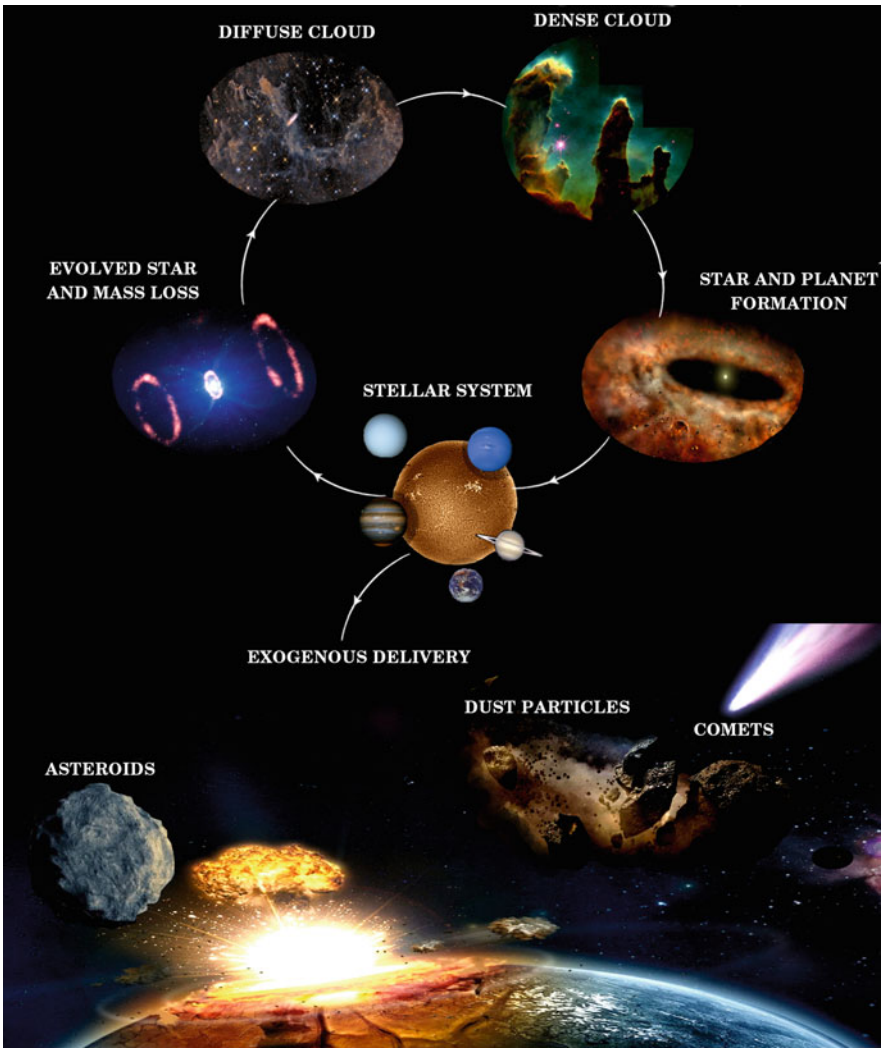

Fig. 1.1 The lifecycle of matter in the galaxy. Picture composition using images from NASA was kindly provided by G. A. Cruz-Díaz

The use of spectroscopic techniques for the observation of dust particles in space, in particular infrared (IR) and UV spectroscopy, allow the study of their composition and physical properties. A proper interpretation of the observed spectral data is done by comparison to laboratory analogs produced under mimicked astrophysical conditions. A recent and excellent review on the physics and chemistry of ice and dust is that of Öberg (2016). Some of the topics presented in this chapter were discussed in Muñoz Caro and Dartois (2013).

1.2 The Importance of Dust in Space

Ice mantles on dust grains may act as coolants during star formation, leading to smaller stars like our Sun. Dust particles also serve as catalysts for the production of H_2 molecules (Gould and Salpeter 1963), and other species present in the ice such as H_2O, detected by IR observations. Some complex molecules detected toward hot cores/corinos, where high/low mass protostars are forming, respectively, are indicative of ice mantle sublimation during warm-up of the dust. Indeed, in many cases, the molecular abundances observed by radio astronomers cannot be explained solely by reactions in the gas phase. A bare dust grain consists of a silicate and/or a carbonaceous core. The composition of the dust and the accreted ice layers is related to the materials and atomic abundances in the environment where they were formed. Relative to hydrogen, the cosmic abundances of oxygen, carbon, and nitrogen are 4.57×10^{-4}, 2.14×10^{-4}, and 0.66×10^{-4}, respectively (Snow and Witt 1996).

Most of the observed solid carbon comprised in dust particles is a type of hydrogenated amorphous carbon, known as a-C:H, or HAC in the astrophysics community. Amorphous carbon consists of an amorphous matrix composed of sp^2, sp^3, and even sp^1, hybridized C atoms. a-C stands for amorphous carbon that contains less than 20% hydrogen, while hydrogenated amorphous carbon, abbreviated as a-C:H, contains between 20% and 60% hydrogen, and therefore has a low number of C–C sp^3 bonds. The macroscopic properties of amorphous carbon are linked to its H content, sp^2/sp^3 bonding ratio, and the degree of sp^2 clustering.

Hydrogen is also abundant in ice mantles, contributing to the formation of water molecules on the dust surface and other molecules like methanol, CH_3OH, ammonia, NH_3, or methane, CH_4. While a diatomic molecule, CO, is the most abundant C-containing species observed in the gas phase, larger C-species include the fullerenes detected toward planetary nebulae (Sellgren et al. 2010; Cami et al. 2010) and the presence of polyaromatic hydrocarbons was postulated based on the observed IR emission lines of aromatic character. Oxygen is a key component in silicate grains and participates in the formation of the most abundant molecules detected in the gas phase and the ice mantles, these include H_2O, CO, and CO_2. Although some nitrogen-bearing species are routinely detected in the gas phase toward dense clouds or circumstellar environments, the presence of nitrogen in solids is rather elusive because N-bonds have intrinsically low band strengths in the IR. Relatively low abundances of NH_3, OCN^-, or HNCO were reported in icy dust. Nevertheless, nitrogen is essential for the formation of prebiotic molecules. In particular, the presence of NH_3 in ice analogs submitted to radiation leads to a very complex network of reactions in laboratory simulations.

1.2.1 Silicate Dust

IR spectroscopy allows the detection of silicate bands in emission and absorption, providing an estimation of the silicate dust column densities along the line of

sight, in Si atoms cm^{-2}, the dust temperature, and the silicate composition and structure, depending on the environment (e.g. Jäger et al. 1998). Two broad bands are observed near 10 and 18 μm (1000 and 550 cm^{-1}) toward various interstellar regions, which correspond to the Si–O stretching and O–Si–O deformation modes in silicates, respectively. The processes involved in the evolution of silicates are heating, photon and ion irradiation, shocks, destruction and recondensation. It has been observed that olivines, with chemical formula $(Mg_xFe_{1-x})_2SiO_4$, and pyroxenes, that consist of $(Mg_xFe_{1-x})SiO_3$, are usually the most abundant silicates. As it was mentioned above, amorphous silicate grains are condensed in oxygen-rich AGB stars, with a small proportion of crystalline silicates (Waters et al. 1996). While amorphous silicates are abundant in the diffuse interstellar medium, crystalline silicates dominate in circumstellar disks and cometary nuclei and comae. For a long time, this transition from amorphous to crystalline silicates remained a mistery. Observations showed that crystalline silicates can be synthesized in the surface of an inner disk by thermal annealing during a stellar outburst (Ábrahám et al. 2009).

1.2.2 Carbonaceous Dust

The presence of various types of carbon-bearing dust is noticeable thanks to the observations performed in a broad spectral range. A band observed around 2175 Å, called "the UV hump", is explained by the absorption of interstellar carbon grains with a sp^2 hybridization. The presence of various dust components and large molecules was inferred from the emission spectra observed in the diffuse medium: These are: the aromatic infrared bands (AIBs), the very small grains (VSGs) of 1–10 nm in radius, and the big grains (BG) of more than 10 nm in radius composed of silicates/carbon. The Diffuse Interstellar Bands (DIBs) in the visible are associated to large molecules. For an introductory review on dust (see Dartois 2005 and references therein).

In the mid-IR range, the 3.4-μm feature of carbon grains in the diffuse medium was not observed toward dense interstellar clouds. Some explanations were provided to solve this dilemma. It was proposed that a more dehydrogenated form of solid carbon should be a component of dust grains in dense clouds (e.g., Godard et al. 2011). This IR absorption was also observed in other galaxies (Dartois et al. 2005; Dartois and Muñoz Caro 2007). It can be decomposed in three bands peaking near 2923, 2958, and 2865 cm^{-1} that are related to the asymmetric-CH_3, asymmetric-CH_2, and symmetric-CH_3 stretching modes in aliphatic compounds, respectively. Other absorptions were observed near 6.85 μm (around 1460 cm^{-1}) and 7.25 μm (around 1380 cm^{-1}), which are attributed to CH bending modes of the same aliphatic material. A laboratory *photoproduced* a-C:H made from photoprocessing of simple aliphatic molecules can reproduce all the observed spectral features (Dartois et al. 2005), which indicates a similar composition. Carbon grains in the diffuse ISM could therefore be a form of "polymer-like" a-C:H that contains a rather

low amount of oxygen. This material is essentially made of hydrocarbon chains with olefinic and aliphatic bonds in the proportion $CH_2/CH_3 \approx 2$. Occasionally, small aromatic units of 1 or 2 rings join its composition (Dartois et al. 2005). This characterization differs from previous works describing a highly aromatic material. Because the collision time scale is too large in the interstellar medium to form a stable polymer, carbon grains likely originated in a more dense environment. It is believed that carbon dust is produced in stellar eject and spread over the interstellar medium. Various types of amorphous carbon with different aromatic and hydrogen contents are also present in small bodies of the solar system, such as comets, meteorites and interplanetary dust particles (see Muñoz Caro and Dartois 2013). Chapter 11 is dedicated to carbonaceous materials in the astrophysical context, with an emphasis on hydrogenated amorphous carbon.

1.3 Ice Mantles

As it was brought forward in Sect. 1.2, the molecular composition of interstellar and pre-cometary ice is mainly H_2O, and the less abundant species include CO, CO_2, CH_3OH, OCN^-, OCS, H_2CO, HCOOH, CH_4, and NH_3 or NH_4^+ (see, e.g., Öberg et al. 2011). The precise structure of the icy phase in dust grains is still an open question. A water-rich and a water-poor phase were proposed, which were probably formed in a H-dominated and later in a CO-controlled environment, respectively (Garrod and Pauly 2011). It is often not clear if the different molecular ice components are intimately mixed or segregated in a multilayer structure. In the case of CO_2, there is evidence for the absence of a pure and amorphous phase (Escribano et al. 2013). The effects of intermolecular forces in the IR spectral bands of multicomponent ice mixtures provides important information on the ice structure and its thermal history; this is presented in Chap. 8. For a recent review on this subject (see Boogert et al. 2015).

1.3.1 Ice Processes

The ice mantle build-up is governated by accretion and desorption of molecules on cold dust. These processes will therefore shape the evolution of dense interstellar clouds and in particular star-forming regions (e.g., Bisschop et al. 2006). Laboratory simulations of these processes under astrophysically relevant conditions are required for our understanding. An adequate interpretation of the observations toward cold interstellar regions requires a good understanding of the processes occurring at the interface between the solid (either bare dust or dust grains covered with ice mantles) and the gas phase. Most observations are performed in the radio and detect molecules in the gas. The dust is often invoked as a sort of "black box" when gas phase reactions alone cannot explain the observed molecular abundances (Fig. 1.2).

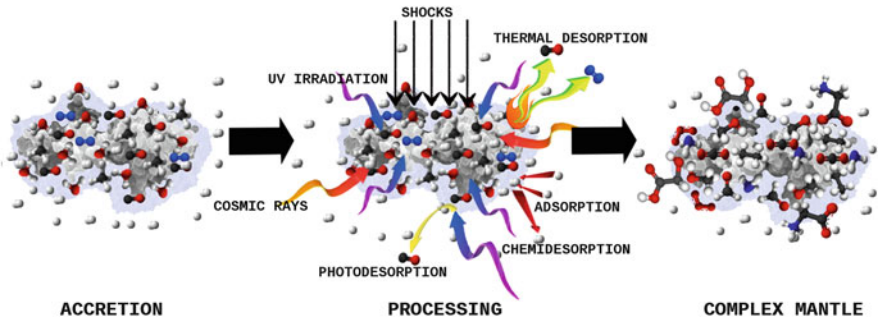

Fig. 1.2 The processes occurring on ice mantles are presumably leading to the formation of more complex species, as observed in laboratory simulations. Image provided by G. A. Cruz-Díaz

In the cold interiors of dark molecular clouds, thermal desorption should be negligible, and therefore the accretion of molecules (other than H_2) on dust particles leads to their depletion in the gas. Although carbon monoxide should deplete below 20 K, it is observed in the gas toward cold clouds at densities below ≈ 3–8×10^4 cm^{-3} (e.g., Pagani et al. 2005 and ref. therein). Other molecules like methanol and formaldehyde are also observed in cold regions (Guzmán et al. 2013). This suggests that there must be a non-thermal desorption mechanism operating in dark clouds. The release of chemical energy was proposed as a non-thermal desorption mechanism (see, e.g., Garrod et al. 2007). Ion and photo-desorption are expected to contribute significantly to the ejection of molecules from ice mantles in the absence of thermal desorption, as it will be discussed in Chap. 9.

Complex organic molecules (COMs) are observed toward dense clouds and hot cores, protoplanetary nebulae and disks, and circumstellar envelopes (see Dalgarno 2006). Among them are relatively large partly hydrogen-saturated molecules of prebiotic interest (e.g., Snyder 2006) with abundances that cannot be explained by gas phase reactions alone. Reactions on dust surfaces, or in the ice bulk, followed by desorption have been invoked to account for their abundances. As it is found experimentally, a gentle warm-up at 1 K/min of ice mixtures representative of interstellar ice does not lead to reactions of the common neutral species observed in the ice, unless a highly reactive molecule like formaldehyde is introduced; even in such case, significant reactions seem to be initiated above 30 K, at this temperature the more weakly bound CO molecules can diffuse in the ice. Irradiation of ice mixtures using energetic (UV/X-ray) photons and/or ions helps to overcome the diffusion barriers of species in the ice, thus enhancing chemical reactions and the complexity of the end products. This energetic processing of the ice mimics the conditions in dense clouds (secondary-UV photons and direct cosmic-ray bombardment), or circumstellar environments around YSOs where also X-rays can play a role in ice chemistry leading to COMs and contribute to their desorption, making these species observable for radio-astronomers. In hot cores, energetically processed ice mantles are evaporated during the warm-up phase, enhancing the

detection of these COMs (e.g., Herbst and van Dishoeck 2009). While different sources of radiation may often lead to similar products in the ice, the protocol used for the subsequent warm-up (continued or intermittent warm-up, different heating rate values) can change the product abundances. Thermal processing of the ice leading to new chemical species is discussed in Chap. 10. The next section summarizes the results of ice irradiation experiments leading to the formation of COMs.

1.3.2 COMs Made by Ice Irradiation

The IR absorptions of the most common molecular ice components hinder the detection of more complex species at cryogenic temperatures. The IR spectroscopy of the simplest biological amino acid, glycine, in the ice matrix shows the difficulty of detecting photoproducts in astrophysical ices (Maté et al. 2011). In the laboratory, the formation of relatively large photoproducts is becomes spectroscopically observable when the starting ice components sublimate (for water, this occurs around 170 K in vacuum). Consequently, the temperatures of formation of larger species are often unknown. Various analytical tools are currently being tested to detect photoproducts at low ice temperatures.

Photon or ion irradiation followed by warm-up of multicomponent ice analogs produces organic residues that are refractory at room temperature and can be extracted from the vacuum chamber for a detailed chemical analysis. At least qualitatively, the products detected in the IR after heavy ion processing were similar to those of UV irradiation using the same CH_3OH:NH_3 ice mixture and the same energy dose (Muñoz Caro et al. 2014). This material contains a large variety of species observed by infrared spectroscopy, such us hexamethylenetetramine (HMT, $[(CH_2)_6N_4]$), ammonium salts of carboxylic acids $\left[\left(\text{R–COO}^-\right)\left(\text{NH}_4^+\right)\right]$, carbamic acid ($NH_2COOH$), amides [$H_2NC(=O)$–R], esters [R–C(=O)–O–R′] and polymeric species associated to polyoxymethylene (POM, $[(–CH_2O–)_n]$) (see e.g., Bernstein et al. 1995; Muñoz Caro and Schutte 2003). Among the species detected in these residues by gas/liquid chromatography-mass spectroscopy (GC/LC–MS) are some of astrobiological interest: it contains *N*- and *O*-heterocycles including hydantoin, which are possible precursors of biological cofactors, glycine, and precursors of other amino acids (Muñoz Caro et al. 2002; Bernstein et al. 2002; Meierhenrich et al. 2005; Nuevo et al. 2006; Chen et al. 2007; de Marcellus et al. 2011; Muñoz Caro and Dartois 2013, and references therein). More recently, the reaction pathways of intermediate species leading to the formation of residue components has been studied in more depth, an example is the formation of HMT (e.g. Vinogradoff et al. 2013 and references therein). A detailed interpretation of the IR spectra of residues made from irradiation of ice mixtures with different compositions showed that CH_2 groups adjacent to OH groups are abundant (Muñoz Caro and Dartois 2009). This was confirmed, and clarified, with the detection of several sugar molecules in the residues, among them are ribose and various

structurally related species that include arabinose, xylose, and lyxose (Meinert et al. 2016). This finding reinforces the prebiotic importance of organics made by ice processing under simulated interstellar conditions.

1.4 Presence of Organics Made from UV-photoprocessing of Ice in Small Solar System Bodies

Comets and primitive meteorites act as "time machines" that allow us to take a glimpse at our solar nebula. These objects contain carbon matter that might predate our solar nebula and compounds that were formed at the early stages of our solar system. We will discuss that pre-cometary icy dust likely hosted the molecules that are found in organic refractory residues. These species are a minor component in carbonaceous chondrites. Halley-type comets might still preserve this material of prebiotic interest, while aqueous alteration of the indigenous organic material in asteroids likely changed its chemical composition.

The amino acids and polyols detected in the Murchison and Murray meteorites, with high D/H abundance ratios that suggest a formation at very low temperatures, were probably formed by ice processing. Several diamino acids, amino acids with two amino groups in their structure, found in irradiated ice residues, were also detected in Murchison (Meierhenrich et al. 2004). Other species detected in meteorites, which originated in asteroids, may have resulted from space weathering and metamorphism occurring later on the surface of these bodies. The identification of organic globules in Tagish Lake and a few other meteorites, with wall thicknesses of the globules compatible with the penetration depth of UV photons in the ice, is very intriguing (Nakamura-Messenger et al. 2006). These globules are often accompanied by elevated D/H and $^{15}N/^{14}N$ ratios, which are also indicative of processes occurring at very low temperatures. They could have formed by UV-processing and evaporation of ice mantles in the local cloud or later in the protosolar disk (Nakamura-Messenger et al. 2006). They were also found in carbonaceous chondrites, micrometeorites, interplanetary dust particles, and cometary Stardust samples (Matrajt et al. 2012). This discovery suggests that the UV-irradiation of ice mantles in space is a common and important phenomenon.

The in situ measurement of the cometary dust, ejected during the first landing of Philae during the Rosetta mission, led to the tentative identification of 16 species using the mass-spectrometer of the COSAC instrument (Goesmann et al. 2015). Unfortunately, this measurement could not be repeated and the gas-chromatograph did not find evidence for molecules on the comet surface, most probably due to the non-nominal landing of Philae. It is striking that most of the molecules inferred from this mass spectrum could in principle be synthesized by either two-radical reactions, or subsequent reactions of the so-formed molecules with a new radical, as it is often observed in ice irradiation experiments. The intervening radicals are indeed those readily synthesized by photodissociation of the simple ice molecules:

OH, NH, NH_2, CH_3, HCO, and CH_2OH. In addition, HCN and the anion OCN^- likely participated in the formation of two of the molecules that were used to fit the COSAC data (CH_3NCO and CH_3CN). The detection of cometary glycine by the ROSINA instrument on board the Rosetta orbiter was recently reported, and two of the molecules proposed based on the COSAC data were confirmed, methylamine (CH_3NH_2) and ethylamine ($CH_3CH_2NH_2$) (Altwegg et al. 2016).

1.5 The Delivery of Exogenous Organic Matter and the Origin of Life on Earth

Shortly after the formation of the Earth, a large number of minor bodies impacted on its surface during the late heavy bombardment about 3.9 Gyr ago. Comets experienced a migration from their original location between Uranus and Neptune due to gravitational pulls of planetesimals. According to our knowledge on the actual composition of comets and asteroids, we expect that their loads occasionally contained prebiotic species that were delivered to our young planet with some degree of alteration. Estimates based on noble metals and gas contents provide a value of the extraterrestrial mass accreted by the Earth a after core formation: 0.7–$2.7 \cdot 10^{22}$ kg. Asteroids would be the main contributors to this mass while comets would only account for 0.1% (Dauphas and Marty 2002). The D/H ratio of water in asteroids is close to the value in the Earth's oceans, while Oort cloud comets display significantly higher values. However, the D/H values in Jupiter family comets and main-belt comets appears to be similar to asteroids (Hsieh and Jewitt 2006; Altwegg et al. 2015). Although these statistics are still rather poor, this might be an indication of the relative contribution of matter from these bodies to our home planet.

The presence of extraterrestrial prebiotic molecules in carbonaceous chondrites is direct evidence of their survivability after collision. The biomass on the Earth's surface, about 10^{15} kg, can be accounted for by a modest delivery of extraterrestrial organic matter. The organic fraction in comet Halley is equivalent to roughly 10% of the actual biomass (Greenberg 1993). In addition, a considerable mass of the carbon content in comets seems to correspond to organic species that are well known as precursors of prebiotic chemistry. At least some of these compounds are common to those made by UV-irradiation of pre-cometary ice analogs in the laboratory. The molecules detected by the Rosetta instruments in the dust of comet 67P/Churyumov–Gerasimenko support this view, see Sect. 1.4. On the other hand, some meteorites of asteroidal origin also contain high amounts of carbon, in particular carbonaceous chondrites, but it is a material similar to amorphous carbon with only small amounts of organic molecules of astrobiological relevance. This seems also to be the case of interplanetary dust collected in the stratosphere. It therefore appears that comets may have driven the delivery of organic matter of biogenic importance, although more evidence for this is clearly necessary. Comets and asteroids experienced different radiation processing and thermal histories, this

is probably behind their different organic compositions. Although comets are not as pristine as we might think, they still (albeit partially) preserved the products of ice processing in space. Cometary molecules could have contributed to the prebiotic soup on the primitive Earth (Muñoz Caro and Dartois 2013, and references therein).

References

Ábrahám, P., Juhász, A., Dullemond, C.P., et al.: Nature. **459**, 224 (2009)
Altwegg, K., Balsiger, H., Bar-Nun, A., Berthelier, J.J., Bieler, A., Bochsler, P., Briois, C., Calmonte, U., Combi, M., De Keyser, J., Eberhardt, P., Fiethe, B., Fuselier, S., Gasc, S., Gombosi, T.I., Hansen, K.C., Hässig, M., Jäckel, A., Kopp, E., Korth, A., LeRoy, L., Mall, U., Marty, B., Mousis, O., Neefs, E., Owen, T., Rème, H., Rubin, M., Sémon, T., Tzou, C.-Y., Waite, H., Wurz, P.: Science. **347**, 1261952 (2015)
Altwegg, K., et al.: Sci. Adv. **2**, e1600285 (2016)
Bernstein, M.P., Sandford, S.A., Allamandola, L.J., Chang, S., Scharberg, M.A.: Astrophys. J. **454**, 327 (1995)
Bernstein, M.P., Dworkin, J.P., Sandford, S.A., Cooper, G.W., Allamandola, L.J.: Nature. **416**, 401 (2002)
Bisschop, S.E., Fraser, H.J., Öberg, K.I., van Dishoeck, E.F., Schlemmer, S.: Astron. Astrophys. **449**, 1297 (2006)
Boogert, A.C.A., Gerakines, P.A., Whittet, D.C.B.: Annu. Rev. Astron. Astrophys. **53**, 541 (2015)
Cami, J., Bernard-Salas, J., Peeters, E., Malek, S.E.: Science. **329**, 1180 (2010)
Cecchi-Pestellini, C., Aiello, S.: Mon. Not. R. Astron. Soc. Lett. **258**, 125 (1992)
Chen, Y.-J., Nuevo, M., Hsieh, J.-M., Yih, T.-S., Sun, W.-H., Ip, W.-H., Fung, H.-S., Chiang, S.-Y., Lee, Y.-Y., Chen, J.-M., Wu, C.-Y.R.: Astron. Astrophys. **464**, 253 (2007)
Dalgarno, A.: Faraday Discuss. **133**, 9 (2006)
Dartois, E.: ASP Conference Series. In: Lidman C., Alloin D. (eds.), pp. 344, 113.M. Astronomical Society of the Pacific, San Francisco (2005)
Dartois, E., Muñoz Caro, G.M.: Astron. Astrophys. **476**, 1235 (2007)
Dartois, E., Muñoz Caro, G.M., Deboffle, D., Montagnac, G., d'Hendecourt, L.: Astron. Astrophys. **432**, 895 (2005)
Dauphas, N., Marty, B.: J. Geophys. Res. **107**(E12), 5129 (2002)
de Marcellus, P., Meinert, C., Nuevo, M., Filippi, J.-J., Danger, G., Deboffle, D., Nahon, L., d'Hendecourt, L., Meierhenrich, U.J.: Astrophys. J. **727**, L27 (2011)
Escribano, R.M., Muñoz Caro, G.M., Cruz-Díaz, G.A., Rodríguez-Lazcano, Y., Maté, B.: Proc. Natl. Acad. Sci. U.S.A. **110**, 12899 (2013)
Garrod, R.T., Pauly, T.: Astrophys. J. **735**, 15 (2011)
Garrod, R.T., Wakelam, V., Herbst, E.: Astron. Astrophys. **467**, 1103 (2007)
Godard, M., Feraud, G., Chabot, M.: Astron. Astrophys. **529**, A146 (2011)
Goesmann, F., Rosenbauer, H., Bredehöft, J.-H., Cabane, M., Ehrenfreund, P., Gautier, T., Giri, C., Krüger, H., Le Roy, L., MacDermott, A.J., McKenna-Lawlor, S., Meierhenrich, U.J., Muñoz Caro, G.M., Raulin, F., Roll, R., Steele, A., Steininger, H., Sternberg, R., Szopa, C., Thiemann, W., Ulamec, S.: Science. **349**, 6247 (2015)
Gould, R.J., Salpeter, E.E.: Astrophys. J. **138**, 393 (1963)
Greenberg, J.M.: In: Greenberg, J.M., Pirronello, V. (eds.) The Chemistry of Life's Origins, p. 195. Kluwer, Dordrecht (1993)
Guzmán, V.V., Goicoechea, J.R., Pety, J., Gratier, P., Gerin, M., Roueff, E., Le Petit, F., Le Bourlot, J., Faure, A.: Astron. Astrophys. **560**, A73 (2013)
Herbst, E., van Dishoeck, E.F.: Annu. Rev. Astron. Astrophys. **47**, 427 (2009)
Hsieh, H.H., Jewitt, D.: Science. **312**, 561 (2006)

Jäger, C., Molster, F.J., Dorschner, J., Henning, T., Mutschke, H., Waters, L.B.F.M.: Astron. Astrophys. **339**, 904 (1998)
Maté, B., Rodriguez-Lazcano, Y., Gálvez, Ó., Tanarro, I., Escribano, R.: Phys. Chem. Chem. Phys. **13**, 12268 (2011)
Matrajt, G., Messenger, S., Brownlee, D., Joswiak, D.: Meteorit. Planet. Sci. **43**, 525 (2012)
Meierhenrich, U.J., Muñoz Caro, G.M., Bredehöft, J.H., Jessberger, E.K., Thiemann, W.H.-P.: Proc. Natl. Acad. Sci. U.S.A. **101**(25), 9182 (2004)
Meierhenrich, U.J., Muñoz Caro, G.M., Schutte, W.A., Thiemann, W.H.-P., Barbier, B., Brack, A.: Chem. Eur. J. **11**, 4895 (2005)
Meinert, C., Myrgorodska, I., de Marcellus, P., Buhse, T., Nahon, L., Hoffmann, S.V., d'Hendecourt, L., Meierhenrich, U.J.: Science. **352**, 208 (2016)
Muñoz Caro, G.M., Dartois, E.: Astron. Astrophys. **494**, A109 (2009)
Muñoz Caro, G.M., Dartois, E.: Chem. Soc. Rev. **42**, 2173 (2013)
Muñoz Caro, G.M., Schutte, W.A.: Astron. Astrophys. **412**, 121 (2003)
Muñoz Caro, G.M., Meierhenrich, U.J., Schutte, W.A., Barbier, B., Arcones Segovia, A., Rosenbauer, H., Thiemann, W.H.-P., Brack, A., Greenberg, J.M.: Nature. **416**, 403 (2002)
Muñoz Caro, G.M., Matrajt, G., Dartois, E., Nuevo, M., D'Hendecourt, L., Deboffle, D., Montagnac, G., Chauvin, N., Boukari, C., Le Du, D.: Astron. Astrophys. **459**, 147 (2006)
Muñoz Caro, G.M., Dartois, E., Boduch, P., Rothard, H., Domaracka, A., Jiménez-Escobar, A.: Astron. Astrophys. **566**, A93 (2014)
Nakamura-Messenger, K., Messenger, S., Keller, L.P., Clemett, S.J., Zolensky, M.E.: Science. **314**, 1439 (2006)
Nuevo, M., Meierhenrich, U.J., Muñoz Caro, G.M., Dartois, E., D'Hendecourt, L., Deboffle, D., Auger, G., Blanot, D., Bredehöft, J.-H., Nahon, L.: Astron. Astrophys. **457**, 741 (2006)
Öberg, K.I.: Chem. Rev. (2016). https://doi.org/10.1021/acs.chemrev.5b00694
Öberg, K.I., Boogert, A.C.A., Pontopidan, K.M., van den Broek, S., van Dishoeck, E.F., et al.: Astrophys. J. **740**, 109 (2011)
Pagani, L., Pardo, J.-R., Apponi, A.J., Bacmann, A., Cabrit, S.: Astron. Astrophys. **429**, 181 (2005)
Ribas, I., Guinan, E.F., Gudel, M., Audard, M.: Astrophys. J. **622**, 680 (2005)
Sellgren, K., Werner, M.W., Ingalls, J.G., Smith, J.D.T., Carleton, T.M., Joblin, C.: Astrophys. J. **722**, L54 (2010)
Shen, C.J., Greenberg, J.M., Schutte, W.A., van Dishoeck, E.F.: Astron. Astrophys. **415**, 203 (2004)
Snow, T.P., Witt, A.N.: Astrophys. J. **468**, L65 (1996)
Snyder, L.E.: PNAS. **103**, 12243 (2006)
Vinogradoff, V., Fray, N., Duvernay, F., Briani, G., Danger, G., Cottin, H., Theulé, P., Chiavassa, T.: Astron. Astrophys. **551**, A128 (2013)
Waters, L.B.F.M., Molster, F.J., de Jong, T., et al.: Astron. Astrophys. **315**, L361 (1996)

Chapter 2
Icy Grains in the Solar System: Cometary and Asteroidal Environments

Fernando Moreno

Abstract Icy grains have been directly detected or inferred in the circumnuclear region of various short- and long-period comets. In particular, comets 103P/Hartley 2, C/2002 T7 (LINEAR), and, recently C/2013 OS10 (Catalina) and 67P/Churyumov–Gerasimenko have been found to eject dust particles with a variable proportion of ice content. In this chapter, we report on the theoretical computation of the equilibrium temperature of sublimating grains composed by a varying amount of water ice, silicate, and carbon materials, and its variation with grain size and heliocentric distance. It is shown that even a small addition of absorbing impurities to a pure water ice grain reduces dramatically its survival. A particular application to comet 67P, the ESA Rosetta Mission target, is provided.

2.1 Introduction

Ices are ubiquitous in the Solar System. They can be found in places as close to the Sun as 0.1 Astronomical Units (AU), in deep craters in permanent shadow in the polar regions of Mercury, and as far as the surface of Oort cloud comet nuclei at distances of the order of 10^5 AU. The primordial interstellar cloud of gas and dust collapsed into a disk with a proto-Sun in its center and a rotating nebula. In the first stages of formation, the temperature of the nebula was as high as 2000 K, but as it cooled down, different elements condensed onto grains of rock and ice. Eventually, the temperature decreased to about 300 K where the condensation of various gases such as water, carbon dioxide, and ammonia, took place. Collisions and subsequent coagulation of the available material led to the formation of planetesimals, which in turn become planets by accretion. In the innermost solar system, rocky planets with few ices formed, because the temperature was too high to allow the ices to be thermodynamically stable in time scales of several Myr, and to retain light

F. Moreno (✉)
Instituto de Astrofísica de Andalucía, CSIC, Granada, Spain
e-mail: fernando@iaa.es

G. M. Muñoz Caro, R. Escribano (eds.), *Laboratory Astrophysics*,
Astrophysics and Space Science Library 451,
https://doi.org/10.1007/978-3-319-90020-9_2

gases like H_2 and He. In the outer solar system regions, large planets with dense rocky/ice cores and extended H_2 and He atmospheres developed. Comets formed beyond the water frost line (also known as snowline), where ices can condense. In order to explain the high production rate of OH molecules found in the coma of the Oort cloud comet Bowell at large heliocentric distances (A'Hearn et al. 1984; Hartman and Cruikshank 1984) hypothesized the existence of water–ice particles in its coma. More recently, the space mission Deep Impact eXtended Investigation (DIXI) encountered comet 103P/Hartley 2 in 2010, where water ice grains were detected unambiguously by infrared reflectance spectra (Protopapa et al. 2014). It seems natural, owing to the comet nuclei composition of rocks and ice, that in those grains a mixture of refractory and volatile components occurs. 103P is one example of the so-called hyperactive comets, the ones that produce more H_2O per unit time than it should be possible by sublimation from the small surface area of their nuclei. Other comets of this class are 46P/Wirtanen and 21P/Giacobini–Zinner. Also, from the Deep Impact Experiment on 9P/Tempel 1, it was found that a sustained water production could be explained by the sublimation of submicron grains (Gicquel et al. 2012). Some Oort cloud comets have also shown evidence of an icy grain halo [e.g., C/2009 P1 (Garradd), see Combi et al. 2013]. Other less active comets, such as 67P/Churyumov–Gerasimenko, the target of Rosetta mission, have not shown such icy grain showers, as comes out from the results of several instruments, including COSIMA (Schulz et al. 2015). Individual spectra of single grains, analyzed with images obtained with the OSIRIS camera (Cremonese et al. 2016) show a red slope for a majority of grains, but a non-negligible fraction of grains having higher reflectivity in the blue than in the red have also been found, whose composition could include hydrated minerals or even some ice (Cremonese et al. 2016). Large boulders ejected near perihelion for which spectral images have been obtained with OSIRIS cameras could also contain ice, as at least one of those boulders observed shows a blue spectrum (Fulle et al. 2016).

In addition to comets, a new class of solar system objects have now appeared, the so-called active asteroids, sometimes also referred to as main-belt comets (see the excellent review by Jewitt et al. 2015). These objects, most of them located in the main asteroid belt, exhibit asteroidal orbits, but cometary-like appearance (coma and tails). It turns out that a variety of physical mechanisms are responsible of their activity, including impact-induced [e.g., the case of (596) Scheila, see Moreno et al. 2011], or rotational instability, leading to a partial or total fragmentation of the parent nucleus (e.g., P/2013 R3, see Jewitt et al. 2014). These mechanisms might be responsible for the excavation of surface layers, exposing fresh ices to the solar radiation, which can sublimate in the same way as on a comet surface. In fact, a sizable amount of these objects show sustained activity over periods of the order of several months that is most easily explained by ice sublimation (Jewitt et al. 2015). However, this is questionable, as no positive detection of any sublimating gases has been reported so far, although this is hampered by the faintness of these objects, most of them being discovered at visual magnitudes in excess of 20.

The interpretation of dust tail data acquired from Earth-based telescope images is a powerful tool to derive the dust physical parameters: size distribution, ejection

velocities, and mass loss rate as functions of the heliocentric distance. Advanced Monte Carlo dust tail modeling (e.g. Moreno et al. 2012) has allowed us to retrieve those quantities for a number of short- and long-period comets, as well as most of the recently discovered activated asteroids. However, in the modeling procedure it is customary to consider the dust particles as having a refractory composition, for which processes like fragmentation (which has been invoked to explain the striae in the tails of e.g. comet West, see Sekanina and Farrell 1980, although the latest research point to a sublimation-driven YORP-like effect, see Steckloff and Jacobson 2016) or size variations due to sublimation, have usually been neglected. In this chapter, we describe the process of sublimation of pure and dirty water ice grains, and provide the necessary background on how to perform calculations of the variation in size expected from sublimation of different grain composition as a function of the heliocentric distance. Although this topic has already been addressed, it is appropriate to re-formulate it by incorporating updated information on the physical parameters involved (e.g., the optical constants of the particles) and providing details on the procedures. As an example, we will describe a study of the evolution of the icy grains possibly ejected from the nucleus of comet 67P.

2.2 Equilibrium Temperature of Icy Grains

For simplicity, we will consider that the grains are compact and spherical. The equilibrium temperature of a single grain of radius a in space is computed from the balance between heating due to the solar energy absorbed and cooling due to the energy emitted plus the energy involved in the ice sublimation process, as:

$$\frac{\pi a^2}{r^2}\int_0^\infty S(\lambda)\, Q_{abs}(\lambda, a)\, d\lambda = 4\pi a^2 \int_0^\infty Q_{abs}(\lambda, a)\, \pi B_\lambda(T) d\lambda + L_v(T) P_v(T)\sqrt{\frac{m}{2\pi k T}}, \tag{2.1}$$

where $S(\lambda)$ is the solar flux at 1 AU, r is the heliocentric distance, λ is the wavelength of the light, $Q_{abs}(\lambda,a)$ is the absorption efficiency of the particle, T is the equilibrium temperature, and B_λ is the Planck function. In the sublimation term, L_v is the latent heat of sublimation, P_v is the equilibrium vapor pressure, m is the mass of a water molecule, and k is the Boltzmann constant. We use the expressions for L_v as given by Murphy and Koop (2005):

$$L_v(T) = 46782.5 + 35.8925T - 0.07414T^2 + 541.5\, exp\{-[T/123.75]^2\} \tag{2.2}$$

which is valid for $T > 30$ K, and where $L_v(T)$ is expressed in units of J mol^{-1}.

We will be dealing with ice grains with some impurities. Thus, assuming that no chemical bonds exist between the host water ice and the absorbing inclusions, the

vapor pressure formula of dirty water ice is expected to be the same as that of pure water ice (Mukai et al. 1989). There are available expressions for the vapor pressure as a function of T, depending on the temperature range. The International Critical Tables (ICT) gives the following formula (Washburn 1928):

$$\log_{10} P_v(T) = -2445.5646/T + 8.2312\log_{10} T - 0.01677006T + 1.20514 \times 10^{-5} T^2 - 3.63227 \tag{2.3}$$

which is valid for temperatures between 173 and 273 K, where $P_v(T)$ is in units of dyn cm^{-2}. At lower temperatures, the expression by Kelley (1935) becomes more appropriate (see Lamy 1974; Mukai 1986):

$$\log_{10} P_v(T) = -2641/T + 3.857\log_{10} T - 3.41 \times 10^{-3} T + 4.875 \times 10^{-8} T^2 - 3.332 \tag{2.4}$$

Léger et al. (1983) deduced another formula which is close to that of the ICT for high temperatures and to that of Kelley (1935) at low temperatures (see Fig. 2.1). This function was parameterized by Mukai et al. (1989), and will be the one used here to obtain the size loss rate (see next section).

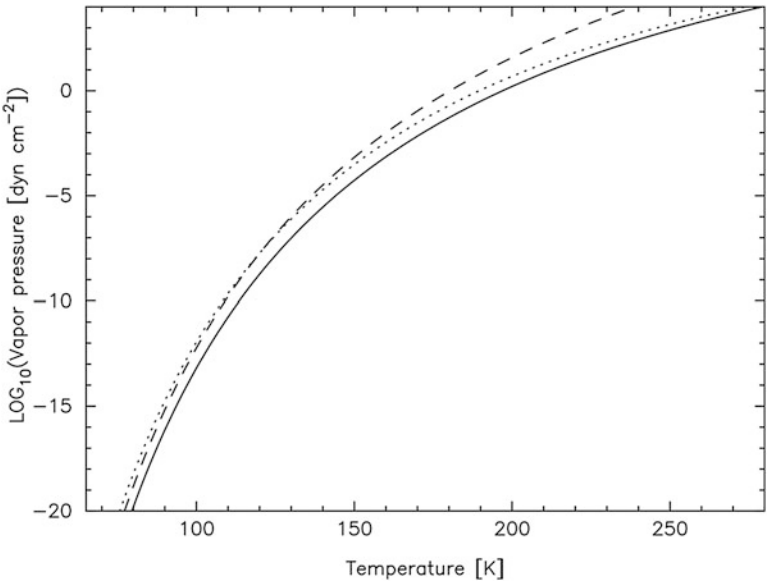

Fig. 2.1 Equilibrium vapor pressure on water ice as a function of temperature. The solid line is the function from the International Critical Tables, valid in the range 173–273 K, the dashed line is that derived by Kelley (1935), appropriate for low temperatures, and the dotted line is the function used in this study, adopted from Mukai et al. (1989), based on Léger et al. (1983)

The Sun is assumed as a black-body radiator at $T_{sun} = 5777$ K (Cox 2000). For a certain refractive index, Mie theory provides the values of the absorption efficiencies as a function of wavelength and size. To obtain these efficiencies, we used the Mie code version as given by Bohren and Huffman (1983). Since we are interested in icy grains with some "dirt" material as inclusions, some effective medium theory must be invoked. We use a generalized Maxwell-Garnett (1904) expression for the case of n-component mixtures as given as (Aspens 1982):

$$\frac{\varepsilon_{eff}-\varepsilon_0}{\varepsilon_{eff}+2\varepsilon_0} = f_1\frac{\varepsilon_1-\varepsilon_0}{\varepsilon_1+2\varepsilon_0} + f_2\frac{\varepsilon_2-\varepsilon_0}{\varepsilon_2+2\varepsilon_0} + f_3\frac{\varepsilon_3-\varepsilon_0}{\varepsilon_3+2\varepsilon_0} + \ldots \tag{2.5}$$

where f_i and ε_i are the volume fraction and (complex) dielectric constant of the i-th component and ε_0 is the dielectric constant of the host material. The effective dielectric constant is denoted as ε_{eff}. The dielectric constant and the refractive index $m = n + ik$ are related by $m = \sqrt{\varepsilon}$. For a given mixture, the refractive index can be then calculated as a function of wavelength and then the equilibrium temperature can be obtained by solving Eq. (2.1). This implicit equation is solved by the van Wijngaarden–Dekker–Brent method, which was improved by Brent (1973). The method combines root bracketing, bisection, and inverse quadratic interpolation. We used the FORTRAN implementation of Brent's method as described in Press et al. (1992).

The refractive index of pure water ice is taken from Warren (1984) (see Fig. 2.2). As inclusions, we consider amorphous silicate ($MgSiO_3$), taken from the JENA database (Jäger et al. 2003) (see Fig. 2.3), and glassy carbon, taken from Edoh (1983) (Fig. 2.4). We denote the volume fraction of silicate and carbon inclusions as f_1 and f_2, respectively. We have computed the equilibrium temperatures for a variety of compositions, as a function of size and heliocentric distances. Figure 2.5 shows the grain temperatures at $r = 1$ AU and $r = 3.5$ AU, as being representative of the orbital distances of short-period comets near perihelion and at the distance where dust production is already significant. The dashed flat lines represent the black-body temperatures at those distances from the Sun, given by $T_{BB} = T_{sun}(R_{sun}/2r)^{1/2}$, where $R_{sun} = 6.955 \times 10^5$ km is the solar radius. As expected, the pure-ice grains attain the lowest equilibrium temperatures. It is interesting to see how the addition of a small amount of impurities to the water ice grains affects the equilibrium temperature. Thus, since small carbonaceous grains of radii smaller than a few microns become much hotter than a theoretical black-body, owing to the fact that they absorb strongly in the visual, but cannot radiate efficiently at infrared wavelengths, a small addition of carbon ($f_1 = 0.0, f_2 = 0.1$) increases dramatically the equilibrium temperature. However, for the same volume fraction of silicate inclusions ($f_1 = 0.1, f_2 = 0.0$), only the grain temperatures of relatively large grains ($a \approx 10$ μm or larger) are larger than the corresponding to pure water–ice grains. This is related to the low absorption (low imaginary index) of these silicate grains in the visual. Intermediate silicate/carbon mixtures, such as the one shown in Fig. 2.5 in dotted line ($f_1 = 0.1, f_2 = 0.001$), show intermediate results between those cases regarding equilibrium temperatures, as expected.

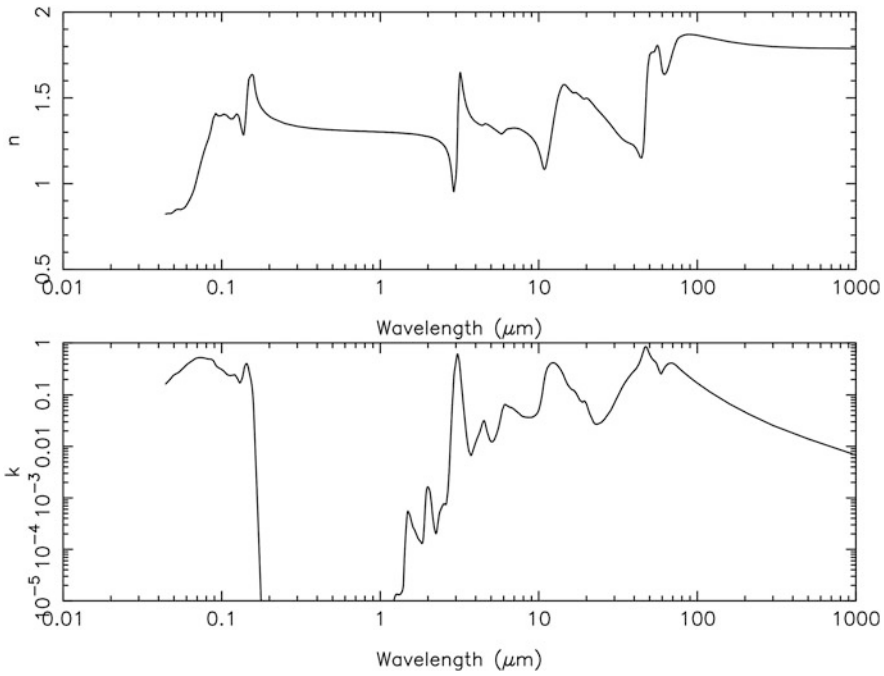

Fig. 2.2 Refractive index of water ice as a function of wavelength from Warren (1984). Upper panel, real part (n). Lower panel, imaginary part (k)

2.3 Size Loss Rate of Pure and Dirty Water Ice Particles in Space

In order to obtain the reduction in size of a grain by sublimation of the water ice, we need to know the temperature of the grain as a function of the radius and the heliocentric distance. This has been described in the previous section.

Adopting the parameterization of the vapor pressure curve by Mukai et al. (1989) (see Fig. 2.1), the size loss rate is given by:

$$\frac{da}{dt} = 7.2 \times 10^7 \mathrm{T}^{7/2} \exp\left[5505 + 165\left(\frac{T}{140}\right)^{2.4}\right] / T\Big\} \tag{2.6}$$

where *da/dt* is in units of cm yr^{-1}. Figure 2.6 shows the results of this quantity as a function of the heliocentric distance for particles of 10 μm and 316 μm of various volume fractions of impurities. For particles of $a = 10$ μm, those with only silicate inclusions ($f_1 = 0.1, f_2 = 0.0$), have loss rates just above the pure water–ice particles. For larger sizes, the difference increases, as expected from the higher equilibrium temperature. For particles contaminated with silicate plus a small

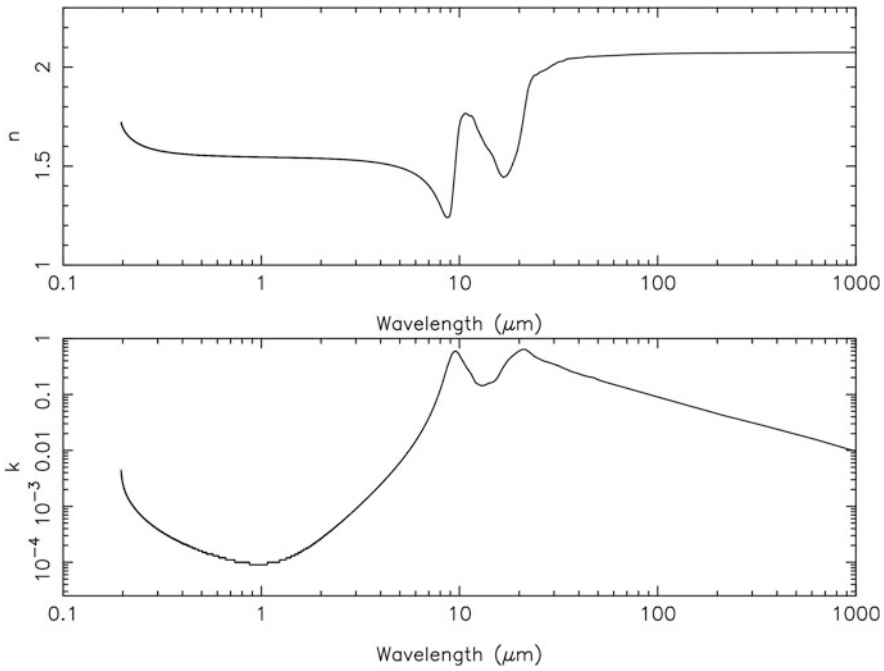

Fig. 2.3 Refractive index of SiO_3 as a function of wavelength Jäger et al. 2003. Upper panel, real part (n). Lower panel, imaginary part (k)

addition of carbon inclusions ($f_1 = 0.1, f_2 = 0.001$), the differences in loss rate are huge (by six and seven orders of magnitude) compared to pure ice-particles for both sizes. This illustrates the fact that even a small amount of impurity (as expected in nature) can change dramatically the survival of dirty ice particles, depending of course on the heliocentric distance at ejection, in agreement with previous results (see, e.g., Mukai et al. 1989, and references therein).

2.4 Application to Icy Grains Ejected from Comet 67P/Churyumov–Gerasimenko

The size loss rate equation can be used to compute the size evolution of a pure or dirty ice grain ejected from a particular comet at a given orbital position. As an example, let us take the target of the successful Rosetta mission, comet 67P/Churyumov–Gerasimenko. The heliocentric distance of the comet as a function of time to perihelion can be obtained precisely from the JPL Horizons Web-Interface Facility (ssd.jpl.nasa.gov/horizons.cgi). We assume that the particles remain close to the comet nucleus, which is strictly true only for large particles, owing to their

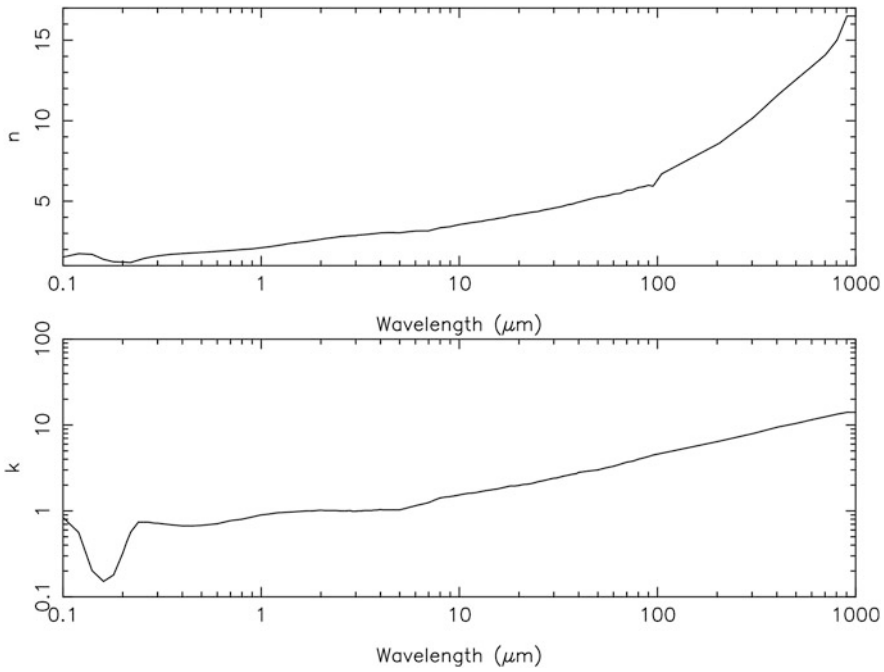

Fig. 2.4 Refractive index of glassy carbon as a function of wavelength (Edoh 1983). Upper panel, real part. Lower panel, imaginary part

low ejection velocities and the weakness of the radiation pressure. To perform the calculations, we generate tables of the size loss rate as function of the heliocentric distance and particle radius. In order to obtain the size of the particle as a function of time, we use a bilinear interpolation to retrieve the loss rate for any size and heliocentric distance. We performed computations at two locations in the orbit at which the icy particles are assumed to be ejected: at 2.5 AU pre-perihelion, i.e., approximately 205 days before perihelion, and at perihelion time. In the two cases, we assume three different compositions: pure water ice, water ice plus silicate inclusions ($f_1 = 0.1, f_2 = 0.0$), and water ice plus silicate inclusions and a small addition of carbon inclusions ($f_1 = 0.1, f_2 = 0.001$). Three initial grain sizes are assumed: 10, 100, and 1000 μm. We study the size evolution for a 300-days period after ejection from the comet nucleus. Figure 2.7 shows the results for ejection at 2.5 AU pre-perihelion, and Fig. 2.8 for ejection at perihelion.

From Fig. 2.7, it can be noticed that pure water ice grains of radii smaller than 100 μm survive perihelion passage with size unchanged. Larger grains experience some size reduction, however, because of their higher equilibrium temperature. Grains with silicate inclusions ($f_1 = 0.1, f_2 = 0.0$) of size 10 μm or smaller are also unaffected, but they start to show significant reduction in size for radii >100 μm. The most dramatic evolution is shown for the grains with both silicate and carbon

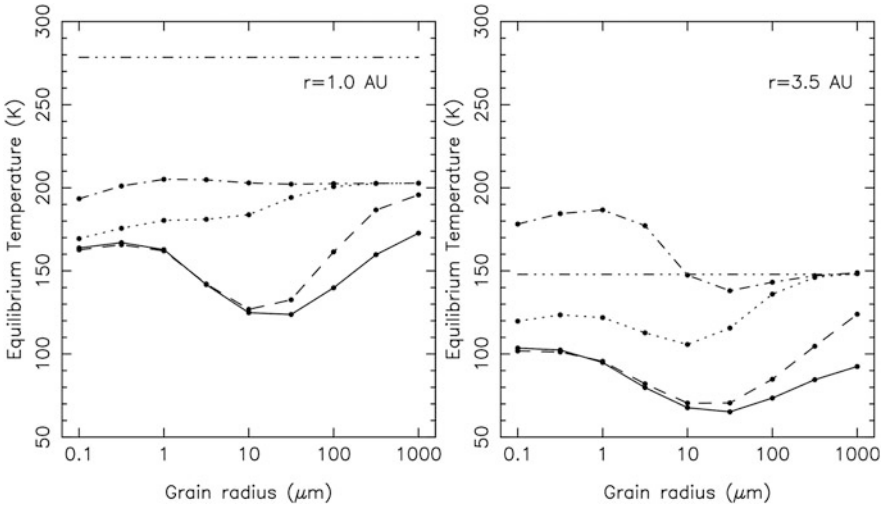

Fig. 2.5 Equilibrium temperatures as a function of grain size at two heliocentric distances, 1 AU (left panel) and 3.5 AU (right panel). The solid lines refer to pure water ice, the dashed lines correspond to water ice with a fraction of $f_1 = 0.1$ of silicate, the dash-dotted line with a fraction of $f_2 = 0.1$ carbon, and the dotted line to volume fractions of silicate ($f_1 = 0.1$) and carbon ($f_2 = 0.001$). The straight dash-dash-dotted lines correspond to the black body temperatures

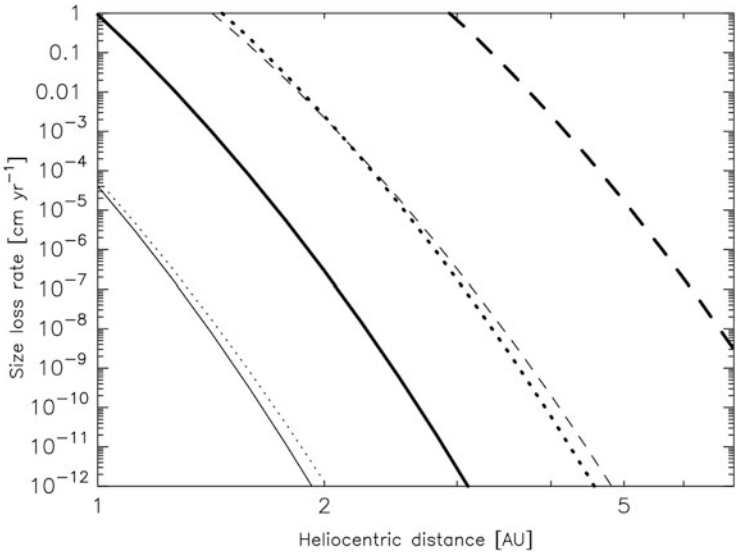

Fig. 2.6 Size loss rate as a function of heliocentric distance for particles of 10 μm (thin lines) and 316 μm (thick lines), for pure water ice (solid lines), water ice with silicate inclusions ($f_1 = 0.1$) (dotted lines), and water ice with both silicate and carbon inclusions ($f_1 = 0.1, f_2 = 0.001$) (dashed lines)

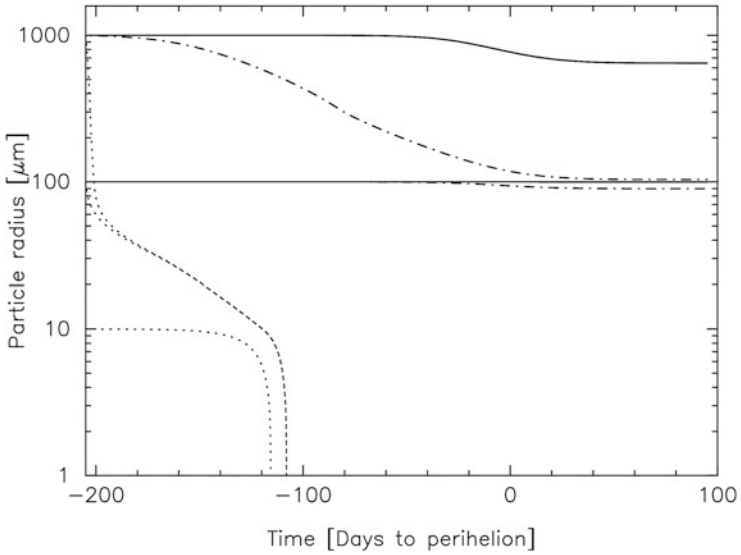

Fig. 2.7 Evolution of size of icy particles launched from 67P at about 2.5 AU pre-perihelion, at three initial radii, 10, 100, and 1000 μm. Pure water ice particles are represented by solid lines, water ice with silicate inclusions ($f_1 = 0.1$) by dash-dotted lines, and water ice with both silicate and carbon inclusions ($f_1 = 0.1, f_2 = 0.001$) by dotted lines. The evolution of 10 μm particles of pure water ice and water ice with silicate inclusions are not drawn because they do not experience any change of size in that time interval

inclusions ($f_1 = 0.1, f_2 = 0.001$), which are completely destroyed by sublimation some 120 before perihelion. Figure 2.8, which displays the grain size evolution during a few days after perihelion ejection, show that those absorbing grains are sublimated in just a few hours at most. Water ice grains with silicate inclusions ($f_1 = 0.1$, $f_2 = 0.0$) of radii smaller than 100 μm survive perfectly if ejected at perihelion, but large grains (1000 μm) of the same composition experience a quick reduction of size first and then, after several days, they converge to a radii of ≈100 μm. On the other hand, pure ice grains do not experience any significant sublimation except those large grains of 1000 μm, which decrease very slowly in radius to about ≈800 μm some 30 days post-perihelion.

2.5 Conclusions

The physical properties of the dust particles are needed for the interpretation of dust tail images from comets and activated asteroids. From this study, it is clear that if icy grains are being ejected from a comet nucleus or an activated asteroid, the nature and precise amount of impurities that those grains might contain will determine their survival. Specifically, pure water ice grains or water ice grains with inclusions of a

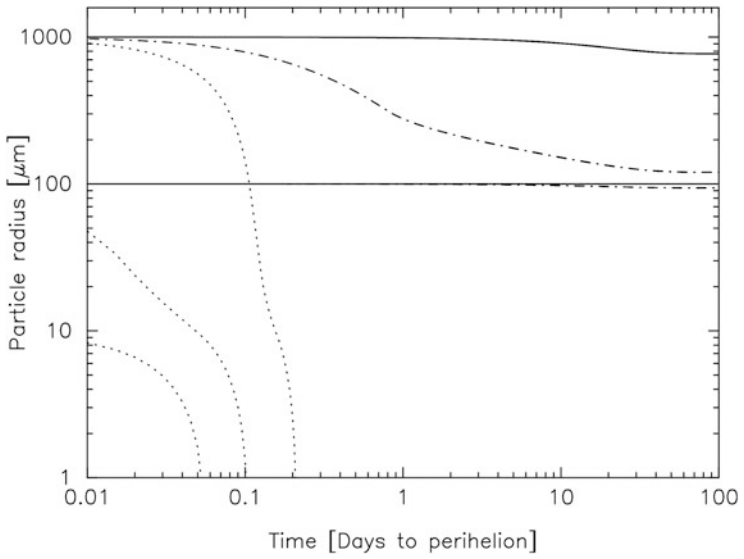

Fig. 2.8 Evolution of size of icy particles launched from 67P at perihelion, at three initial sizes, 10, 100, and 1000 μm. Pure water ice particles are represented by solid lines, and water ice with silicate inclusions ($f_1 = 0.1$) by dash-dotted lines. The evolution of 10 μm particles of pure water ice and water ice with silicate inclusions are not drawn because they do not experience any significant change in size in that time interval. Grains of water ice with both silicate and carbon inclusions ($f_1 = 0.1, f_2 = 0.001$) (dotted lines) are quickly sublimated after a few hours since ejection

material poorly absorbing in the visual, such as $MgSiO_3$, i.e., silicates with no iron content, can survive perihelion passage, experiencing at most a modest reduction in size. However, even a small addition of a highly absorbing material to the water ice grain can produce a very strong increase in the equilibrium temperature, especially important for the largest sizes, implying a very short lifetime, limiting in practice the detectability of those particles. Although this study is based on the assumptions of compact and spherical grains, and relays on the validity of the effective medium theories (e.g. Maxwell-Garnett), it provides an order-of-magnitude estimate of the sublimation lifetime of those icy particles along the orbital path.

References

A'Hearn, M., et al.: Astrophys. J. **89**, 579 (1984)
Aspens, D.E.: Am. J. Phys. **50**, 704 (1982)
Bohren, C.F., Huffman, D.R.: Absorption and Scattering of Light by Small Particles. Wiley, New York (1983)
Brent, R.P.: Algorithms for Minimization Without Derivatives. Prentice-Hall, Englewoods Cliffs, NJ (1973)
Combi, M., et al.: Icarus. **225**, 740 (2013)

Cox, A.N.: Allen's Astrophysical Quantities, 4th edn. Springer, New York (2000)
Cremonese, G., et al.: Astron. Astrophys. **588**, 59 (2016)
Edoh, O.: Optical constants of carbon from the far infrared to the far ultraviolet. Ph.D. Thesis, University of Arizona (1983)
Fulle, M., et al.: Astrophys. J. **821**, 19 (2016)
Gicquel, A., et al.: Astron. Astrophys. **542**, A119 (2012)
Hartmann, W.K., Cruikshank, D.P.: Icarus. **57**, 55 (1984)
Jäger, C., et al.: Astron. Astrophys. **408**, 193 (2003)
Jewitt, D., et al.: Astrophys. J. **784**, L8 (2014)
Jewitt, D., et al.: The active asteroids. In: Michel, P., DeMeo, F., Bottke, W.F. (eds.) *Asteroids IV*, pp. 221–242. University of Arizona, Tucson, AZ (2015)
Kelley, K.K.: US Bur. Mines Rep. Invest. **383**, 35 (1935)
Lamy, P.L.: Astron. Astrophys. **35**, 197 (1974)
Léger, A., et al.: Astron. Astrophys. **117**, 164 (1983)
Maxwell-Garnett, J.C.: Philos. Trans. R. Soc. A. **203**, 385 (1904)
Moreno, F., et al.: Astrophys. J. **738**, 130 (2011)
Moreno, F., et al.: Astrophys. J. **752**, 136 (2012)
Mukai, T.: Astron. Astrophys. **164**, 397 (1986)
Mukai, T., et al.: Icarus. **80**, 254 (1989)
Murphy, D.M., Koop, T.: Q. J. R. Meteorol. Soc. **131**, 1539 (2005)
Press, W.H., et al.: Numerical Recipes in FORTRAN. Cambridge University, Cambridge (1992)
Protopapa, S., et al.: Icarus. **238**, 191 (2014)
Schulz, R., et al.: Nature. **518**, 216 (2015)
Sekanina, Z., Farrell, J.A.: Astron. J. **85**, 1538 (1980)
Steckloff, J.K., Jacobson, S.A.: Icarus. **264**, 160 (2016)
Warren, S.G.: Appl. Opt. **23**, 1206 (1984)
Washburn, E.W.: International Critical Tables of Numerical Data, Physics, Chemistry and Technology, vol. III. McGraw-Hill, New York (1928)

Chapter 3
Introduction to Spectroscopy and Astronomical Observations

Rafael Escribano and Guillermo M. Muñoz Caro

Abstract This chapter presents an introduction to the techniques and tools used in astronomy and astrophysics research, mainly focused on spectroscopy. The basic concepts of spectroscopy are first described, from the Schrödinger equation to the Lambert–Beer's law. The spectroscopy of solid systems, widely found in astronomical media, is studied in more detail. An introduction is provided also to the basic concepts of astronomical observations, and the information that can be obtained from them, both in the gas phase and in solid systems. An appendix is included with conversion factors for some of the many magnitudes and units employed in this area.

3.1 Introduction

The aim of this chapter is to provide an introduction to the basic tools employed in research in astronomy and astrophysics. Spectroscopy is the branch of science that studies the interaction between matter and electromagnetic radiation, and therefore it spans a wide range of wavelengths or energies. Most of this book is focused on a narrower region, the infrared field, where the interaction with radiation affects the molecular structure or molecular state of the matter. The quantum mechanical description of the matter leads to the appearance of energy levels, and from them, to the processes of absorption and emission. The Lambert–Beer's law, also known as Beer–Lambert's law, sets the fundamental relationship between the intensity of the radiation reaching a sample and the capacity of the sample to absorb it. It provides

R. Escribano (✉)
Instituto de Estructura de la Materia, IEM-CSIC, Madrid, Spain
e-mail: rafael.escribano@csic.es

G. M. Muñoz Caro
Centro de Astrobiología, INTA-CSIC, Torrejón de Ardoz, Madrid, Spain

G. M. Muñoz Caro, R. Escribano (eds.), *Laboratory Astrophysics*,
Astrophysics and Space Science Library 451,
https://doi.org/10.1007/978-3-319-90020-9_3

the basic framework for the quantitative study of most spectroscopic processes. When the sample is in the solid state, as many relevant samples are in astronomical or astrophysical media, special effects may take place that add new features to the spectrum, and can provide further information on different properties of the material. The observation of astronomical objects requires the confluence of several disciplines, like optics, detection technology, signal processing and others, and moreover a sophisticated data treatment is required to convert those observations to the magnitudes that are normally used in spectroscopy, i.e. transmitted radiation versus wavelength or wavenumber.

Many of these topics are developed in this chapter, which ends up with a short summary and a list of pertinent references.

3.2 Electromagnetic Radiation

3.2.1 Quantum Description

The interaction between electromagnetic radiation and matter is best described for spectroscopy using quantum mechanics. The first step is the well-known time dependent Schrödinger equation:

$$H\Psi = \mathrm{i}\hbar\,(\partial/\partial \mathrm{t})\,\Psi \tag{3.1}$$

where Ψ is the wavefunction that fully describes the system under study, H is the Hamiltonian operator that defines the energy of the system and $\hbar$ is the reduced Planck constant, $\hbar = h/2\pi$. The square of the wavefunction $|\Psi|^2 = \Psi^* \Psi$ represents the probability of finding the system at a given time t and position r. This equation specifies how the system evolves with time. To solve it, time-dependent perturbation theory is usually applied. The Hamiltonian is assumed to consist in two terms, one which depends only on the space coordinates, H^0, and another one where the dependence with time is treated as a perturbation, H':

$$H = H^0 + H' \tag{3.2}$$

The space-dependent Hamiltonian leads to the time-independent Schrödinger equation:

$$H^0 \psi_m = E_m \psi_m \tag{3.3}$$

where the eigenvalues E_m represent the total energy of the system in a given stationary state m, described by its eigenfunction $\psi_{m,}$, which depends on the space coordinates only. These stationary states are referred to as energy levels in the spectroscopic jargon. The solution of the time-dependent Schrödinger equation

yields the wavefunctions:

$$\Psi(r,t) = \sum c_m(t)\psi_m(r)\exp(-E_m i t/\hbar) \tag{3.4}$$

where the $c_m(t)$ coefficients represent the contribution of each stationary state to the total eigenfunction at a given time t, and $\hbar = h/2\pi$, with h, the Planck constant. If a system evolves from an initial state i to a final state f, the probability of finding the system in this final state is given by:

$$P_{fi}(t) = \mid c_f(t)^2 \mid \tag{3.5}$$

If the final state corresponds to an ensemble of energy levels between E and $E + dE$ of density n_f, the total probability amounts to:

$$P(T) = \sum P_{fi}(t) = \left(t/\hbar^2\right)\left|H'_{fi}\right|^2 n_f \tag{3.6}$$

The transition rate is therefore a constant:

$$W_{fi} = \left(1/\hbar^2\right)\left|H'_{fi}\right|^2 n_f \tag{3.7}$$

The H'_{fi} term represents the integral between the initial and final states of the time-dependent Hamiltonian operator H', with $H'_{fi} = H'_{if}$. For molecules under electromagnetic radiation, the time perturbation operator can be written in terms of the molecular dipole moment operator μ and the electric component of the field, $F(t)$:

$$H' = -\mu\ F(t) \tag{3.8}$$

The rate constant can then be written as (the derivation of these equations can be followed in the book by P.W. Atkins, listed in the references below):

$$W_{fi} = \left(1/6\epsilon_0\hbar^2\right)\left|\mu_{fi}\right|^2\rho_{fi} \tag{3.9}$$

where ϵ_0 is the permittivity of vacuum ($\epsilon_0 = 8.8541878 \times 10^{-12}$ F m^{-1}), ρ_{fi} is the density of energy, given as the product of density of states times their energy, and we have introduced the transition dipole moment, $|\mu_{fi}|$, a fundamental magnitude in spectroscopy. It represents the integral:

$$\mu_{fi} = \int \psi_f^* \mu \psi_i dr \tag{3.10}$$

The conditions under which this integral is nil constitute the so-called selection rules. A transition between states i and f is called forbidden when this integral is

necessarily zero, and it is called allowed when the integral may differ from zero. In practice, forbidden transitions can become allowed under certain circumstances, like symmetry breaking or parity violation. These constitute an interesting field of research by its own.

For solids, the dipole moment operator has to be replaced by the polarization of the medium. In crystals, the selection rules are more complex, and the presence of several molecules of the same species inside a unit cell sometimes leads to degeneracy breaking and the appearance of otherwise forbidden transitions in a spectrum. For amorphous solids, on the other hand, the asymmetry of the environment prevents the prevalence of selection rules, and all transitions are allowed, although with diverse degrees of intensity.

3.2.2 Spectral Regions

The energy levels that satisfy Eq. (3.3) represent stationary states of a system characterized by a given energy, and correspond to different configurations of the nuclei and electrons of the system. Within the Born–Oppenheimer approximation, valid for most of the cases under consideration in this study, the motions of nuclei and electrons can be treated separately, owing to the orders of magnitude's difference in their masses. The nuclei may be assumed to be frozen at a given position, and the electronic wavefunction equation at that configuration may be solved using various possible approximate methods. This process can be repeated at different nuclear configurations. On the other hand, the motions of the nuclei may be treated independently assuming a certain average distribution of the electronic cloud that surrounds them. When the nuclei undergo small displacements around their equilibrium configuration and the potential energy is restricted to the quadratic term, we are using the so-called harmonic potential approximation, the most frequently model employed in molecular spectroscopy. The solution of the electronic wavefunction yields electronic energy levels in the range from units to thousands of electron-volts (eV to keV, roughly 10^{-19}–10^{-16} J). The corresponding nuclear energy levels span also four orders of magnitude, where the wavenumber rather than the energy is often used, from 1 to 10,000 cm^{-1} (roughly 10–10^5 J mol^{-1}, in molar energy units. See the Appendix for a list of units and their conversion factors). The nuclear energy levels can be further classified according to the nuclear motion involved. Thus, molecular rotations cover the lower energy range, up to around two hundreds of wavenumbers, and molecular vibrations span an interval between approximately 300 and 10,000 cm^{-1}. Traditionally, rotational energy levels are mainly represented by the rotational quantum number J, and vibrational energy levels by the vibrational quantum number v. Electronic energy labels are given capital letters, reserving X for the ground electronic state. Figure 3.1 offers a simplified picture for the energy levels of a diatomic molecule in the harmonic approximation. For polyatomic molecules with N atoms, there would be $3N$-6 similar stacks of vibrational energy levels, one for each vibrational mode. For

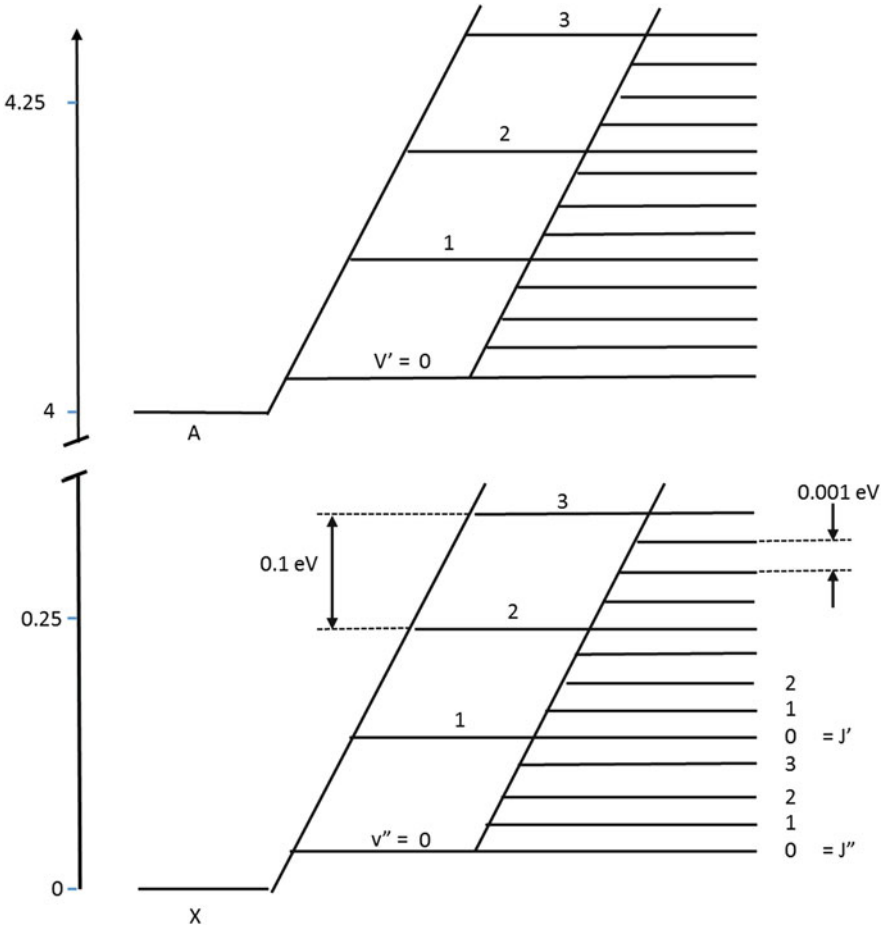

Fig. 3.1 Schematic representation of energy levels of a diatomic molecule. The ground *X* and first excited *A* electronic states are shown, with stacks of vibrational *v* and rotational *J* energy levels. The separation between levels of different types is not drawn to scale; approximate values are given numerically. Double quotes ” are normally used for the initial state of a transition, and a single quote ’ for the final state

crystals, the density of states, or number of states per unit of energy, is sometimes depicted (see Fig. 3.2).

The numbers quoted above for electronic and vib-rotational energies provide rough values for the limits of the corresponding zones in the electromagnetic spectrum. These zones are depicted in Fig. 3.3, where a pictorial representation of the atomic, molecular or electronic motions is also offered.

The main focus of interest of this book is set on the infrared region, where molecular vibrations take place. Specific atomic motions, like bond stretchings, angle bendings, torsions and so on, give rise to well-known spectral features, usually

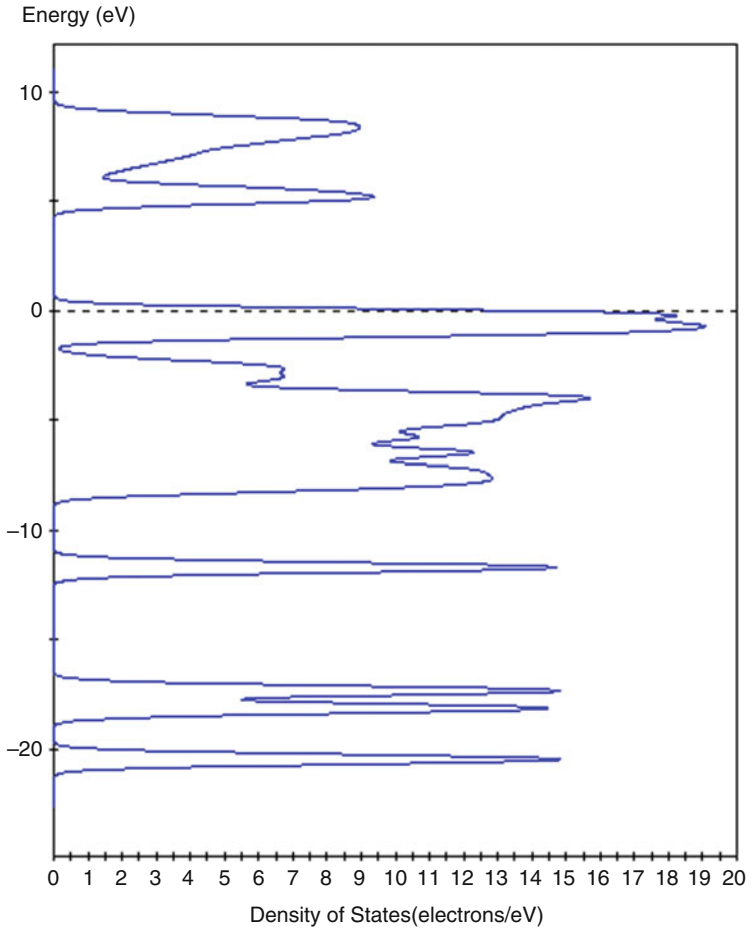

Fig. 3.2 Calculated density of states distribution for a crystal of α-glycine (M.A. Moreno, unpublished)

called characteristic vibrations. Interatomic forces associated to these vibrations reveal the structure of the molecules in the sample. Other electromagnetic regions are also extremely interesting from the astrophysical point of view, of course, but they will only occasionally be mentioned in this work.

It is interesting to ponder briefly over the time domain associated to the different nuclear processes. Rotational energies are of the order of a few wavenumbers, or equivalently of 10^{10} Hz, whereas vibrational energies are two or three orders of magnitude larger. If we use a classical picture and focus on the period of each motion, as inverse of its frequency, this implies that in the time employed by a molecule to rotate around itself, its atoms are vibrating hundreds of times back and forth around their equilibrium positions. A small amount of energy is required to

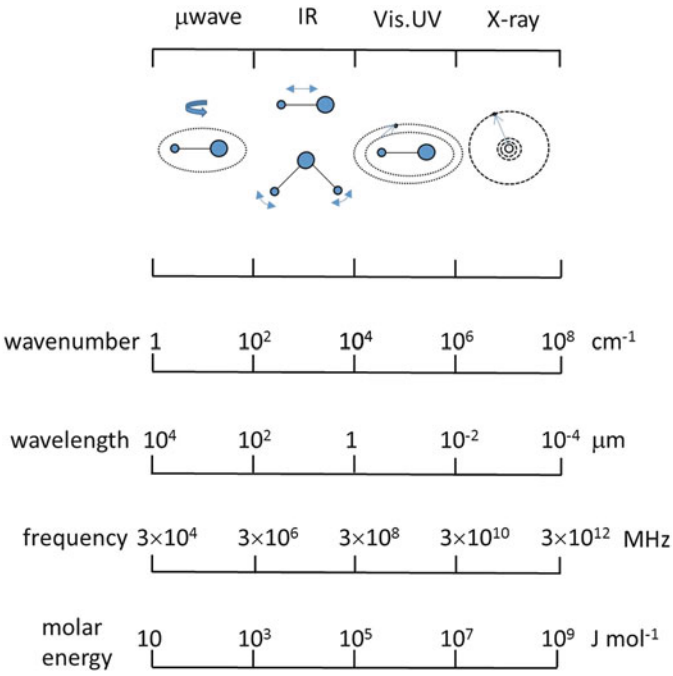

Fig. 3.3 Regions of the electromagnetic spectrum with a schematic representation of the electronic or nuclear processes associated to each zone. The equations relating each magnitude and the basic units are: Molar energy (J mol^{-1}): $\Delta E = h\nu N_A$; wavelength (m): $\lambda = c/\nu$; wavenumber (cm^{-1}): $1/\lambda = \nu/c$; frequency (Hz): $\nu = c/\lambda$. Other frequently used units and accurate conversion factors are given in the Appendix

change the rotational state of a molecule; a value hundreds or thousands times bigger is necessary to produce a similar change to its vibrational state.

3.3 Lambert–Beer's Law

3.3.1 Einstein's Coefficients

According to Eq. (3.9), the probability for a molecule to access a final state f from an initial state i through interaction with electromagnetic radiation is proportional to the density of energy ρ_{fi}. In spectroscopy, it is customary to use radiation density in terms of frequency for a frequency corresponding to the energy difference between initial and final state, $\nu_{fi} = (E_f - E_i)/h$. If the process involves absorption of energy, $E_f > E_i$, the coefficient of proportionality is called Einstein's stimulated absorption coefficient, B_{fi}, and in the opposite situation, when $E_f < E_i$, it is called Einstein's stimulated emission coefficient, B_{if}. Since the rate constant is the same for both

processes, as $H'_{fi}=H'_{if}$, it follows that both coefficients are equal, with a value:

$$B_{fi} = B_{if} = \left(1/6\epsilon_0\hbar^2\right)\left|\mu_{fi}\right|^2 \tag{3.11}$$

Einstein also showed that to achieve thermal equilibrium with radiation, a spontaneous emission process, independent of the density of the incident radiation, must take place. The coefficient associated to this process is consequently called Einstein's spontaneous emission coefficient A_{if}. It is given by:

$$A_{if} = \left(8\pi^2/3\epsilon_0\hbar c^3\right)\nu_{fi}^3\left|\mu_{fi}\right|^2 \tag{3.12}$$

3.3.2 Lambert–Beer's Law

Most of the spectroscopic measurements in a laboratory correspond to absorption spectroscopy. The intensity of the radiation incident on a sample is attenuated by a factor that depends on several properties of the material and the experimental setup. The ratio of the intensity of the transmitted radiation $I(\nu)$ to that of the incident radiation $I_0(\nu)$ is given by the well-known Lambert–Beer's law:

$$I\left(\nu\right)/I_0\left(\nu\right) = \exp\left[-\alpha\left(\nu\right)rl\right] \tag{3.13}$$

This simple equation is the ground stone of absorption spectroscopy. Here r and l represent the concentration in the sample and optical path length, i.e. the distance the radiation travels through the medium, respectively, and $\alpha(\nu)$ is the absorption coefficient, directly related to Einstein's stimulated absorption coefficient by:

$$\int \alpha\left(\nu\right)d\nu = \sum\left(n_i - n_f\right)\left(h\nu_{fi}/c\right)B_{fi} \tag{3.14}$$

where n_i and n_f represent the molecular density at the initial and final states of the transition. If the system is at thermal equilibrium at a given temperature T satisfying Boltzmann's model, the population ratio between these states is given by:

$$n_f/n_i = \exp\left(-h\nu/kT\right) \tag{3.15}$$

where k is Boltzmann's constant.

Care must be taken not to mistake the absorption coefficient, a magnitude intrinsically related to the system, with the absorbance, which depends also on the experimental conditions. The absorbance is defined as:

$$A\left(\nu\right) = -\log_{10}\left[I\left(\nu\right)/I_0\left(\nu\right)\right] = 0.434\,\alpha\left(\nu\right)rl \tag{3.16}$$

The optical depth is also frequently used, as a measure of the attenuation of the intensity as the radiation passes through the sample. The relation between absorbance and optical depth is:

$$\tau = \alpha\,(\nu)\,rl = 2.303\,A\,(\nu) \tag{3.17}$$

But spectra are often represented using yet another magnitude, the transmittance $T(\nu)$, which expresses the actual intensity ratio $I(\nu)/I_0(\nu)$. Transmittances can therefore only vary between 0 and 1, for total absorption by the sample or when the sample is transparent to the radiation of frequency ν, respectively. Figure 3.4 shows a simple diagram relating in a linear scale these two typical spectroscopic magnitudes.

Finally, to add confusion, percent transmittance is sometimes used as percent ratio of the incident intensity, $100 \times I(\nu)/I_0(\nu)$, i.e. $100 \times T(\nu)$ as defined above.

Whereas $I(\nu)$ describes the transmitted intensity at a given frequency ν, the spectrometer collects in practice the convolution of the absorption coefficient $\alpha(\nu)$ with the shape function $f(\nu)$, which may adopt different forms, like Lorentzian, Gaussian or other functions. When the absorption coefficient is integrated along the whole profile of a band, we obtain the so-called band strength (sometimes called line strength) or integrated absorption coefficient:

$$S = \int_{-\infty}^{\infty} \alpha\,(\nu)\,d\nu \tag{3.18}$$

The number of different units employed to represent S is too large to mention here. The reader is directed to the excellent text by Pugh and Rao (1976).

Besides absorption (or transmission) spectroscopy, other techniques are also relevant in the infrared region. Emission spectroscopy has similar characteristics to absorption except that the radiation is directly emitted by the sample when its temperature is higher than that of the environment. The intensity of the emitted radiation is in this case related to Einstein's spontaneous emission coefficient, A_{if}. Scattering spectroscopy is based on the scattering of radiation by particles of finite

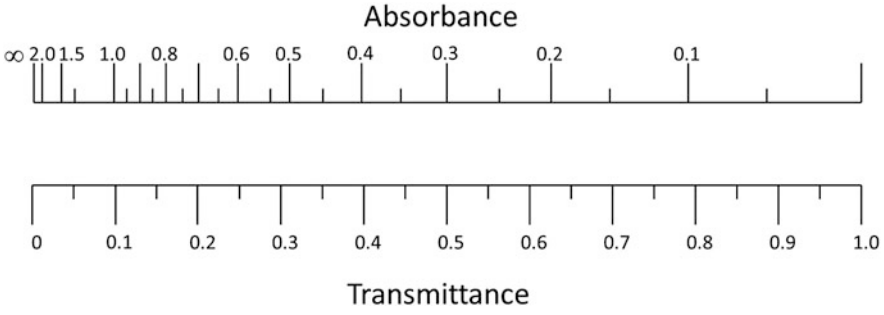

Fig. 3.4 Equivalence between absorbance and transmittance, the two magnitudes often employed to represent absorption spectra. Both of these magnitudes are dimensionless

size. The intensity of the scattered radiation depends on the size and shape of the particle and on the wavelength of the radiation. Whereas this effect is sometimes a hindrance to the analysis of a spectrum, in other circumstances it may provide very useful information on the characteristics of the sample, as will be shown in other chapters of this book.

3.4 IR Spectroscopy of Solids

When the sample is a solid, further effects can take place that may induce important modifications in a spectrum. Besides transmission spectra, the technique known as Reflection–Absorption Infrared Spectroscopy (RAIRS) is often employed. Since the solid sample must be held on a substrate, reflection on the substrate forces the radiation to pass a number of times through the sample. Depending on the angle of incidence and the thickness of the sample, the appearance of the spectrum can change substantially. Moreover, the use of a polarizer to select the perpendicular (S) or parallel (P) components of the incident light allows enhancing specific vibrations of the sample, or detecting surface or stacking configuration effects. Figure 3.5 displays spectra of films of nitric acid of various thicknesses, grown at 150 K. The spectra are taken at grazing incidence angle (75°), under the polarization conditions indicated. Large variations can be seen in the spectra.

Long-range dipole–dipole interactions throughout a sample can induce the so-called Longitudinal Optical modes (LO modes). When the incident radiation is not normal to the surface, but tilted at a given angle, the component of the incoming radiation perpendicular to the surface is absorbed by these modes. They differ from the modes arising by the component of the incident radiation parallel to the surface, the Transverse Optical modes (TO modes).

Figure 3.6 depicts a scheme of the interaction of oblique incident radiation with both types of vibrations in the slab-shaped sample. The LO modes have interesting properties, that reveal information on the structure and shape of the solid. They always appear together with, or at higher frequency than, the TO modes, and their separation depends on the intensity of the vibrational mode and on the shape of the particle. The splitting between the frequencies of these modes, ν_{LO} and ν_{TO}, is given by:

$$\nu_{LO}^2 - \nu_{TO}^2 = \frac{4\pi}{\varepsilon m V_c}\left(\frac{d\mu}{dq}\right)^2 \tag{3.19}$$

where V_c is the volume of the unit cell of a crystal, ε is the dielectric constant at frequencies far from resonance, $(d\mu/dq)$ is the dipole moment variation at the q normal mode, and m is the reduced mass associated to that mode. The intensity of the transition, proportional to the square of the variation of the normal mode, can be thus determined from the observed LO–TO splitting.

These effects will not be discussed in detail in this text; the reader is referred to extensive literature on this topic given at the end of this chapter. To show just one

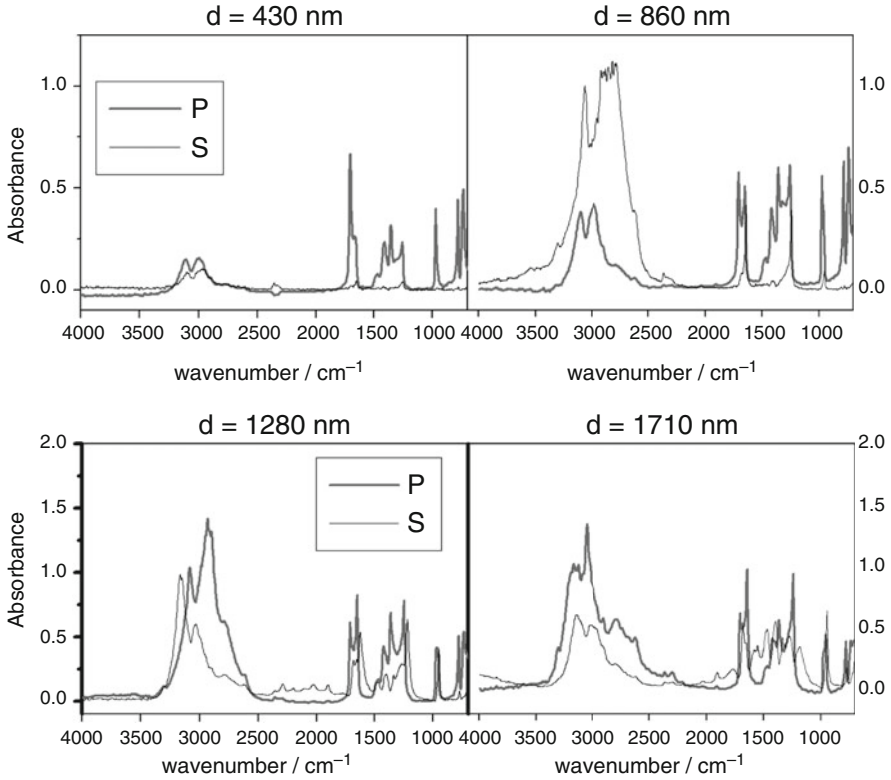

Fig. 3.5 Reflection–absorption experimental infrared spectra of films of nitric acid of increasing thickness, from 430 nm (left, top) to 1710 nm (right, bottom), grown at 150 K, with incident radiation at 75°, using polarized light in the plane of incidence (P polarization) and in a perpendicular plane (S polarization). Adapted from D. Fernández Torre, PhD Thesis (2005)

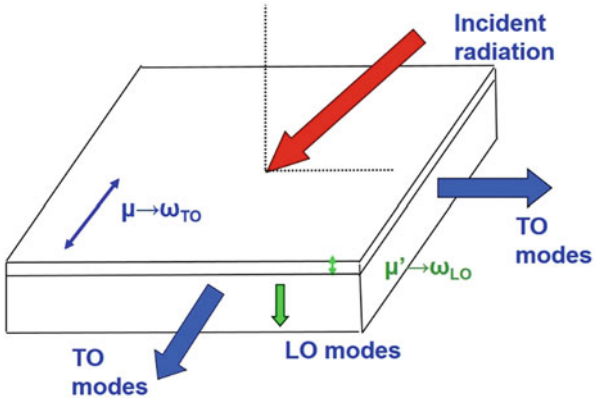

Fig. 3.6 Schematic representation of the generation and geometrical characteristics of LO and TO modes for oblique incident radiation on a slab or thin film sample

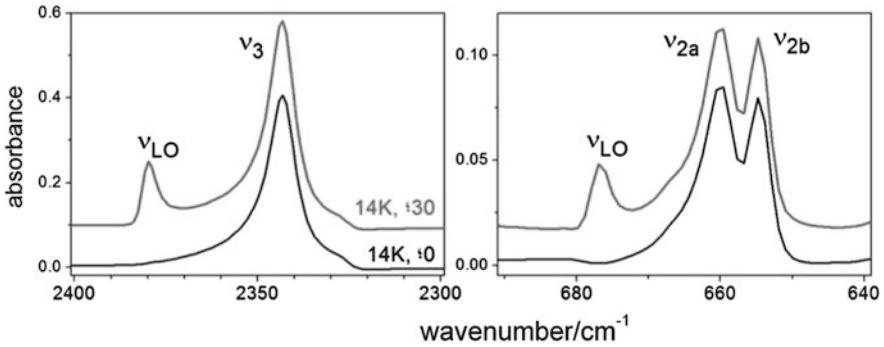

Fig. 3.7 IR transmission spectra of a film (200 monolayers) of CO_2 ice grown at 14 K, at normal incidence (black) and 30° incidence angle (grey). The LO peaks are detached from the TO peaks of ν_3 and ν_2, the LO–TO splitting being proportional to the relative intensities of these transitions. Spectra are offset for clarity. Adapted from Escribano et al. (2013)

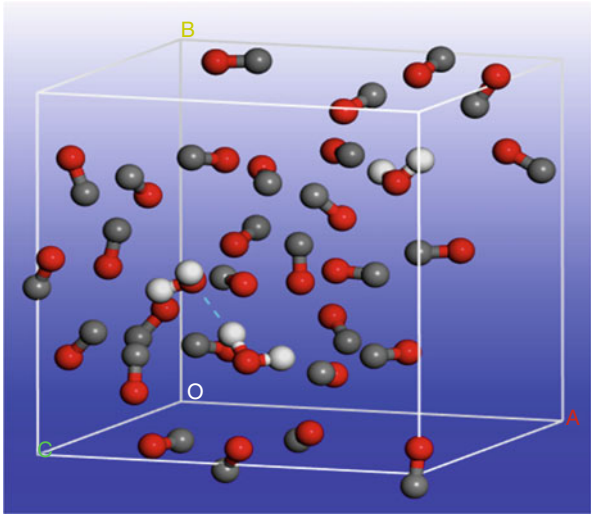

Fig. 3.8 Theoretical model for an amorphous mixture of 29 CO and 3 H_2O molecules contained inside an enlarged unit cell of size $a = 11.26$ Å

example, we reproduce in Fig. 3.7 spectra of a film of CO_2 ice deposited at 14 K. Spectra are recorded using incident normal radiation and 30° tilted radiation. The more intense ν_3 band induces a larger splitting than the weaker ν_2 mode.

Theoretical models are often used to study solid samples and to predict their spectra. Density Functional Theory (DFT) provides a powerful yet accessible approach to deal with this kind of samples, either as crystals or as amorphous solids. Two of the most widely employed platforms using DFT are the SIESTA code, and the Materials Studio set of programs. They use different approaches discussed in another chapter of this book. Figure 3.8 presents a model for an amorphous mixture

of CO and H_2O molecules, designed using CASTEP, from the Materials Studio package, to study the behavior of water molecules within a CO matrix.

3.5 Astronomical Observations

There is ample literature on the preparation, reduction, and interpretation of astronomical observations of molecules in the gas phase, while the introductory works on observations of bare dust particles, or dust covered with ice mantles is scarce in comparison. There is indeed a large community of observers dedicated to the detection of molecules in space and gas-phase spectroscopy is better understood. The intermolecular interactions in solids like astrophysical ices have a strong effect in their observed spectra; this is discussed in this book. Telescope facilities generally provide a toolkit for the preparation of observing proposals and data reduction and processing. Here we will only provide some of the basic concepts that are necessary to understand the papers reporting observations in the context of Astrochemistry, and in particular the observations of dust particles.

The total power emitted by a star over the full spectral range is known as the bolometric luminosity L_{bol}. Because the emission is in practice not known for all wavelengths, this value is obtained from the visible emission using a correction factor. The so-called effective temperature of a star, T_{eff}, can be approximated using the Stefan–Boltzmann law for the power emitted by a blackbody, $\sigma\ T^4$. For a spherical star of radius R_*, the total emission is

$$L_{bol} = 4\pi R_*^2 \sigma T_{eff.}^4 \tag{3.20}$$

If the wavelength λ_{max} corresponding to the maximum intensity of the blackbody radiation is known, an estimate of the temperature can be obtained from

$$\lambda_{max}\ \mathrm{T}_{Wien} = 2890\ \mu\mathrm{m\ K}, \tag{3.21}$$

where T_{Wien} is the Wien temperature. Also based on the blackbody approximation of stellar emission is the "color temperature". It is obtained from the ratio of fluxes at two different wavelengths; this value corresponds to a certain temperature of the blackbody.

Along the imaginary path between a light source and the observer, called the "line of sight", there can be absorption of colder matter in the form of gas molecules or microscopic particles. The optical depth τ, described above, can then be estimated for this line of sight. At the start of the twentieth century, the presence of interstellar dust was inferred from its effect on starlight. The absolute luminosity of a star L is related to its apparent luminosity S by

$$S = L/4\pi D^2 \tag{3.22}$$

where D is the distance. Also the apparent diameter Φ can be related to the absolute diameter d using $\Phi = d/D$. It was found that stellar cluster distances obtained from the luminosity of the stars were greater than those obtained from their dimensions, and this difference increased with increasing distance, suggesting the presence of absorbing and/or scattering particles along the line of sight.

3.5.1 Gas Phase

Our current knowledge of interstellar gas is based on observations in the radio and millimeter range where these molecules emit, and their absorption in the ultraviolet, optical and infrared. It was found that neutral atomic hydrogen (HI) is the main gas component, and becomes molecular hydrogen in dense clouds. The ground state of neutral hydrogen is split in energy due to the spin–spin interaction between the electron and the proton. The result is the hyperfine splitting of HI atoms that is observed as a 21 cm emission line (frequency of 1421 MHz) which traces the structure of our Galaxy. This Galactic map is complemented with the rotational transitions of CO. HII regions around hot massive stars are composed of hydrogen ionized by ultraviolet photons emitted by the star. The ionic (in addition to ionized hydrogen, other ions are observed such as CaII or MgII) and electron components complete the gallery of species in the interstellar medium.

For convenience, radioastronomers use temperature units in their observations. The kinetic temperature, T_{kin}, is the only real temperature and corresponds to the thermal temperature of the gas. The excitation temperature, T_{ex}, represents the relative population between the lower and upper states, l and u respectively, as they are often referred to in radioastronomy textbooks[1] at energies E_l and E_u. It follows from

$$n_u/n_l = (g_u/g_l)\ \exp\left(-\left(E_u - E_l\right)/kT_{ex}\right) = (g_u/g_l)\ \exp\left(-h\nu_{ul}/kT_{ex}\right) \quad (3.23)$$

where n_u and n_l are the volume densities of gas species in the u and l states of the transition, g_u and g_l are the statistical weights or degeneracies of the corresponding states, and ν_{ul} is the frequency difference between them. It can be shown that when the total gas density increases and/or the optical depth of the line increases, local thermodynamic equilibrium is attained and then $T_{ex} = T_{kin}$.

In a gaseous medium with no dust, the radiative transport of a line at frequency ν with intensity I_ν (in cgs units, it is expressed in erg s^{-1} cm^{-2} Hz^{-1} sr^{-1}) that changes in an infinitesimal element dz along the line of sight through an interstellar

[1]There might arise some confusion with the i and f nomenclature for energy levels in Sect. 3.3 above, which is more usually employed in spectroscopy. Subindices i and f refer to the initial and final states of a transition, whereas l and u refer to the lower and upper states. They coincide for absorptions but have the opposite meaning for emissions.

cloud is

$$dI_\nu/dz = (h\nu/4\pi)\,\Phi(\nu)\,n_u A_{ul} - (h\nu/4\pi)\,\Phi(\nu)\,I_\nu\,(n_l B_{lu} - n_u B_{ul}) \tag{3.24}$$

where A_{ul}, $B_{ul}I_\nu$, and $B_{lu}I_\nu$ have the same units (s^{-1}). The above-mentioned Einstein coefficients are A_{ul} for spontaneous emission from the transition between u and l, B_{ul} and B_{lu} for stimulated emission and absorption, respectively. The following relations are valid for the Einstein coefficients:

$$A_{ul} = \left(2\pi h\nu_{ul}^3/c^3\right) B_{ul} \tag{3.25}$$

$$g_u B_{ul} = g_l B_{lu} \tag{3.26}$$

It should be noted that the relationship Eq. (3.25) can differ by a factor of 4π or $4\pi/c$ depending on the adopted definition of B. The parameter $\Phi(\nu)$ is the probability per frequency interval that a photon is emitted at ν ($\int \Phi(\nu)d\nu = 1$). In astrophysics, this factor is often related to the velocity structure v in the medium (turbulences, outflows, etc.). Since $d\nu/\nu = d\,v/c$ (Doppler effect), this parameter is

$$\int \Phi(\nu)\,d\nu = (\nu/c)\;\Phi(v)dv \tag{3.27}$$

The radiative transport equation can be abbreviated as

$$dI_\nu/dz = \varepsilon_\nu - \kappa_\nu I_\nu \tag{3.28}$$

where $\varepsilon_\nu = (h\nu/4\pi)\Phi(\nu)n_u A_{ul}$ is the energy emitted at frequency ν per volume (volume emissivity) and $\kappa_\nu = (h\nu/4\pi)\Phi(\nu)(n_l B_{lu} - n_u B_{ul})$ is an absorption coefficient. The optical depth is defined as $d\tau_\nu = \kappa_\nu dz$.

There is a third definition of temperature, which is very handy in radioastronomy. This is the brightness temperature T_B defined as

$$I_\nu = B_\nu^{BB}\;(T_B) \tag{3.29}$$

where I_ν is the specific intensity and the blackbody brightness B_ν^{BB} is given by the Planck law, in the Rayleigh–Jeans approximation

$$B_\nu^{BB} \approx \left(\frac{2\nu^2 k}{c^2}\right) T_B = \left(\frac{2k}{\lambda^2}\right) T_B \tag{3.30}$$

where ν is in Hz and λ in cm, B_ν is in erg s^{-1} cm^{-2} Hz^{-1} sr^{-1}, k (the Boltzmann constant) in erg K^{-1} and c (the speed of light) in cm s^{-1}.

The excitation temperature and the brightness temperature are related by

$$T_B = \frac{h\nu}{k}\left(\exp\left(\frac{h\nu}{kT_{ex}}\right) - 1\right)^{-1}. \tag{3.31}$$

What follows is just a hint of how the brightness temperature is estimated from the real observations in the radio. Radioastronomy includes many other concepts that are not presented here. There are many book references that introduce sub-mm and mm observations (see reference list below). Radio-telescopes allow the detection of rotational emission lines of molecules. They are in fact antennas, but radio-telescopes can also emit radiation like a resistor. Therefore, in a way analogous to a resistor, a power P (in erg s^{-1}) will be emitted by the radio-telescope if it is maintained at the so-called "antenna temperature" T_A(in Kelvin) in the frequency bin $\Delta\nu$ following

$$P = k\ T_A\ \Delta\nu \tag{3.32}$$

But antennas can also be viewed as thermometers and will reach a temperature T_A if they receive radiation from a source. The temperatures T_A and T_B, the later is defined in Eq. (3.30), are related following the expression

$$T_A = \left(\frac{A_e}{\lambda^2}\right)\int_{4\pi} T_B\,(\theta,\phi)\ \ P_n\,(\theta,\phi)\,d\Omega \tag{3.33}$$

where 4π is the integration over the total solid angle of the sky and A_e is the effective area of the antenna. Therefore, in the absence of atmospheric extinction, the measured value of T_A provides an estimation of the *beam (spatially) averaged brightness temperature* of a source T_B, but this is only a rough estimation. Figure 3.9 provides a simple scheme of observation of cold dust towards a background star.

3.5.2 Solids

The types of dust particles present in the interstellar medium are described in Chap. 1. The emission of dust grains can also be detected in the millimeter region, with an emissivity proportional to ν^{α}, where ν is the frequency and α a constant. Interstellar and circumstellar dust particles absorb/emit efficiently in the infrared but the Earth's atmosphere is only transparent to this radiation in a few narrow regions of the spectrum called "windows", and therefore, observations in orbit around the Earth become necessary. Hot grains emit with variable efficiency as a function of wavelength, providing information about their size, composition, and other dust parameters.

The lines of sight toward embedded infrared sources in dense interstellar clouds can probe material that has been partially processed by the nearby source.

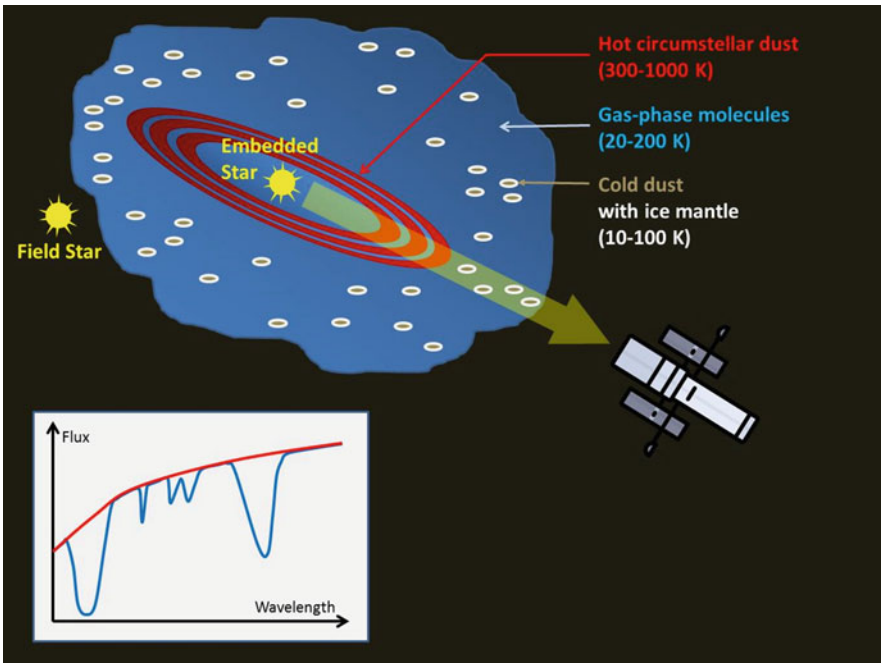

Fig. 3.9 Observations in the infrared of absorbing cold dust covered by an ice mantle are possible when a background star surrounded by hot dust or an embedded star act as infrared source. The hot circumstellar dust, in red, emits in the infrared and provides a continuum of emission in the spectrum shown in the lower left corner, also in red. The superposed spectral bands, in blue, are attributed to the absorptions of cold interstellar dust particles covered with ice mantles, which are located in the line of sight between the embedded star and the observer. The band positions allow the identification of ice molecules and the silicate grain cores; the absorption areas provide the column densities, and therefore an estimate of their relative abundances

Background field stars, located behind the cloud, serve to trace interstellar dense cloud dust. Red giants with a cool photosphere can be used as background field stars, although the number of suitable objects is scarce. Infrared observations of icy dust will be discussed in Chap. 8.

The observed ice column density of species X is obtained from integration of the infrared band

$$N(X) = \tau_{int}(X)/A(X) \tag{3.34}$$

where τ_{int} is the integrated optical depth of the band and $A(X)$ the absolute integrated band strength (cm^2 cm^{-1} molecule^{-1}, or equivalently cm molecule^{-1}). It is common to give the abundance of an ice component relative to the value of H_2O ice, since water is the most abundant species in ice mantles.

Historically, the optical observations showed the first evidence for the existence of dust in space, which was considered an annoyance because it perturbed the

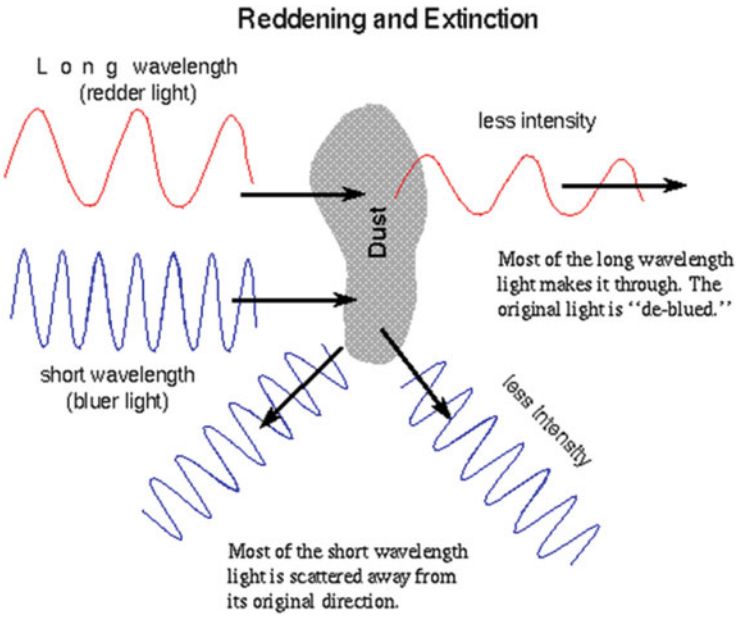

Fig. 3.10 Effect of dust on incident light. Courtesy of W.-F. Thi

observations of stars. Dust scattering causes "nebulosity", i.e. stars are seen as blurred objects. Information about the extinction, scattering and polarization of dust is inferred from the optical signal**.** The wavelength-dependent extinction and polarization gives an estimate of the particles' sizes. Figure 3.10 shows a schematic view of the interaction of radiation with a dust particle. The diffuse absorption features in stellar spectra are likely associated with dust, but they remain unidentified. These features are observed in the optical, but also in the infrared and ultraviolet.

Observations in the ultraviolet are accessible from satellites at wavelengths shorter than 300 nm. Below 91.2 nm (13.6 eV) the interstellar medium is practically opaque due to hydrogen ionization. As mentioned in Chap. 1, the strongest feature in this range is the 2175 Å extinction hump that is commonly attributed to a carbonaceous material.

It is fortunate that the opacity in the extreme ultraviolet does not affect equally the X-rays. The reason is that the ionization cross section of hydrogen declines with the photon frequency as ν^3, allowing X-ray observations from satellites. Interstellar dust scatters X-ray photons, and dust in a hot gas environment, about 10^6 K, emits in this wavelength range.

3.6 Summary

Many readers will be familiar with some of the topics described in this chapter. The Lambert–Beer's law or the Einstein coefficients are discussed in many good texts. Yet, we believe it can be useful for some readers to count with a quick guide where energy levels can be visualized, the orders of magnitude of the energy involved in molecular processes can be assessed, or different aspects of the spectroscopy of solids, like the LO–TO splitting, are described with practical examples. On the other hand, molecular spectroscopists are normally not used to the type of data that is directly collected in astronomical observations. A short description of the nature and treatment of such data should provide a valuable introduction to this subject. Similarly, the units and unit conversion factors listed in the Appendix, may hopefully be useful, as well as the list of references to general or specific literature.

Acknowledgments We gratefully acknowledge financial support from Projects FIS2016-C331P, AYA2014-60585-P and AYA2015-71975-REDT of the Spanish MINECO. We are grateful to Angel González Valdenebro for help with the figures.

Appendix: Units and Conversion Factors

Several units are used in spectroscopy which are especially suitable for specific spectral regions, or traditionally used by spectroscopists or astrophysicists. Some of them are listed below, where <> means equivalent to, and $c = 2.99792458 \times 10^{10}$ cm s^{-1}, Avogadro's number $N_A = 6.0221367 \times 10^{23}$ molec mol^{-1}, Boltzman's constant $k = 1.38064852 \times 10^{-23}$ m^2 kg s^{-2} K^{-1} ($1.38064852 \times 10^{-16}$ erg K^{-1} in cgs units) and Planck's constant $h = 6.6260755 \times 10^{-34}$ J s:

Frequency ν (microwave region) to wavenumber $\overline{\nu}$: 1 GHz $= 10^9$ Hz <> $1/c$ cm^{-1} $= 3.33564 \times 10^{-2}$ cm^{-1}; 1 kHz $= 10^3$ Hz <> 3.33564×10^{-8} cm^{-1}.

Wavenumber $\overline{\nu}$ (infrared region) to wavelength λ: mid-IR region: 1000 cm^{-1} <> 10 μm; 3000 cm^{-1} <> 3.333 μm; near-IR region: 6000 cm^{-1} <> 1.6 μm.

Wavelength λ (visible and UV regions) to energy E: 1 μm <> (hc/λ) 1.986447×10^{-19} J <> (hcN_A/λ) 11.96266×10^4 J mol^{-1}; 665 nm (approx. red light) <> 17.98899×10^4 J mol^{-1}.

Other energy units (X-ray region): 100 eV <> 9.64853×10^6 J mol^{-1} <> 1.23984×10^{-2} μm.

References

Electromagnetic Radiation, Quantum Mechanics:

Atkins, P.W.: Molecular Quantum Mechanics. Clarendon, Oxford (1970)
Pauling, L., Wilson, E.B.: Introduction to Quantum Mechanics. McGraw Hill, New York (1935)

Spectroscopy:

Herzberg, G.: Molecular Spectra and Molecular Structure (3 Volumes). Krieger, Malabar, FL (1991)
Wilson, E.B., Decius, J.C., Cross, P.C.: Molecular Vibrations. McGraw Hill, New York (1955)

Solid State:

Born, M., Kun, H.: Dynamical Theory of Crystal Lattices. Clarendon, Oxford (1988)
Decius, J.C., Hexter, R.M.: Molecular Vibrations in Crystals. McGraw Hill, New York (1977)
Ovchinnikov, M.A., Wight, C.A.: J. Chem. Phys. **99**, 3374 (1993)

Theoretical Calculations:

Jensen, P., Bunker, P.R.: Computational Molecular Spectroscopy. Wiley, Chichester (2003)

SIESTA:

Ordejón, P., Artacho, E., Soler, J.M.: Phys. Rev. B Condens. Matter. **53**, R10441 (1996)
Soler, J.M., et al.: J. Phys. Condens. Matter. **14**, 2745 (2002)

CASTEP:

Clark, S.J., et al.: Z. Kistallogr. **220**, 567 (2005)

Units and Conversion Factors:

Mills, I.M., et al.: Quantities, Units and Symbols in Physical Chemistry, IUPAC. Blackwell, Oxford (1988)
Pugh, L.A., Narahari Rao, K.: Intensities from Infrared Spectra. In: Ch. 4 in Molecular Spectroscopy: Modern Research. Academic, New York (1976)

Radioastronomy:

Kraus, J.D.: Radio Astronomy, 2nd edn. Cygnus-Quasar, Powell, OH (1986)
Wilson, T.L., Rohlfs, K., Hüttemeister, S.: Tools of Radio Astronomy. Springer (2017)

Specific References:

Escribano, R.M., et al.: Proc. Natl. Acad. Sci. U.S.A. **110**, 12899 (2013)
Fernández-Torre, D.: Ph.D. Thesis, Universidad Complutense, Madrid (2005)

Part II
Ice Properties

Chapter 4
Density of Ices of Astrophysical Interest

Miguel Ángel Satorre, Ramón Luna, Carlos Millán, Manuel Domingo, and Carmina Santonja

Abstract Density plays an important role in the understanding of chemical and physical evolution of ices in space. It is related with abundances, energetic processing, porosity, buoyancy, etc.

The experimental values available are scarce and, often, corresponding to ices without pores (bulk density) despite many experiments devoted to astrophysics form porous ices. Additionally, ice density frequently depends on the formation temperature, and these studies are even scarcer.

In this chapter, bulk and average density are defined, and experimental methods to determine both densities are reviewed. Ice density values are presented covering from the lighter to the denser ones. The relationship between density and ice structure is exemplified. The examples cover temperature phase transitions, amorphous and crystalline structures. The possibility to detect metastable crystalline structures is also proposed. The case of ice mixtures is presented to warning about the impossibility to obtain density values from those of the pure constituents. Finally, ice porosity experimentally obtained is tabulated to reveal that high density ices (>1 g cm^{-3}) can be as porous as low density ices (<0.5 g cm^{-3}).

4.1 Introduction

Infrared observations of objects in space have brought many advances in the understanding of the composition and phase (state of matter) of materials present in the Universe. The appearance in the mid 1970s of infrared CCD devices opened

M. Á. Satorre (✉) · R. Luna · C. Millán · C. Santonja
Escuela Politécnica Superior de Alcoi, Centro de Tecnologías Físicas, Universitat Politècnica de València, Alcoi (Alicante), Spain
e-mail: msatorre@fis.upv.es

M. Domingo
Escuela Técnica Superior de Ingenieros Industriales, Centro de Tecnologías Físicas, Universitat Politècnica de València, Valencia, Spain

G. M. Muñoz Caro, R. Escribano (eds.), *Laboratory Astrophysics*,
Astrophysics and Space Science Library 451,
https://doi.org/10.1007/978-3-319-90020-9_4

the Universe to a molecular world posing many interesting questions. Silicates and carbonaceous materials of different compositions were identified as bearing icy surfaces, in the interstellar medium (ISM). Ice is understood as the solid phase of molecules that at normal temperature and pressure (20°C and 1 atm) are liquids or gases. In the Solar System it was known that ices are present in many objects before any infrared observations were carried out. As examples of icy surfaces, our own Earth polar caps, or those on Mars, optically observed, or on the Galilean satellites as Europa whose high albedo reveals the icy surface. Other objects known from ancient times such as comets should contain ice, because they produce a coma compatible with ice sublimation. Now in the infrared era, ground, airborne, satellite observations, and space missions confirm the presence of a plethora of frozen molecules, from the simplest ones as CO, H_2O, N_2 ... to the more complex ones such as amino acids. To understand the physico-chemical behavior of these molecules research groups throughout the world have built different laboratories with common or different techniques and scopes. One of these laboratories is our Astrophysical Ice Characterizations Laboratory (LCHIA, from the Spanish words). We mainly focus our research on determining physical parameters of non-processed ice films such as density, refractive index, sublimation energy, desorption kinetics, porosity, structure ... The goal of this chapter is to explain the relevance of ice density to astrophysics, to relate average density and refractive index with the structure of the ice and how this density can be obtained with our experimental setup. Other experimental techniques will be briefly reviewed to compare advantages and disadvantages and to clarify the differences about density values obtained. Many times in the literature, apparently discrepant results can be found but often they are complementary and perfectly concordant. Finally, because of the relevance of porosity and its direct relationship with density, a brief comparison among ices will be presented.

4.2 Density

This section is devoted to highlight the importance of ice density for solid-state astrophysics, to clarify different concepts of density that many times could cause confusion, and to show succinctly different methods to obtain it.

The density used so far for any ice in space and for any application is 1 g cm^{-3} (with very few exceptions), a value that is not correct even for water ice in terrestrial conditions. Only recently the actual values of ice density, in conditions relevant to astrophysics, are beginning to be demanded. Let us show a few examples to demonstrate why this value is so important.

4.2.1 Relevance

(a) *The integrated absorbance*. As has previously been mentioned, in many lines of sight appear ice absorption bands corresponding to vibrational modes of

icy molecules. To identify these bands diverse laboratories have grown ices, in a high or ultra-high vacuum chambers, providing the observers candidates to match observational spectra. Laboratory results let identify molecules and even, in some cases, the ice phase. As the structure depends on the thermal history, many experimental works are devoted to study the relationship between structure and temperature. Once the molecules have been identified, their abundances have been estimated by means of the integrated absorbance,

$$A = \frac{\int \nu d\nu}{N} \tag{4.1}$$

$$N = \frac{d \cdot \rho \cdot N_A}{M} \tag{4.2}$$

where A is the integrated absorbance; the integral represents the area of a band for a certain absorption; N is the column density (molecules cm^{-2}); d is the ice thickness (cm); ρ is the density (g cm^{-3}), N_A is Avogadro's number; and M is the molecular mass (g mol^{-1}). As can be seen, the uncertainty on the determination of the integrated absorbance is directly related with the density value. As the quality of the observations improves, a better estimation of molecular abundances is expected, but this is not possible without actual density values [see Eqs. (4.1) and (4.2)]. It may serve as example that methane density is less than half the value accepted so far, 1 g cm^{-3}. To solve this situation it is necessary to provide specific density data for pure molecules and mixtures.

(b) Another direct application of density is the ice *buoyancy*. Ices tend to sink or float on a terrain depending on their density, relating the interior of satellites or planets with their surfaces. This property is important even for life at Earth, as water ice floats due to its lower density than liquid water, only superficial water freezes and deeper water remains liquid preserving life. In the Solar System the buoyancy could play an important role in different objects with an icy crust, as the satellites Europa (Jupiter), Enceladus (Saturn), or Triton (Neptune), or the transneptunian object (TNO) Pluto. In Triton, for example, the presence on its surface of fresh methane is an intriguing question because its surface is energetically processed, and it is known that methane evolves with any kind of irradiation to more complex hydrocarbons. One of the possible explanations is the existence of a reservoir of pure methane beneath the processed surface. This methane will appear on the surface by mechanisms as cryovolcanism or emerging by buoyancy in a nitrogen rich surface, because nitrogen ice almost doubles the density of methane.

(c) *Porosity* is directly related to the densities that will be defined in the next section. Ice porosity rules the chemical and physical evolution of many astrophysical environments such as the surface of the grains in the dense interstellar medium, or many icy surfaces in the Solar System (planets, satellites, comets, TNOs, etc).

It can delay the release of molecules retained inside the pores, to temperatures well above than their corresponding temperatures of sublimation (i.e. pure methane sublimes at about 40 K in high vacuum systems, but can be retained in water ice over 140 K). Besides, in porous materials, the surface exposed to the outside (effective area) is increased by many orders of magnitude. This allows the surface to capture molecules, let them move and react with each other to produce larger compounds, becoming a powerful catalyst for chemical reactions.

4.2.2 Bulk and Average Density, Avoiding Confusion

Density (ρ) is defined as the ratio between mass and volume, usually in units of g cm^{-3}. It is widely employed in astrophysics, but this is a misleading word because it is used for two different concepts: the bulk and the average density. In many cases it is not specified which type of density a certain value is referred to. This causes confusion and provokes apparent disagreements between experimental results, making that completely consistent data seem not to be. The most common disagreement appears in the most abundant ice, water ice. The two concepts we are referring are bulk (or intrinsic), and average density. Mass is the same for both concepts but the first one considers the volume occupied by the material itself without voids and the second accounts for the whole volume, voids included. Using a sponge as an example, it is possible to consider the mass of the sponge and divide it by the volume occupied by the material itself, without voids. The value obtained in this way is the intrinsic density. On the contrary, if voids are considered, we obtain the average density. In everyday life it is often used this last meaning. The average density of a warship is lower than that of liquid water, despite the bulk density is much higher, almost seven times that of water, as steel is its main component.

Concerning intrinsic density an observation should be done. For ices, it can be expected that the intrinsic value corresponds to the highest density the material can achieve, and that would be constrained by the crystalline structure of the ice. If there are different crystalline structures, there will be as many intrinsic densities. In some cases, special amorphous ices can even reach higher bulk density values than that of crystalline ones. That is the case for water ice deposited at temperatures below 25–30 K that reaches 1.1 g cm^{-3}, that is the so called high density amorphous solid water (ASW). In contrast, its crystalline ice density is about 0.91–0.94 g cm^{-3}. In view of this, we should be particularly careful when taking the density value for a certain application.

Let's keep in this example, trying to clarify this problem. The fact that the high density ASW has the highest bulk density value is in perfect agreement with the fact that this ice has the lowest average density at the same time (about 0.65 g cm^{-3}). To disentangle this question, imagine the structure of a perfect faced centered cubic structure with water molecules completely ordered at certain distances. In this circumstance, if measured, bulk and average density have a coincident value

because no voids are present in that structure. Now imagine the same structure and subtract randomly 40% of water molecules from inside. In that case the bulk density remains unaltered, but the average density is 60% of the initial one. Going further, if the remaining water molecules become closer, maintaining the total volume, the intrinsic density increases but the average one will remain constant. As it has been shown concerning this simple problem, as with everything in science, we should take with a pinch of salt when published data does not specify which density it refers to. This is a quite complicated problem because it is possible that the highest intrinsic density of an ice corresponds to an amorphous structure instead to a crystalline one.

If there is no confusion, combining the intrinsic values with the average ones a better comprehension of ice structure is obtained. Here it is worth to stop for a moment to state two important experimental facts:

(a) An ice deposited, even a crystalline one, almost never reaches the maximum theoretical intrinsic density, which would mean that every molecule would be perfectly arranged in the structure and no defects were present in any site. Special procedures must be followed to obtain almost a perfect crystal, and these procedures do not coincide with the way ices are formed in astrophysical laboratories around the world.
(b) The words amorphous and crystalline, referred to the structure, can provoke confusion in another way. If we refer to the intrinsic structure, amorphous is "not ordered" and crystalline is "ordered". But if we refer to the whole structure, amorphous refers to the average, but a certain region could be amorphous or crystalline. An average amorphous structure could be formed by crystals arranged randomly, disordered, (Jenniskens and Blake 1996 denote this structure as polycrystalline) or by a completely disordered material. In addition, it must be considered that most of the amorphous structures can be transformed into crystalline ones by warming them up, and the transformation can be partial depending on time and temperature.

To obtain the bulk and average densities many experimental methods can be used. For an overview of these methods, the next subsection briefly describes the most commonly used in the literature and concisely the method used by us to determine the average density of ices of astrophysical interest.

4.2.3 Methods to Determine Density

4.2.3.1 Bulk Density

As it has been defined before, bulk density refers to the mass per unit volume regardless voids. Listed below are the methods commonly used to determine this quantity.

(a) Picnometric method. Manzhelii and Tolkachev (1964) developed a method to determine the density of ammonia and methane where an almost perfect crystal was grown from the liquid phase by slowly lowering a picnometer into a cryostat, which was kept at the temperature of the experiment.
(b) Electron (Jenniskens and Blake 1996) or X-ray (van Nes 1978) diffraction. Briefly, they deduce the crystalline system in which the molecules are ordered, the distances between molecules and the d-spacing. Knowing the molecules per unit cell and the molecular weight, it is possible to assign a mass per unit volume. In consequence this procedure assumes all the molecules are perfectly ordered and no vacancies are in any position of the crystalline system. Under this point of view, this density should be the highest density an ice can achieve as a crystal.
(c) Recently, transmission electron microscopy is used to determine the d-spaces, relate them with pressure and that with density (Kouchi et al. 2016). Values obtained were compared with those of Jenniskens and Blake's (1996) to validate this new method.

4.2.3.2 Average Density

(a) Buoyancy. One of the methods used to determine the density of ices is their buoyancy in liquids. Liquid nitrogen (0.81 g cm^{-3}) and oxygen (1.1 g cm^{-3}) were used to determine water ice density (Ghormley and Hochanadel 1970). Roe and Grundy (2012) studied the buoyancy in the CH_4–N_2 ice system. Methane ice density is about 50% that of nitrogen.
(b) Refractive index and Lorentz–Lorenz coefficient. Knowing the density and refractive index of a species, there exists a theoretical expression (Born and Wolf 1999) that relates density and refractive index, the Lorentz–Lorenz relationship.

$$L \cdot \rho = \frac{n^2 - 1}{n^2 + 2} \tag{4.3}$$

where L is the Lorentz–Lorenz factor, calculated by obtaining the density and the refractive index by direct methods. Brunetto et al. (2008) and Fulvio et al. (2009) reported it from density and refractive index experimental values obtained by Wood and Roux (1982). This method has been used to determine the density for ices at the same and at different temperatures than the reference. Some assumptions are usually made: L is constant irrespectively of the material phase and temperature, and refractive index does not vary for visible wavelengths for non-absorbing ices. It seems to work properly for non-polar ices (Labello 2011).

(c) The Quartz Crystal Micro-Balance (QCMB). Essentially it consists in measuring the mass deposited per square centimeter (g cm^{-2}) by means a QCMB, and determining the thickness of the sample (cm), usually by laser interferometry, or infrared spectra. The quotient gives the average density. Depending on whether these measures are carried out on different or on the same surface, this method can be divided in two:

1. Thickness and mass measured on different surfaces

   Many times, the surface of the QCMB is not appropriate to conduct other simultaneous experiments. For example, if the thickness should be obtained by means of laser interferometry, the surface of the QCMB must me polished, but some commercial crystals are rough. In this case, the mass deposited per surface unit is determined by means the QCMB and the thickness by interferometry on other polished surface as silicon. Other cause that makes necessary measuring in different surfaces is because the surface of the QCMB must be an electrode, covered by a metal (i.e. gold). In the case of obtaining the thickness from IR transmission spectroscopy, it must be obtained with the ice deposited on an IR transparent surface such as silicon or KBr. Errors appear by using different surfaces to determine the mass deposited and thickness because probably the material deposited is not exactly the same on both surfaces. If the amount deposited on the quartz is higher, the material will seem denser; if the contrary occurs the material will seem lighter. Another cause of error could be temperature differences between both sample holders because they are located in different positions and the sticking coefficient is strongly dependent on the temperature.
2. Thickness and mass measured on the same surface

   Optically plane QCMB surfaces are adequate to obtain both parameters simultaneously. It is recommended to use laser interferometry to obtain ice thickness (wavelength far from absorptions) because, as has been already said, the absorbance strength depends on the density, and the use of absorption bands in the infrared requires to know in advance the density of the sample, which is not usually known. There are many possibilities to measure the thickness by interferometry. One possibility is to obtain a laser interference signal at a certain angle of incidence. Since for many ices the refractive index is unknown at temperatures relevant for astrophysics, we are faced with two unknowns (the refractive index and the thickness) and only one equation. This can be solved computationally by fitting the interference pattern. Another possibility is to obtain two patterns at different angles of incidence. Then, two equations with two unknown parameters are attained, and the refractive index can be easily calculated. The latter procedure is going to be explained in detail in the next section, because it is the method we use in our laboratory to determine the thickness.

4.3 Experimental Methods

4.3.1 Experimental Setup

The experiments are carried out in a high vacuum chamber. The temperature of the QCMB can be controlled from 10 K to room temperature. Two laser signals (with angles of incidence α and β, and polarization perpendicular to the plane of incidence, see Fig. 4.1) reflect on the surface of the QCMB where the ice accretes. To form the solid film, gases enter accurately controlled to the vacuum chamber, fill it and deposit randomly onto the QCMB surface (so called background deposition). A detailed description can be found in Luna et al. (2012a).

4.3.2 Density by Means of Double Laser Interferometry and the QCMB

During deposition the optical path of the laser beam reflected on the surface of the ice and on the QCMB surface varies, producing an interference pattern with the maximum when the optical path of both beams differs on 2nπ, and the minimum when it differs on (2n+1) π. Thickness between two adjacent peaks can be obtained as

$$\Delta d = \frac{\lambda}{2n\sqrt{1 - (\sin\alpha/n)^2}} \tag{4.4}$$

If the real part of the refractive index is known, thickness is directly obtained. But, as we have already mentioned, this is not the case for many ices at temperatures

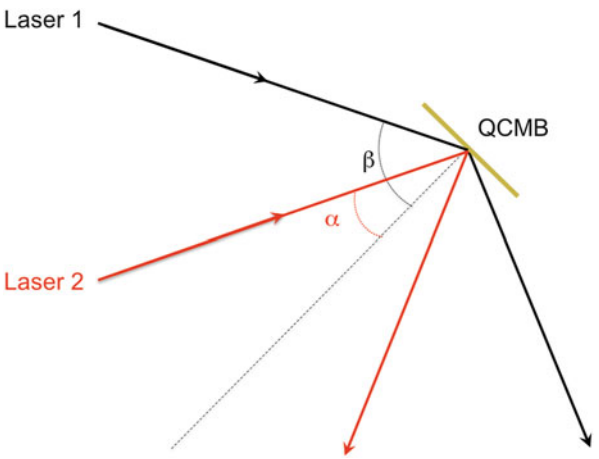

Fig. 4.1 Scheme of the setup, with QCMB gold surface and two laser beams for double laser interferometry

relevant for astrophysics. Sometimes, even when these data are available, the way the ices are grown makes incompatible these values with the actual ones grown by vapor deposition. To solve it, another equation is needed, and a second interference pattern with other angle of incidence must be obtained.

If β and α are both incidence angles and β > α (see Fig. 4.1), n can be determined as

$$n^2 = \frac{\sin^2\beta - (\Delta d_2/\Delta d_1)^2 \sin^2\alpha}{1 - (\Delta d_2/\Delta d_1)^2} \tag{4.5}$$

Here, Δd is another unknown quantity, because to obtain it n is needed. To solve easily this point, a constant rate of deposition is employed. Then $d = v_g \cdot t$, and as both interference patters are obtained simultaneously the quotient between thickness is equal to the ratio of the periods, provided that the deposition rate v_g is constant. To obtain it, gas inlet pressure is maintained constant within four significant figures during deposition, and two turbomolecular systems, working in parallel, evacuate continuously the chamber. In this steady state, some molecules randomly impinge on the gold QCMB surface and, with a certain probability, depending on the surface, molecule and temperature, they stick onto the surface at a certain constant rate. The interference patterns of both laser signals and the variation in frequency of the QCMB against time are displayed in Fig. 4.2. The constant deposition rate can be

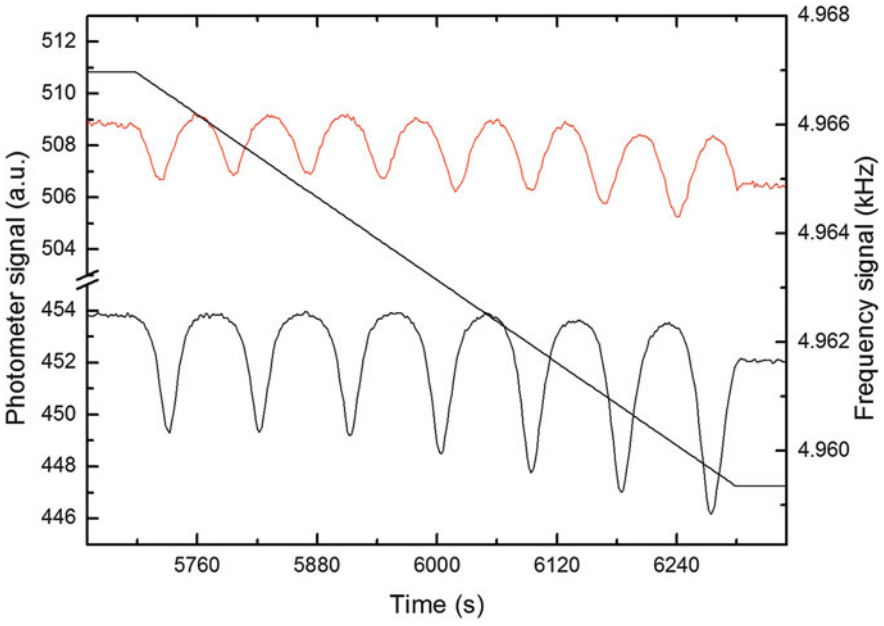

Fig. 4.2 Left axis, photometer signals of both laser beams (lower angle of incidence top signal); right axis, frequency of the QCMB during an ethane deposition experiment

observed on the constancy of both periods and the straight line corresponding to the decrease in frequency of the QCMB as the mass is deposited onto its surface. At this point, a consideration must be done: the more periods are obtained, the lower the uncertainties are, but as the thickness increases, the temperature on the surface of the ice is hardly controlled because the ice is not a good thermal conductor. Depending on the temperature and the ice molecule, different structures along the ice can be observed (Kouchi et al. 1992), or even ice cracks can appear (Ghormley and Hochanadel 1971). These limitations must be taken into account especially at those temperatures where a phase change is known or detected. Then the ideal thickness depends on the ice and the temperature of the experiment.

When constant deposition rate is guaranteed, n is easily obtained by using

$$n^2 = \frac{\sin^2\beta - \gamma^2\sin^2\alpha}{1 - \gamma^2} \tag{4.6}$$

where $\gamma = (\Delta t_2/\Delta t_1)$. Once n is determined, the thickness is obtained from Eq. (4.4). The mass per square centimeter is calculated from the Sauerbrey equation

$$\Delta \mathrm{f} = -\mathrm{S}\Delta \mathrm{m} \tag{4.7}$$

that relates the frequency variation of the oscillator (QCMB) and the mass variation on it for the interval of time considered (straight line in Fig. 4.2). In Eq. (4.7), S is the quartz constant expressed in cm^2 Hz ng^{-1}, being specific for any crystal and experimental arrangement. Density (in g cm^{-3}) is finally determined dividing mass deposited per square centimeter and thickness corresponding to the same time interval of deposition.

$$\rho = \frac{m}{d} \tag{4.8}$$

The interference signals do not decay to zero at the minimum (destructive interferences) because the intensity of the reflected beam on the ice surface is less than 5% of the impinging laser signal. This relation depends on the reflectivity of the ice and the surface of the QCMB, despite the periods only depend on the refractive index of the ice.

4.4 Results and Discussion

4.4.1 Density and Refractive Index

This section will provide some experimental results of n and ρ available for different ices to give an example on the variability of these values, and to relate them with ice structure. Even though in our method all the disadvantages have been tried

to be dodged, experimental errors calculated from the error propagation theory is about 2% for the refractive index, and the QCMB constant about 1%. To increase in precision many experiments are repeated, and statistical error calculated. When a molecule is studied, typically two experiments are repeated at every temperature of deposition and for selected temperatures even ten experiments are carried out. Most of experimental published results express their errors in precision not in accuracy because the actual values are unknown. To estimate the actual value many different experiments involving complementary techniques, theoretical calculations, etc. should be considered.

The molecules that will be used as examples are N_2, NH_3, CO_2, and C_2H_4 because they cover a range of densities from 0.4 g cm^{-3} to 1.5 g cm^{-3}; non-polar (CO_2) or polar (NH_3); single bond (NH_3), double (CO_2 or C_2H_4) or triple as N_2; with hydrogen bonds (NH_3) or without them (CO_2) . . .

All the figures in this section plot refractive index (left axis) and density (right axis), for different temperatures of deposition (X axis) ranging from the lowest temperature our system achieves, up to near the sublimation temperature of each ice.

4.4.1.1 Pure Ices

Nitrogen (Fig. 4.3) is the most volatile molecule selected. Temperatures of deposition vary from 10 K to 22 K (X axis). At 10 K two experiments have been plotted to show the experimental repeatability for this molecule. To plot the errors we overestimated slightly the errors and take 2.5% for the refractive index and 5% for density. With our procedure, both parameters reflect no variations for any temperature of deposition, despite nitrogen crystallizes in two forms, α and β.

Carbon dioxide's (Fig. 4.4) density varies from about 1 g cm^{-3} at temperatures of deposition below 20 K, up to 1.5 g cm^{-3} for temperatures higher than 50 K, where a plateau is obtained. We bring this example to highlight that this high density should not be confused with non-porous materials (see last section in this chapter). As a matter of fact, species with lower temperature of sublimation (hereafter hypervolatiles) are retained efficiently in the CO_2 ice structure as Temperature Programmed Desorption (TPD) proves (Satorre et al. 2009). Many can be the mechanisms to retain hypervolatiles; one possibility is that the ice itself is organized in perfectly crystalline islands but the voids (pores) among them retain it. Another possibility is that the amorphous structure of the ice permits to adsorb other molecules, and then when the ice crystallizes hypervolatiles are pushed out passing through the ice to the gas phase. Finally, some molecules substitute carbon dioxide sites in the ice structure, subliming with the carbon dioxide itself (see also the detailed study by Collings et al. 2004 for water ice).

Our results were compared with those obtained by Schulze and Abe (1980). They obtained the refractive index and density by using the polarizability of carbon dioxide and a Knudsen cell. They got a similar profile for all the temperatures, but only agree for low temperatures, up to around 40 K. For the highest temperatures they obtained values higher than ours. The maximum value they obtained was

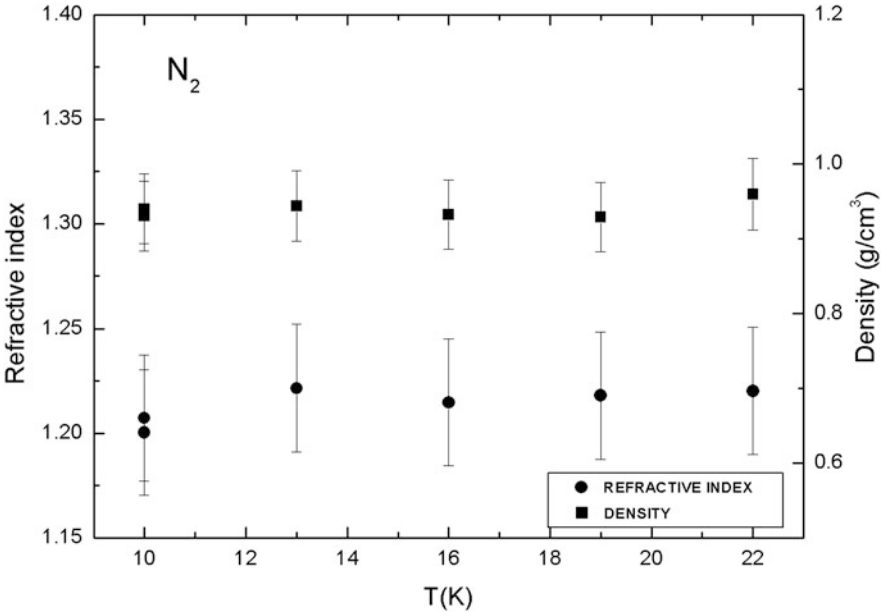

Fig. 4.3 Density and refractive index of nitrogen deposited at different temperatures (Satorre et al. 2008)

1.78 g cm^{-3}, that it is higher than the maximum theoretical density, 1.64 g cm^{-3}. All the discrepancies seem to come from the refractive index determination that depends on the deposition procedure as has been recently demonstrated by Loeffler et al. (2016). Despite these discrepancies, all experimental results show that the refractive index varies as the density does, increasing up to about 50 K, maintaining it almost constant for higher temperatures of deposition.

4.4.1.2 Ice Structure

Figure 4.5 shows NH_3 density and refractive index. Both parameters increase their values with the temperature of deposition up to around 60 K where a plateau is reached. Our results are compared with data previously published in the literature, with good coincidence at low and high temperatures. The refractive index matches previous results at low temperatures, and, in the 80–100 K range, we obtained the same values as Romanescu et al. (2010). These authors used double laser interferometry and a reference laser beam that allowed them to avoid laser signal fluctuations. Moreover, they repeated each temperature up to 19 times, obtaining the most precise experimental results.

Our NH_3 results complete the previous ones for the whole range of temperatures of deposition. This fact enables us to investigate if density and refractive index are

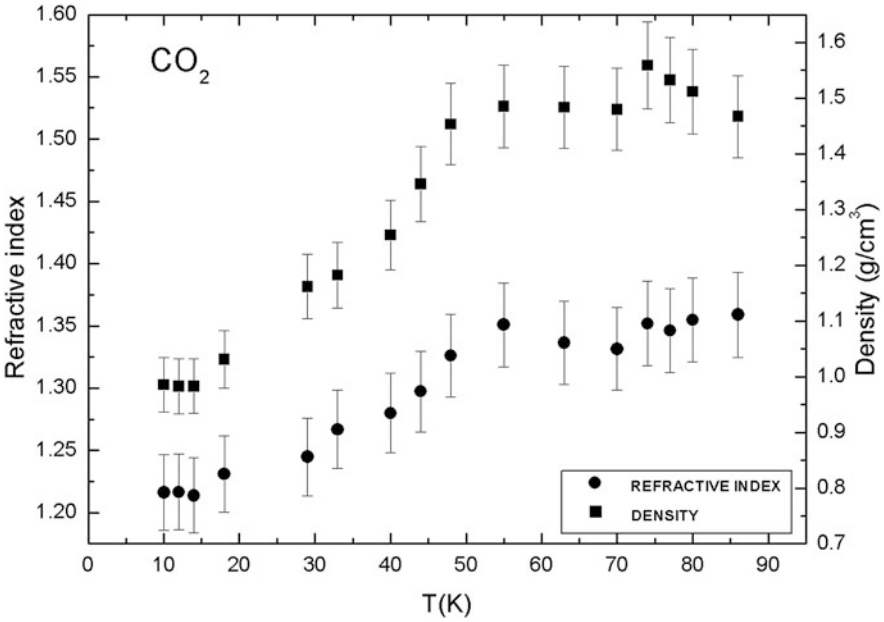

Fig. 4.4 Carbon dioxide density and refractive index obtained at different temperatures of deposition (Satorre et al. 2008)

related with ice structure and how they vary with the temperature of deposition. To that end, we use two specific studies about ammonia structure and its temperature dependence (Dawes et al. 2007; Zheng and Kaiser 2007). These two works were aimed to disclose if ammonia presented a metastable structure, which had been a controversial question during many decades. Both concluded that ammonia does not present a metastable structure, but an amorphous one at low temperatures and a stable crystalline one at high temperature. They determined the transition temperature at 58 K. The low-temperature amorphous structure becomes more ordered as the temperature increases. All their findings match our results. Then we can relate the increasing ρ and n values with the amorphous structure and the stability of both magnitudes, in the plateau region, with a crystalline stable structure.

Bearing in mind the precedent discussion, we can assume a crystalline structure for nitrogen because this molecule presents constant values of n and ρ for all the temperatures of deposition (see Fig. 4.3). CO_2 (Fig. 4.4) and NH_3 (Fig. 4.5) have a similar behaviour, which suggests that carbon dioxide must be amorphous, in average, for temperatures below 50 K and crystalline above this temperature. On the other hand, despite this similarity, we must emphasize that carbon dioxide does not attain the theoretical maximum density [1.64 g cm^{-3} (Schulze and Abe 1980)], but ammonia does [see results (Manzhelii and Tolkachev 1964; Olovsson and Templeton 1959 in Fig. 4.5)].

Sometimes, it is also possible to detect metastable structures. This is the case for ethylene that presents a crystalline metastable phase around 30 K. In Fig. 4.6,

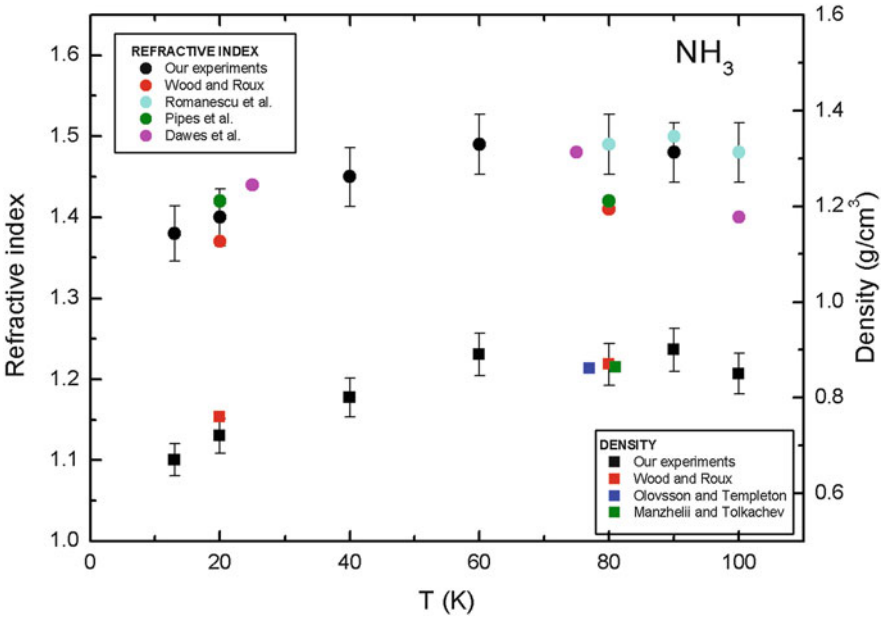

Fig. 4.5 Density and refractive index of ammonia at different temperatures of deposition (Satorre et al. 2013) compared with previous results: Wood and Roux (1982), Olovsson and Templeton (1959), Manzhelii and Tolkachev (1964), Romanescu et al. (2010), Pipes et al. (1978), Dawes et al. (2007)

bars indicate precision of our measurements, taken statistically from the *t*-student value for a confidence interval of 95%. The intrinsic density value obtained by van Nes (1978) at 85 K is plotted (green square). The dotted line is the average of the measurements over 35 K where a plateau seems to be reached. These values correspond to the crystalline structure as has been described with the other molecules. Up to 22 K, n and ρ rise as the temperature of deposition is increased (dashed lines in Fig. 4.6). This behaviour is associated with an amorphous structure. For temperatures of deposition between 22 K and 35 K, the measurements follow neither the crystalline behaviour nor the amorphous one.

To check this anomalous behaviour, our results were compared with those of Hudson et al. (2014) who studied ethane and ethylene at different temperatures of deposition by infrared spectroscopy. To do that, they also obtained the refractive index of ethylene at three relevant temperatures, shown by blue solid circles in Fig. 4.6. The point at 11 K corresponds to an amorphous structure; at 30 K, to a phase that they describe as crystalline metastable; and to a stable crystalline ice at temperatures higher than 35 K. As can be seen, there is a stark disagreement at 30 K with our results. The reason is that those authors, to obtain a pure metastable phase, had to deposit 60 times faster than the rate of deposition they used for the rest of the

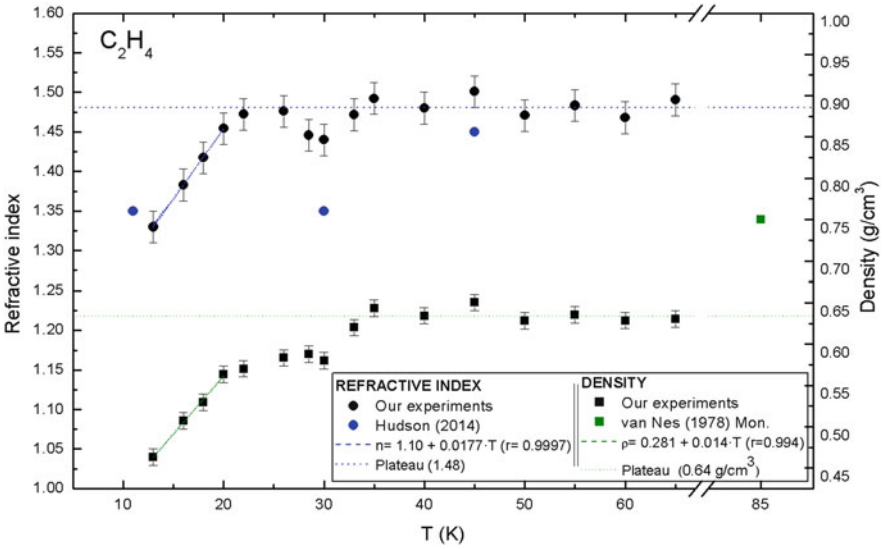

Fig. 4.6 Ethylene density and refractive index at different temperatures of deposition (Satorre et al. 2017) compared with previous results. Hudson et al. (2014), van Nes (1978)

experiments. The rate of deposition is usually around 1 micron h^{-1} for most of the experimental laboratories, including ours.

It is generally understood that a metastable phase changes irreversibly to another phase if it is warmed up and cannot be obtained again cooling down the ice. In fact, this definition makes all the amorphous phases metastable, even though in the literature they are labelled as amorphous. Usually a crystalline phase is stable, but sometimes it isn't. This is the case for the ethylene phase grown at 30 K. Hudson et al. (2014) and Wisnosky et al. (1983) show that around 30 K ethylene presents a certain metastable crystalline structure. In these studies, they confirm that if ethylene is deposited below 20 K and warmed up, it passes directly to the stable crystalline structure. When deposited at 30 K the structure is metastable because if it is warmed up, changes irreversibly to the stable crystalline structure, although the spectra have crystalline characteristics.

4.4.1.3 Ice Mixtures

Density and refractive index of ice mixtures are not, in general, the arithmetic mean of the values of their pure constituents at a given temperature. At least for the binary mixtures studied in our group, with the exception of CO_2:CH_4 mixtures. Figure 4.7 plots in the left panel the density of a binary mixture of nitrogen and carbon dioxide. The solid line shows the theoretical density value obtained from that of pure ices (Luna et al. 2012b). On the right panel, the results for a mixture of methane and

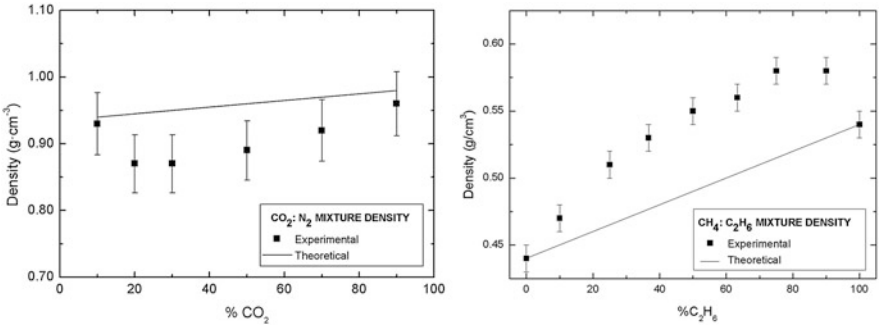

Fig. 4.7 Nitrogen:carbon dioxide (left panel) (Luna et al. 2012b) and methane:ethane (right panel) (Molpeceres et al. 2016) mixtures at constant temperatures (14 K and 30 K, respectively). The abscissa axis represents enrichment of carbon dioxide and ethane respectively

ethane are represented (Molpeceres et al. 2016). The abscissa collects the proportion of carbon dioxide and ethylene in the appropriate ice, respectively. Solid squares are the experimental results with their error bars.

These examples have been selected to clarify that, depending on the mixture, the ice formed can be denser or lighter than expected. The variation is not symmetric with respect to the 50% mixture. It reveals that the effect of one molecule on the structure of the other is not the same than the opposite. In the case of the N_2:CO_2 mixture, carbon dioxide modifies more deeply the nitrogen structure than nitrogen does to the carbon dioxide one. On the right panel, it can be seen the stronger influence of methane on the structure of ethane. In both cases the maximum deviation from the theoretical values occurs when the molecule that more affects the structure (carbon dioxide, left, and methane, right) is about 25%. This effect has also been observed by Isokoski et al. (2014) who measured the refractive index of mixtures of water and carbon dioxide at different temperatures of deposition. They found that water dominated ices (66%) behave like carbon dioxide, instead of following the expected behaviour of pure water ices.

4.4.2 Porosity

The importance of porosity has been mentioned above in Sect. 4.2.1.c. This parameter is defined as the void volume fraction (pores) on the total volume of the material. It can be expressed as a function of the density

$$p = 1 - \frac{\rho_a}{\rho_i} \tag{4.9}$$

Where ρ_a is the average density, considering the material as homogeneous and, therefore, including pores, and ρ_i the intrinsic density, which corresponds to the

Table 4.1 Porosity (in %) obtained from Eq. (4.9), taking ρ_i from the literature: CO_2 (Schulze and Abe 1980); NH_3 (Manzhelii and Tolkachev 1964; Olovsson and Templeton 1959) and C_2H_4 (van Nes 1978)

Molecule	Amorphous (high p)	Metastable	Crystalline (low p)
CO_2	40		10
NH_3	32		0
C_2H_4	40	23	16

material without pores. The latter is usually measured by diffraction methods, using radiation at a suitable wavelength (method that can be aggressive to the material), or, sometimes, taking the value at temperatures in which it is assumed that the material is not porous, like for crystalline ices formed at high temperatures.

From their definition, the porosity of the pure ices presented here can be calculated if the intrinsic density is known, as it is the case for CO_2, NH_3 and C_2H_4. We want to underline that the intrinsic density has been obtained at different temperatures and with different procedures than those used by most of the laboratories devoted to astrophysics applications.

Table 4.1 shows the porosity obtained for these three molecules at the lowest temperature of deposition, where all three have an amorphous structure, and close to their temperature of sublimation corresponding to a stable crystalline structure. The porosity of metastable ethylene is also added. As can be observed, amorphous structures are porous (>30%), irrespectively on the density of the molecule. It is remarkable that ethylene and carbon dioxide have the same porosity, but the density of carbon dioxide is twice that of ethylene. These molecules are still porous even when they crystallize. In the case of metastable ethylene its porosity is almost half of the amorphous ice.

4.5 Summary and Conclusions

In astrophysics there are many parameters that help us to understand observations and test simulations. Among them, we focus on the refractive index and density.

To exemplify the relevance of density, we have described the relationship with integrated absorbance, buoyancy, and porosity.

The nomenclature used is often misleading. We define here the intrinsic, or bulk, density and the average density. The basic ideas behind the different methods used to measure both densities are also shown. We describe as well the advantages of determining the average density by a double laser interferometric technique using the same surface to measure the mass deposited per square centimetre (QCMB).

We present and discuss representative examples of the variation of n and ρ with the temperature of deposition and their relationship with ice structure. We conclude that the average density of amorphous ices is lower than that of crystalline ones.

The maximum average density of vapor deposited ices is obtained at higher temperatures of deposition when the crystalline form is achieved. Often this density is lower than the maximum theoretical density that a crystal can achieve, which is obtained with other specific methods.

Known density values for ices range from about 0.4 g cm^{-3}, for amorphous light hydrocarbons, to 1.5 g cm^{-3}, for crystalline carbon dioxide.

All results of refractive index and density presented here are obtained depositing at certain temperatures. We must also make clear that the density of an ice deposited at a given temperature (T), is always greater than when depositing at a lower temperature and warming up to T, except if the ice is deposited at high temperatures that form the stable crystalline structure.

Porosity does not depend on the average density; dense molecular ices may present a more porous structure than lighter ones. Amorphous ices are more porous than crystalline ones. Some stable crystalline ices are still porous when they are background deposited.

Acknowledgements The authors thank the Ministerio de Economía y Competitividad that funded this research, with grants FIS2013-48087-C2-2-P, FIS2016-77726-C3-3-P and AYA2015-71975-REDT.

References

Born, M., Wolf, E.: Principles of Optics: Electromagnetic Theory of Propagation, Interference and Diffraction of Light, 7th edn. Cambridge University, Cambridge (1999)
Brunetto, R., et al.: Astrophys. J. **686**, 1480 (2008)
Collings, M.P., et al.: MNRAS **354**, 1133 (2004)
Dawes, A., et al.: J. Chem. Phys. **126**, 244711 (2007)
Fulvio, D., et al.: Spectrochim. Acta A. **72**, 1007 (2009)
Ghormley, J.A., Hochanadel, C.J.: Science. **171**, 62 (1971)
Hudson, R.L., et al.: Icarus. **243**, 148 (2014)
Isokoski, K., et al.: Phys. Chem. Chem. Phys. **16**, 3456 (2014)
Jenniskens, P., Blake, D.F.: Astrophys. J. **473**, 1104 (1996)
Kouchi, A., et al.: Astrophys. J. **388**, L73 (1992)
Kouchi, A., et al.: Chem. Phys. Lett. **658**, 287 (2016)
Labello, J.M.: Ph.D. Dissertation, University of Tennessee (2011)
Loeffler, M.J., et al.: Astrophys. J. **827**, 98 (2016)
Luna, R., et al.: Vacuum. **86**, 1969 (2012a)
Luna, R., et al.: Icarus. **221**, 186 (2012b)
Manzhelii, V.G., Tolkachev, A.M.: Sov. Phys. Solid State. **5**, 2506 (1964)
Molpeceres, G., et al.: Astrophys. J. **825**, 156 (2016)
Olovsson, I., Templeton, D.H.: Acta Crystallogr. **12**, 832 (1959)
Pipes, J.G., et al.: AIAA J. **16**, 984 (1978)
Roe, H.G., Grundy, W.M.: Icarus. **219**, 733 (2012)
Romanescu, C., et al.: Icarus. **205**, 695 (2010)
Satorre, M.Á., et al.: Planet. Space Sci. **56**, 1748 (2008)
Satorre, M.A., et al.: Planet. Space Sci. **57**, 250 (2009)
Satorre, M.Á., et al.: Icarus **225**, 703 (2013)

Satorre, M.Á., et al.: Icarus **296**, 179 (2017)
Schulze, W., Abe, H.: Chem. Phys. **52**, 381 (1980)
van Nes, G.J.H.: Ph.D. Thesis, University of Groningen (1978)
Wisnosky, M.G., et al.: J. Chem. Phys. **79**, 3513 (1983)
Wood, B.E., Roux, J.A.: J. Opt. Soc. Am. **72**, 720 (1982)
Zheng, W., Kaiser, R.: Chem. Phys. Lett. **440**, 229 (2007)

Chapter 5
Infrared Optical Constants and Band Strengths of Ices

Belén Maté

Abstract Infrared optical constants of ices allow us reproducing astrophysical observations of absorption, reflection or extinction infrared spectra of these species. They are also needed as input in some astrophysical models. Infrared band strengths provide a direct tool to quantify the composition of ices in astrophysical media. In this chapter we describe different experimental ways to obtain these magnitudes. They are based on infrared transmission absorption spectra of ice layers grown on infrared transparent substrates. The main approximations implicit in the procedures are reviewed.

5.1 Introduction

Infrared (IR) spectroscopy is one of the most popular spectroscopic techniques in solid-state physics, and the reason for this is that nearly all solid materials exhibit absorptions in the IR spectral range. The main sources of absorptions are IR active phonons or vibrational modes, apart from contributions due to transitions across the energy gap, from excitons or from impurity states. In this chapter we will describe the dielectric function and the functions directly related to it, the optical constants, which are fundamental in spectroscopy. We will describe how these magnitudes can be derived from experiments. The definition of IR band strengths and its relation with IR optical constants will be given and the astrophysical interest of these magnitudes will be highlighted at the end of the chapter.

Attending on how the atoms or molecules that form a solid are packed together, solids can be divided into three categories. Crystalline solids have a regular structure, in which the atoms are organized in a repeating pattern from one edge of the solid to the other. Amorphous solids have a random structure, with little if any long-range order. Polycrystalline solids are an aggregate of a large number of

B. Maté (✉)
Instituto de Estructura de la Materia, IEM-CSIC, Madrid, Spain
e-mail: belen.mate@csic.es

G. M. Muñoz Caro, R. Escribano (eds.), *Laboratory Astrophysics*,
Astrophysics and Space Science Library 451,
https://doi.org/10.1007/978-3-319-90020-9_5

small crystals or grains in which the structure is regular, but the crystals or grains are arranged in a random fashion. The extent to which a solid is crystalline has important effects on its physical properties.

Attending to the binding forces that hold the atoms or molecules together, the solids have another classification. Depending on the qualitative differences in the distribution of electrons around the atoms or molecules, solids can be classified as ionic, covalent, metallic, molecular, or hydrogen bonded. Ionic solids, like salts such as NaCl, are formed by ions that are held together by the strong force of attraction between their opposite charges. Covalent solids, such as diamond, form crystals that can be viewed as a single giant molecule made up of an almost endless number of covalent bonds. In metals, the valence electrons are delocalized over many metal atoms and are free to migrate. Molecular solids are characterized by relatively strong intramolecular bonds and much weaker intermolecular forces. The weak forces between molecules, known as Van der Waal forces, arise from interaction of their permanent dipole moments or by the fluctuating dipole moment associated with the instantaneous position of the electrons in the atoms. Due to the unique characteristic of the hydrogen atoms, molecular solids that present hydrogen bonds are considered an important subgroup in this classification.

In this chapter we are dealing with ices of astrophysical interest. When those ices are grown in the laboratory by vapor deposition of gases on a cold surface, depending on the generation conditions polycrystalline or amorphous solid phases are obtained. Ices are a clear example of molecular solids where the molecules that constitute the solid are weakly bound by van der Waals forces or hydrogen bonds.

5.2 Lattice Vibrations and Infrared Absorption

The theory of lattice vibrations will allow us to describe the interaction of infrared radiation with a molecular/ionic crystalline solid (Kittel 1953, Ashcroft and Mermin 1976, and Decius and Hexter 1977). Due to the connections between atoms in a crystalline solid, the displacement of one or more atoms from their equilibrium positions gives rise to a set of vibration waves propagating through the lattice. However, not every possible lattice vibration has a well-defined wavelength and frequency. The ones that do possess them are called normal modes.

Here, to simplify the analysis, a one dimensional latice is modeled, in order to define normal modes and the dispersion relation. We will consider a lattice or linear chain of Z similar atoms of mass M spaced a distance a. The forces between the atoms are assumed to be linear and nearest-neighbor, and they are represented by an elastic spring. Let u_n denote the displacement of the nth atom from its equilibrium position, and β the force contant. The force F_n acting on the nth atom is given by:

$$F_n = \beta\left(u_{n+1} - u_n\right) - \beta\left(u_n - u_{n-1}\right), \tag{5.1}$$

where the terms in parentheses on the right side are the increase in length of the bonds between the atoms n and $n+1$, or between the atoms n and $n-1$. The equation of motion of the nth atom, of mass M, is

$$M\,\ddot{u}_n = \beta\,(u_{n+1} + u_{n-1} - 2u_n). \tag{5.2}$$

This is a set of coupled equations and since the solutions are expected to be oscillatory, we can look for solutions of the form:

$$u_n = \xi\, e^{i(\omega t + qna)}. \tag{5.3}$$

These are running waves solutions where ω is the angular frequency, q is the angular wavenumber, and a is the nearest neighbor distance. The allowed normal modes of vibration of the one-dimensional lattice are constructed taking linear combinations of these solutions and have the form:

$$u_n = C_q\, e^{i\omega_q t} \sin qna; \tag{5.4}$$

where due to periodic boundary conditions there are just N allowed values of q given by $q = \frac{2\pi}{a}\frac{s}{Z}$, with s a running number, $1 \leq s \leq \mathrm{Z}$, and C_q is an arbitrary complex number determining the amplitude and phase of the motion. In a normal mode, all the atoms of the solid move with the same frequency. A linear chain with Z atoms has Z normal modes. It is possible to describe lattice vibrations with quantum mechanics and in that way define a phonon as the quantum of vibrational energy $\hbar\omega$ in a normal mode labelled by ω and q.

Substituting the trial wave function (5.3) in the equation of motion (5.2) we have a solution if

$$\omega(q) = \pm\left(\frac{4\beta}{M}\right)^{1/2} \sin\left(\frac{qa}{2}\right). \tag{5.5}$$

Equation (5.5) is known as the dispersion relation, and gives the dependence of the angular frequency ω of the normal mode with its wavenumber, $q = \frac{2\pi}{\lambda}$. It can be seen that the maximum angular frequency that can propagate in the one dimensional lattice is $\omega_m = \pm\left(\frac{4\beta}{M}\right)^{1/2}$, corresponding to a q maximum of $q_m = \pm\frac{\pi}{a}$. A Brillouin zone represents one-unit cell of the crystal in the reciprocal space, and q_m coincides with the limit of the first Brillouin zone of the one dimensional lattice. Larger values of q merely reproduce motions already described by values of $q < q_m$. This finding simply indicates that since a perfect crystal is a periodic structure, the behavior of the normal modes within the crystal could be modeled within the first Brillouin zone.

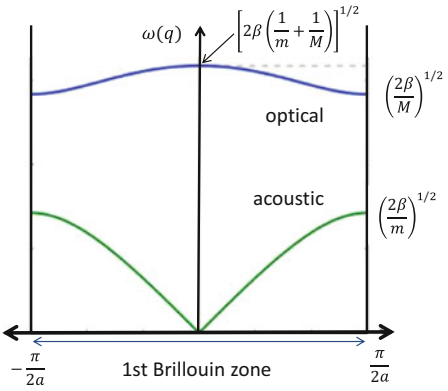

Fig. 5.1 Dispersion curves for a linear diatomic chain

In the case of a one-dimension lattice with two kinds of atoms with mass M and m, the dispersion relation is given by

$$\omega^2(q) = \beta\left(\frac{1}{m}+\frac{1}{M}\right) \pm \beta\left[\left(\frac{1}{m}+\frac{1}{M}\right)^2 - \frac{4\sin^2 qa}{Mm}\right]^{1/2} \tag{5.6}$$

The variation of ω with q is represented in Fig. 5.1. It is seen that, if the Brillouin zone contains more than one atom, the dispersion relation has two branches, one is called acoustic and the other optical. In real three dimensional solids with p atoms in the unit cell, the results are extrapolations of the cases already considered. The main effect of introducing polyatomic basis is the appearance of optical branches. In the three dimensional case, for each value of $\overrightarrow{q}$ there are $3p$ normal modes. Three of the $3p$ modes are acoustic, i.e., they describe vibrations with frequencies that vanished linearly with $\overrightarrow{q}$ when $\overrightarrow{q} \to 0$. The other $3(p-1)$ modes are optical modes, i.e., their frequencies do not vanish in the $\overrightarrow{q} \to 0$ limit.

The acoustic modes are named like that because of their similitude to light or sound waves propagating in a continuous media, with constant group and phase velocity $\frac{w}{q} = v$. This is what happens for acoustic modes in the large frequency limit, i.e., when the wavelength of phonons is large in comparison to the interatomic distance, $q = \frac{2\pi}{\lambda} \ll \frac{\pi}{a}$, and the medium behaves like a continuum. When the q value approaches the limit of the first Brillouin zone, the acoustic phonons feel the discrete nature of the solid and deviate from linear behavior.

On the other hand, the optical modes are called like that because they can be excited by electromagnetic radiation, in the optical-infrared part of the spectrum. In the two atom chain optical mode, the atoms move out of phase, generating a dipole. In the more general case of a three dimensional solid with a base, in the optical modes, the atoms within the unit cell move to generate a non-vanishing polarization. The energy of these lattice vibrations generally falls in range of 0.5–0.01 eV that corresponds to energies of infrared photons.

When dealing with electromagnetic excitations of the optical branch of solids, as in the case we are interested in this chapter, i.e., infrared spectroscopy of ices, a good approximation can be made. It is possible to assume that the wavenumber of the excited normal mode in the solid is zero, i.e., $q = 0$. This is due to the large wavelength of the infrared radiation as compared to the size of the unit cell, a, of the crystal. For example, an infrared radiation with a wavelength of 10 microns is 10^4 times larger than a unit cell length of 10 Å. Or, what is the same, the wavenumber of the infrared photon, $\frac{1}{\lambda} \approx 10^3 \text{cm}^{-1}$, is much smaller than $q_m = \frac{\pi}{a} \approx 10^8 \text{ cm}^{-1}$, the cut off of the wavenumber lattice vibrations. Therefore the interaction of the infrared photon will happen only with phonons in the $q \to 0$ limit, and considering only phonons with $q = 0$ is a good approximation.

5.3 The Dielectric Function

To describe the behavior of an ionic or molecular solid when interacting with infrared radiation it would be necessary to calculate the normal mode dispersion relations in the crystal following the approach described in the previous section, but considering more complex long range interactions between the atoms in the solid. However, for long-wavelength optical modes, like the ones that interact with infrared radiation, we can treat the problem from another point of view, describing the solid with the macroscopic Maxwell equations, and calculating its wavelength dependent dielectric function.

The dielectric function describes the reaction of an insulator material to an external force. The macroscopic Maxwell equations in a medium are the most valuable tool to describe this problem. We will assume the reaction of the medium is linear, i.e., the response functions are properties of the solid system and are independent of the driving force. The dielectric function is defined as the medium response function (ε) that relates the displacement ($\overrightarrow{D}$) to the applied electric field ($\overrightarrow{E}$),

$$\overrightarrow{D} = \varepsilon \overrightarrow{E} \tag{5.7}$$

Note that both field and displacement are vectors, and therefore the response function is a second-rank tensor. For simplicity in this chapter we will assume $\overrightarrow{D}$ parallel to $\overrightarrow{E}$ and ε a scalar. This assumption is valid in cubic symmetry crystals, and in isotropic polycrystalline or amorphous solids, like most of the ices we are dealing with. The frequency dependence of the dielectric function in the infrared spectral range reflects the infrared optical properties of the material.

5.3.1 Relation Between the Dielectric Function and the Refractive Index (or Optical Constants)

From the Maxwell equations for a non-conducting non-magnetic medium in one dimension we have:

$$\frac{\partial^2 E\,(x,t)}{\partial x^2} = \frac{\varepsilon}{c_0^2}\frac{\partial^2 E}{\partial t^2}, \tag{5.8}$$

where c_0 is the speed of light in vacuum. An electric field with wavenumber ν and angular frequency ω is described by a plane electromagnetic wave

$$E\,(x,t) = E_0 e^{i(2\pi\nu x - \omega t)}. \tag{5.9}$$

The dispersion relation for the propagation of the electromagnetic field in the media with dielectric constant ε, can be obtained from equations (5.8) and (5.9) and is

$$\nu^2 = \frac{\omega^2}{4\pi^2 c_0^2}\varepsilon \tag{5.10}$$

Moreover, the wavenumber is related with the angular frequency via the velocity of light in the media, c, or the index of refraction of the media, N, and the velocity of light in vacuum, c_0,

$$\nu_c = \frac{\omega}{2\pi c} = \frac{\omega\, N}{2\pi c_0}. \tag{5.11}$$

Comparing equations (5.10 and 5.11) we obtain $N = \sqrt{\varepsilon}$. We have used the sub-index in the wave vector ν_c to indicate that it can be a complex number, if N and ε are. The two functions may be expressed as:

$$N = n + ik, \tag{5.12}$$

$$\varepsilon = \varepsilon_r + i\varepsilon_i. \tag{5.13}$$

The complex notation for the index of refraction leads to an electromagnetic field attenuated in space like

$$E\,(x,t) = E_0 e^{-2\pi\nu k x} e^{i(2\pi\nu n x - \omega t)}, \tag{5.14}$$

where $2\pi\nu k$ describes the attenuation of the field. At this point we can introduce the absorption coefficient, α, that describes the intensity attenuation of the field via the

Lambert–Beer's law

$$I(x) = EE^* = I_0 e^{-\alpha\rho x}, \tag{5.15}$$

where E^* is the complex conjugate of E, ρ is the concentration or density of absorbers in the sample, and x the optical path length. Combining equations (5.14, 5.15) the absorption coefficient can be expressed as

$$\alpha = \frac{4\pi\nu k}{\rho} \tag{5.16}$$

that has units of $cm^2\ g^{-1}$. Within the linear response theory, the real and imaginary part of the complex response functions, ε or N,are related via the Kramers–Kronig dispersion relations. With these relations one component of the function can be calculated step by step if the other component is known for the whole spectral range. For example the relation between the real and imaginary part of the refractive index is given by:

$$n(\nu) = n(\infty) + \frac{2}{\pi} P \int_o^\infty \frac{\nu' \kappa(\nu')}{\nu'^2 - \nu^2} d\nu' \tag{5.17}$$

$$k(\nu) = -\frac{2}{\pi} P \int_o^\infty \frac{n(\nu')}{\nu'^2 - \nu^2} d\nu' \tag{5.18}$$

in which P denotes the Cauchy principal value of the integral. These relations are a very useful property since only one component of the refractive index, the imaginary part, can be determined experimentally via the Lambert-Beer law. However, in order to apply equations (5.17) or (5.18) to determine the real part of the refractive index, the frequency dependence of the other component must be known in the whole spectral range, which is not usually the case, and proper extrapolations are needed.

5.4 Experimental Determination of Infrared Optical Constants

Along this chapter we will call infrared optical constants to the complex refractive index, $N(\nu) = n(\nu) + ik(\nu)$, in the IR spectral range.

To determine $N(\nu)$ in the infrared spectral range, of thin solid films of an isotropic material it is very convenient to use normal incidence IR transmittance measurements. In the case of anisotropic materials the problem is more complicated, and non-normal incidence and polarization measurements are needed. Nevertheless, as mentioned above, most of the ices of astrophysical interest investigated in the laboratory are grown by vapor deposition on a cold substrate under vacuum. Under

these conditions, crystalline ice layers consist on small crystal domains randomly oriented, and the macroscopic solid formed could be considered isotropic. On the other hand, if the ice generated is amorphous, it will be more probably isotropic due to its structural disorder. For these reasons we will consider normal transmission infrared spectroscopy in this chapter to determine complex refractive index of ices, but it has to be kept in mind that the procedure is only valid for isotropic solids. As mentioned previously, this condition is necessary to have a dielectric constant which is scalar instead of a tensor.

Next, we describe the steps followed for deriving the optical constants. First, we develop the equations to calculate absorbance spectra. Second, we use experimental absorbance spectra to obtain initial values of the properties of the ice films, like layer thickness or imaginary part of the refractive index. Third, we use the Kramers–Kronig relation to obtain an initial value for the real part of the refractive index. Fourth, we use an iterative procedure to minimize the differences between the calculated absorbance and the measured absorbance spectra. Similar approaches have been employed in the literature by Wood and Roux (1982) or Toon et al. (1994) to obtain optical constants of ices. The procedure described in this section has been developed at the IEM-CSIC, to determine mid IR optical constants of ices of NH_3, NH_3:N_2, CH_4, CH_4:C_2H_6, CH_4:C_2H_4 (Zanchet et al. 2013; Molpeceres et al. 2016).

In general, applying Fresnel formulae, it is possible to obtain expressions of the transmitted or reflected radiation by a medium as function of the real and imaginary part of its refractive index. The particular case of an ice film deposited on a cold substrate complicates somehow the expressions since we have to deal with several interfaces, the vacuum-ice plus the ice-substrate, for an appropriate determination of the transmitted radiation. Moreover, usually ice layers are grown on both sides of the cold substrate (see Fig. 5.2). In particular, our system is composed of film 1, a thick substrate S, and film 2. In the following 1 and 2 refer to the ice films (of equal thickness), 0 to air and S to substrate.

The substrate layer is made of an infrared transparent material, like silicon, KBr or ZnSe. These materials are non-absorbing in the IR spectral region, and therefore their refractive indices, *N*s, are real in this spectral range. Since the thickness of the window (about 1–2 mm) is larger than the coherence length of the radiation, waves reflected on its front and back surfaces add incoherently. On the other hand, ice layers grown on top have thickness between one hundred nm and several microns. This thickness interval is chosen to have a compromise between a good signal to noise ratio and no saturation of the IR absorptions. Also, it is important for the ice layers to be thick enough to avoid surface effects, since we are interested in determining the optical properties of the bulk ice material. Thickness between 0.1 and several microns are comparable with the wavelength of the infrared radiation, and consequently some degree of coherence can be maintained by the IR radiation while traveling through the ice layers. Therefore, a coherence parameter has to be introduced into the model and fitted for each film thickness considered.

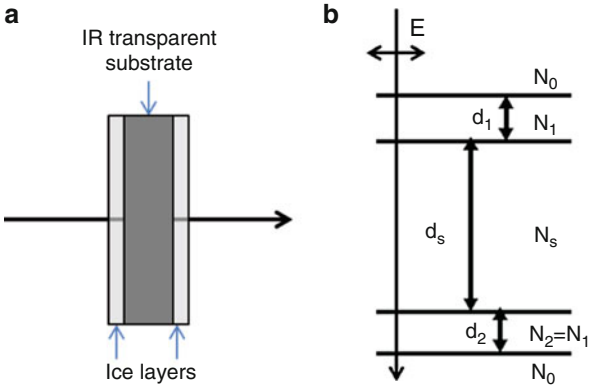

Fig. 5.2 (**a**) Three layer system scheme illustrating the formation of ice on both sides of an IR transparent substrate. (**b**) Three layered system scheme with notation. $N_1 = N_2 = N_f$ are the ice complex refractive index and *Ns* the substrate refractive index. $d_1 = d_2 = d$ are the ice layer thickness at each side of the substrate. In this chapter we have considered normal incidence, $\Theta_0 = 0$, but expressions for non-normal incidence can also be derived

The calculated absorbance spectrum at a given wavenumber is defined by the ratio of the transmittance T of the three layered system to that of the bare substrate, T_S.

$$\mathrm{A}\,(\nu) = -\log\left(\frac{\mathrm{T}\,(\nu)}{\mathrm{T_S}\,(\nu)}\right) \tag{5.19}$$

From the previous discussion it follows that transmittance of the three-layer system depends on several parameters as indicated schematically in the following equation:

$$T = f\,\left(N_f, N_S, d, c, \theta, \nu\right), \tag{5.20}$$

where N_f and N_S are the complex refractive indices of the film and real refractive index of the substrate, d is the film thickness, c is the degree of coherence of the film ($0 \leq c \leq 1$), θ is the angle of incidence (0° for normal incidence in our experiments) and ν the wavenumber of the radiation. We refer with this magnitude to the inverse of the wavelength of the infrared radiation, usually given in cm^{-1}. The transmission of a three-layered system contains coherent and non-coherent contributions. Whereas the substrate gives rise to non-coherent contributions, the transmitted light through the two thin films is partly coherent and partly non-coherent. This system can be expressed by means of two transmission terms

$$T = cT^c + (1 - c)\,T^{nc}, \tag{5.21}$$

where T^c and T^{nc} are the coherent and non-coherent transmittance components. The expressions to calculate the different transmissions are given by the following equations. The bare substrate transmission is:

$$T_S = \frac{T_{0S}T_{S0}}{1 - R_{S0}^2} \tag{5.22}$$

where $T_{ij} = 1 - R_{ij}$ and $R_{ij} = |r_{ij}|^2$, and r_{ij} are the Fresnel coefficients for reflection in the interface between layers i and j.

$$r_{ij} = \frac{N_i - N_j}{N_i + N_j} \tag{5.23}$$

The three-layer coherent ($X = c$) or non-coherent ($X = nc$) normal incidence transmission is given by:

$$T^x = \frac{T_{f1}^x T_{f2}^x}{1 - R_{f1}^x R_{f2}^x} \tag{5.24}$$

where the composite transmission and reflection factors can be written as (Fernández-Torre 2005; Heavens 1995):

$$T_{f1}^c T_{f2}^c = \left| \frac{t_{01}t_{1S}e^{i\delta_1}}{1 + r_{01}r_{1S}e^{i(2\delta_1 - \varphi_1)}} \right|^2 \left| \frac{t_{S2}t_{20}e^{i\delta_2}}{1 + r_{S2}r_{20}e^{i(2\delta_2 - \varphi_1)}} \right|^2$$

$$R_{f1}^c = \left| -\frac{\mathrm{r_{1S}} + \mathrm{r_{01}e^{i(2\delta_1 - \varphi_1)}}}{1 + \mathrm{r_{1S}r_{01}e^{i(2\delta_1 - \varphi_1)}}} \right|^2$$

$$R_{f2}^c = \left| \frac{r_{S2} + r_{20}e^{i(2\delta_2 - \varphi_1)}}{1 + r_{S2}r_{20}e^{i(2\delta_2 - \varphi_1)}} \right|^2 \tag{5.25}$$

and

$$T_{f1}^{nc} T_{f2}^{nc} = \frac{T_{01}T_{1S}e^{-2\mathrm{Im}(\delta_1)}}{1 - R_{01}R_{1S}e^{-2\mathrm{Im}(2\delta_1 - \varphi_1)}} \frac{T_{S2}T_{20}e^{-2\mathrm{Im}(\delta_2)}}{1 - R_{S2}R_{20}e^{-2\mathrm{Im}(2\delta_2 - \varphi_1)}}$$

$$R_{f1}^{nc} = R_{1S} + \frac{T_{S1}T_{1S}R_{01}\, e^{-2\mathrm{Im}(2\delta_1 - \varphi_1)}}{1 - R_{1S}R_{01}e^{-2\mathrm{Im}(2\delta_1 - \varphi_1)}}$$

$$R_{f2}^{nc} = R_{S2} + \frac{T_{S2}T_{2S}R_{20}\, e^{-2\mathrm{Im}(2\delta_2 - \varphi_1)}}{1 - R_{S2}R_{20}e^{-2\mathrm{Im}(2\delta_2 - \varphi_1)}} \tag{5.26}$$

with phases in normal incidence given by:

$$2\delta_1 - \varphi_1 = 2\delta_{12} - \varphi_1 = \frac{4\pi}{l} d\ N_f \ \ ; \ \ \delta_1 = \delta_2 = \frac{2\pi}{l} d\ N_f \tag{5.27}$$

and the Fresnel coefficient for transmission through the interface between layers i and j:

$$t_{ij} = \frac{2\ N_i}{N_i + N_j} \tag{5.28}$$

Expressions (5.20)–(5.27) allow calculating the transmitted radiation through a three layered system, providing that we know the complex optical constants of the different media.

The procedure to extract the optical constants of the ice film from transmittance measurements of ices of different thicknesses is to minimize iteratively two merit functions M and W that evaluate the difference between calculated and experimental absorbance spectra. M is a function that gives, for a particular wavenumber, the square of the difference between the experimental and the simulated absorbance, weighted by the sample thickness, and summed over all spectra,

$$\mathrm{M}(\nu) = \sum_{1}^{\mathrm{n_d}} \frac{\left(\mathrm{A_{exp}}(\nu) - \mathrm{A_{theo}}(\nu)\right)^2}{\mathrm{d}}, \tag{5.29}$$

with $\mathrm{n_d}$ the number of spectra used. Weighting by the respective thickness is included to take into account of the different relative errors for each spectrum. The function W calculates the quadratic error summed over the frequency range of the experiments:

$$\mathrm{W} = \sum_{\nu_1}^{\nu_2} \left(\mathrm{A_{exp}}(\nu) - \mathrm{A_{theo}}(\nu)\right)^2, \tag{5.30}$$

where ν_1 and ν_2 define the frequency interval we want to consider.

To calculate the absorption spectrum of the three-layer system via equations (5.19, 5.20, and 5.22) initial values of the different physical properties of the ice films and the substrate must be provided. The choice of a good initial guess is critical to achieve convergence in the minimization procedure, and therefore good estimations of the thickness of each ice layer, of the real part of the refractive index at high frequencies, $n_0 = n(\infty)$, and of the initial optical constant of the ice, are needed. Fortunately, ice layer thickness and n_0 can be determined quite accurately from He–Ne laser interference fringe experiments, as it is described in Chap. 4 of this book. Moreover, an initial value of the imaginary part of the refractive index $k(\nu)$ of the ice can be estimated from one of the experimental absorbance spectra, usually the thickest one, using Lambert's law. From the definition of absorbance and

equations (5.15 and 5.16) the following relation between the imaginary part of the refractive index and the absorbance spectrum is obtained:

$$k\,(\nu) = 2.303 \frac{1}{4\pi\ \nu\ d}\ \mathrm{A}\,(\nu)\,. \tag{5.31}$$

The corresponding $n(\nu)$ is then derived from the Kramers–Kronig equation (5.17)

$$n\,(\nu) = n_0 + \frac{2}{\pi} P \int_{\nu_1}^{\nu_2} \frac{\nu' k\left(\nu'\right)}{\nu'^2 - \nu^2} d\nu' \tag{5.32}$$

where the integral is taken between a limited range of frequencies in the IR spectral region, the real refractive index is measured in the visible n_0, and P indicates the Cauchy principal value of the integral.

With those initial values, the optimization procedure is set to refine $k(\nu)$ using the complete set of absorbance spectra as input data. The minimization of these M and W functions, for the different variables, is done using the steepest descent method as described by Verleur (1968). A detailed description of the process is given in Zanchet et al. (2013). First, the initial $k(\nu)$ values are refined using the complete set of absorbance spectra as input data. From the improved values of $k(\nu)$, the real part of the complex index, $n(\nu)$, is estimated, and the procedure is repeated until convergence is achieved. The second step includes an adjustable baseline subtraction from each spectrum to correct for spectral deformations due to scattering effects, and a refinement of the corresponding coherence parameter. Next, n_0 and the sample thicknesses are adjusted to their final values, and last, the final refined set of $n(\nu)$ and $k(\nu)$ values is obtained. Fig. 5.3a shows an example of how well the experimental MIR spectra of (1:1) CH_4:C_2H_6 ice layers of different thickness are reproduced with the set of optical constants obtained at the end of the fitting procedure. The set of optical constants are shown in Fig. 5.3b.

The procedure described above has been developed in the group at IEM-CSIC in Madrid to determine IR optical constants of ice layers from normal transmission IR spectra. Although a three-layered ice-substrate-ice system has been employed in the examples, changes to other geometries of experiment could be implemented easily, like for example, an ice layer covering only one of the substrate surfaces, or infrared spectra taken in non-normal transmission configurations (see for example, Bossa et al. 2015).

This methodology is especially suited to determine mid infrared optical constants. In the near infrared spectral range, the intensity of the absorptions is weak and in order to obtain good signal to noise ratios in the absorbance spectrum, ice layers of several microns must be grown. Under these conditions, sometimes the amplitude of the infrared interference fringes observed in the baseline of the spectrum is larger than the infrared absorptions, and the minimization procedure fails to converge properly. In those cases, other approaches must be followed. The most straightforward idea is to apply directly Lambert's Law, in particular expressions (5.31 and 5.32), and obtain the imaginary part of the refractive index

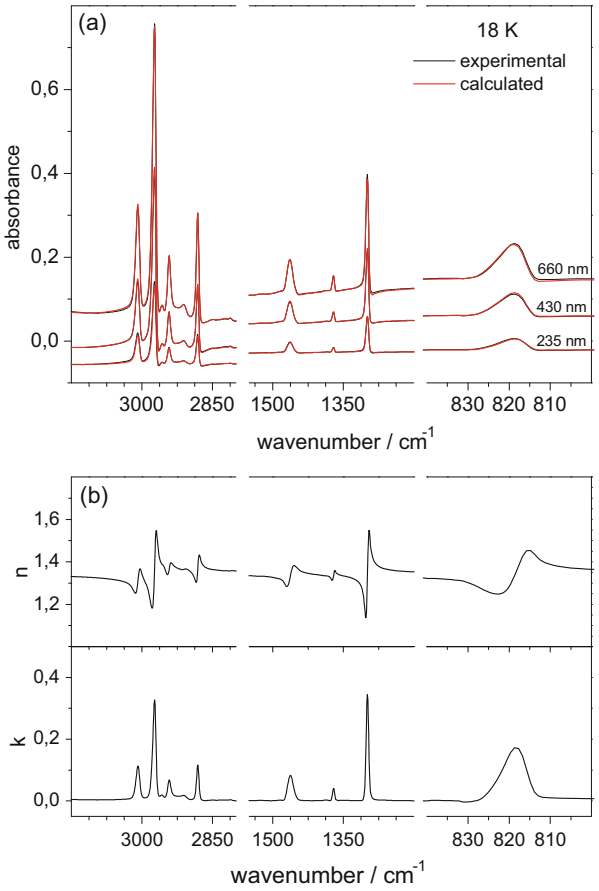

Fig. 5.3 (**a**) Mid infrared spectra of three (1:1) CH_4:C_2H_6 ice layers grown at 18 K. Ice layers are 660 nm, 430 nm, and 235 nm thick respectively from top to bottom. Black lines: experimental spectra, red lines: spectra calculated with the optical constants obtained from the fitting procedure described in the text. Both black and red lines are practically coincident. Spectra have been vertically offset for clarity in the representation. (**b**) Mid-IR optical constants for (1:1) CH_4:C_2H_6 ice mixtures at 18 K

from a single absorbance spectrum of an ice layer of known thickness. Subsequently apply Eq. (5.32) to determine the real component. In this situation, in order to obtain correct values for k, an adequate baseline must be subtracted from the absorbance spectrum. The baseline in the absorbance spectrum, as mentioned above, is modulated by infrared interferences and also could be affected by wavelength-dependent scattering effects. Obviously, the major problem within this approach is that the choice of the baseline is somewhat subjective. On the contrary, if the optical constants are extracted with the procedure described in this section, the raw absorbance spectra are used as input and there is no necessity of baseline correction

since the IR interferences are properly simulated. Moreover, the use of ice layers of different thickness makes the results more reliable. We estimate overall uncertainties of 1% for the real component of the refractive index. The uncertainty is also 1% for the imaginary component, k, except when $k < 0.01$, which induces larger errors due to the lower signal-to-noise ratio in the film-substrate transmittance.

An intermedium approach between the two previously mentioned ones was employed by Hudgins et al. (1993), and later by Hudson et al. (2014). It consists of subtracting a baseline that flattens the transmittance spectra to set them to 100% transmittance. Then a program calculates the oscillation of the baseline expected for the given sample thickness, and this is added to the flattened spectrum prior to calculation of the optical constants by minimization of the difference between experimental and calculated spectra. Since only one spectrum is considered, the estimated uncertainty in the calculated optical constants is limited mainly to the error in film thickness measurements. Nonetheless, sets of constants obtained by these less accurate procedures, provide still very useful information for the astrophysical community, and were used to interpret large number of astrophysical observations (Gibb et al. 2004; Boogert et al. 2015).

5.5 Integrated Band Strengths

The band strengths, also called integrated absorption coefficients, S, (see Chap. 3), of the different infrared bands in the absorbance spectrum are intrinsic properties of the material. These magnitudes are related to the optical constants, and are also very useful to the astrophysical community since they allow an immediate quantification of the amount of the different species present in astrophysical ices. The band strengths can be determined experimentally in two ways, directly integrating the bands of the absorbance spectra, by means of the expression:

$$S' = 2.303 \frac{1}{\rho d} \int A(\nu)\ d\nu. \tag{5.33}$$

or from the imaginary part of the optical constants using this other equation:

$$S = \frac{4\pi}{\rho} \int k(\nu)\ \nu\, d\nu. \tag{5.34}$$

In both cases the integral is taken along the whole profile of the band. Note that to use Eq. (5.33) it is necessary to know the column density of absorbers in the ice, or the ice density, ρ, and the layer thickness, d. In the second case, Eq. (5.34), only the imaginary part of the refractive index and the ice density are needed. Both methods do not give exactly the same results: the spectral intensity integrated to calculate S' includes losses due to reflection and interference effects that are not present when S is calculated from the $k(\nu)$. That is why S' is called the "effective" band strength in comparison with the "real" band strength S.

The integrated band strengths are intrinsic properties of the material, and as the optical constants do, vary significantly with the temperature due to morphology and phase changes. For example, the band strength of the OH stretching mode of amorphous water ice grown at 15 K is $1.9 \cdot 10^{-16}$ cm/molecule while for crystalline water grown at 150 K is $2.7 \cdot 10^{-16}$ cm/molecule (Mastrapa et al. 2009). These magnitudes are also different in ice mixtures as compared with pure species, due to the interaction between the different kinds of molecules within the ice. The intensity variations are usually accompanied with frequency shifts of the IR absorptions. Both modifications must be taken into account for a proper description of the composition of ice samples.

5.6 Summary and Conclusions

Many species of astrophysical interest are present on Earth and their IR properties were already known. However, they were investigated at room temperature or in conditions that do not resemble the astrophysical environments. For this reason, during the last decades, laboratory astrophysicists over the world have devoted their efforts to measure those magnitudes for different species known to be present or suspected to be present in astrophysical ices, at astrophysical relevant temperatures. In particular, IR absorbance spectra, IR optical constants, and IR band strengths are needed to extract information about the composition and history of different icy environments. In this chapter the procedures to derive accurate optical constants and band strengths from IR absorbance spectra of ice layers were described.

The infrared data obtained in laboratories are subsequently organized in open access databases. Some of the most important ones are in the Astrophysics & Astrochemistry lab at NASA Ames, the Astrochemistry lab at NASA Goddard, the Experimental Astrophysics Laboratory at Catania Astrophysical Observatory, the Sackler Laboratory for Astrophysics in Leiden, the Jena-St. Petersburg Database (JPDOC), or the Inst. Planetology and Astrophysics of Grenoble (GhoSST). Nowadays, a SSHADE project for building an European Database Infrastructure in Solid Spectroscopy with a large number of data of solids (ices, minerals, organics, cosmomaterials, ...) of astrophysical interest has been founded within the Europlanet-RI Horizon 2020 program.

References

Ashcroft, N.W., Mermin, N.D.: Solid State Physics. Saunders Company, Philadelphia, PA (1976)
Boogert, A.C.A., Gerakines, P.A., Whittet, D.C.B.: Annu. Rev. Astron. Astrophys. **53**, 541–481 (2015)
Bossa, J.-B., Maté, B., Fransen, C., Cazaux, S., Pilling, S., Rocha, W.R.M., Ortigoso, J., Linnartz, H.: Astrophys. J. **814**, 47 (2015)
Decius, J., Hexter, R.M.: Molecular Vibration in Crystals. McGraw-Hill, New York (1977)

Fernández-Torre, D.: Estudio teórico de sistemas de relevancia atmosférica: espectroscopía infrarroja de cristales de ácido nítrico y sus hidratos. PhD Thesis, Universidad Complutense, Madrid (2005).

Gibb, E.L., Whittet, D.C.B., Boogert, A.C.A., Tielens, A.G.G.M.: Astrophys. J. Suppl. Ser. **151**(1), 25–73 (2004)

Heavens, O.S.: Optical Properties of Thin Solid Films. Butterworth Scientific, London (1995)

Hudgins, D.M., Sandford, S.A., Allamandola, L.J., Tielens, A.G.G.M.: Astrophys. J. Suppl. Ser. **86**, 713–870 (1993)

Hudson, R.L., Ferrante, R.F., Moore, M.H.: Icarus. **228**, 276–287 (2014)

Kittel, C.: Introduction to Solid State Physics. Wiley, New York (1953)

Mastrapa, R.M., Sandford, S.A., Roush, T.L., Cruikshank, D.P., Dalle Ore, C.M.: Optical constants of amorphous and crystalline H_2O-ice:2.5–22 μm (4000–455 cm^{-1}). Astrophys. J. **701**, 1347–1356 (2009)

Molpeceres, G., Satorre, M.A., Ortigoso, J., Millán, C., Escribano, R., Maté, B.: Astrophys. J. **825**(156), 12 (2016)

Toon, O.B., Tolbert, M.A., Koehler, B.G., Middlebrook, A.M., Jordan, J.: Infrared optical constants of H_2O ice, amorphous nitric acid solutions, and nitric acid hydrates. J. Geophys. Res. Atmos. **99**, 25631 (1994)

Verleur, H.W.: J. Opt. Soc. Am. **58**, 1356 (1968)

Wood, B.E., Roux, J.A.: Infrared optical properties of thin H_2O, NH_3, and CO_2 cryofilms. J. Opt. Soc. Am. **72**, 720 (1982)

Zanchet, A., Rodríguez-Lazcano, Y., Gálvez, Ó., Herrero, V.J., Escribano, R., Maté, B.: Optical constants of NH_3 and NH_3:N_2 amorphous ices in the Near-Infrared and Mid infrared regions. Astrophys. J. **777**(26), 11 (2013)

Chapter 6
Quantum Chemical Description of Solids: DFT Approach

Oscar Gálvez

Abstract The aim of this chapter is to introduce the basic concepts underlying density functional theory (DFT), which has been turned into a practical tool employed in molecular astrophysics studies. We have also outlined the characteristic features of the basis sets most extensively used in DFT programs, namely plane waves or atom centered basis set.

6.1 Quantum Chemical Description of Solids: DFT Approach

Density functional theory (DFT) has over the past decades emerged as a versatile and useful computational method to simulate the interaction of atoms in gas, solid and liquid states.

Contrary to the traditional wave function methods, the keystone in DFT is the electron density, $\rho(\vec{r})$, which is defined as:

$$\rho(\vec{r}) = N \int \Psi^* \left(\vec{r_1}, \vec{r_2}, \ldots, \vec{r_N}\right) \Psi \left(\vec{r_1}, \vec{r_2}, \ldots, \vec{r_N}\right) d\vec{r}' \qquad (6.1)$$

In this equation spin coordinates are implicit. $\rho(\vec{r})$ depends on 3N (plus spin) spatial coordinates, and it is an experimental observable (using e.g. X-ray diffraction techniques), giving the probability to find an electron in a region on interest. In Fig. 6.1 the experimental and calculated $\rho(\vec{r})$ for the $Ni(C_4N_4H_2)_2$ molecule are represented.

P. Hohenberg and W. Kohn are usually referred to as the fathers of DFT. They published two theorems (Hohenberg and Kohn 1964) in 1964, giving the

O. Gálvez (✉)
Dpto. Física Interdisciplinar, Facultad de Ciencias, UNED, Madrid, Spain
e-mail: oscar.galvez@ccia.uned.es

G. M. Muñoz Caro, R. Escribano (eds.), *Laboratory Astrophysics*,
Astrophysics and Space Science Library 451,
https://doi.org/10.1007/978-3-319-90020-9_6

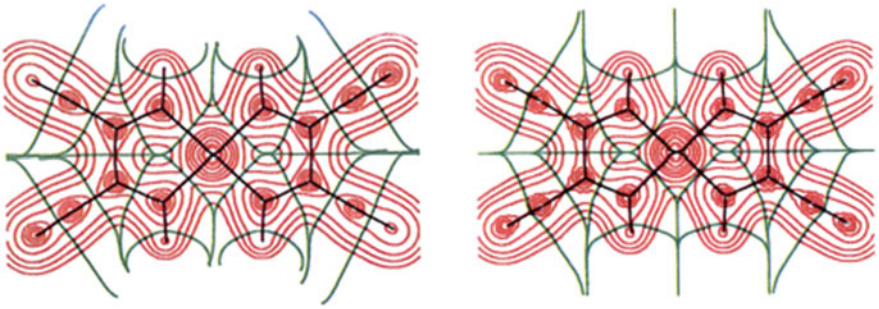

Fig. 6.1 Electron density (red) and basin domains (green), and molecular structure (black, thick trace) for the $Ni(C_4N_4H_2)_2$ molecule, (left) obtained by X-ray diffraction, and (right) calculated by ab initio methods. Contour lines display 2×10^n, 4×10^n and 8×10^n, with n from -3 to 0 in a.u. Figure adapted from ref. Hwang and Wang (1998)

fundaments to develop the formalism of the theory. The formulation of the theorems is:

1. *For any system of interacting particles in an external potential,* $V(\vec{r})$*, the electron density* $\rho(\vec{r})$ *is uniquely determined* (*in other words, the external potential is a unique functional of the density*).
2. *A universal functional for the energy* $E_V[\rho]$ *can be defined in terms of the density. The exact ground state is the global minimum value of this functional.*

According to these theorems the total energy of an n-electron system can be written without approximations as:

$$E_V[\rho] = -\tfrac{1}{2}\sum_i \int \varphi_i(\vec{r}_1)\,\nabla^2\varphi_i(\vec{r}_1)\,d\vec{r}_1 + \sum_A \int \frac{Z_A}{|\vec{R}_A - \vec{r}_1|}\rho(\vec{r}_1)d\vec{r}_1 + \tfrac{1}{2}\int \frac{\rho(\vec{r}_1)\rho(\vec{r}_2)}{|\vec{r}_1 - \vec{r}_2|}d\vec{r}_1 d\vec{r}_2 + E_{XC} \tag{6.2}$$

The first term in Eq. (6.2) represents the kinetic energy of n non-interacting electrons, the second term accounts for the electron-nucleus attraction and the third term for the Coulomb interaction between the two charge distribution $\rho(\vec{r}_1)$ and $\rho(\vec{r}_2)$. The last term contains the exchange correlation energy, E_{XC}.

Equation (6.2) can be rewritten as:

$$E_V[\rho] = T[\rho] + V_{ne}[\rho] + V_{ee}[\rho] = \int \rho(\vec{r})\,V(\vec{r})\,d\vec{r} + F_{HK}[\rho] \tag{6.3}$$

It is customary in DFT to use square brackets to indicate functional dependence. $T[\rho]$ is the kinetic energy functional, $V_{ee}[\rho]$ is the potential energy functional of the interelectronic interaction, and $V_{ne}[\rho]$ is the potential energy functional of the electron-nucleus interaction which is in fact the external potential of the system,

$V\left(\overrightarrow{r}\right)$. $F_{HK}[\rho]$ is the Hohenberg and Kohn functional:

$$F_{HK}\left[\rho\right] = T\left[\rho\right] + V_{ee}\left[\rho\right] \tag{6.4}$$

And the electron-electron term can also be written as:

$$V_{ee}\left[\rho\right] = J\left[\rho\right] + V_{XC}\left[\rho\right] \tag{6.5}$$

where $J[\rho]$ is the Coulomb interaction functional and $V_{XC}[\rho]$ contains the non-classical interelectronic interaction, which is the exchange-correlation functional.

To implement this theory, and to carry out calculations, Kohn and Sham (KS) (1965) introduced the following strategy.

They propose to calculate the kinetic term in an ideal system where the electrons are non-interacting. In this system, the exact kinetic energy functional is:

$$\begin{aligned} T_S\left[\rho_{exact}\right] &= \sum_{i=1}^{\infty} n_i \left\langle \psi_i^{NO} \right| -\tfrac{\nabla^2}{2} \left| \psi_i^{NO} \right\rangle \\ \rho_{exact} &= \sum_{i=1}^{\infty} n_i \left| \psi_i^{NO} \right|^2 \\ N &= \sum_{i=1}^{\infty} n_i \end{aligned} \tag{6.6}$$

where ψ_i^{NO} are the natural spin-orbitals and n_i are the occupation coefficients, $0 \leq n_i \leq 1$. Since the exact density matrix in unknown, the electron density can be expressed as an ensemble of mono-electron orbitals:

$$\rho\left(\overrightarrow{r}\right) = \sum_{i=1}^{N} \left| \psi_i\left(\overrightarrow{r}\right) \right|^2 \tag{6.7}$$

The kinetic energy calculated in this way is similar to that from the Hartee-Fock (HF) theory.

In this ideal system, the energy functional can be given as:

$$E\left[\rho\right] = T_S\left[\rho\right] + V_{ne}\left[\rho\right] + J\left[\rho\right] + V_{XC}\left[\rho\right] \tag{6.8}$$

where again the term $V_{XC}[\rho]$ can be separated as:

$$V_{XC}\left[\rho\right] = \left(T\left[\rho\right] - T_S\left[\rho\right]\right) + \left(V_{ee}\left[\rho\right] - J\left[\rho\right]\right) \tag{6.9}$$

$V_{XC}[\rho]$ includes the non-classical interelectronic interactions (exchange and correlation) and the difference between the exact kinetic energy and that given by the non-interacting system. This last contribution is usually small; for example, in a HF calculation the kinetic term accounts for around 99% of the real kinetic energy. In fact the dominant term in Eq. (6.9) is the exchange energy.

Because the exact expression of the $V_{XC}[\rho]$ exchange-correlation functional is also unknown, there are many different approximations in DFT to define these terms. Usually this functional is divided into two main contributions, namely exchange and correlation:

$$V_{XC}\left[\rho\right] = V_X\left[\rho\right] + V_C\left[\rho\right] \tag{6.10}$$

It is important to remind that exchange is the dominant part.

In general, in DFT the term "local" refers to expressions of the $V_{XC}[\rho]$ which only depend on ρ but not on powers or gradients of it, which are termed as "non-local". In the local density approximation (LDA) the electron density can be obtained from a homogenous electron gas, which was used for Dirac (1930) to find the expression of the exchange potential energy:

$$V_X^{LDA} = -c_x \rho^{1/3}\left(\overrightarrow{r}\right) \tag{6.11}$$

This expression was used later for Slater (1951) to simplify the calculation of the exchange term using the HF approximation (which is implicitly non-local).

The correlation term in the LDA approximation was studied in 1980 by Vosko, Wilk and Nusair (VWN) (Vosko et al., 1980), who obtained an analytic expression for it.

To improve the LDA approximation, the expressions of the exchange and correlation functionals depend also on gradients of the electron density. These methods are usually known as generalized gradient approximations (GGA) and the functionals depend on $\nabla\rho$. One of the most popular non-local exchange functionals is that given by Becke (1988), usually employed in combination with the non-local correlation functional of Lee–Yang–Parr (Lee et al. 1988), LYP; both include corrections up to product of gradients of electron density. The combination BLYP $V_X^B\left[\rho\right] + V_C^{LYP}\left[\rho\right]$ has been extensively used in the past in quantum chemical calculations giving excellent results.

To include these corrections in practical quantum-chemical calculations, the subsequent scheme can be followed (Fig. 6.2).

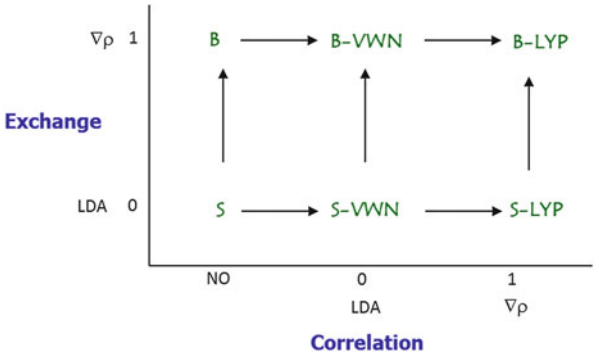

Fig. 6.2 Scheme of the methods of calculation in DFT. *S* refers to the Slater's approximation to the exchange term; *B* refers to Becke's exchange approximation; *LYP* refers to the Lee–Yang–Parr correlation functional and *VWN* to the correlation functional given by Vosko, Wilk and Nusair

In the Kohn–Sham approximation, the exchange functional can be given in terms of the spin-orbitals of the system. The exchange contribution can also be calculated by the HF method, which leaves the correlation functional as the only task to be tackled. Based in this idea, Becke suggests using hybrid functionals, in which the exchange contributions is calculated in a HF approximation and the correlation is given by DFT methods:

$$V_{XC}^{hybrid} = c_{HF} V_X^{HF} + c_{DFT} V_{XC}^{DFT} \tag{6.12}$$

In this expression, c_i are selected coefficients for the different methods. It is worth to mention, because of its extensive use and success, the three parameter hybrid functional B3LYP, which includes: a mixing of exchange HF and LDA–DFT, with non-local Becke corrections to the exchange term, and VWN correlation functional with LYP corrections. The formulation is:

$$E_{XC}^{B3LYP} = E_X^{LDA} + c_0 \left(E_X^{HF} - E_X^{LDA} \right) + c_X E_X^B + E_C^{VWN} + c_C \left(E_C^{LYP} - E_C^{VWN} \right) \tag{6.13}$$

being $c_0 = 0.20$, $c_X = 0.72$, *and* $c_C = 0.81$, coefficients calculated by Becke to fit different experimental values in selected molecules (Becke 1993).

One of the most intensive uses of DFT methods is in periodic solid systems calculations. In these cases, we have to deal with an infinite number of non-interacting electrons moving in the static potential of an infinite number of nuclei or ions. Two difficulties must be overcome: a wave function, needed to construct the electron density, must be calculated for each of the infinite number of electrons in the system, and, since each electronic wave function extends over the entire solid, the basis set required to expand each wave function is infinite. Fortunately, both problems can be solved by applying Bloch's theorem to the electronic wave function on periodic systems.

Bloch's theorem states that in a periodic solid each electronic wave function can be written as the product of a cell-periodic part and a wavelike part (Payne et al. 1992):

$$\psi_{n\vec{k}}\left(\vec{r}\right) = e^{i\vec{k}\vec{r}} u_{n\vec{k}}\left(\vec{r}\right) \tag{6.14}$$

$$u_{n\vec{k}}\left(\vec{r}\right) = u_{n\vec{k}}\left(\vec{r} + \vec{R}\right) \tag{6.15}$$

$\vec{R}$ refers to lattice positions. The cell periodic part of the wave function, $u_{n\vec{k}}\left(\vec{r}\right)$, can be expanded using a basis set consisting of a discrete set of plane waves whose wave vectors are reciprocal lattice vectors of the crystal:

$$u_{n\vec{k}}\left(\vec{r}\right) = \sum_{\vec{G}} c_{i,\vec{G}} e^{i\vec{G}\vec{r}} \tag{6.16}$$

where $\vec{G}$ is the reciprocal lattice vector, that, making use of a Fourier expansion, is defined by $\vec{G}\,\vec{l} = 2\pi m$ where $\vec{l}$ is a lattice vector of the crystal and $\boldsymbol{m}$ is an integer. Therefore, each electronic function can be written as a sum of plane waves:

$$\psi_{n\vec{k}}\left(\vec{r}\right) = \sum_{\vec{G}} c_{i,\vec{k}+\vec{G}}\, e^{i\left(\vec{k}+\vec{G}\right)\vec{r}} \tag{6.17}$$

From the Bloch theorem, a plane wave basis set is a natural (but not the only) choice of basis set. Finally, the application of Bloch's theorem gives that, instead of computing an infinite number of electronic wave functions, we should compute a finite number of wave functions (bands) at an infinite number of *k*-points (reciprocal space). However, the electronic wave functions at k-points that are very close together will be almost identical. This suggests that the DFT expressions that contain a sum over *k*-points (or, equivalently, an integral over the Brillouin zone, BZ) can be efficiently evaluated using a numerical scheme that performs a summation over a small number of special points in the Brillouin zone [see Eq. (6.18) below]. The Brillouin zone is a uniquely defined primitive cell in reciprocal space. In addition, symmetry considerations suggest that only k-points within the irreducible segment of the Brillouin zone should be taken into account. Especially relevant is the Gamma Point (Γ), defined by $k_x = 0$, $k_y = 0$, $k_z = 0$, located at the center of the BZ. Typically, we can say that we will need more k-points for: small unit cells, metals or magnetic materials.

$$\rho\left(\vec{r}\right) = \sum_{i=1}^{N} \left|\psi_i\left(\vec{r}\right)\right|^2 = \sum_{i=1}^{N} \int_{BZ} n\left(\vec{k}\right) \left|\psi_i\left(\vec{k}\right)\right|^2 d\vec{k} = \sum_{i=1}^{N} \sum_{\vec{k}} n\left(\vec{k}\right) \left|\psi_i\left(\vec{k}\right)\right|^2 \tag{6.18}$$

There are several recipes (e.g. Baldereschi, Chadi and Cohen, Monkhorst-Pack) to compute sets of special *k*-points for the different symmetries to accelerate the convergence of BZ integrations. In general, the magnitude of the error introduced by sampling the Brillouin zone with a finite number of *k*-points can always be reduced by using a denser set of points.

A common feature in periodic quantum chemical packages is the use of pseudopotential approximations. Core electrons present wave functions with many nodes which need a large basis set, and in many cases, relativistic effects should also be taken into account (due to the high kinetic energy experienced in the inner shells of many-electron atoms). These wave functions barely change by chemical bonding (which corresponds to the valence electrons), so that, as a general rule, instead of this tough task, the core electrons are replaced with potential functions that "look like a core" to valence electrons outside the core area. This approximation enormously simplifies the calculations.

In addition, many times we may be interested in simulating systems that are intrinsically not periodic, like for example: isolated molecules, defects in structures,

surfaces, amorphous materials, etc. In those cases, the supercell approximation can be used, which basically consists in that systems with open and mixed periodic boundary conditions are made artificially periodic. The system is contained within a supercell which is then artificially replicated periodically throughout space. The supercell must be large enough so that the systems contained within, which in reality are isolated, do not interact significantly. Under this approximation, DFT solid methods using the Bloch's theorem can be applied as well.

Finally, we can say that the major differences among solid state quantum chemical programs arise from the different basis sets used. In general, two different approximations are the most extended: plane waves or atom centered basis sets. Both present advantages and disadvantages (see Table 6.1).

For atom centered basis sets, there are different types of functions commonly used: Gaussian, Slater and numerical. There are even methods which mix both approximations, using atom centered functions in non-overlapping spheres and plane waves in interstitial regions.

In the webpage of "Psi-k community" (http://psi-k.net/) there is an ample description of the different computational electronic methods specially devoted for crystalline quantum systems. Nevertheless, we would like to highlight two packages that have been successfully used in the past in the simulation of astrophysical and atmospheric systems: SIESTA (Soler et al. 2002) (based in numeric atomic orbitals) and CASTEP (Clark et al. 2005) (using plane waves).

Examples of properties that can be calculated using DFT methods are: total energy, equilibrium structures with and without optimizing the unit cell, dynamics, band structures, local density of states DOS (projected on axis or atom), Mulliken charges, phonon spectrum, NMR: chemical shift, electric field gradients, vibrational (IR or Raman) spectra, energies of adsorption, diffusion processes, etc.

Table 6.1 Description of the advantages and disadvantages of different basis sets

Plane waves	Atom centered
👍 Good at describing periodic systems	👍 Good at describing core
👍 Straightforward way of extending basis	👍 Correspond to atomic orbitals
👍 No geometry dependence (BSSE)[a]	👍 Relatively few functions necessary
👍 Mathematically simple	👍 Better scaling for large systems due to integral screening
👎 Not good at describing "rough" features	👎 Not orthogonal
👎 Do not take advantage of geometric knowledge (e.g. empty space)	👎 BSSE and linear dependencies
👎 Need many functions for result to converge	

[a]BSSE: Basis set superposition error

References

Becke, A.D.: J. Chem. Phys. **88**, 1053 (1988)
Becke, A.D.: J. Chem. Phys. **98**, 5648 (1993)
Clark, S.J., Segall, M.D., Pickard, C.J., Hasnip, P.J., Probert, M.I.J., Refson, K., Payne, M.C.: Z. Kristallogr. **220**, 567 (2005)
Dirac, P.A.M.: Proc. Cambridge Phil. Soc. **26**, 376 (1930)
Hohenberg, P., Kohn, W.: Phys. Rev. **136**, B3864 (1964)
Hwang, T., Wang, Y.: J. Phys. Chem. A. **102**, 3726 (1998)
Kohn, W., Sham, L.J.: Phys. Rev. **140**, A1133 (1965)
Lee, C., Yang, W., Parr, R.G.: Phys. Rev. B. **37**, 785 (1988)
Payne, M.C., Teter, M.P., Allan, D.C., Arias, T.A., Joannopoulos, J.D.: Rev. Mod. Phys. **64**, 1045 (1992)
Slater, J.C.: Phys. Rev. **81**, 385 (1951)
Soler, J.M., Artacho, E., Gale, J.D., García, A., Junquera, J., Ordejón, P., Sánchez-Portal, D.: J. Phys. Condens. Matt. **14**, 2745–2779 (2002)
Vosko, S.H., Wilk, L., Nusair, M.: Can. J. Phys. **58**, 1200 (1980)

Chapter 7
Monte Carlo Simulations of the Formation and Morphology of Interstellar Ices

Stéphanie Cazaux, Jean Baptiste Bossa, Rafael Martin-Doménech, Guillermo M. Muñoz Caro, Yu-Jung Chen, Harold Linnartz, and Alexander Tielens

Abstract The porosity present in ices contains many clues on the conditions of their formation and evolution, as well as their trapping capacities. Laboratory experiments studying such porosity are essential to better understand interstellar ices. In this work, we present recent theoretical results on water and CO ices that aim at reproducing laboratory experiments. We use Monte Carlo methods in order to describe the fate of each molecule present in the ices, which is determined by the different processes that molecules can experience, such as accretion, diffusion and evaporation. For water ices, we show that porosity depends on the conditions of deposition, and that with increasing temperature, small pores connect and merge, allowing trapped molecules to meet and react within the pores network and thus increasing the efficiency of the reaction. For CO ices, we show that deposition conditions can also give different types of CO ices, with many weakly bound CO molecules as the deposition occurs at very low temperatures. The presence of weakly bound CO molecules could explain the far less important freeze out seen in pre-stellar cores, compared to what is commonly expected.

S. Cazaux (✉)
Kapteyn Astronomical Institute, Groningen, The Netherlands
e-mail: S.M.Cazaux@tudelft.nl

J. B. Bossa · H. Linnartz · A. Tielens
Leiden Observatory, University of Leiden, Leiden, Netherlands

R. Martin-Doménech
Harvard-Smithsonian Center for Astrophysics, Cambridge, MA, USA

G. M. Muñoz Caro
Centro de Astrobiología, INTA-CSIC, Torrejón de Ardoz, Madrid, Spain

Y.-J. Chen
Department of Physics, National Central University, Taoyuan, Taiwan

G. M. Muñoz Caro, R. Escribano (eds.), *Laboratory Astrophysics*,
Astrophysics and Space Science Library 451,
https://doi.org/10.1007/978-3-319-90020-9_7

7.1 Introduction

In star forming regions, an icy mantle grows on dust particles from accretion of gas phase species on their surfaces (Whittet et al. 2001). These species are mainly water (Tafalla et al. 2006; Williams et al. 1992; Whittet et al. 1998; Gibb et al. 2004; Pontoppidan et al. 2004; Boogert et al. 2008), and in a much smaller proportion CO_2, CO, CH_3OH, NH_3 and others (Gibb et al. 2004). Once a protostar is formed, the ices covering dust grains evaporate (Ceccarelli et al. 2007), releasing into the gas phase many complex molecules (Schoïer et al. 2002; Cazaux et al. 2003), which have been generated within the ices after extensive chemical reactions and thermal and energetic processing (Theulé et al. 2013; Öberg et al. 2009; Fedoseev et al. 2015). Ices provide the appropriate substrate for dust grains to coagulate and thus lead to the formation of planets (Ormel et al. 2007)

Many recent studies have focused on ice composition as well as morphology. Such characteristics provide information on a number of physical processes: accretion, desorption, segregation and others. Amorphous water ice with trapped impurities (Tielens and Allamandola 1987) are assumed to conform ices in molecular clouds. This structure is consistent with ices grown by a hit and stick ballistic mechanism (Cuppen and Herbst 2007). In the laboratory, gas-phase species deposited through background deposition on a cold substrate result in highly porous ices (Brown et al. 1996; Dohnàlek et al. 2003; Maté et al. 2012a; Bossa et al. 2014a). While ices in space could in theory be porous, no observational evidence has been found since the OH dangling bonds of water on the surface of the pores, at 2.7μm, have never been observed (Keane et al. 2001; Gibb et al. 2004). Laboratory studies also showed that, if initially present in the ices, pores would disappear with UV photon and ion irradiation (Palumbo 2006, 2010; Raut et al. 2007a), or change with thermal energy (Bossa et al. 2014a). It may therefore be assumed that changes in the ice morphology due to external factors are the reason for the lack of porosity in interstellar ices.

The missing evidence of dangling OH bonds may not by itself exclude a certain degree of porosity in the ice (Raut et al. 2007a; Isokoski et al. 2014a). Since the catalytic potential of icy grains is a fundamental factor to understand many chemical processes, it is greatly important to assess the compactness of water ice in astrophysical environments. The specific nature of the pores, their size or intercommunications, are key factors that must be realized. In this light, Monte Carlo simulations are used to follow the formation of water ices and their porosity upon deposition, as well as the thermal evolution of this porosity. Applied to CO ices, Monte Carlo simulations allow a deep view of the morphology of the ices studied in laboratory experiments under diverse conditions. Such simulations can shed light on the reasons for the depletion of CO seen in starless cores. Also, recent observations of embedded protostars show that the presence of CO in the gas is much more extended than evaporation would allow (Jørgensen et al. 2015). The fact that CO is present in environments where it should be frozen could be due to accretion bursts that occurred in the history of the protostar (Jørgensen et al. 2015).

7.2 Monte Carlo Simulations

Monte Carlo simulations are used to follow the formation of ices in different conditions. The formation and evolution of pores can be followed simultaneously. In a Monte Carlo simulation, gas-phase molecules reach a random spot of the surface at random time and execute a random walk. The arrival time is driven by the collision rate of gas molecules with the surface, whereas the diffusion time depends on the temperature of the ices and the binding energy of individual molecules.

7.2.1 Structure of the Water Ices

Low-density amorphous ice consists mainly of four coordinated tetrahedrally ordered water molecules (Brovchenko and Oleinikova 2006). As already discussed in (Cazaux et al. 2015), amorphous water ice is modeled using a grid in which the water molecules are organized as tetrahedrons, as shown in Fig. 7.1. In such grid, each sphere represents an oxygen atom, and the yellow and blue colors indicate odd and even grid cell planes. The bonds between the oxygen atoms represent hydrogen bonds, as H atoms are not shown in this representation.

A water molecule in an ice has a binding energy that increases linearly with the number of water molecules in its neighborhood, estimated at 0.22 eV per hydrogen bond (Brill and Tippe 1967; Isaacs et al. 1999; Dartois et al. 2013). While hydrogen bond strengths can vary with the number of water molecules involved as donors

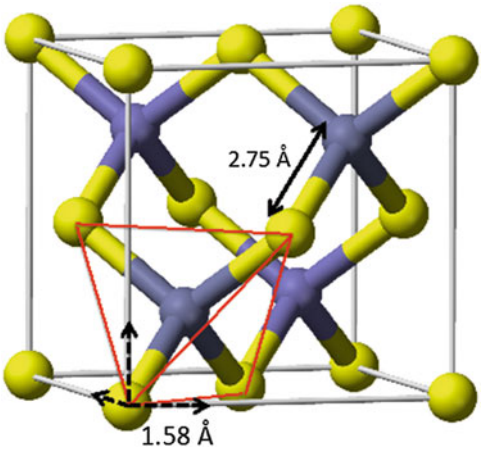

Fig. 7.1 Structure of water ices in a 4 × 4 × 4 grid. Each sphere represents an oxygen atom where odd vertical planes are in yellow and even vertical planes in blue. (See Fig. 7.2 to better appreciate the odd and even vertical planes in this representation). The red lines show the tetrahedrons in the grid employed to calculate surface and volume

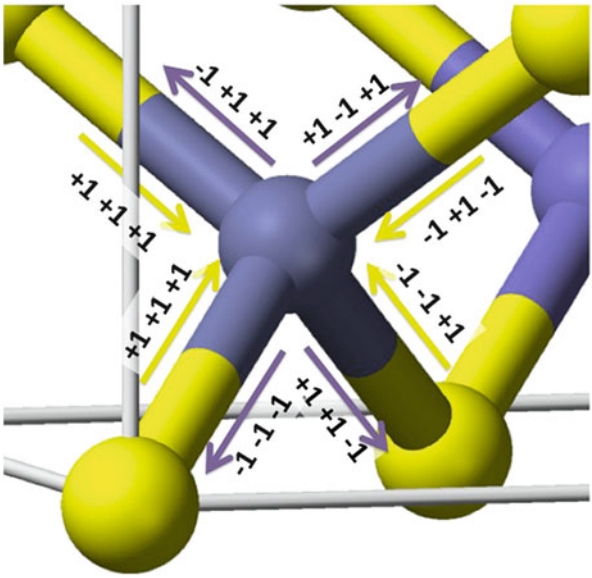

Fig. 7.2 Motion of water molecules in the grid: those within odd vertical planes (yellow) can move following the yellow arrows, while those with even coordinates (blue) can move along the blue arrows

and acceptors in the neighborhood (Huš and Urbic 2012; Collings et al. 2003), we here assume that water molecules linked to one neighbor have a binding energy of 0.22 eV and 0.88 eV for water molecules surrounded by four neighbors. The motion of water molecules in the grid from one site to another one is depicted Fig. 7.2. According to their positions, the molecules can move in four different directions to unoccupied sites.

7.2.2 Structure of the CO Ices

CO molecules are bound to each other through van de Waals interactions and can fill each site of the grid, with a distance between two sites of 3 Å. The lowest interaction between two CO molecules is around 16 meV (185 K) (Karssemeijer and Cuppen 2014). In a multilayer regime, the binding energy of a CO molecule on the surface (and not in the bulk) is about 72 meV (830 K) (Fayolle et al. 2016; Muñoz Caro et al. 2010; Noble et al. 2011; Pontoppidan 2006; Acharyya et al. 2007; Karssemeijer et al. 2014). To estimate how the binding energy of CO molecules increases with its number of neighbors, we employ a simple approximation, as shown in Fig. 7.3. The interaction of one single CO molecule with another single CO molecule appears at low energy in the plot, at about 185 K. The multilayer regime is represented by the point at 860 K, corresponding to one CO molecule linked to three CO neighbors. With a fit through these points we mimic saturation for a high number of neighbors. This allows to calculate the binding energy of a CO molecule as a function of its number of neighbors, nn. The CO molecules present in the grid can move in any direction as long as they are bound to the substrate or to other CO molecules.

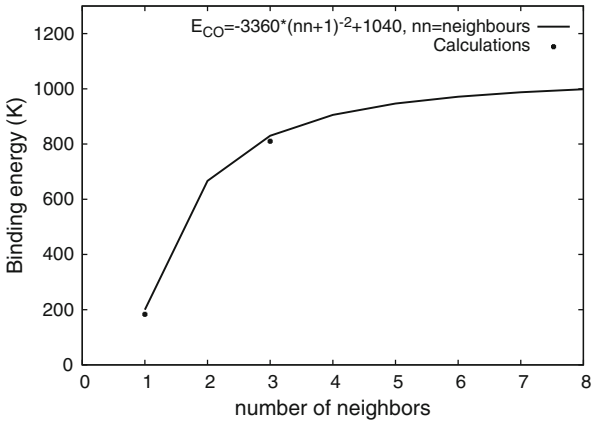

Fig. 7.3 Binding energies of CO molecules as a function of number of neighbors. The points, derived from calculations, correspond to the interaction between two CO molecules and between one CO and a CO surface (Karssemeijer and Cuppen 2014)

7.2.3 Accretion

Accretion is produced by the attachment of gas-phase molecules to species at the surface of the grid via hydrogen bonding for water or van der Waals binding for CO. The accretion rate (in s^{-1}) depends on the density of the gas-phase species, their velocity and the cross section of the surface. It can be represented by:

$$R_{acc} = n_X v_X S\sigma \tag{7.1}$$

where n_X is the density of the gas-phase molecules in cm^{-3}, v_X is their thermal velocity, S is the sticking coefficient and σ is the cross section of the surface, which is proportional to the size of the grid used for the simulations. We take $S = 1$ for the low temperature used as a starting point in this study. The sticking of molecules on the substrate is assumed to be identical to the sticking on the ices.

7.2.4 Diffusion

Molecules can diffuse in the grid as long as they are bound to the substrate or to other molecules. The diffusion rate for a molecule to move from one site to another depends on the activation energy for diffusion, which is usually assumed to be a fraction of the binding energy Eb(X). For a position (i,j,k) in the grid, the initial binding energy Ei is calculated. The possible sites where the molecule can diffuse (see Sect. 7.2.1) can then be identified and the final binding energy calculated. Molecules can diffuse through thermal hopping or tunneling from one site to another. Since the distance between two sites is quite large, and the mass of the molecules is also large, we do neglect the tunneling effect. If the initial and final

sites have identical binding energies, the diffusion rate, in s^{-1}, can be written as:

$$R_{diff} = \upsilon \times \exp\left(-\frac{\alpha Eb(X)}{T}\right) \tag{7.2}$$

where υ is the vibrational frequency of a water molecule in its site (adopted as 10^{12} s^{-1}), Eb(X) is the binding energy depending on the molecule, and α × Eb(X) is the activation energy for diffusion. For water on water α can be in the range between 30%, derived from experiments of water-on-water diffusion (Huš and Urbic 2012), and 50% (Cuppen and Herbst 2007). For the diffusion of CO on a water ice surface, diffusion barriers of the order of 30 meV have been derived (Karssemeijer et al. 2014; Mispelaer et al. 2013), which represent only ∼ 30% of the binding energy, but more recent studies indicate barriers that can be even lower ∼20% (Lauck et al. 2015).

7.2.5 Desorption

Only species present at the top layers of the ices can desorb and return to the gas-phase. The desorption rate depends on the binding energy of the water molecules Eb(X), which in turn depends on the number of neighbors *nn*. The desorption rate (in s^{-1}) of a species with binding energy Eb(X) can thus be written as:

$$Evap = \upsilon \times \exp\left(-\frac{Eb(X)}{T}\right) \tag{7.3}$$

Molecules at the top layer of the ice have fewer neighbors than those in the bulk, and therefore they have a higher probability to thermally desorb.

7.3 Water Ices

7.3.1 Porosity Upon Deposition

7.3.1.1 Experiments

In two recent experimental works, pure and compact H_2O ices were grown by front deposition at 30 K using two different deposition rates, of 0.2 nm s^{-1} at the Sackler Laboratory for Astrophysics (SLA), and 10 nm s^{-1} at the Laboratório de AStroquímica e Astrobiologia da univap in Brazil [LASA (Pilling et al. 2009)]. The mid-infrared spectra of the two ices have been measured and are reported in Fig. 7.4. From the OH stretch band and the lack of OH dangling bond (see inset) it seems that the ice grown at 0.2 nm s^{-1} is more compact and more crystalline

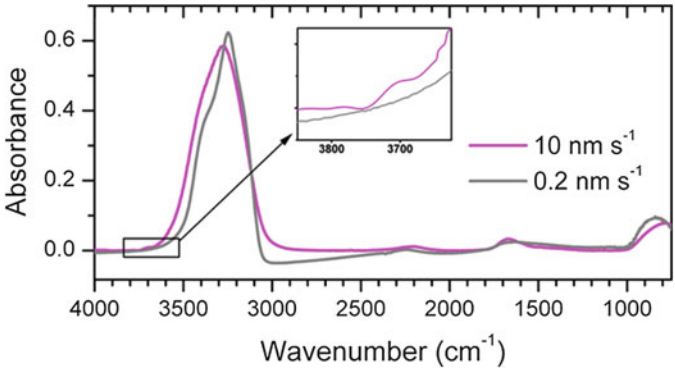

Fig. 7.4 Mid-infrared spectra of pure and compact H_2O ice grown at 30 K with two different deposition rates, 0.2 and 10 nm s^{-1}

(possibly amorphous ice made of polycrystals) than the one deposited at 10 nm s^{-1} (Zondlo et al. 1997; Maté et al. 2012b).

7.3.1.2 Simulations

With the simulations reported in this section, we aimed at reproducing the different ice morphologies obtained with the two different deposition rates of 10 and 0.2 nm s^{-1}. For this purpose, several simulations have been performed. We varied the diffusion rate of the water molecules in the ice by considering different values of the diffusion barriers. The accretion rate, R_{acc}, can be calculated as in Sect. 7.2.3, where the surface cross section, σ, scales with the size of the grid, made up of 100 × 100 sites in these calculations, corresponding to a surface size of $(1.58 \times 10^{-8} \times 100)^2$ Å^2, the distance between two sites being 1.58 Å. This yields a rate of: $R_{acc} = 1.86 \times 10^{-7}\ n_{H2O}$. To mimic experimental conditions with deposition rates of 0.2 nm s^{-1} and 10 nm s^{-1}, the density of gas phase water molecules is set as $n_{H2O} = 4 \times 10^9$ cm^{-3} and $n_{H2O} = 2 \times 10^{11}$ cm^{-3} respectively.

In order to reproduce the fact that the ice deposited at 0.2 nm s^{-1} is compact while the ice deposited at 10 nm s^{-1} is still porous, our simulations show that the diffusion needs to be efficient enough. For diffusion barrier being 15% of the binding energies, we can reproduce the two ice morphologies, as depicted in Fig. 7.5. Each square shows the position of each water molecule while their colors correspond to the number of hydrogen bonds (number of neighbors). Water molecules with one neighbor are represented in blue, while water molecules with 2, 3, and 4 neighbors are represented in green, yellow, and red, respectively. With 0.2 nm s^{-1} deposition rate, water molecules have more time to diffuse onto the

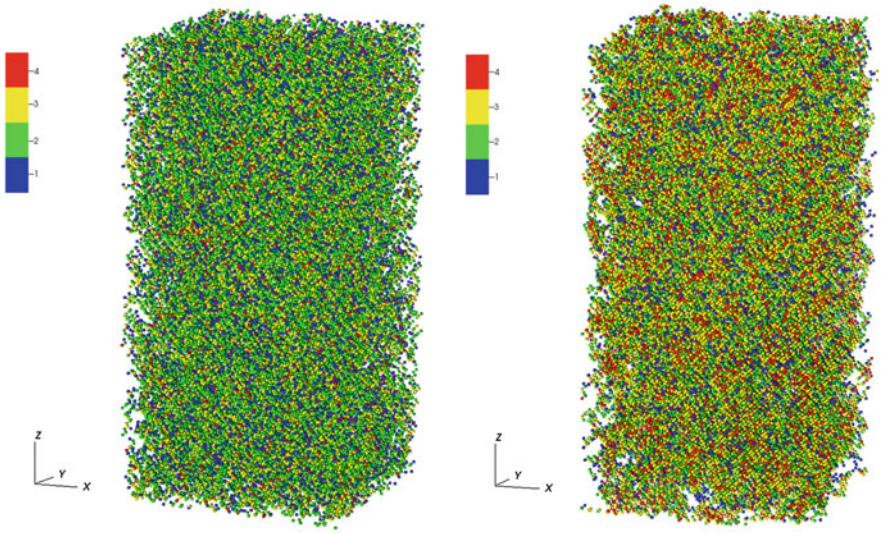

Fig. 7.5 Structure of an amorphous solid water ice in a 100 × 100 × 800 grid, grown at 30 K. Left panel: deposition rate of 10 nm s^{-1}. Right panel: deposition rate of 0.2 nm s^{-1}. The colors represent the number of neighbors of each water molecule. The diffusion barrier is assumed to be 15% of the desorption energy

surface, rearrange, and form hydrogen bonds, than with 10 nm s^{-1} deposition rate. Therefore, the deposition rate is an important parameter that determines whether water molecules can reorganize or not, and thus sets the morphology of the water ice.

7.3.1.3 Astrophysical Implications

The efficiency of many relevant processes such as adsorption, diffusion and reaction, as well as the seizing capacities of molecules in interstellar ices, are all strongly dependent on the porosity of the ices. For interstellar ices, the porosity and its evolution during the different stages of star formation can play an important role in the molecular complexity seen toward low and high mass protostars, as well as in comets. The simulations shown in this section illustrate that deposition rates set the morphology of the water ices. In the interstellar medium, water molecules freezing onto an icy surface have ample time to reorganize which will create compact ice with large pores. These ices can therefore be assumed to be filled up with large pores.

7.3.2 Thermal Evolution of Porosity

7.3.2.1 Experiments

In previous experiments (Isokoski et al. 2014b; Bossa et al. 2014b, 2015) several thousands of monolayers of water ice have been deposited on a 2.5 × 2.5 cm slab in order to measure the thermal evolution of the ice thickness. The thickness of different types of ices has been followed upon heating (from 20 K to 120 K) by combining optical interference with Fourier transform infrared spectroscopy. For porous ASW, heating from 20 to 120 K induces a reduction in thickness of $12 \pm 1\%$, while a lower value is measured for more compact ices, and it is negligible for crystalline ice. In parallel, the O-H dangling mode of the two- and three-coordinate surface water molecules, at 3720 and 3696 cm^{-1} respectively are measured. While the two absorption bands can be seen for porous and less-porous ASW, there is no O–H dangling mode for crystalline solid water. These experiments suggest that the porosity decreases from porous ASW to less-porous ASW, and follow a similar trend to crystalline ice.

7.3.2.2 Simulations

In this section we report the result from (Cazaux et al. 2015), where the evolution of water ices and its porosity is studied as the temperature is increased. The position of each molecule as well as their number of neighbors is followed as a function of temperature. As mentioned in Sect. 7.2.1, the binding energy of water molecules increases with their number of neighbors. The empty spaces between the water molecules determine the level of porosity in the ice. Fig. 7.6, top panels, shows the water molecules in the grid of size 60 × 60, and for each water molecule, its number of neighbors. The left panel presents the water ice at 10 K. At this temperature, the water molecules have mostly one or two neighbors and fill up the grid homogeneously. As the temperature increases and reaches 60 K, which is shown in the middle panel, the molecules diffuse within the ice to be in a more stable configuration and mostly have two to three neighbors. At 100 K, as presented in the right panel, the water molecules have mostly three to four neighbors. At this high temperature, the ice is not homogeneous in comparison with 10 K, and large empty spaces representing pores become visible in our simulations. In Fig. 7.6, bottom panels, the pores and their evolution is followed as function of temperature. These figures, representing the emptiness in the ice, are the negative image of the top panels. At 10 K many small holes can be seen. As the temperature increases to 60 K, the water molecules diffuse and become more bound, leading to the appearance of larger empty spaces, called pores, which can reach sizes of a few Å. At temperatures of 100 K, the pores grow, become connected to each other, and have sizes which can reach radii of $\sim$ 15 Å, in good agreement with other studies (Raut et al. 2007b).

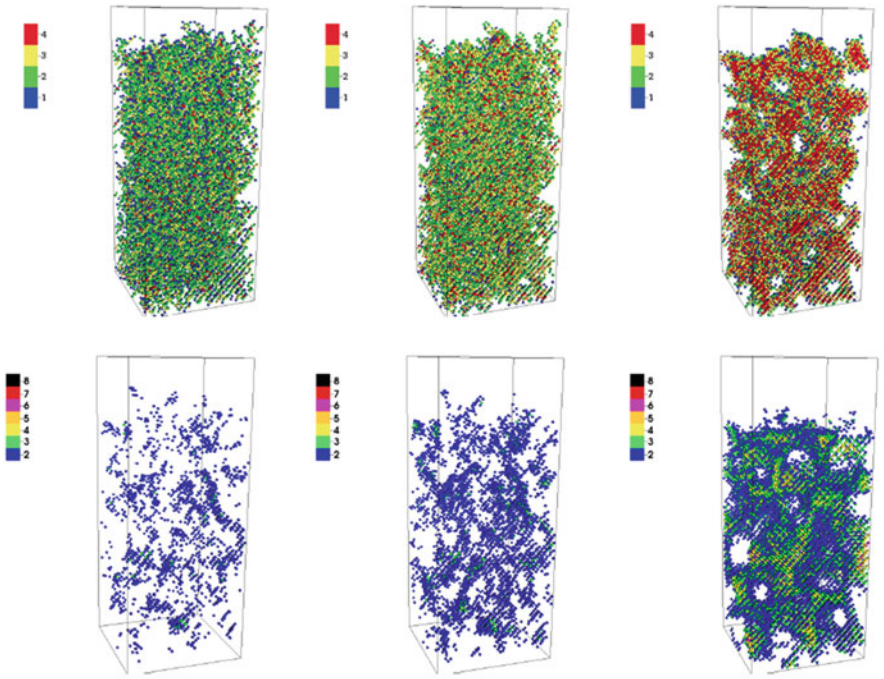

Fig. 7.6 Top: evolution of water molecules in the ice with temperature. Left, 10 K; middle, 60 K and right, 100 K. The numbers indicate the numbers of neighbours of each water molecule. Bottom: evolution of the size of the pores with temperature. Same temperature arrangement as above. The numbers indicate the number of empty spaces around the cell

7.3.2.3 Astrophysical Implications

For different simulations considering different grid sizes, we determined the total surface from the pores and the porosity (volume of the pores divided by the total volume of the ice). These are reported in Fig. 7.7, left panel, for different grid sizes. It can be seen that the porosity does not change drastically with increasing temperature. However, the total surface decreases by a factor of 3.5 between 10 and 120 K, due to the increase of average pore size. This is consistent with experimental studies (Mitterdorfer et al. 2014) showing that the specific surface area decreases from 90 to 100 K. In the interstellar medium, the conditions of deposition and thermal evolution are extremely different than in laboratory experiments. In dense molecular clouds temperatures can be as low as 10–14 K. The mechanism of restructuration, which implies breaking and re-forming bounds, would take times longer than 10^7 years at 14 K. The evolution of interstellar ices through diffusion is therefore negligible in molecular clouds. However, the evolution of the porosity in star forming environments, where the temperature increases, could be important. We use a model to simulate the increase of temperature due to the formation of a

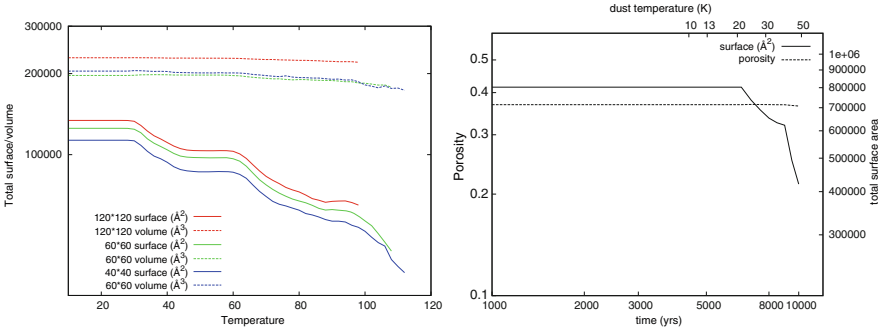

Fig. 7.7 Left: Total surface and volume of the pores as a function of temperature for different grid sizes (120 × 120, 60 × 60 and 40 × 40). For a better comparison, the total surface and volume are divided by four and two for the 120 × 120 and 60 × 60 grids, respectively. Right: Porosity evolution in star forming regions. The temperature of the dust is assumed to grow from 10 to 200 K in a time interval of 5×10^4 years

massive star, similar to what is used in (Garrod and Herbst 2006). The gas and dust temperatures, initially at 10 K, reach 200 K after 5×10^4 years, with a temperature increase following time t as $T = 10 + kt^2$. In Fig. 7.7, right panel, the evolution of the volume and surface of the pores in such a star-forming environment is presented. From a temperature as low as 30 K, which corresponds to $\sim 8 \times 10^3$ years, the ices re-organize and the porosity begins to change. The restructuring occurs until temperatures of 50 K have been attained, which corresponds to a time scale of 10^4 years. As the ice re-organizes, pores connect to each other to form larger pores. If chemical species are trapped in these pores, they can then encounter only when a certain temperature is reached. Ices could then trap chemical species in their pores during long time scales and let them meet when pores coalesce and more favorable conditions for reactions among them are found.

7.4 CO Ices

7.4.1 Experiments

To study the effect of deposition conditions on the desorption of CO ices, two different laboratory experiments have been devised. In one experimental setup, the Interstellar Photoprocess System (IPS; Chen et al. 2014), CO molecules are deposited on a surface at 14 K to create CO ices, and in a second step the substrate is warmed up to follow the desorption of the CO in the gas. The ice thickness is monitored using a Fourier Transform Infrared spectrometer, while the molecules desorbing from the sample are measured with a Quadrupole Mass Spectrometer (QMS). In a second experiment, performed using the InterStellar Astrochemistry

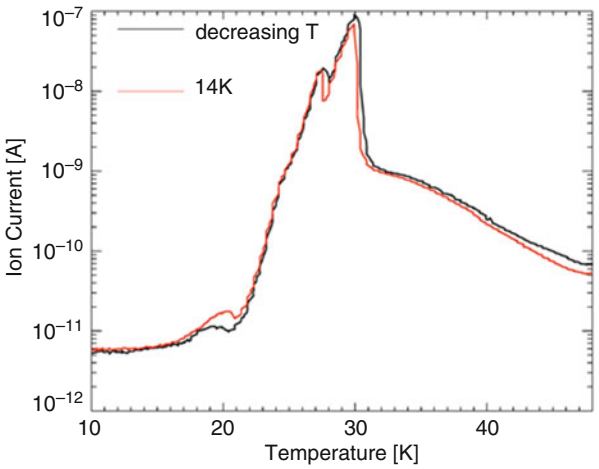

Fig. 7.8 TPD measurements using QMS to record the gas phase CO with deposition at 14 K or with deposition as the surface temperature is decreased from 80 K to 14 K

Chamber (ISAC) at the Centro de Astrobiología (Fayolle et al. 2016), CO molecules are deposited on a water ice surface at decreasing temperatures from 80 K to 14 K. While deposition conditions are different in both experiments, they both result in identical TPD measurements at first sight, in which the multilayer of CO desorbs at 30 K, while the monolayer of CO desorbs between 30 and 60 K. TPD of CO deposited at 14 K and at decreasing temperature are reported in Fig. 7.8. We represent here the TPD in a logarithmic scale to highlight the differences. One striking characteristic of both TPD is a small bump at 20 K. This bump illustrates that some CO molecules are desorbing at these temperatures, which indicate that they have binding energies around 600 K.

7.4.2 Simulations

The formation of CO ices is simulated under the conditions met in the two experimental approaches. In the first experiment, CO is deposited at 14 K on different types of surface (with a deposition rate of 7.8 ML/min). In the present case, and as reported in Cazaux et al. 2017, the simulations concentrate on the adsorption of CO on water ice. CO molecules are admitted on a grid of 40 × 40 sites, and the build-up of the CO ice is followed at 14 K. In the second experiment, the CO molecules are deposited for decreasing temperature of the substrate, from 80 K to 14 K (with a deposition rate of 1.4 ML/min). The TPD simulating CO deposited at 14 K with two different diffusions (90% of the binding energy in red and 70% in blue) are reported in Fig. 7.9. Our simulations show that to explain the bump at 20 K

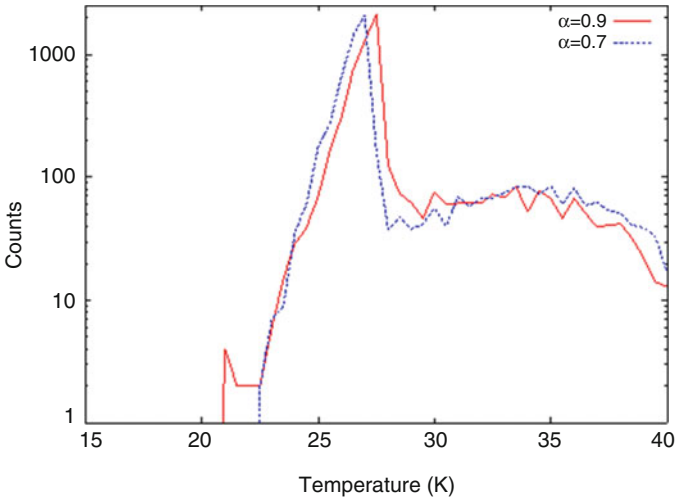

Fig. 7.9 TPD experiments from our simulations with slow diffusion of 90% of binding energy (red) and 70% of the binding energy (blue)

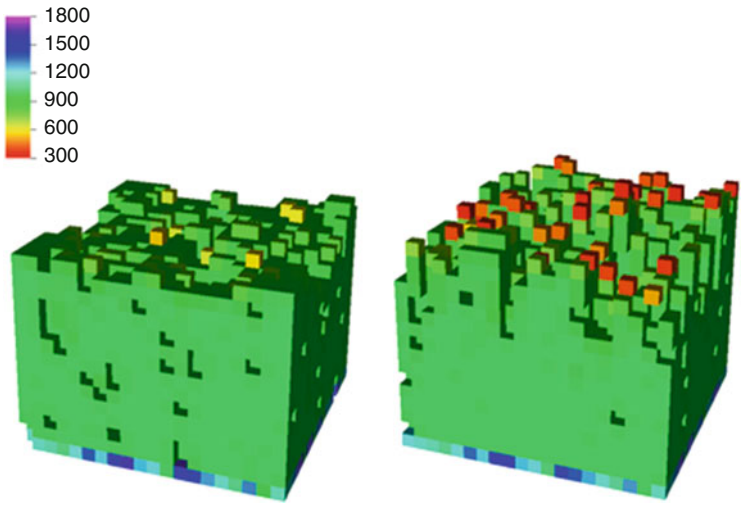

Fig. 7.10 Top: Morphology of the CO ices in experiment 1 (left, deposited at 14 K) and 2 (right, deposited from 80 K to 8 K). The colors represent the binding energies in K

that was observed experimentally, low mobility is required so that molecules desorb instead of diffusing and being re-organized.

The morphology of the ices deposited at 14 K compared to those grown at decreasing temperature is shown in Fig. 7.10.

Ices grown at 14 K (left panel) contain mainly weakly bound CO molecules, with many empty spaces. At this low deposition temperature, the weakly bound

CO molecules do not evaporate or migrate on the surface. Molecules reaching the surface at a site with low binding energy (∼200 K) move on to a site with higher binding energy and stay there. Clearly, the morphology of the ice, and the binding energy of CO molecules to the ice, is set by the deposition temperature. In the second experiment, depicted on the right panel, CO molecules reach the surface while the substrate temperature is lowered from 80 K to 8 K. The CO ices are grown layer by layer at decreasing temperatures. This leads to "mixed ices", where the first layers, deposited at higher temperatures, are compact while the last layers, deposited at low temperatures, show weakly bound CO molecules and many holes. The conclusion is that the temperature at which the ice is grown greatly affects the structure of the ice. As the TPD results are very similar, the ices must indeed re-organize during the warming up.

Therefore, TPD measurements do wash away the structure of the ices, and the binding energies measured from these experiments correspond to the well-organized structures of the ices. These binding energies, however, can be very different than those of species accreted at very low temperatures, as it is the case in the interstellar medium.

7.4.3 Astrophysical Applications

In starless cores, an important CO depletion has been measured (Tafalla et al. 2004) by comparing line observations of CO isotopologues with the submillimeter dust continuum or extinction maps. Evidence of depletions by a factor of 4–15 in 7 cores have been found (Bacmann et al. 2002) when using CO isotopologues, whereas a CO abundance depletion of ∼1000 and ∼100 was measured in the center of the L1544 and B68 respectively (Caselli et al. 1999; Bergin et al. 2002). However, current models do overestimate the depletion of CO in prestellar cores and mechanisms such as cosmic rays bombardment could explain the higher observed CO abundances (Keto and Caselli 2010). With this study we show that the less severe depletion observed could possibly be due to the loose binding of CO molecules deposited at very low temperatures. Also, observations of embedded protostars reveal more CO that desorption can allow (Jørgensen et al. 2015), which could be explained by outburst history during the accretion phase. However, the loosely bound CO molecules, desorbing at temperatures lower than 27 K, could also be a possibility to explain the extended CO gas in embedded protostars.

7.5 Conclusions

The porosity present in water ices strongly depends on the conditions (temperature and density) during the deposition of the ices. In astrophysical ices, pores will grow as the temperature increases, connect with other pores, and form larger entities,

where the conditions for reactions to take place will be favorable, thus boosting the solid-sate formation of new molecules. As in the case of water ices, but at much lower temperatures, CO ices also present a structure with loose-bound CO and many holes in the ices. However, TPD experiments, commonly used to derive binding energies, imply a strong re-organization of the ices before their desorption (and measurement). This implies that the binding energies derived in the laboratory with such techniques and the values that are found in space can be very different. Binding energies of species depend on the conditions at which ices were formed. The CO depletion observed in pre-stellar cores can shed light on the binding energy of CO molecules in space and the reason for the CO freeze-out in such environments.

References

Acharyya, K., Fuchs, G.W., Fraser, H.J., van Dishoeck, E.F., Linnartz, H.: Astron. Astrophys. **466**, 1005 (2007)
Bacmann, A., Lefloch, B., Ceccarelli, C., et al.: Astron. Astrophys. **389**, L6 (2002)
Bergin, E.A., Alves, J., Huard, T., Lada, C.J.: Astrophys. J. Lett. **570**, L101 (2002)
Boogert, A.C.A., Pontoppidan, K.M., Knez, C., et al.: Astrophys. J. **678**, 985 (2008)
Bossa, J.-B., Isokoski, K., Paardekooper, D.M., et al.: Astron. Astrophys. **561**, A136 (2014a)
Bossa, J.-B., Isokoski, K., de Valois, M.S., Linnartz, H.: Astron. Astrophys. **545**, A82 (2014b)
Bossa, J.-B., Mate, B., Fransen, C., et al.: Astrophys. J. **814**, 47 (2015)
Brill, R., Tippe, A.: Acta Crystallogr. **23**, 343 (1967)
Brovchenko, I., Oleinikova, A.: J. Chem. Phys. **124**, 164505 (2006)
Brown, D.E., George, S.M., Huang, C., et al.: J. Phys. Chem. **100**, 4988 (1996)
Caselli, P., Walmsley, C.M., Tafalla, M., Dore, L., Myers, P.C.: Astrophys. J. Lett. **523**, L165 (1999)
Cazaux, S., Tielens, A.G.G.M., Ceccarelli, C., et al.: Astrophys. J. **593**, L51 (2003)
Cazaux, S., Bossa, J.-B., Linnartz, H., Tielens, A.G.G.M.: Astron. Astrophys. **573**, A16 (2015)
Cazaux, S., Martìn-Doménech, R., Chen, A., Muñoz Caro, G.: prep. Astrophys. J. **849**, 80 (2017)
Ceccarelli, C., et al.: Protostars and planets V. In: Reipurth, B. (eds.), p.47, Univ. of Arizona Press (2007)
Chen, Y.-J., Chuang, K.-J., Muñoz Caro, G.M., et al.: Astrophys. J. **781**, 15 (2014)
Collings, M.P., Dever, J.W., Fraser, H.J., McCoustra, M.R.S., Williams, D.A.: Astrophys. J. **583**, 1058 (2003)
Cuppen, H.M., Herbst, E.: Astrophys. J. **668**, 294 (2007)
Dartois, E., Ding, J.J., de Barros, A.L.F., et al.: Astron. Astrophys. **557**, A97 (2013)
Dohnàlek, Z., Kimmel, G.A., Ayotte, P., Smith, R.S., Kay, B.D.: J. Chem. Phys. **118**, 364 (2003)
Fayolle, E.C., Balfe, J., Loomis, R., et al.: Astrophys. J. Lett. **816**, L28 (2016)
Fedoseev, G., Cuppen, H.M., Ioppolo, S., Lamberts, T., Linnartz, H.: Mon. Not. R. Astron. Soc. **448**, 1288 (2015)
Garrod, R.T., Herbst, E.: Astron. Astrophys. **457**, 927 (2006)
Gibb, E.L., Whittet, D.C.B., Boogert, A.C.A., Tielens, A.G.G.M.: Astrophys. J. Suppl. Ser. **151**, 35 (2004)
Huš, M., Urbic, T.: J. Chem. Phys. **136**, 144305 (2012)
Isaacs, E.D., Shukla, A., Platzman, P.M., et al.: Phys. Rev. Lett. **82**, 600 (1999)
Isokoski, K., Bossa, J.-B., Triemstra, T., Linnartz, H.: Phys. Chem. Chem. Phys. **16**, 3456 (2014a)
Isokoski, K., Bossa, J.-B., Triemstra, T., Linnartz, H.: Phys. Chem. Chem. Phys. **16**, 3456 (2014b)
Jørgensen, et al.: Astron. Astrophys. **579**, A23 (2015)
Karssemeijer, L.J., Cuppen, H.M.: Astron. Astrophys. **569**, A107 (2014)
Karssemeijer, L.J., Ioppolo, S., van Hemert, M.C., et al.: Astrophys. J. **781**, 16 (2014)

Keane, J.V., Tielens, A.G.G.M., Boogert, A.C.A., Schutte, W.A., Whittet, D.C.B.: Astron. Astrophys. **376**, 254 (2001)
Keto, Caselli, P.: Mon. Not. R. Astron. Soc. **402**, 1625 (2010)
Lauck, T., Karssemeijer, L., Shulenberger, K., et al.: Astrophys. J. **801**, 118 (2015)
Maté, B., Rodríguez-Lazcano, Y., Herrero, V.J.: Phys. Chem. Chem. Phys. **14**, 10595 (2012a)
Maté, B., Rodríguez-Lazcano, Y., Herrero, V.J.: Phys. Chem. Chem. Phys. **14**, 10595 (2012b)
Mispelaer, F., Theule, P., Aouididi, H., et al.: Astron. Astrophys. **555**, A13 (2013)
Mitterdorfer, C., Bauer, M., Youngs, T.G.A., et al.: Phys. Chem. Chem. Phys. **16**, 16013 (2014)
Muñoz Caro, G.M., Jiménez-Escobar, A., Martìn-Gago, J.A., et al.: Astron. Astrophys. **522**, A108 (2010)
Noble, J.A., Dulieu, F., Congiu, E., Fraser, H.J.: Astrophys. J. **735**, 121 (2011)
Öberg, K.I., Garrod, R.T., van Dishoeck, E.F., Linnartz, H.: Astron. Astrophys. **504**, 891 (2009)
Ormel, C.W., Spaans, M., Tielens, A.G.G.M.: Astron. Astrophys. **461**, 215 (2007)
Palumbo, M.E.: Astron. Astrophys. **453**, 903 (2006)
Palumbo, M.E., Baratta, G.A., Leto, G., Strazzulla, G.: J. Mol. Struct. **972**, 64 (2010)
Pilling, S., Andrade, D.P.P., Neto, A.C., Rittner, R., de Brito, A.N.: J. Phys. Chem. A. **113**, 11161 (2009)
Pontoppidan, K.M.: Astron. Astrophys. **453**, L47 (2006)
Pontoppidan, K.M., van Dishoeck, E.F., Dartois, E.: Astron. Astrophys. **426**, 925 (2004)
Raut, U., Teolis, B.D., Loeffler, M.J., et al.: J. Chem. Phys. **126**, 244511 (2007a)
Raut, U., Famà, M., Teolis, B.D., Baragiola, R.A.: J. Chem. Phys. **127**, 204713 (2007b)
Schoïer, F.L., Jørgensen, J.K., van Dishoeck, E.F., Blake, G.A.: Astron. Astrophys. **390**, 1001 (2002)
Tafalla, M., Myers, P.C., Caselli, P., Walmsley, C.M.: Astrophys. Space Sci. **292**, 347 (2004)
Tafalla, M., Kumar, M.S.N., Bachiller, R.: Astron. Astrophys. **456**, 179 (2006)
Theulé, P., Duvernay, F., Danger, G., et al.: Adv. Space Res. **52**, 1567 (2013)
Tielens, A.G.G.M., Allamandola, L.J.: NATO ASIC Proc. 210: Physical Processes in Interstellar Clouds. Morfill, G.E., Scholer, M. (eds.), pp. 333–376. (1987)
Whittet, D.C.B., Gerakines, P.A., Tielens, A.G.G.M., et al.: Astrophys. J. **498**, L159 (1998)
Whittet, D.C.B., Gerakines, P.A., Hough, J.H., Shenoy, S.S.: Astrophys. J. **547**, 872 (2001)
Williams, D.A., Hartquist, T.W., Whittet, D.C.B.: Mon. Not. R. Astron. Soc. **258**, 599 (1992)
Zondlo, M.A., Onasch, T.B., Waeshawsky, M.S., Tolbert, M.A., Mallick, G., Arenz, P., Robinson, M.S.: J. Phys. Chem. B. **101**, 10887 (1997)

Part III
Ice Processes

Chapter 8
Infrared Spectroscopy and Programmed Thermal Desorption of Ice Mixtures

Rafael Martín-Doménech and Guillermo M. Muñoz Caro

Abstract In the coldest regions of the interstellar medium, ice mantles are accreted on the surface of dust grains. These ice mantles are detected by infrared telescopes, revealing their composition, structure, etc. This wouldn't be possible without a proper characterization of ice analogs in laboratories under astrophysically relevant conditions. In this Chapter, we highlight the differences in the infrared features of the different components that are usually detected in interstellar ice mantles that arise when the spectrum of a pure ice is compared with the spectrum of an ice mixture. These differences are due to molecular interactions, and give us information on both the composition and the structure of the ice mantle. In addition, thermal processing of the ice mantles may induce structural changes that are also studied here. In space, thermal processing of the ice mantles during a star formation event ultimately leads to the sequential sublimation or desorption of the different ice components, leading to the formation of a chemically-rich hot core around the forming protostar. In the laboratory, this process can be also simulated, as it is explained by the end of the Chapter.

8.1 Introduction to the Use of IR Spectroscopy in the Study of Ice Processes

Infrared (IR) spectroscopy is a powerful tool in the study of interstellar solids, like the ice mantles accreted on top of the dust grains in the coldest regions of the interstellar medium (ISM). In space, these ice mantles are detected by IR

R. Martín-Doménech (✉)
Harvard-Smithsonian Center for Astrophysics, Cambridge, MA, USA
e-mail: rafael.martin_domenech@cfa.harvard.edu

G. M. Muñoz Caro
Centro de Astrobiología, INTA-CSIC, Torrejón de Ardoz, Madrid, Spain

G. M. Muñoz Caro, R. Escribano (eds.), *Laboratory Astrophysics*,
Astrophysics and Space Science Library 451,
https://doi.org/10.1007/978-3-319-90020-9_8

spectroscopy in absorption, thanks to telescope observations using an IR source situated in or behind the dense molecular clouds where ice mantles are formed. In particular, when a star formation process is triggered in the interior of a dense cloud, circumstellar dust grains are heated by the central young stellar object, emitting IR light that is subsequently absorbed by the molecules in the ice present in the colder circumstellar envelope, and also in the parent dense cloud, before reaching our telescopes. Field stars located behind dense clouds can act as IR sources, allowing the observation of interstellar ice mantles in quiescent dense cores with no star formation processes in their interior.

In Laboratory Astrophysics, IR spectroscopy in transmittance or in reflection–absorption is widely used to characterize and monitor the evolution of ice samples during the experimental simulations of different processes (see Chap. 3).

IR spectroscopy has allowed astrophysicists not only to detect interstellar (and circumstellar) ices, but also to reveal their composition from the observed IR features. This is achieved by comparing the data from the observations with the IR spectra of ice analogs collected in the laboratory under astrophysically relevant conditions. Every species in the ice leads to particular IR features, and their intensity is related to the abundance of the species (see Chap. 5). This way, we know that water is the main component of astrophysical ices, with a typical abundance of (0.5–1.5) $\times$ 10^{-4} with respect to gas-phase H_2 in circumstellar ices around solar-type protostars (van Dishoeck 2006). Other species are also present in astrophysical ices. Carbon monoxide and carbon dioxide are the following most abundant molecules, with abundances up to ~50% relative to water toward some lines of sight. Methanol, ammonia and methane have been detected with abundances around 5–10%, while other species like H_2CO, OCN^-, OCS, C_2H_5OH, or SO_2 are probably also present in ice mantles. A careful study of the IR spectroscopy of ice analogs in the laboratory is thus necessary to understand the composition, and also the structure of the ice mantles present in space, since both the band profiles (peak positions, and band widths and profiles) and intensities are affected by the environment of the molecules in the ice, as it is explained in Sect. 8.3. A recent review of ice observations in space and their compositions can be found in Boogert et al. (2015).

8.2 Experimental Study of the Thermal Processing of Astrophysical Ices

The experimental study of ice analogs is currently carried out in different laboratories around the world. Most of the results presented in this Chapter have been obtained with the InterStellar Astrochemistry Chamber (ISAC, described in detail in Muñoz Caro et al. 2010). This particular experimental set-up is located at the Centro de Astrobiología (CAB, INTA-CSIC) near Madrid (Spain). It is an ultra-high vacuum (UHV) chamber with a base pressure around 4 $\times$ 10^{-11} mbar, similar to that found in dense cloud interiors where ice mantles are grown. A schematic

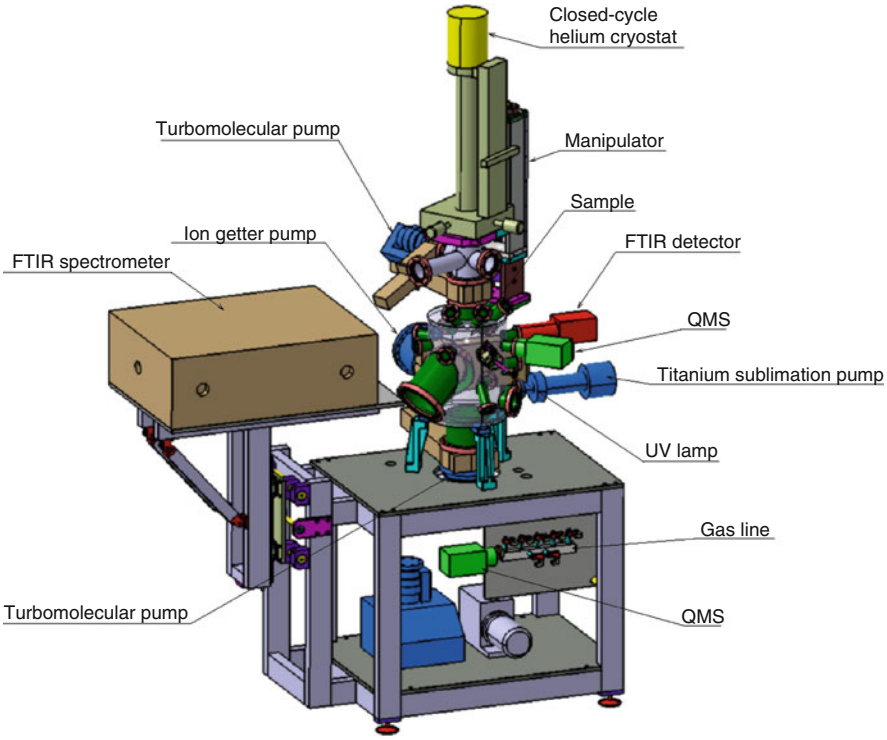

Fig. 8.1 Schematic cartoon of the ISAC experimental set-up. The UV lamp is described in Chap. 10

cartoon of this set-up is shown in Fig. 8.1, but other experimental set-ups look quite similar, and the description in this Chapter can be extrapolated to most of them.

In this kind of set-ups, the ultra-high vacuum is achieved thanks to the combination of several rotatory and turbomolecular pumps, with possible additional help of other types of pumps such as the ion-getter pumps and the titanium sublimation pumps. A pressuremeter (in the case of ISAC, a Bayard-Alpert pressuremeter) monitors the pressure in the chamber, so it is possible to control that the experimental simulations are being carried out at astrophysically relevant conditions. Inside the chamber, an infrared transparent window (usually a CsI, KBr, or MgF_2 window, or even a diamond window if spectroscopy in the far-IR region is required) is used as the substrate where ice analogs are grown. The substrate is placed in a sample holder located at the tip of a cold finger from a closed-cycle helium cryostat. This way, the substrate can be cooled down to 8 K, the typical temperature inside quiescent dense clouds. The combination of a tunable heater with a silicon diode temperature sensor, and a temperature controller allows the substrate to be held at a temperature between 8 K and 400 K, which is of particular interest for the thermal processing experiments addressed in this Chapter.

Ice samples are grown by gas and/or vapor deposition onto the substrate through capillary tubes controlled by needle valves that introduce them in the chamber at very low doses. These capillaries are connected to a gas line that allows the preparation of gas mixtures with several of the components typically found in ice mantles. Most UHV chambers have a second capillary that is used to introduce reactive species, like NH_3, not allowing them to react with the rest of components before forming the ice analog. Different valves control the abundance of the components in the gas line, which can be monitored by a quadrupole mass spectrometer (a Pfeiffer Prisma QMS with a Faraday detector for ISAC). The abundance of the component introduced through the second capillary relative to the rest of the mixture can be controlled by its partial pressure in the chamber during deposition. After deposition of the ice mixture, its composition can be confirmed by IR spectroscopy in transmittance (as it is the case for the ISAC set-up) or in reflection–absorption, usually with a Fourier transform infrared (FTIR) spectrometer (a Bruker Vertex 70 model is used for ISAC). The spectrometer is usually equipped with a deuterated triglycine sulfate (DTGS) detector working in the 7500–400 cm^{-1} ($\sim$1.3–25 μm, corresponding to the near- and mid-IR). Another DTGS detector working in the 500–50 cm^{-1} range (20–200 μm) is available for measurements in the far-IR region of the spectrum. Alternatively, more sensitive mercury–cadmium–telluride (MCT) detectors cooled with liquid nitrogen can be also used. Spectra are usually collected with a resolution of 1–4 cm^{-1}.

In addition to the FTIR spectrometer, in ISAC a Pfeiffer Prisma QMS with a Channeltron detector of mass spectral range from 1 to 200 amu monitors the gas phase inside the main chamber, both during deposition and during the experimental simulations of different astrophysical processes involving thermal or non-thermal desorption of the ice samples. Once they reached the QMS, the desorbed gas-phase molecules are ionized by low energy ($\sim$70 eV) electron bombardment forming the molecular ion. These ions are subsequently fragmented due to the deposited excess energy, and therefore, different fragments are detected for every desorbing species. The fragments are separated according to their mass:charge (m/z) ratio by a quadrupolar mass analyzer, and they are finally detected, for example with a secondary-emission multiplier (SEM) detector.

As mentioned above, thanks to the combination of the closed-cycle helium cryostat, the tunable heater, and the temperature controller (LakeShore Model 331 in ISAC), ice samples deposited at 8 K can be warmed up at a constant heating rate until complete sublimation is attained, simulating the thermal processing suffered by ice mantles in circumstellar environments. Desorption of the ice components is subsequently detected by the QMS. This is known as a temperature-programmed desorption (TPD) experiment of ice analogs. Recent results on TPD experiments of astrophysical ice analogs are presented in the next Section.

8.3 Results and Discussion

8.3.1 Overview of Mixture Effects on the IR Spectra of Astrophysical Ice Analogs at 8 K

A transition between two vibrational levels of an ice molecule as a consequence of the excitation of one of its intramolecular vibrational modes leads to a particular band feature in the near- and mid-IR spectral range, as explained in Chap. 3. Despite being intramolecular modes, these vibrations are affected by the local molecular environment in the ice, and therefore, the ice composition and structure may induce changes in the IR band peak positions (i.e., in the frequency of the vibration), band profiles (band widths and shapes) and even band strengths. Since interstellar ices are composed of several species, it is very important to know how the IR bands of the ice components at 8 K are affected in different water-rich multicomponent ice mixtures (and, in particular, in realistic astrophysical ice analogs) when compared to the spectra of pure ice analogs at the same temperature.

What we call an astrophysical ice analog is an ice mixture composed by the five most abundant species detected in interstellar ices with realistic proportions (70% H_2O, 10% CO, 10% CO_2, 5% CH_3OH, and 5% NH_3, approximately, see Boogert et al. 2015 and references therein). In Fig. 8.2, the IR spectrum of such an ice analog collected at 8 K is compared to the sum of the five spectra corresponding to the pure ice samples at the same temperature (scaled by a factor to reproduce the astrophysical abundance of the multicomponent ice mixture). Even when the

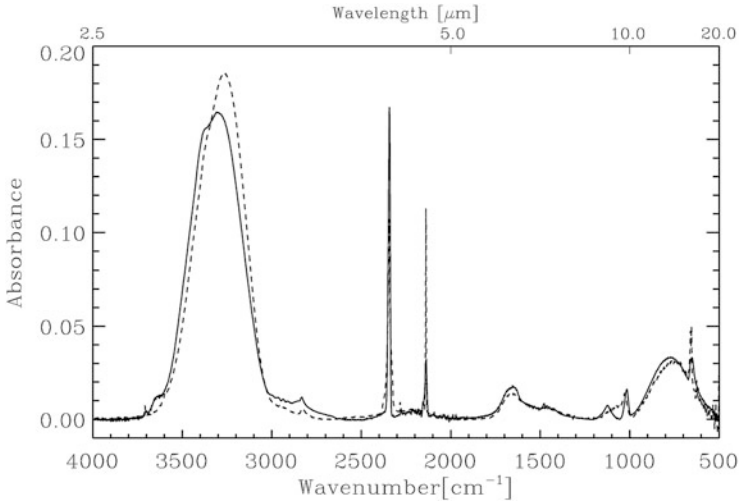

Fig. 8.2 Solid: IR spectrum of an astrophysical ice analog (see text). Dashed: Sum of the IR spectra of the pure ices of the above species, scaled to reproduce the abundance of the multicomponent ice analog

general look of the IR spectrum of an astrophysical ice analog can be reproduced by the sum of pure ice spectra, several differences arise, mostly due to the interactions between water molecules (the major component) and the rest of molecules. These differences can be seen in Fig. 8.2, and are highlighted below for each component.

8.3.1.1 H_2O

The O–H stretching band of H_2O at $\sim$3260 cm^{-1} ($\sim$3.0 μm) is blueshifted in mixtures with apolar components such as CO or CO_2 that interfere with the hydrogen-bonded network formed by H_2O molecules, as seen in Fig. 8.2 for the astrophysical ice analog case. CO molecules are not able to form hydrogen bonds, while those formed between CO_2 and H_2O molecules are weaker than the ones formed between water molecules. The result is a decrease in the overall strength of the intermolecular hydrogen bonds formed between the water molecules, leading to an increase of the O–H intramolecular bond strength and the frequency of this particular vibrational mode. As a consequence, the O–H stretching band is blueshifted. Moreover, water molecules not connected at all to the hydrogen bonded network present the O–H stretching modes with the highest frequencies, and may lead to the appearance of a new feature at $\sim$3650 cm^{-1} on the blue side of the O–H stretching band.

In addition, the presence of the non-polar species in the ice mixture increases the intensity of the O–H bending mode at $\sim$1650 cm^{-1}. The different behavior between this band and the O–H stretching band (whose intensity is reduced) in the mixture is due to the different nature of both vibrational modes.

At the same time, the hydrogen bonds formed between H_2O and polar molecules like NH_3 can be stronger than those formed between H_2O molecules. These O–H bonds would be weaker, and their frequency lower, leading to an increase in the intensity of the low frequency wing in the O–H stretching band, which has been attributed in the literature to the O–H stretching mode of water molecules forming ammonia hydrates (Knacke and McCorkle 1987; Dartois and d'Hendecourt 2001).

These effects were previously reported in water-rich binary mixtures with polar and non-polar species in Hagen et al. (1983), and they are all present in the IR spectrum of an astrophysical ice analog (Martín-Doménech et al. 2014).

8.3.1.2 CO

The C=O stretching band of CO, peaking at 2139 cm^{-1} (4.67 μm) in pure CO ices, is usually broadened in ice mixtures due to the larger variety of molecular environments where the CO molecules can be found, leading to the contribution of polar and apolar components to the band (Boogert et al. 2015). For example, CO mixtures with CH_3OH are invoked to account for the polar component of the observed C=O stretching band (Cuppen et al. 2011).

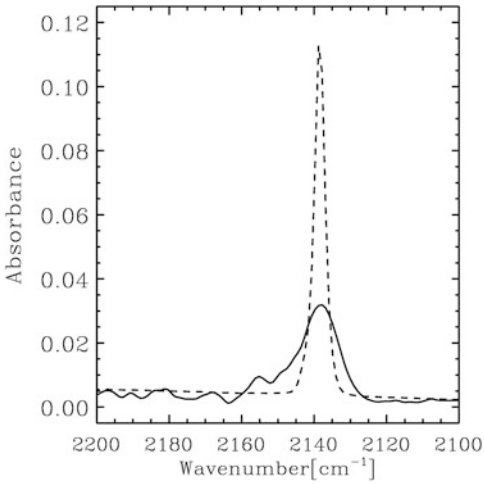

Fig. 8.3 C=O stretching band of CO in pure CO ice (dashed) and in an astrophysical ice analog (solid)

For water-rich ice mixtures as the astrophysical ice analog presented in Fig. 8.2, the band presents a shoulder on its blue side, peaking at ~2152 cm^{-1} as shown in Fig. 8.3. This shoulder is believed to originate from the interaction of CO molecules with dangling O–H bonds of water molecules at the ice surface or at pores within the amorphous water–ice matrix (Collings et al. 2003a), and it is therefore related to the peak at ~3650 cm^{-1} mentioned in Sect. 8.3.1.1. However, this shoulder is not detected in astronomical observations (Sandford et al. 1988), suggesting that CO ice is accreted at a different stage in ice formation, after H_2O ice has already formed, thus leading to a bi-layered ice structure (see Boogert et al. 2015, and references therein).

8.3.1.3 CO_2

Just like for CO, the behavior of the C=O stretching band of CO_2 molecules (peaking at 2342 cm^{-1} or 4.27 μm) in ice mixtures depends on the presence of other polar and apolar species. However, despite the similarities with CO, the final induced changes in the band are somehow more difficult to be systematically studied and predicted (Sandford and Allamandola 1990; Ehrenfreund et al. 1999). For the water-rich, astrophysical ice analog presented in Fig. 8.2, this band ends up being narrower than in the pure ice case (see left panel of Fig. 8.4).

On the other hand, the degenerate bending modes of CO_2 at ~655 cm^{-1} (15.2 μm) lose the characteristic double-peak structure of pure and crystalline ices in any ice mixture, including an astrophysical ice analog (right panel of Fig. 8.4), as previously reported for binary mixtures with water in Sandford and Allamandola (1990). The observed 15.2 μm band in astronomical spectra toward different lines of sight can be fitted with a combination of up to five different contributions, including

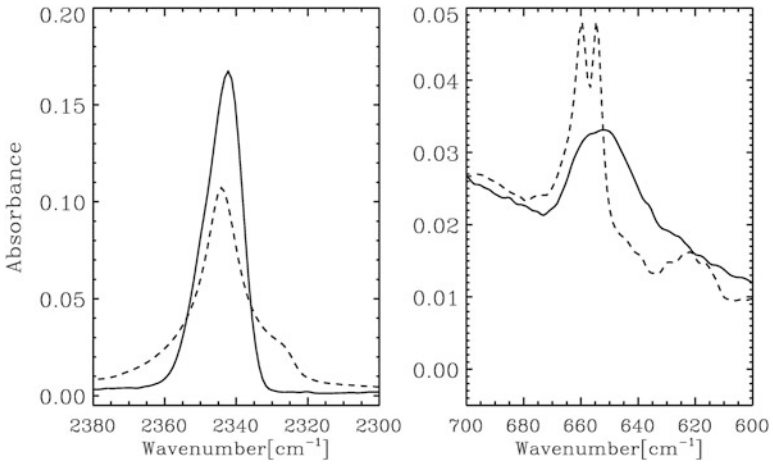

Fig. 8.4 Left: C=O stretching band of CO_2 in pure CO_2 ice (dashed) and in an astrophysical ice analog (solid). Right: Degenerate bending modes corresponding to CO_2 molecules in pure CO_2 ice (dashed) lose the double-peak structure in an astrophysical ice analog (solid)

contribution from pure CO_2 ice toward selected lines of sight (see, e.g., Pontoppidan et al. 2008).

8.3.1.4 CH_3OH

In water-rich ice mixtures, the O–H and C–H stretching and deformation vibrational modes are usually hindered by the corresponding modes of water molecules. On the other hand, the C–O stretching band of CH_3OH is observed to be slightly redshifted in water-rich ice mixtures, as the astrophysical ice analog presented in Fig. 8.2, from 1025 cm^{-1} (9.76 μm, typical of the pure ice case) to 1016 cm^{-1} in the ice mixture (see Fig. 8.5). This relatively small shift (d'Hendecourt and Allamandola 1986) indicates that the hydrogen bonds formed between methanol and water molecules in the ice mixture are only slightly stronger than those formed between methanol molecules in the pure ice case (similar to the interaction between water and ammonia molecules presented in Sect. 8.3.1.1). The C–O bond strength in CH_3OH molecules is thus similar in both cases (slightly weaker in the mixture), and so is the frequency of the vibrational mode (slightly lower in the mixture).

8.3.1.5 NH_3

Similar to the methanol vibration modes, the N–H stretching and deformation bands are also hindered by those of water in water-rich ice mixtures, and the so-called umbrella mode is used to monitor the presence of ammonia in this kind of mixtures.

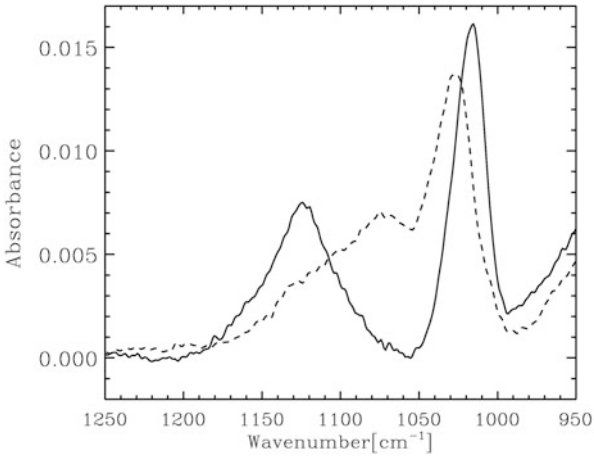

Fig. 8.5 NH_3 umbrella band (left) and C–O stretching band of CH_3OH (right) in an astrophysical ice analog (solid) compared to the sum of pure ice spectra reproducing the composition of the ice mixture (dashed)

The hydrogen bonds formed between H_2O and NH_3 molecules are also stronger than those formed between water molecules, as explained in Sect. 8.3.1.1. This strong interaction between water and ammonia molecules also leads to a strong blueshift in the NH_3 umbrella band from 1067 cm^{-1} to 1124 cm^{-1}, as seen in Fig. 8.5 for the astrophysical ice analog case, and previously observed in binary mixtures with water (Hagen et al. 1983; d'Hendecourt and Allamandola 1986). This shift to higher frequencies, opposite to the shift in the O–H stretching mode of water molecules bonded to ammonia molecules (whose frequency was redshifted) is due to the different nature of the umbrella vibrational mode compared to a stretching mode.

8.3.2 Evolution of IR Spectra During Thermal Processing

As shown in Sect. 8.3.1, IR features of the ice components depend on the molecular environment, leading to differences in the frequencies, profiles and strengths when the IR bands of pure ices at 8 K are compared to the same features in the spectrum of ice mixtures at the same temperature. Differences are also expected between the spectra of ices collected at different temperatures, since the ice structure, and therefore the molecular environment of the molecules, is temperature-dependent. Heating of ice analogs deposited at 8 K leads to structural changes involving phase changes, diffusion of molecules, and even ice segregation in mixtures. Ice diffusion barriers are proportional to the binding energy of the species, and segregation is expected to occur whenever diffusion of molecules is possible and it is energetically favorable for molecules of the same kind to group together (Öberg et al. 2009). Evolution with the temperature of the IR features studied in Sects. 8.3.1.1–8.3.1.5 for ice mixtures (and astrophysical ice analogs in particular) is presented below.

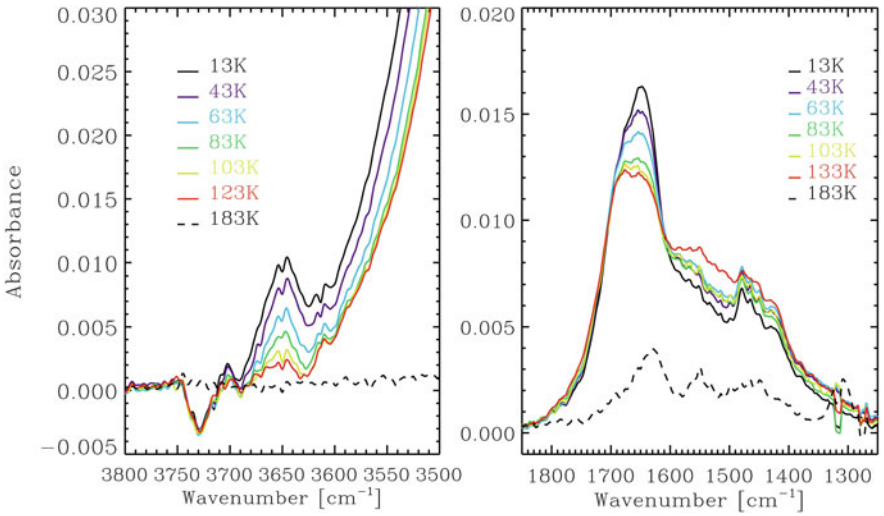

Fig. 8.6 Evolution of two IR bands corresponding to water molecules in an astrophysical ice analog. Left: O–H stretching mode at ∼3650 cm^{-1} of water molecules not connected to the hydrogen bonded network. Right: bending mode at ∼1654 cm^{-1}

8.3.2.1 H_2O

The feature at ∼3650 cm^{-1} corresponding to the O–H stretching mode of H_2O molecules not connected to the hydrogen bonded network of the water–ice matrix in a multicomponent ice mixture (see Sect. 8.3.1.1) gradually disappears during the warm-up of an astrophysical ice analog (left panel of Fig. 8.6). This is probably an effect of the transition to a more compact ice structure (as stated in Isokoski 2013) favoring the formation of hydrogen bonds between the water molecules in the ice mixture.

At the same time, the intensity of the bending band decreases in the same temperature range (right panel of Fig. 8.6), and can be therefore attributed also to compaction. Therefore, in line with the observations presented in Sect. 8.3.1.1, these two features are affected by a common process, probably compaction of the ice during warm-up.

8.3.2.2 CO

The shoulder on the blue side of the C=O stretching band due to the interaction of some CO molecules with dangling O–H bonds corresponding to water molecules in an astrophysical ice mixture gradually disappears during warm-up, as observed in Fig. 8.7. This shoulder is negligible at ∼63 K and has completely disappeared at ∼83 K. As for the feature at ∼3650 cm^{-1} studied in the previous section, this is

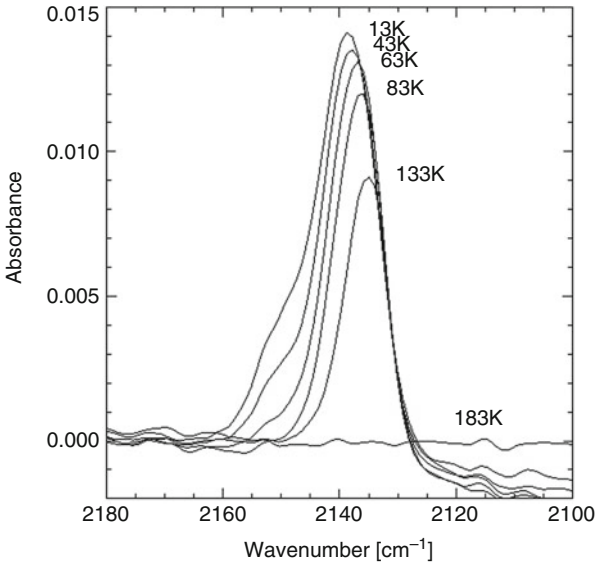

Fig. 8.7 Evolution of the C=O stretching band of CO during warmup of an astrophysical ice analog

probably due to the transition from the highly porous to the less porous amorphous solid water (Sandford et al. 1988; Collings et al. 2003b), since it reduces the number of dangling O–H bonds in the ice (it is mentioned in Sect. 8.3.1.2 that both features are clearly related) with which the CO molecules are able to interact.

Along with the loss of this shoulder, a redshift of the main peak is observed in Fig. 8.7. This redshift is characteristic of binary mixtures with water (Sandford et al. 1988, although it is not observed in Sect. 8.3.1.2). Therefore, at least a fraction of the CO is probably mixed within the water–ice matrix during warm-up. Moreover, desorption of CO molecules (see Sect. 8.3.3) increase the dilution of this species in the water–rich ice mixture, which leads to the gradual increase observed for the redshift (as reported in Sandford et al. 1988). No strong evidences of major CO segregation in the ice mixture are thus found in the ice IR spectrum, which could have been another explanation for the loss of the shoulder in the blue side of the band. Segregation is not completely ruled out, though, as it could still be taking place to a small extent, not detectable by the FTIR spectrometer.

8.3.2.3 CO_2

No significant changes are observed in the C=O stretching and bending bands of CO_2 during warm-up of an astrophysical ice analog (see Fig. 8.8). The stretching band is redshifted as the temperature increases, and its intensity rises between 65 K and 125 K. However, the behavior of this band in multicomponent mixtures is

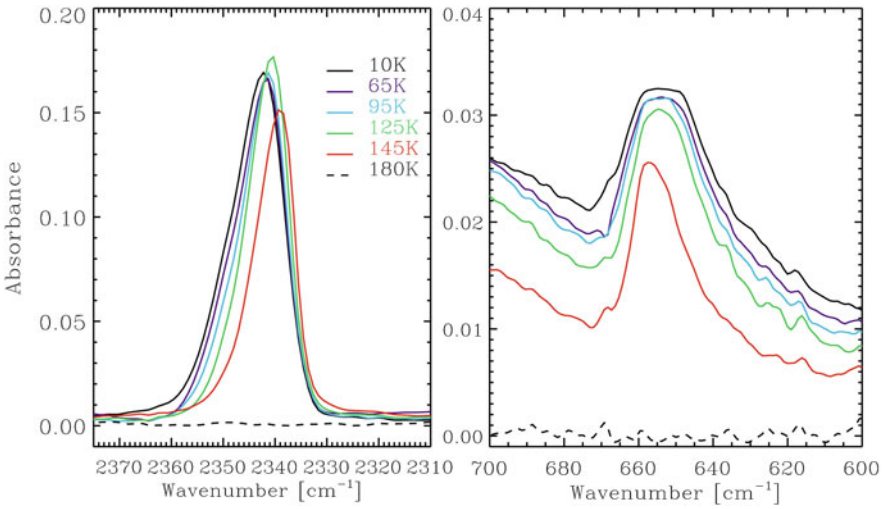

Fig. 8.8 Evolution of two IR bands of CO_2 during warm-up of an astrophysical ice analog. Left: C=O stretching mode at ~2342 cm^{-1}. Right: bending mode at ~655 cm^{-1}

somehow difficult to determine, as explained in Sect. 8.3.1.3, since it varies with the concentration of the different species present in the mixture. On the other hand, the double-peak structure of the degenerate bending modes characteristic of pure and crystalline CO_2 ice is not observed at any temperature. This is an indication that during the thermal processing of an astrophysical ice analog, segregation only takes place, at most, to a small extent as it does for the case of CO molecules.

Segregation of both CO and CO_2 in binary ice mixtures with water is reported in Öberg et al. (2009). This process is known to be time and composition dependent, which may be the origin for the lack of segregation observed by IR spectroscopy during the thermal processing of an astrophysical ice analog. Moreover, segregation of CO_2 molecules is invoked to explain astronomical observations of pure CO_2 ice toward low- and high-mass protostars (Gerakines et al. 1999; Nummelin et al. 2001; Pontoppidan et al. 2008; Zasowski et al. 2009).

8.3.2.4 CH_3OH

The C–O stretching band of CH_3OH undergoes a significant blueshift during warm-up of an astrophysical ice analog, particularly above ~110 K, when the band broadens and the peak shifts from 1016 cm^{-1} toward shorter wavelengths, getting closer to the frequency corresponding to pure methanol ice (1025 cm^{-1}). This indicates segregation of a fraction of the methanol molecules in the mixture. At even higher temperatures, the red component of the band gradually disappears due to thermal desorption (see Sect. 8.3.3), and the peak is shifted to ~1034 cm^{-1},

characteristic of type II clathrate hydrates, formed at temperatures above ∼140 K (Blake et al. 1991), which mainly desorb at higher temperatures.

While the most volatile ice species, like CO, can diffuse easily within the water–ice structure (ice diffusion barriers are proportional to the binding energy, and therefore, to the volatility of the species), and eventually meet with other molecules of the same kind, the interactions between them would be weak. Therefore, only small groups of segregated molecules can be formed in those cases before thermal desorption of these volatile species takes place, or alternatively, before the segregated seed is torn apart by stronger interactions with other species. On the other hand, less volatile species like CH_3OH can form larger groups of segregated molecules during thermal processing, at temperatures high enough for diffusion to take place before reaching the thermal desorption temperature, since interactions between them are stronger (methanol molecules can form hydrogen bonds of similar strength to those formed between water molecules, as evidenced by their similar temperatures of their desorption rate peaks, see, e.g., Collings et al. 2004 and Sect. 8.3.3). These larger regions of segregated methanol can be detected with the FTIR spectrometer.

The C–O stretching band of CH_3OH in an astrophysical ice analog presented in Fig. 8.9 can be fitted to three Gaussians to estimate the contribution of the three types of methanol present in the mixture: methanol mixed within the water–ice structure (whose band peaks at ∼1016 cm^{-1}), segregated methanol (peaking at 1025 cm^{-1}), and methanol forming type II clathrate hydrates with water molecules (peaking at ∼1034 cm^{-1}). The evolution of the contribution of each methanol type with temperature in an astrophysical ice analog is shown in Fig. 8.10.

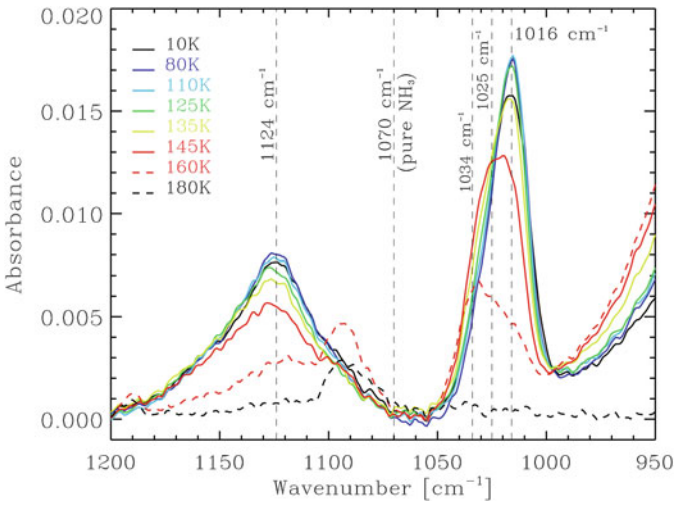

Fig. 8.9 Evolution of the umbrella band of NH_3 and the C–O stretching band of CH_3OH during warm-up of an astrophysical ice analog

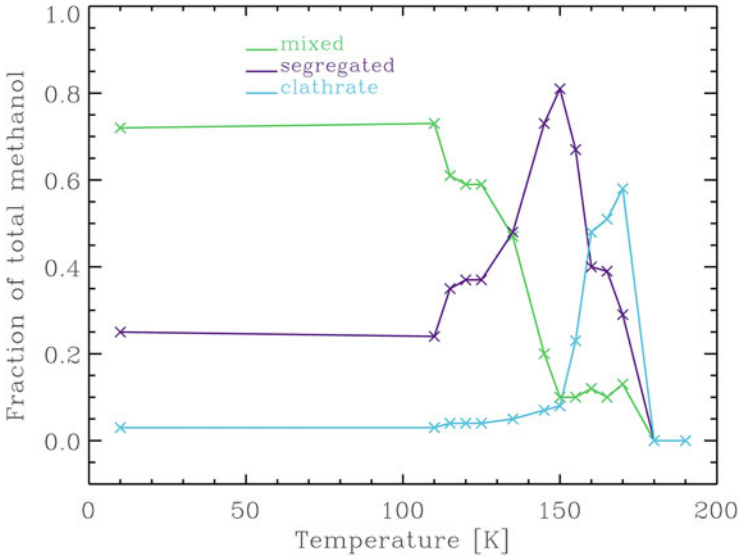

Fig. 8.10 Evolution of the contribution if mixed methanol (green), segregated methanol (purple), and methanol forming a type II clathrate hydrate (blue) to the total area of the C–O stretching band of CH_3OH during warm-up of an astrophysical ice analog

8.3.2.5 NH_3

No substantial changes are observed in the umbrella band corresponding to NH_3 molecules detected at 1124 cm^{-1} in an astrophysical ice analog during warm-up (see Fig. 8.9).

8.3.3 Temperature-Programmed Desorption of an Astrophysical Ice Analog

Thermal processing of ices takes place in different astrophysical environments. For example, during star formation, circumstellar ices are heated by the central young stellar object, and once the star is formed, cometary ices are warmed as the comets get closer to the star during their orbits. Thermal processing of the astrophysical ices drives the sublimation (usually called desorption) of the ice components. In the early stages of star formation, this leads to the formation of hot cores and hot corinos (high density and warm temperature chemically-rich gas-phase regions) around high- and low-mass protostars, respectively (e.g., Viti et al. 2004). Later, in protoplanetary disks, the distance to the central object at which different ice components are thermally desorbed is known as the snowline (e.g., Qi et al. 2013), which has an influence on the planet formation process and composition. Finally,

desorption of cometary ices leads to the formation of the so-called coma around comets.

In Laboratory Astrophysics, experimental simulations on the thermal processing of ice samples are key to derive the binding energies of different species in different ice environments. According to their binding energy, molecules are able to diffuse within the ice toward the surface and subsequently desorb. More volatile species diffuse better and desorb at a lower temperature, since their binding energies are lower (see, e.g., Öberg et al. 2009). During these experimental simulations, thermal desorption can be observed through IR spectroscopy (along with the structural changes also caused by thermal processing, as shown in the previous Section) of the ice samples as a (significant) decrease in the intensity of the corresponding IR bands at temperatures above the desorption temperature of the species (see, for example, Figs. 8.7, 8.8, 8.9 and 8.10). Mass spectrometry is also a very suitable analytical technique for studying desorption of molecules from ice samples, as stated in Sect. 8.2, since it allows direct detection of the desorbed molecules in the gas phase. In this Section, recent results on the temperature-programmed desorption (TPD) of an astrophysical ice analog (as defined in the previous Sections) studied through mass spectrometry are briefly reviewed. The focus is on the qualitative differences with respect to the TPD experiments of pure ices and simpler ice mixtures, instead of a more quantitative approach, stressing the importance of performing this kind of experimental simulations with realistic ice analogs.

In a TPD experiment, after deposition of the ice sample at 8 K, a constant heating rate (1 K/min for the results presented in this Chapter) is applied to the ice, which is warmed-up until complete sublimation is attained. Desorbing molecules are subsequently detected by the QMS. Each species is monitored through a different mass fragment (see Sect. 8.2). The results are thus presented as a TPD curve for each species, plotting the ion current produced by the desorbing molecules in the QMS (which corresponds to the desorption rate) as a function of the temperature. Desorption is observed as a broad feature, as shown in Fig. 8.11, and the kinetics of the process can be modelled with the Polanyi–Wigner equation:

$$-\frac{dN}{dt} = N^i A_i \exp\left(-\frac{E_{des}}{T}\right), \tag{8.1}$$

where N is the column density of the species in the ice, i is the order of the process, A_i is a pre-exponential factor characteristic of every species (but it also depends on the ice temperature, see Luna et al. 2015), E_{des} is the species binding energy, and T the ice temperature (Polanyi and Wigner 1925). Since the heating rate (β) during the TPD experiment is constant and known, the above equation can be written as follows:

$$-\frac{dN}{dT} = N^i A_i \frac{1}{\beta} \exp\left(-\frac{E_{des}}{T}\right), \tag{8.2}$$

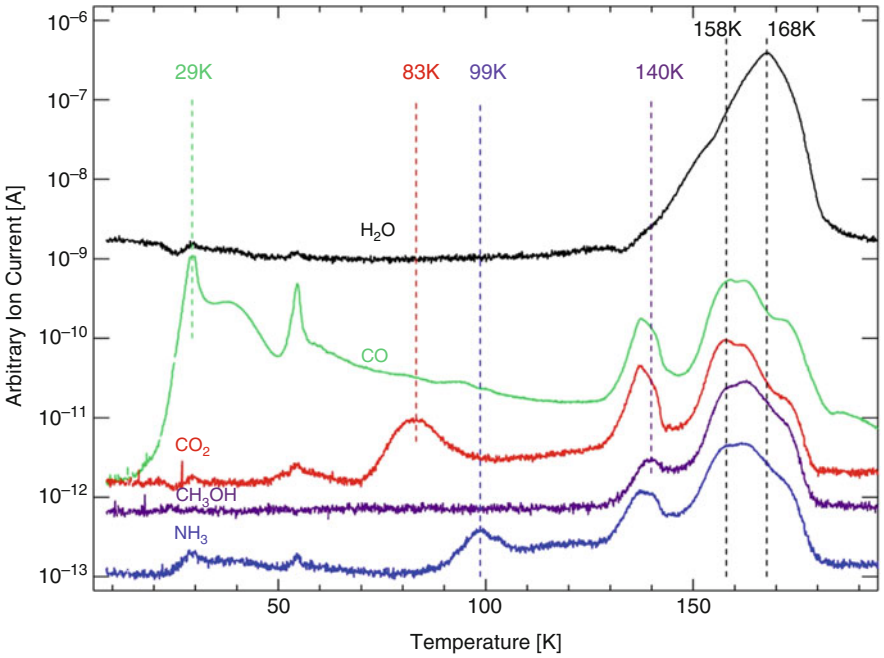

Fig. 8.11 TPD curves of each component of an astrophysical ice analog. Approximate desorption temperatures are indicated. Curves are shifted for clarity

where $-\frac{dN}{dT}$ is the desorption rate directly measured by the QMS. In the case of pure ices, thermal desorption is a zeroth order process where the desorption rate is independent from the ice coverage (see, e.g., Bisschop et al. 2006; Smith et al. 2016; Luna et al. 2017); except for the desorption of the last monolayer of molecules on top of the substrate, which follows a first order kinetics. The peak of the broad feature (i.e., the peak of the desorption rate or T_{peak}) does not depend on the ice coverage for the latter case, only on the volatility (i.e., the binding energy or E_{des}) of the species, but an approximate binding energy can be calculated from T_{peak} even for a zeroth order desorption process: $E_{des} = 30.9 \times T_{peak}$ (Luna et al. 2017). A deep study on the ice desorption kinetics is beyond the scope of this Chapter.

Several studies have revealed the differences in the measured binding energies of the species in pure ices compared to the same species in water-rich binary mixtures (see, e.g., Collings et al. 2004; Noble et al. 2012; Fayolle et al. 2016). In this Chapter, the focus is on the differences between those cases and a more realistic multicomponent ice mixture case (what we call an astrophysical ice analog).

During warm-up of any ice mixture, all minor components show a peak on the desorption rate at a temperature near the one corresponding to the pure ice case (see, e.g., Collings et al. 2004; Fayolle et al. 2011). This is also observed for an astrophysical ice analog (see Fig. 8.11), with temperatures for the desorption peak of every species similar to those reported, for example, in Collings et al. (2004): CO

at ∼29 K, CO_2 at ∼83 K, NH_3 at ∼99 K, and CH_3OH at ∼140 K. Desorption of molecules from a pure ice environment is an evidence of segregation of molecules taking place in the ice mixture, at least to some extent. As explained in Sect. 8.3.2, methanol is the only species able to segregate during thermal processing of an astrophysical ice analog to an extent large enough to be detected by the FTIR spectrometer. The second CO desorption peak detected above 50 K in binary and multicomponent mixtures was assigned to a monolayer desorption in previous works (see, e.g., Collings et al. 2004). Recently, Cazaux et al. (2017) showed that this desorption peak is actually an artifact due to desorption of CO molecules from the surface of the cryostat, not from the ice sample. Nevertheless, Fig. 8.11 shows that CO keeps desorbing continuously at temperatures above 30 K during warm up of the ice analog. This is confirmed by the decrease in the intensity of the corresponding IR band between ∼43 K and ∼133 K (see Fig. 8.8).

In addition, all the minor components present desorption peaks at temperatures well above the desorption temperatures corresponding to the pure ices, both in water-rich binary mixtures (see, e.g., Fayolle et al. 2011) and in our astrophysical ice analog (see Fig. 8.11). This indicates that a fraction of these species is trapped in the water–ice matrix during warm-up (see also Bar-Nun et al. 1985; Collings et al. 2004). The fraction of trapped molecules depends, among other factors, on the ability of the molecules to diffuse through the water–ice structure, and therefore, on the volatility of the species (Collings et al. 2004). The less volatile a species is, the higher diffusion barrier and the larger the fraction of molecules trapped. In the case of the not-very-volatile species NH_3 and CH_3OH, only a small fraction of molecules is able to desorb at their corresponding temperature (see the small desorption peaks in Fig. 8.11), and the major part remains trapped within the water–ice structure. In fact, desorption of these two species at temperatures near the ones of the pure ices is not detected if their abundance in the ice mixture is below ∼3% (Martín-Doménech et al. 2014).

A fraction of the trapped molecules is released at ∼160 K, right after the phase change from amorphous to cubic crystalline water ice. This is known as the "volcano" desorption (Smith et al. 1997).

The remaining fraction of trapped molecules finally co-desorb with water at ∼168 K.

Interestingly, in an astrophysical ice analog, a fraction of the CO, CO_2, and NH_3 trapped molecules co-desorb with CH_3OH at ∼140 K, when a small fraction of the methanol molecules desorbs at the corresponding temperature of the pure methanol ice. Since methanol molecules are able to segregate within the water ice matrix during thermal processing (see Sect. 8.3.2), some regions in the ice mixture become dominated by methanol molecules instead of water molecules, allowing co-desorption of the above mentioned molecules not only with water, but also with methanol, that is able to play a similar role to water once it is segregated (e.g., similar hydrogen-bonding). This co-desorption cannot be reproduced in TPD experiments with water-rich binary mixtures, widely used in the literature.

Finally, it is worth mentioning the shift observed in Fig. 8.11 between the peak on the desorption rate of water at ∼168 K and the co-desorption peak of the rest of

ice components at a slightly lower temperature. Contribution from a second volcano desorption due to the phase change from cubic to hexagonal water ice may be the responsible for this shift (Martín-Doménech et al. 2014). This transformation takes place at higher temperatures in pure ices (Dowell and Rinfret 1960), but the presence of trapped molecules in the astrophysical ice analog eases the phase change, and allows the transition to occur at lower temperatures (Notesco and Bar-Nun 2000).

8.4 Astrophysical Implications. Sequential Desorption of Ices in Hot Cores

As explained in the previous Section, thermal processing of ices takes place in different astrophysical environments. Therefore, TPD experimental simulations may have different astrophysical applications. One easy example is shown in this Section. Chemical models of hot cores use the experimental data on TPD of ice analogs in their study of their astrochemical network (see, e.g., Viti et al. 2004; Wakelam et al. 2004). Water-rich binary mixtures are often used in these TPD experiments. However, experiments with more realistic ice analogs show that some behaviors, like co-desorption of the more volatile species with methanol, cannot be reproduced with binary mixtures (see Sect. 8.3.3). Therefore, appropriate TPD experiments with astrophysical ice analogs are needed to improve the chemical models. The TPD curves presented in Sect. 8.3.3, along with the IR spectral evolution during thermal processing shown in Sect. 8.3.2, allow us to build the schematic representation of the thermal processing of ice mantles in hot cores during star formation shown in Fig. 8.12. In this scheme, the temperatures for the desorption rate peaks measured in the laboratory are scaled to the star-formation scenario, assuming that dust grains at a certain distance of the central object are heated at a slower heating rate than that used in laboratory experiments (1 K/century, Collings et al. 2004). A factor of 0.62 is thus applied to all temperatures, corresponding to the ratio between the temperature expected for the peak of water desorption in an experiment with this slow heating rate (Collings et al. 2004), and the temperature observed in the experiments presented in Sect. 8.3.3 (while this is true for water, it is an approximation for the rest of species).

8.5 Conclusions

Infrared spectroscopy is a powerful tool in the study of interstellar ices. The local molecular environment of the species in ice mantles induces changes in the band positions, profiles and even band strengths of the features of the ice components. Therefore, the presence of certain species is revealed not only by their own IR features, but also by their influence in the features of the rest of ice

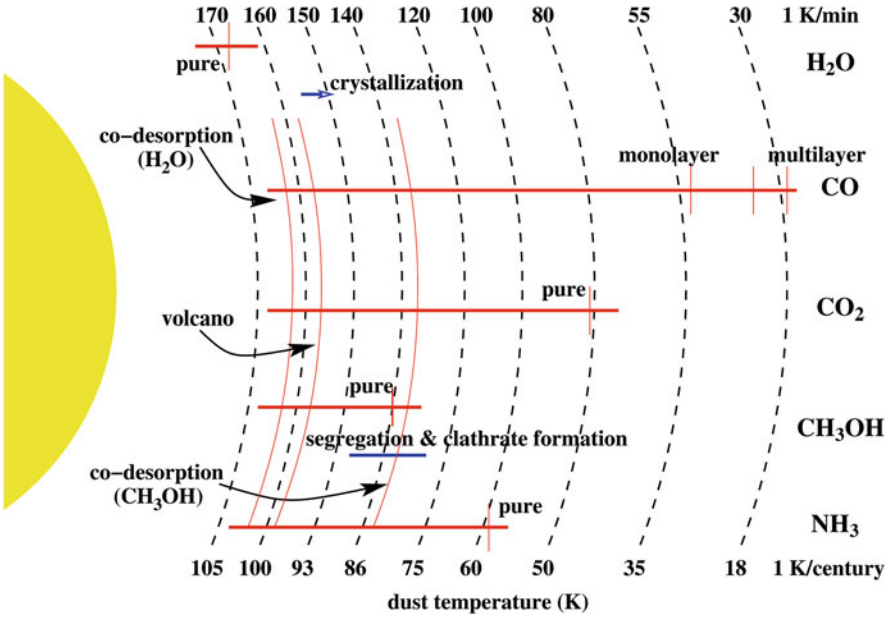

Fig. 8.12 Schematic representation of the thermal processing of ice mantles in hot cores based on the TPD experiments of astrophysical ice analogs. Solid lines represent the temperature ranges at which the studied species desorb. Approximate positions of desorption rate peaks are indicated with red vertical lines. Additional solid lines are used to represent the temperature ranges at which structural changes in the ice take place, as indicated in the figure. See text for the temperature scales

components (see Sect. 8.3.1). In addition, changes in the ice structure induced by thermal processing also lead to changes in the spectra of ice mantles (Sect. 8.3.2). Altogether, astrophysical ice analogs spectra collected in the laboratory allow astrophysicists to extract information from the observed spectra, not only on the composition of interstellar ices, but also on their structure. Thermal processing of ices leads ultimately to the sequential desorption of the ice components. Mass spectrometers allows detection of desorbing molecules in the gas phase, and TPD curves describing the desorption process can be acquired in the laboratory (Sect. 8.3.3). The information of these TPD curves can be subsequently incorporated to chemical models of, for example, hot cores, as shown in Sect. 8.4.

References

Bar-Nun, A., Herman, G., Laufer, D.: Icarus. **63**, 317 (1985)
Bisschop, S.E., Fraser, H.J., Öberg, K.I., van Dishoeck, E.F., Schlemmer, S.: Astron. Astrophys. **449**, 1297 (2006)
Blake, D., Allamandola, L., Sandford, S., Hudgins, D., Freund, F.: Science. **254**, 548 (1991)

Boogert, A.C.A., Gerakines, P.A., Whittet, D.C.B.: Annu. Rev. Astron. Astrophys. **53**, 541 (2015)
Cazaux, S., Martín-Doménech, R., Chen, Y.-J., Muñoz Caro, G.M.: Astrophys. J. **849**, 80 (2017)
Collings, M.P., Dever, J.W., Fraser, H.J., McCoustra, M.R.: Astrophys. J. **583**, 1058 (2003a)
Collings, M.P., Dever, J.W., Fraser, H.J., McCoustra, M.R.: Astrophys. Space Sci. **385**, 633 (2003b)
Collings, M.P., Anderson, M.A., Chen, R., et al.: Mon. Not. R. Astron. Soc. **354**, 1133 (2004)
Cuppen, H.M., Penteado, E.M., Isokoski, K., et al.: Mon. Not. R. Astron. Soc. **417**, 2809 (2011)
d'Hendecourt, L.B., Allamandola, L.J.: Astron. Astrophys. Suppl. Ser. **64**, 453 (1986)
Dartois, E., d'Hendecourt, L.B.: Astron. Astrophys. **365**, 144 (2001)
Dowell, L.G., Rinfert, A.P.: Nature. **188**, 1144 (1960)
Ehrenfreund, P., Kerkhof, O., Schutte, W.A., et al.: Astron. Astrophys. **350**, 240 (1999)
Fayolle, E.C., Öberg, K.I., Cuppen, H.M., Visser, R., Linnartz, H.: Astrophys. J. **529**, A74 (2011)
Fayolle, E.C., Balfe, J., Loomis, R., et al.: Astrophys. J. Lett. **816**, L28 (2016)
Gerakines, P.A., Whittet, D.C.B., Ehrenfreund, P., et al.: Astrophys. J. **522**, 357 (1999)
Hagen, W., Tielens, A.G.G.M., Greenberg, J.M.: Astron. Astrophys. Suppl. Ser. **51**, 389 (1983)
Isokoski, K., Ph.D. Thesis. (2013)
Knacke, R.F., McCorkle, S.M.: Astron. J. **94**, 972 (1987)
Luna, R., Millan, C., Domingo, M., Santonja, C., Satorre, M.A.: Vacuum. **122**, 154 (2015)
Luna, R., Luna-Ferrandiz, R., Satorre, M.A., et al.: Astrophys. J. **852**(1), 51 (2017)
Martín-Doménech, R., Muñoz Caro, G.M., Bueno, J., Goesmann, F.: Astron. Astrophys. **564**, A8 (2014)
Muñoz Caro, G.M., Jiménez-Escobar, A., Martín-Gago, J.A., et al.: Astron. Astrophys. **522**, A108 (2010)
Noble, J., Congiu, E., Dulieu, F., Fraser, H.J.: Mon. Not. R. Astron. Soc. **421**, 768 (2012)
Notesco, G., Bar-Nun, A.: Icarus. **148**, 456 (2000)
Nummelin, A., Whittet, D.C.B., Gibb, E.L., Gerakines, P.A., Chiar, J.E.: Astrophys. J. **558**, 185 (2001)
Öberg, K.I., Fayolle, E.C., Cuppen, H.C., et al.: Astron. Astrophys. **505**, 183 (2009)
Polanyi, M., Wigner, E.Z.: Physik. **33**, 429 (1925)
Pontoppidan, K.M., Boogert, A.C.A., Fraser, H., et al.: Astrophys. J. **678**, 1005 (2008)
Qi, C., Öberg, K.I., Wilner, D.J., et al.: Science. **341**(6146), 630 (2013)
Sandford, S.A., Allamandola, L.J.: Astrophys. J. **355**, 357 (1990)
Sandford, S.A., Allamandola, L.J., Tielens, A.G.G.M., Valero, G.J.: Astrophys. J. **329**, 498 (1988)
Smith, R.S., Huang, C., Wong, E.K.L., Kay, B.D.: Phys. Rev. Lett. **79**, 909 (1997)
Smith, R.S., May, R.A., Kay, B.D.: J. Phys. Chem. B. **120**, 1979 (2016)
van Dishoeck, E.F.: Proc. Natl. Acad. Sci. **103**, 12249 (2006)
Viti, S., Collings, M.P., Dever, J.W., McCoustra, M.R.S.: Mon. Not. R. Astron. Soc. **354**, 1141 (2004)
Wakelam, V., Caselli, P., Ceccarelli, C., Herbs, E., Castets, A.: Astron. Astrophys. **422**, 159 (2004)
Zasowski, G., Kemper, F., Watson, D.M., et al.: Astrophys. J. **694**, 459 (2009)

Chapter 9
Photon-Induced Desorption Processes in Astrophysical Ices

Guillermo M. Muñoz Caro and Rafael Martín Doménech

Abstract This chapter presents the photon-induced desorption processes in interstellar ice analogs simulated in dedicated laboratory experiments. In dense interstellar clouds, most molecules are expected to accrete on dust grains and remain frozen. The observed gas-phase abundances of certain molecules like carbon monoxide in dense clouds suggest that a non-thermal desorption mechanism is active in ice mantles. In addition to chemical desorption and direct cosmic-ray bombardment of the ice, photon-induced desorption is expected to drive the expected non-thermal desorption. Well inside the cloud, ice mantles are processed by the secondary-UV field generated by cosmic-ray excitation of molecular hydrogen. Because the photodesorption of volatiles like CO is less efficient in water-dominated ices, we introduce another type of photon-induced desorption, i.e., the photochemical desorption, which consists in the inmediate desorption of new molecules triggered by photons after their formation on the ice surface. Photochemical desorption operates in multi-component ice mixtures and can therefore play an important role in the real astrophysical scenario.

9.1 Introduction

The recent interest in the astronomical community for photon-induced desorption processes was triggered by the publication of a work that reported a significant desorption rate of molecules during the irradiation of pure CO ice (Öberg et al. 2007a, b). It was earlier proposed as a non-thermal desorption mechanism that

G. M. Muñoz Caro (✉)
Centro de Astrobiología, INTA-CSIC, Torrejón de Ardoz, Madrid, Spain
e-mail: munozcg@cab.inta-csic.es

R. Martín Doménech
Harvard-Smithsonian Center for Astrophysics, Cambridge, MA, USA

G. M. Muñoz Caro, R. Escribano (eds.), *Laboratory Astrophysics*,
Astrophysics and Space Science Library 451,
https://doi.org/10.1007/978-3-319-90020-9_9

could account for the observed abundances of certain molecules like CO in very cold astrophysical environments. In particular, dense cloud interiors shielded from the external UV field and cold regions in circumstellar disks with temperatures as low as 10 K, lead to an efficient accretion of all the molecules in the gas, except H_2, forming ice mantles. For the typical lifetime of these objects, all the molecules are expected to accrete on dust grains, unless a non-thermal desorption process is at work. In addition to photon-induced desorption, direct cosmic-ray bombardment of icy dust is expected to drive the non-thermal desorption. In fact, due to the low penetration depth of ultraviolet (UV) photons, only the outskirts of dense clouds are fully processed by UV; well inside the cloud, ice mantles are processed by the secondary-UV field generated by cosmic-ray excitation of molecular hydrogen. The direct impact of cosmic rays on icy dust is expected to desorb volatiles significantly (Dartois et al. 2015), while X-rays could also contribute to the desorption of ice mantles in circumstellar regions around young stars. Release of chemical energy was also proposed as a non-thermal desorption mechanism (e.g., Garrod et al. 2007).

9.2 Experimental Methods

9.2.1 Experimental Setup

The study of photodesorption requires an ultra-high vacuum system (with a base pressure in the 10^{-10}–10^{-11} mbar range) to maintain the ice sample surface clean from background accretion of water, and other volatile contaminants in the chamber, during the irradiation process. The optimum vacuum conditions also favor the identification of desorbed molecules in the gas, using mass spectrometry, and the detection of a decrease in the initial molecular ice abundances due to desorption or formation of photoproducts, monitored by infrared (IR) spectroscopy. The ice samples are grown by deposition of gas onto a cold substrate at about 10 K. An infrared transparent window composed of KBr or CsI acts as the deposition substrate if IR spectroscopy in transmission is performed (Muñoz Caro et al. 2010, 2016; Yuan and Yates 2013, 2014; Cruz-Díaz et al. 2016, 2018; Chen et al. 2014; Martín-Doménech et al. 2015, 2016, 2018); in the reflexion–absorption (RAIRS) experiments the substrate is a reflecting metal surface like Au (Öberg et al. 2007a, b, 2009a, b; Fayolle et al. 2011, 2013; Bertin et al. 2013, 2016; Fillion et al. 2014; Dupuy et al. 2017a,b). Other authors use a microbalance to measure the ice weight during the irradiation (Westley et al. 1995; Bahr and Baragiola 2012). Usually a quadrupole mass spectrometer (QMS) is used to detect the molecules in the gas phase, although resonance enhanced multiphoton ionization (REMPI) was also employed (Yabushita et al. 2009).

9.2.2 Experimental Techniques

The experimental techniques used in photodesorption experiments are those commonly employed for the study of astrophysical ice analogs. It is therefore worth to describe in more detail the methodology that allows a quantification of the ice properties and the radiation-induced processes.

IR spectroscopy in transmittance of the ice sample allows the most straightforward estimation of the column density for the molecular ice components by integration of the absorption bands, using the formula

$$N = \left(\frac{1}{A}\right) \int \tau\,(\nu)\; d\nu \tag{9.1}$$

where N is the ice column density in molecules cm^{-2}, $\tau(\nu)$ the optical depth of the band, $d\nu$ the wavenumber differential in cm^{-1}, and A the band strength in cm molecule^{-1}. The integrated absorbance is equal to 0.43 τ, where τ is the integrated optical depth of the band. In the case of pure solid CO, the band strength is $A(\mathrm{CO}) = 1.1 \times 10^{-17}$ cm molecule^{-1} (Jiang et al. 1975).

The VUV-source used routinely in these experiments is a microwave-stimulated hydrogen flow discharge lamp (MDHL) that provides a flux of about 10^{14} photons cm^{-2} s^{-1} at the sample position with average photon energy of 8.6 eV. The characterization of the MDHL spectrum was previously reported (Cruz-Diaz et al. 2014a) and was discussed in more detail by Chen et al. (2014). The VUV spectrum is measured during the experiments with a VUV monochromator equipped with a photomultiplier tube. The VUV absorption spectrum of the ice samples deposited at different temperatures is the difference of the cold substrate spectra before and after ice deposition. In combination with the ice column density value measured with IR spectroscopy, this method allows the estimation of the VUV absorption cross sections of the ice analogs, σ in cm^2, using equation

$$\sigma\,(\lambda) = -\frac{1}{N} \ln\left(\frac{I_t\,(\lambda)}{I_0\,(\lambda)}\right) \tag{9.2}$$

where $I_t(\lambda)$ is the transmitted intensity for a given photon of wavelength λ, $I_0(\lambda)$ the incident intensity, and N is the ice column density. For more details on the experimental protocol employed for VUV spectroscopy, see Cruz-Diaz et al. (2014a). This procedure leads to the measurement of VUV absorption cross sections on an everyday basis with no need to use a synchrotron facility for the same purpose.

The direct detection of molecules desorbing to the gas phase can be performed using a QMS installed on the vacuum ice chamber. Calibration of this technique is based on the CO ice photodesorption experiment, where the desorption rate is estimated using the IR spectrometer, and hence a proportionality constant is estimated to convert the QMS intensity of the CO signal into the number of desorbing molecules per unit of irradiation time. This proportionality constant of

CO is then used to obtain a similar constant for other species desorbing during the irradiation of different ice samples (Martín-Doménech et al. 2015).

9.3 Experimental Results

There are two categories of molecular ice components, depending on whether their energy of dissociation, E_d, falls above or below the incident photon energy, E_{ph}. Except CO and N_2, molecules in astrophysical ice analogs become efficiently dissociated by the hydrogen lamp acting as a continuum VUV source with $E_{ph} < 11$ eV; these species include H_2O, CO_2, CH_3OH, NH_3, etc. If direct dissociation of the molecules is allowed, photodesorption of the starting ice species displays a low efficiency, while some of their photoproducts can desorb during the irradiation; it was observed that there are two different desorption patterns of photoproducts. Of course, only the fraction of photons absorbed in the ice can lead to desorption. If the absorption cross-section of the ice is known in the VUV, it is possible to estimate the desorption rate as the number of desorbed molecules per absorbed photon in the ice. The temperature of ice deposition can affect the photodesorption rate quite significantly; its influence will be discussed below for the case of CO ice.

9.3.1 Photodesorption of Molecules in the Absence of Dissociation: The Case of CO Ice

Carbon monoxide deposited as pure solid offers an excellent test case to study photodesorption. The decrease of the CO ice column density is mainly driven by the photodesorption of CO molecules, since typically no more than 5% of the UV photons absorbed in the ice leads to product formation in these experiments (Muñoz Caro et al. 2010). A more detailed study of the formation of CO_2 during solid CO irradiation is that of Chen et al. (2014). The CO ice column density obtained from Eq. (9.1) is often expressed as the number X of ice monolayers (ML), where 1 ML is defined as 1×10^{15} molecules cm^{-2} and, therefore, $N = 10^{15}\,X$ molecules cm^{-2}. The decrease of the CO ice column density is linear with VUV fluence until about 5 ML of ice are left on the substrate, i.e., the photodesorption yield is constant in this regime; see middle panel of Fig. 9.1 (Muñoz Caro et al. 2010; Fayolle et al. 2011; Chen et al. 2014; Muñoz Caro et al. 2016). The slope of the linear fit provides an estimate of the photodesorption rate in the constant desorption regime; this value is 3.5×10^{-2} or 8.9×10^{-2} CO molecules per incident VUV photon. These values differ by a factor of 2.55, which is exactly the difference in the VUV flux values of the hydrogen F-type lamp estimated using two different methods, 2.5×10^{14} and 9.8×10^{13} photons cm^{-2} s^{-1}, respectively (Muñoz Caro et al. 2010 used actinometry to estimate the UV flux; Chen et al. 2014 used a Ni-mesh). Later, the

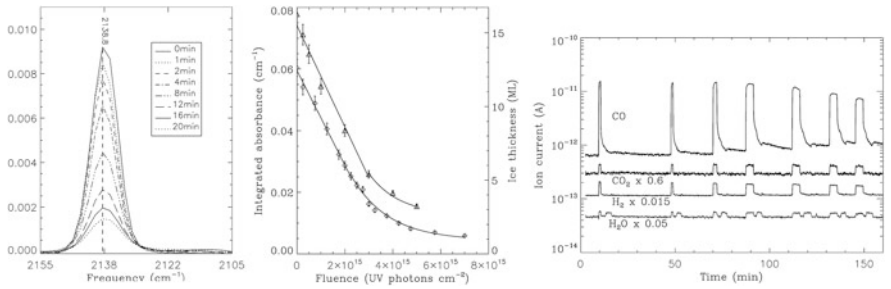

Fig. 9.1 Left: Decrease of the infrared absorption band in pure CO ice for various irradiation intervals. Middle: Integrated absorbance values of these bands as a function of UV fluence. Right: Increase of the partial gas pressures measured by QMS at various irradiation intervals during the same experiment. Adapted from Muñoz Caro et al. (2010)

use of the same Ni-mesh led to the same value of the UV flux in both laboratories, which means that they measured the same CO photodesorption yield. The constant photodesorption rate starts to decrease exponentially for X below 5 ML, as the IR and QMS data show in Fig. 9.1. The following equations provide a fit of the consecutive data points in the middle panel of Fig. 9.1:

$$N(i) = N\,(i-1) - R_{ph-des}\,(X \;<\; 5ML)\,(i-1) \times (t\,(i) - t\,(i-1))\,, \quad (9.3)$$

where t is the irradiation time and $R_{ph\,-\,des}(X \;<\; 5ML)$ is the photodesorption rate in molecules cm^{-2} s^{-1}, which depends on the number of photons absorbed as a function of the decreasing ice column density N during irradiation, and

$$\begin{aligned} R_{ph-des}\,(X \;<\; 5ML) &= (I_0 - I) \times QY = I_0 \times \left(1 - \frac{I}{I_0}\right) \times QY \\ &= I_0 \times \left(1 - k \times e^{-\sigma N}\right) \times QY, \end{aligned} \quad (9.4)$$

where $I_0 = 2.5 \times 10^{14}$ photons cm^{-2} s^{-1} is the VUV flux at the sample position. The value of the VUV-absorption cross-section is $\sigma = 4.7 \times 10^{-18}$ cm^2 for the average photon energy (8.6 eV) of the VUV lamp; this energy falls within the absorbing spectral region of CO ice (Cruz-Diaz et al. 2014a). The quantum yield value, QY, at 8 K is 2.24 desorbing molecules per absorbed photon in the top 5 ML. The dimensionless k parameter is unity in the analytical expression and it was introduced to improve the fit; for instance, a k value of 1.0045 was used to fit the data in the experiment performed at 8 K (Muñoz Caro et al. 2016).

The interpretation of the results in the CO ice irradiation experiment indicate that only the VUV photons absorbed in the top 5 ML of the ice participate in the photodesorption. Therefore, a CO molecule below the ice surface that was excited

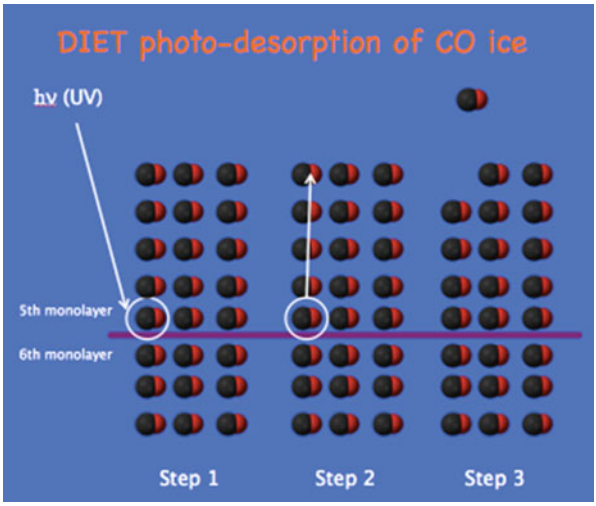

Fig. 9.2 Schematic representation of DIET photodesorption in pure CO ice. In step 1 the photon is absorbed by a molecule in the top five monolayers. During step 2 the energy is transmitted to neighboring molecules. After step 3 a molecule on the ice surface received sufficient energy to allow desorption from the ice

by a photon must transfer a fraction of the absorbed photon energy to neighboring molecules, and eventually a molecule on the surface will receive enough energy to desorb. For the emission spectrum of the VUV lamp and the case of CO ice, this transmission of energy is only sufficient in the top 5 ML to allow photodesorption (Muñoz Caro et al. 2010; Fayolle et al. 2011; Chen et al. 2014; Muñoz Caro et al. 2016). This process is often called desorption induced electronic transition (DIET) and is depicted schematically in Fig. 9.2. It was found that the photodesorption rate of solid CO measured at a specific monochromatic wavelength of the VUV photons is strongly related to the absorption at the same photon wavelength, thus providing a strong evidence for the DIET mechanism (Fayolle et al. 2011). The indirect desorption of DIET was further explored in experiments where two different species were deposited in the ice, e.g. CO and N_2. It was observed that the photodesorption of CO and N_2 in binary ices depends on the absorption spectra of the dominant species in the sub-surface ice layer (Bertin et al. 2013).

It was found that the UV absorption bands of CO ice are shifted as a function of deposition temperature. It therefore appears that the CO dipole orientation changes for increasing deposition temperature while the spontaneously generated electric field in the ice decreases. During CO ice irradiation, electron-hole pairs of sizes up to 5 nm can be approached as units weakly bound by Coulomb attraction, known as Wannier-Mott excitons. The electric field causes the electron to move in one direction and the hole in the opposite, causing the band shifts in the UV spectra (Chen et al. 2017).

9.3.2 *Photodesorption of Molecules in the Presence of Dissociation: The Case of CO_2 and CH_3OH Ice*

Most molecular ice components in astrophysical ice analogs are, either efficiently photodissociated, or not active in the infrared. These species include CH_3OH, CO_2, O_2, CH_4, NH_3, etc. Their photon-induced desorption is at least two orders of magnitude lower than that of CO. On the other hand, their photoproducts were found to desorb during irradiation. Figure 9.3 represents the two patterns observed by QMS that lead to the photon-induced desorption of photoproducts. These different trends in the desorption are characterized by a) an increasing desorption up to a maximum value as the ice bulk concentration of the product grows, probably driven by an indirect mechanism like the DIET mentioned above, and b) a constant desorption that is explained by formation on the ice surface and immediate desorption, since there is no dependency with the concentration of these species in the ice bulk; this effect was abbreviated to photochemidesorption (Martín-Doménech et al. 2015, 2016; Cruz-Díaz et al. 2016). Both types of desorption are illustrated in Figs. 9.4 and 9.5.

The pure CO_2 ice irradiation experiment involves the formation of a reduced number of photoproducts; in order of decreasing abundance CO, CO_3, O_2, and O_3 were observed (Bahr & Baragiola 2012; Martín-Doménech et al. 2015). Photon-induced desorption of CO and, to a lesser extent, O_2 took place through the DIET process, leading to an increasing desorption with fluence, with maximum

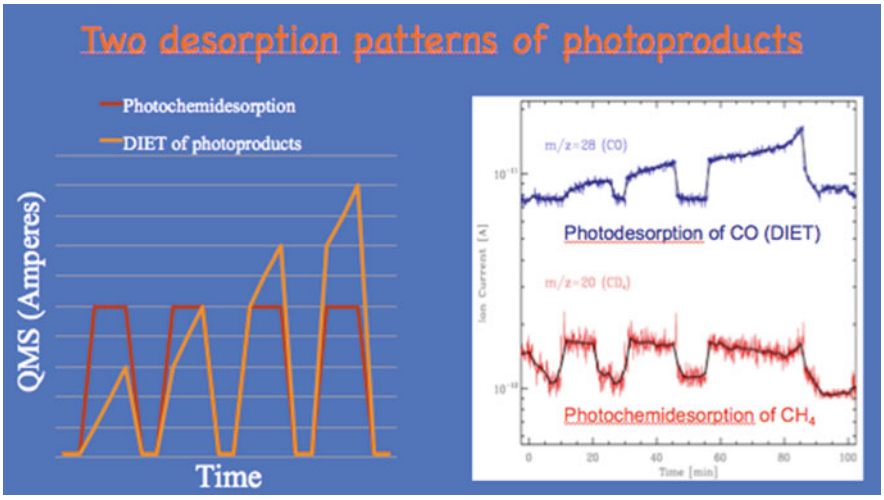

Fig. 9.3 The desorption patterns observed by QMS during ice irradiation. The constant signal is attributed to immediate desorption of species formed on the ice surface, while the cumulative desorption signal was associated to the desorption of products formed in the ice bulk. The inlet corresponds to the desorption of CO, following a DIET photodesorption, and CH_4 photochemidesorption, during irradiation of pure CH_3OH ice. Adapted from Cruz-Díaz et al. (2016)

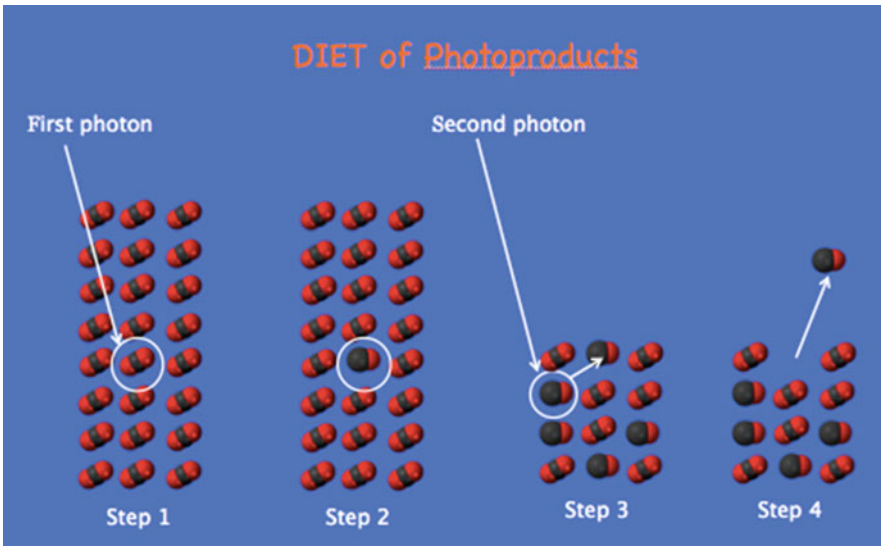

Fig. 9.4 The desorption of CO formed during irradiation of pure CO_2 ice appears to follow the DIET mechanism. A molecule in the ice bulk is photoprocessed and, after removal of the above ice monolayers during irradiation, the product will be eventually exposed on the ice surface. Finally, a second photon leads to desorption of the product molecule

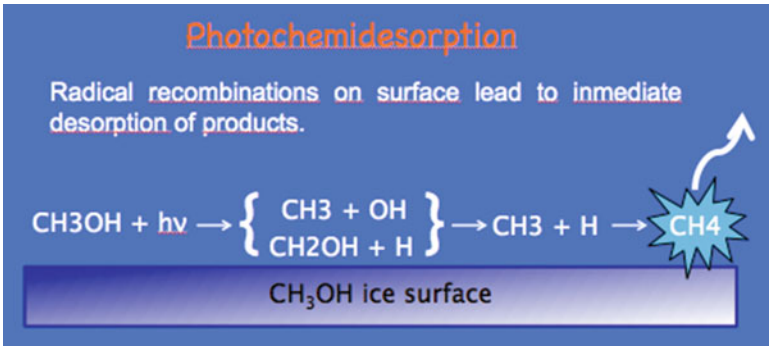

Fig. 9.5 The constant desorption of the CH_4 photoproduct, during irradiation of pure CH_3OH ice, is probably the result of radical recombinations on the ice surface. The excess energy overcomes the binding energy and the new molecule desorbs immediately after its formation

photodesorption yields of $\sim 1.2 \times 10^{-2}$ and $\sim 9.3 \times 10^{-4}$ molecules per incident photon, respectively. The observed photodesorption yield of the initial component, CO_2, is very low, about 1.1×10^{-4} molecules per incident photon. Only 4% of the CO molecules formed were found to desorb after a VUV fluence similar to the one expected by ice mantles during the dense interstellar cloud lifetime (Martín-Doménech et al. 2015).

The irradiation of pure methanol, CH_3OH, ice did not lead to a significant photodesorption of this molecule (Bertín et al. 2016; Cruz-Díaz et al. 2016). Instead, several new species were found to desorb during irradiation, either via DIET as it is the case of molecules like CO formed in the ice bulk, or by photochemidesorption on the ice surface as it was the case of CH_4. The photon-induced desorption of methanol molecules formed in ice mixtures, such as CH_4:H_2O, did not lead to a non-thermal desorption of methanol (Martín-Doménech et al. 2016); in this experiment the desorption of formaldehyde (H_2CO) during irradiation was observed. To date, there is no explanation for the observed gas abundances of CH_3OH toward cold interstellar regions.

9.3.3 The Effect of Ice Absorption on the Photodesorption Rate

There is a clear correspondence between the photodesorption rates measured for different monochromatic photon energies and the VUV absorption spectrum for the same photon energies. This indicates that photodesorption of some ice species like N_2 and CO is mainly driven by a desorption induced by electronic transition (DIET) process (Fayolle et al. 2011, 2013). The photodesorption rate of an ice, expressed in photodesorbed molecules per incident photon, will depend on the ice thickness. It is therefore more relevant to estimate the photodesorption rate as the number of photodesorbed molecules per absorbed photon.

The VUV-photoabsorption of the molecular ice components has been also measured to estimate the absorption cross sections of pure ices. This allows the estimation of the photodesorption rates as the number of photodesorbed molecules per absorbed photon in the ice. The photodesorption rate per absorbed photon for the UV field present in interstellar regions, or the emission range of the UV lamp in the simulation experiments, R^{abs}_{ph-des},can be estimated as follows

$$R^{abs}_{ph-des} = \frac{I_0}{I_{abs}} R^{inc}_{ph-des}, \tag{9.5}$$

where R^{inc}_{ph-des} is the photodesorption rate per incident photon in the ice and

$$I_{abs} = \sum_{\lambda_i}^{\lambda_f} I_0\,(\lambda) - I\,(\lambda) = \sum_{\lambda_i}^{\lambda_f} I_0\,(\lambda)\left(1 - e^{-\sigma(\lambda)N}\right) \tag{9.6}$$

where I_0 is the total photon flux emitted (in photons cm^{-2} s^{-1}), I_{abs} is the total photon flux absorbed by the ice, $I_0(\lambda)$ is the photon flux emitted at wavelength λ, $\sigma(\lambda)$ is the VUV-absorption cross-section at the same wavelength, and N is the column density of the ice sample. Therefore, if the VUV-absorption cross-section of a certain ice composition is known, it is possible to know what the efficiency of the photodesorption per absorbed photon is. In the case of N_2 and CO ices, for

VUV photon energies that do not lead to direct dissociation of these molecules in the ice, these values are higher than unity. For this reason, the VUV-absorption cross-sections of the common molecular ice components were estimated (Cruz-Díaz et al. 2014a, b, c).

The values of $R_{ph-des}^{abs} > 1$ and the fact that the photons absorbed deeper than the top ice monolayer (up to five monolayers for CO) can lead to a photodesorption event, indicate that the excess photon energy is transmitted to neighboring molecules in the ice within a certain range (we mentioned above that this range may indeed correspond to about five monolayers in the case of CO ice); if a molecule on the ice surface gains sufficient energy from a molecule that received a photon, it may photodesorb (e.g., Muñoz Caro et al. 2010).

9.3.4 *The Effect of Ice Deposition Temperature on the Photodesorption Rate*

The CO ice irradiation temperature does not affect the photodesorption yield; only the temperature of CO ice deposition plays a role in the photodesorption, since the estimated photodesorption was inversely proportional to the deposition temperature in the 15–27 K range (Öberg et al. 2009b).

Figure 9.6 represents the decrease of the CO ice IR absorption as a function of UV fluence for two ice samples deposited at 8 K and 20 K. In the linear

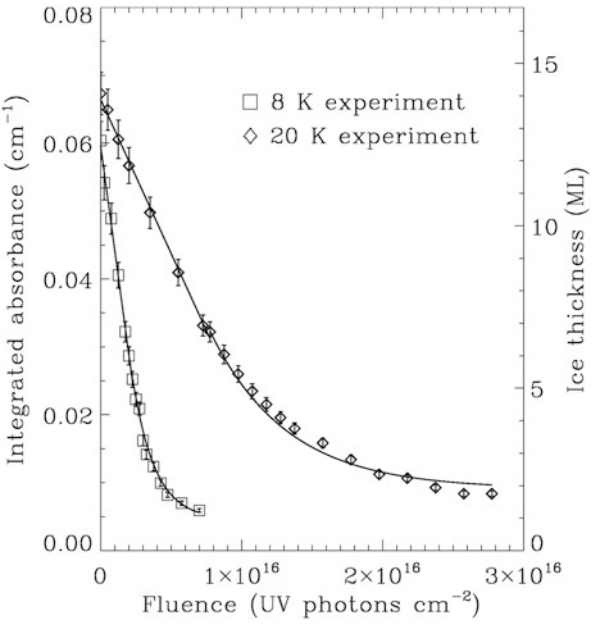

Fig. 9.6 Decrease of the integrated infrared absorption area in pure CO ice as a function of increasing UV fluence. Adapted from Muñoz Caro et al. (2016)

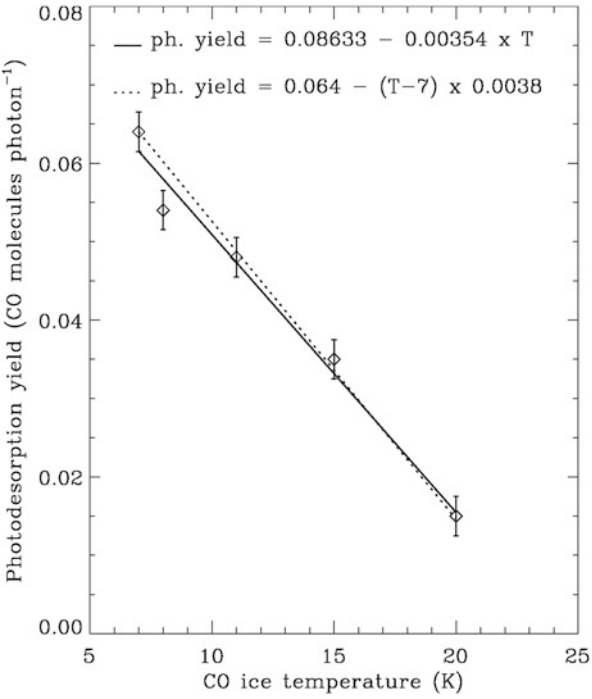

Fig. 9.7 Linear dependence of the pure CO photodesorption rate with the deposition temperature of the ice. Adapted from Muñoz Caro et al. (2016)

regime, the difference in the slope indicates that the photodesorption rate varies very significantly; it is about 3.4 times lower at 20 K. In both experiments, the transition from a constant value to an exponential decrease in the photodesorption occurs when the ice thickness is equivalent to about five monolayers (Muñoz Caro et al. 2016).

Figure 9.7 displays the photodesorption yield values with estimated error bars, in molecules per incident photon for $X > 5$ ML, measured in several irradiation experiments where the CO ice samples were deposited at different temperatures of 7, 8, 11, 15, and 20 K, respectively. The linear equation that provides the best fit for the photodesorption yield as a function of CO ice deposition temperature T is included in this figure (solid line), while the dotted line is an alternative fit.

9.4 A Simple Model of Ice Accretion, Thermal and Photo-desorption in a Dense Interstellar Cloud

The model presented in this section is applicable to pure CO ice, but the same expressions of the accretion and desorption also hold for other species present in astrophysical ices, except for the photodesorption rate. The rates of photon-induced desorption for other molecules and the different desorption patterns are discussed

in Sect. 9.3. The rates for the accretion $R_{acc}(CO)$, thermal desorption $R_{th-des}(CO)$, and photodesorption $R_{ph-des}(CO)$, can be estimated as a function of time using the equations provided below. In the case of quiescent dark cloud interiors, where no processing by external UV flux occurs, the UV photon flux value induced by cosmic rays is of $F{\sim}1 \times 10^4$ photons cm^{-2} s^{-1}. The initial cloud parameters are typically: $T_{gas} = T_{dust}{\sim}10$K are the gas and dust temperatures, $n_H = 1 - 3 \times 10^4$ cm^{-3}, and $n_{CO} = 9.5 \times 10^{-5} n_H$ are the densities of H and CO. The masses of H and CO in grams are m_H and m_{CO}, and $m_{CO}(amu) = 28$ *amu* for CO. A dust density of $n_{dust} = (0.01 \times n_H \times m_H)/(1.33 \times \pi \times \rho \times r^3) = 1.33 \times 10^{-12} n_H$ dust grains is often assumed, with a constant radius $r = 0.05 \times 10^{-4}$ cm and density $\rho = 3$ g cm^{-3} (silicate core density). The sticking probability near 10 K is expected to be close to unity, $f = 1$. The rate of ice mantle build-up is

$$\frac{dn_s(CO)}{dt} = R_{acc}(CO) - R_{th-des}(CO) - R_{ph-des}(CO) \tag{9.7}$$

The accretion rate of CO molecules onto grains is given by

$$R_{acc}(CO) = n_g(CO) \times n_{dust} \times \pi \times r^2 \times \sqrt{\frac{3kT_{gas}}{m_{CO}}} \times f \tag{9.8}$$

in molecules cm^{-3} s^{-1}, where k is the Boltzmann constant.

The thermal desorption of CO is given by the well-known Polanyi–Wigner equation, multiplied by the dust density and the surface of a spherical dust grain:

$$R_{th-des}(CO) = \nu_0(CO) \times e^{-E_d(CO)/T_{dust}} \times n_{dust} \times 4 \times \pi \times r^2 \tag{9.9}$$

in molecules cm^{-3} s^{-1}, with $\nu_0(CO) = 6.5 \times 10^{26}$ molecules cm^{-2} s^{-1} and $E_d(CO) = 834$K.

At temperatures near 10 K, $R_{th-des}(CO) = 0$, and therefore $R_{ph-des}(CO)$ drives the desorption. Based on laboratory results, for ice thicknesses $X = n_s(CO)(t)/(10^{15}\ n_{dust}\ 4\ \pi\ r^2) < 5M$, where $n_s(CO)(t) = n_g$ (CO)(0)$-n_g$ (CO)(t), the photodesorption rate can be expressed as

$$R_{ph-des}\ (X < 5ML)\ (CO) = F \times \left(1 - e^{-\sigma N}\right) \times QY \times n_{dust} \times \pi \times r^2, \tag{9.10}$$

in molecules cm^{-3} s^{-1}, and for $X \geq 5$ ML where $R_{ph-des}(CO)$ is constant, we have that

$$R_{ph-des}\ (X \geq 5ML)\ (CO) = F \times \left(1 - e^{-\sigma \times 5 \times 10^{15}}\right) \times QY \times n_{dust} \times \pi \times r^2, \tag{9.11}$$

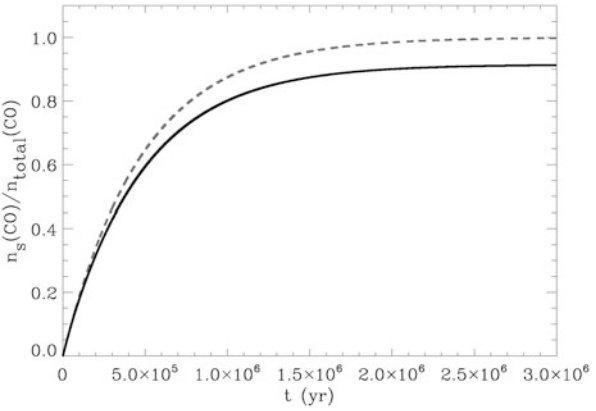

Fig. 9.8 CO ice mantle build-up during the lifetime of the cloud for a cloud density of 1×10^4 cm^{-3}, gas and dust temperatures of $T_{gas} = T_{dust} = 7$ K. The dashed line is when no photodesorption takes place, only accretion, while the solid line corresponds to a photodesorption rate balancing the accretion rate. Adapted from Muñoz Caro et al. (2010)

in molecules cm^{-3} s^{-1}. Here F is the UV flux in photons cm^{-2} s^{-1}, N is the ice column density, and QY is the quantum yield, i.e. the number of photodesorbed molecules per incident UV photon. For more details, we refer to the original publication (Muñoz Caro et al. 2010).

Figure 9.8. reproduces the calculated CO ice mantle build-up as the fraction of molecules depleted in the ice relative to the total number of CO molecules per unit volume in the cloud. According to this simple estimation, the secondary VUV flux inside the cloud could account for about 9% of the total number of CO molecules in the gas-phase after 2.5 million years, and the remaining 91% would remain frozen in the ice mantles (Muñoz Caro et al. 2010).

9.5 Conclusions

In recent years, various experimental studies of photon-induced processes in astrophysical ice analogs have demonstrated that this mechanism could contribute to explain the observed gas-phase abundances of certain molecules like CO toward very cold regions in dense clouds or circumstellar environments where thermal desorption is not active. In addition to energetic photons, cosmic rays are also expected to trigger the ejection of molecules from the ice and will be further explored in the laboratory in the coming years. Such study was performed for water ice exposed to swift heavy ions (Dartois et al. 2015). In circumstellar regions, X-rays are expected to drive the photodesorption, and we wait for experimental evidence of this process. While most of the experimental work was so far dedicated to pure ices or binary mixtures, in space the different molecular ice components can be mixed and embedded in the water-dominated ice mantles. Even the efficient photodesorption of pure CO ice becomes very significantly reduced when CO is mixed with water in the ice. Fortunately, photochemidesorption, i.e. the immediate desorption of molecules triggered by a photon after their formation on the ice

surface, operates in multi-component ice mixtures and can therefore play an important role in the real astrophysical scenario. The observed presence of methanol in the gas toward cold environments remains a mystery since no efficient photon-induced desorption of methanol was reproduced in the laboratory. Here chemical desorption might enhance the methanol abundances in the gas. Future work should aim to combine the experimental data on photodesorption with the observational evidence from cold regions with a significant UV field where gas-phase molecules were detected. In addition to the accretion and desorption of molecules from the ice, briefly elucidated in Sect. 9.4 for the simple case of CO, models reproducing these scenarios also need to incorporate other parameters, in particular the reactivity and destruction cross-sections of these species during their residence time in the gas phase.

References

Bahr, D.A., Baragiola, R.A.: Astrophys. J. **761**, 36 (2012)
Bertin, M., Fayolle, E.C., Romanzin, C., Poderoso, H.A.M., Michaut, X., Philippe, L., Jeseck, P., Öberg, K.I., Linnartz, H., Fillion, J.-H.: Astrophys. J. **779**, id. 120 (2013)
Bertin, M., Romanzin, C., Doronin, M., Philippe, L., Jeseck, P., Ligterink, N., Linnartz, H., Michaut, X., Fillion, J.-H.: Astrophys. J. Lett. **817**, L12 (2016)
Chen, Y.-J., Chuang, K.-J., Muñoz Caro, G.M., et al.: Astrophys. J. **781**, 15 (2014)
Chen, Y.-J., Muñoz Caro, G.M., Aparicio, S., et al.: Phys. Rev. Lett. **157703**, 119 (2017)
Cruz-Diaz, G.A., Muñoz Caro, G.M., Chen, Y.-J., Yih, T.-S.: Astron. Astrophys. **562**, A119 (2014a)
Cruz-Diaz, G.A., Muñoz Caro, G.M., Chen, Y.-J., Yih, T.-S.: Astron. Astrophys. **562**, A120 (2014b)
Cruz-Diaz, G.A., Muñoz Caro, G.M., Chen, Y.-J.: Mon. Not. R. Astron. Soc. **439**, 2370 (2014c)
Cruz-Díaz, G.A., Martín-Doménech, R., Muñoz Caro, G.M., Chen, Y.-J.: Astron. Astrophys. **592**, A68 (2016)
Cruz-Díaz, G.A., Martín-Doménech, R., Moreno, E., Muñoz Caro, G.M., Chen, Y.-J.: Mon. Not. R. Astron. Soc. **474**, 3080 (2018)
Dartois, E., Augé, B., Boduch, P., et al.: Astron. Astrophys. **576**, A125 (2015)
Dupuy, R., Bertin, M., Féraud, G., et al.: Astron. Astrophys. **603**, A61 (2017a)
Dupuy, R., Féraud, G., Bertin, M., et al.: Astron. Astrophys. **606**, A9 (2017b)
Fayolle, E.C., Bertin, M., Romanzin, C., et al.: Astrophys. J. Lett. **739**, L36 (2011)
Fayolle, E.C., Bertin, M., Romanzin, C., et al.: Astron. Astrophys. **556**, A122 (2013)
Fillion, J.-H., Fayolle, E., Michaut, X., et al.: Faraday Discuss. **168**, 533 (2014)
Garrod, R.T., Wakelam, V., Herbst, E.: Astron. Astrophys. **467**, 1103 (2007)
Jiang, G.J., Person, W.B., Brown, K.G.: J. Chem. Phys. **62**, 1201 (1975)
Martín-Doménech, R., Manzano-Santamaría, J., Muñoz Caro, G.M., Cruz-Díaz, G.A., Chen, Y.-J., Herrero, V.J., Tanarro, I.: Astron. Astrophys. **584**, id.A14 (2015)
Martín-Doménech, R., Muñoz Caro, G.M., Cruz-Diaz, G.A.: Astron. Astrophys. **589**, id.A107 (2016)
Martín-Doménech, R., Cruz-Diaz, G.A., Muñoz Caro, G.M.: Mon. Not. R. Astron. Soc. **473**, 2575 (2018)
Muñoz Caro, G.M., Jiménez-Escobar, A., Martín-Gago, J.Á., et al.: Astron. Astrophys. **522**, A108 (2010)

Muñoz Caro, G.M., Chen, Y.-J., Aparicio, S., Jiménez-Escobar, A., Rosu-Finsen, A., Lasne, J., McCoustra, M.R.S.: Astron. Astrophys. **589**, id.A19 (2016)
Öberg, K.I., Fuchs, G.W., Awad, Z., Fraser, H.J., Schlemmer, S., van Dishoeck, E.F., Linnartz, H.: Astrophys. J. **662**, L23 (2007a)
Öberg, K.I., Fuchs, G.W., Awad, Z., et al.: Astrophys. J. **662**, L23 (2007b)
Öberg, K.I., Garrod, R.T., van Dishoeck, E.F., Linnartz, H.: Astron. Astrophys. **504**, 891 (2009a)
Öberg, K.I., van Dishoeck, E.F., Linnartz, H.: Astron. Astrophys. **496**, 281 (2009b)
Westley, M.S., Baragiola, R.A., Johnson, R.E., Baratta, G.A.: Nature. **373**, 405 (1995)
Yabushita, A., Hama, T., Yokoyama, M., Kawasaki, M., Andersson, S., Dixon, R.N., Ashfold, M.N.R., Watanabe, N.: Astrophys. J. **699**, L80 (2009)
Yuan, C., Yates Jr., J.T.: J. Chem. Phys. **138**, 154303 (2013)
Yuan, C., Yates Jr., J.T.: Astrophys. J. **780**, 8 (2014)

Chapter 10
Thermal Reactivity Dynamics in Interstellar Ice

Patrice Theulé, Jennifer A. Noble, and Pierre Ghesquière

Abstract Ever more complex organic molecules are being observed in space. Star forming regions, planets and small bodies in our solar system exhibit a rich molecular diversity which culminates in the diverse molecular composition of meteorites. While many complex organic molecules can be formed through gas-phase reactions, solid-state chemistry on interstellar grains plays an important role. In this chapter, we discuss the specific case of purely thermal reactions in ice mantles, which do not require any extra energy input other than thermal energy. Thermal reactions are important because they are not limited by UV or cosmic rays fluxes or the scarcity of radicals on the surface because they involve only dominant mantle molecules. Thermal reactions represent an important step in the formation of complex organic molecules that constitute the primitive material of comets and asteroids.

10.1 Introduction

Radio observations have reported an ever increasing molecular diversity in the interstellar medium (ISM), in the circumstellar medium, and in comets (Herbst and van Dishoeck 2009; Delsemme 1983), with new interstellar complex organic molecules (iCOMs) being detected every year in the ISM (Müller et al. 2005). High abundances of COMs are observed, particularly in hot cores and hot corinos (Herbst and van Dishoeck 2009; Bacmann et al. 2012), associated with high- and

P. Theulé (✉)
Aix-Marseille Université, PIIM UMR-CNRS 7345, Marseille, France
e-mail: patrice.theule@univ-amu.fr

J. A. Noble
Université Lille 1 Sciences Technologies, PHLAM UMR-CNRS 8523, Villeneuve d'Ascq, France

P. Ghesquière
Université de Bourgogne Franche-Comté, LICB UMR-CNRS 6303, Dijon, France

G. M. Muñoz Caro, R. Escribano (eds.), *Laboratory Astrophysics*,
Astrophysics and Space Science Library 451,
https://doi.org/10.1007/978-3-319-90020-9_10

low-mass star formation, respectively. Recent space missions to solar system bodies also reported the abundances of several COMs, for example the Cassini-Huygens mission (Gudipati et al. 2015; Postberg et al. 2017). Even amino acids have been found in Solar System bodies and meteorites (Cronin and Pizzarello 1983). The NASA Stardust mission demonstrated that cometary grains can contain glycine (NH_2CH_2COOH) (Elsila et al. 2009). The COSAC instrument on the ROSETTA mission to comet 67P/Churyumov-Gerasimenko reported several organic compounds, including numerous carbon and nitrogen-rich molecules, in cometary ices (Gudipati et al. 2015; Goesmann et al. 2015). Moreover, meteorite samples exhibit an incredibly rich molecular composition in which amino acids have been detected (Ehrenfreund and Charnley 2000). The different formation mechanisms which give rise to this molecular complexity are poorly understood and have been the subject of numerous investigations. Both gas-phase and solid-state reactions are at work in producing the observed COMs. Solid-state chemistry is important to increase the molecular complexity since the icy grain: (1) offers a place where molecules can meet and react, (2) acts as a third body that can evacuate the excess energy released by the creation of a chemical bond in exothermic reactions, (3) plays a catalytic role by potentially lowering the activation energies of reactions. As such, grain chemistry is at the origin of complex molecular species that cannot be created via gas-reactions.

However, because solid-state reactions often have a barrier, an energy input—thermal or otherwise—is needed to overcome this barrier. In the dense, cold regions where interstellar ice is formed, the production of COMs can be induced by irradiation by the secondary UV radiation field (Bernstein et al. 2002; Muñoz Caro et al. 2002), by permeating X-rays (Chen et al. 2013; Ciaravella et al. 2010, 2012), or by charged particle bombardment by electrons (Lafosse et al. 2009) or protons (Baratta et al. 2002; Cottin et al. 2001). In star-forming regions, the energy input can, however, be merely thermal. This thermal heating affects most of the volume of the material in hot cores and hot corinos, as well as a large part of the protoplanetary disk (the IR-heated warm molecular layer, rather than the photon dominated layer or ice inner region) (van Dishoeck 2014). Similarly, cometary ice is heated to a larger depth than UV photon penetration depths.

In this chapter we will demonstrate how it is possible to investigate thermal ice chemical dynamics in the laboratory (Theulé et al. 2013), by simply warming up an interstellar ice analogue containing only the set of basic molecules observed to date in simple interstellar ices (Dartois 2005) (H_2O, NH_3, CH_4, CO, H_2CO, CO_2, etc). This chosen initial set consists of only closed-shell molecules, since no radical has been positively identified so far in interstellar ices. We will first describe the experimental procedures used to produce and characterize COMs in ice analogues, as well as the quantum chemistry and molecular dynamics methods which are instrumental in interpreting laboratory experiments. We will go on to show how we can study the reactivity of a binary mixture A:B and measure the relevant kinetic parameters of the reaction. As ice mantle chemistry is dominated by a Langmuir-Hinshelwood process, driven by the reaction-diffusion of the reactants in the ice mantle, we will study the reaction-diffusion of a binary mixture A:B

diluted in amorphous water ice. We will end by discussing, on the basis of kinetic arguments, the importance of these purely thermal reactions compared to other solid-state reactions like radical-radical reactions.

10.2 Experimental and Numerical Methods

In our experimental set-up "RING" (Reactivity in INterstellar Grains), binary ice films of a few hundreds of monolayers, and composed of the two reactants A and B, are formed by vapour deposition. First, reactant gases are mixed together at room temperature in a precise concentration ratio in a pumped vacuum line. Then this homogeneous gas-phase mixture is sprayed onto a gold-plated copper surface cooled to 10–100 K by a cold head (ARS Cryo, model DE-204 SB, 4 K cryogenerator) inside a high vacuum chamber with a background pressure of a few 10^{-9} hPa. The surface temperature is controlled using a Lakeshore Model 336 temperature controller and a cylindrical heating resistance mounted inside the copper sample holder. The temperature is measured with a DTGS 670 Silicon diode with a 0.1 K uncertainty. For thin films (less than one hundred monolayers), the thicknesses are derived from IR band strengths and for thicker films, laser interferometry is used. The chemical evolution of the composition of the binary ice can be measured either in the solid state by Fourier-transform infrared (FTIR) spectroscopy in the reflection mode with a Vertex 70 spectrometer, or in the gas phase by quadrupole mass spectrometry (QMS Hidden) when molecules desorb from the surface of the ice. Mass spectrometry has a very high sensitivity, capable of measuring partial pressures down to 5×10^{-13} hPa, while FTIR spectroscopy is sensitive to around one monolayer.

Theoretical chemistry methods can be employed to model chemical systems in the condensed phase, with a global strategy of gradually improving the solvation treatment. First, the reactive systems can be simulated under vacuum, performing standard DFT calculations with the hybrid functional B3LYP and the triple-zeta basis set 6-311G (d,p) in the GAUSSIAN software package (Frisch et al. 2016) to investigate the mechanisms. Once the underlying mechanism is understood, a few molecules of solvent, eventually in addition with an implicit solvation using a Polarisable Continuum Model, are added to model the impact of the direct environment on the reaction, and yield a good description of the reaction mechanism and energetics (Noble et al. 2014). Free energy barriers can then be refined with ab initio Molecular Dynamics calculations, for example using CP2K with DFT for electronic density calculations and following the reaction pathways in a periodic model for the amorphous ice (for instance generated using classical molecular dynamics with GROMACS).

10.3 Reactivity in the Ice Mantle

In a typical experiment, the binary mixture A:B is held at a fixed temperature until the appearance of the product(s). The identification of the product(s) of the reaction:

$$A + B \rightarrow P_1 + P_2 \tag{10.1}$$

is performed by FTIR spectroscopy, based upon the assignment of characteristic IR absorption bands, as seen in Fig. 10.1A. The product identification is later confirmed by mass spectroscopy upon desorption of the ice mixture using thermal programmed desorption (TPD). Several complex organic molecules can be formed by purely

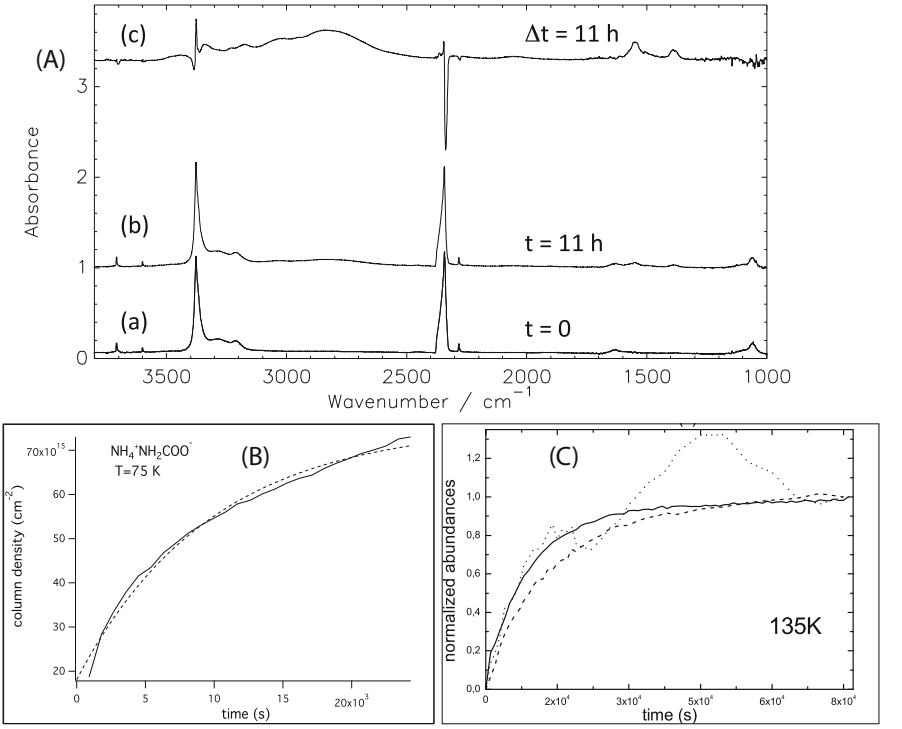

Fig. 10.1 (**A**) Infrared absorption spectrum of a NH_3:CO_2 binary mixture at 80 K prior to reaction at t = 0 (a) and at 80 K after 11 h (b). The difference spectrum (c) of these two spectra enables the isolation of characteristic vibration bands of the $NH_4^+NH_2COO^-$ product. (**B**) Growth of the $NH_4^+NH_2COO^-$ product monitored from its band at 1393 cm^{-1} (solid line), produced in a NH_3:CO_2 binary mixture held at T = 75 K, along with the fit to a first-order kinetic law (dashed lines). (**C**) Growth of the $NH_4^+NH_2COO^-$ product monitored from its band at 1553 cm^{-1} (dotted line); decay of the CO_2 reactant monitored from its band at 2342 cm^{-1} (dashed line); and structural evolution of amorphous ice monitored from the point at 3307 cm^{-1} (solid line), all measured in a tertiary NH_3:CO_2:H_2O mixture of a 5:2:100 concentration held at T = 135 K

thermal reactions from simple precurors (NH_3, H_2CO, HCN, etc) (Theulé et al. 2013). Some of these COMs, such as carbamic acid (NH_2COOH), polyoxymethylene (POM, a polymer of H_2CO), or the cyclic polymer hexamethyltetramine (HMT) are refractory and could be detected in the organic residue left on comets after the water ice sublimates.

The kinetics of a thermal reaction can be experimentally measured in the solid-state at low-temperature and modelled using a formalism derived from liquid-phase chemistry (Bossa et al. 2009). In an isothermal experiment, the binary ice mixture A:B is held at a fixed temperature and the time decay of the characteristic IR absorption bands of the reactants and the growth of the products bands can be fitted with the kinetic equation:

$$\frac{dP_1}{dt} = -\frac{dA}{dt} = k(T)A^{\alpha}B^{\beta}, \tag{10.2}$$

to measure both the reaction rate constant k(T) and the partial orders of the reaction α and β, as displayed in Fig. 10.1B. The reaction rate constants are measured at different temperatures in several isothermal experiments, and their temperature dependence can subsequently be fitted with an Arrhenius law: $k(T) = \nu_0 \times \exp\frac{-E_a}{RT}$. The value of the pre-exponential factor, ν_0 (s^{-1}), and of the activation energy for the reaction, E_a ($kJ\,mol^{-1}$), for several solid-state reactions are listed in Table 3 of Theulé et al. (2013). While the measured reaction activation energy E_a is related to the highest potential barrier, the pre-exponential factor value contains all the details of the intermediate steps of the reaction. Quantum chemistry calculations enable us to picture the intermediate mechanisms involved in one reaction (Noble et al. 2014).

10.4 Reaction-Diffusion in the Ice Mantle

In a Langmuir-Hinshelwood description of the reaction-diffusion process, the characteristic diffusion time of the reactants is larger than their reaction time due to the dilution of the reactants in the water-dominated ice mantle and to the low reaction activation energy. In this diffusion-limited regime the reactivity is mainly driven by the diffusion of the reactants, which can be expressed by a Fick law:

$$\frac{\partial n(\mathbf{r}, t)}{\partial t} - D(T) \times \Delta n(\mathbf{r}, t) = 0, \tag{10.3}$$

where $n(\mathbf{r}, t)$ is the concentration and $D(T)$ the diffusion coefficient of one reactant. Experimentally, to measure the diffusion coefficient (Livingston et al. 2002; Varotsos and Zellner 2010; Mispelaer et al. 2013; Cooke et al. 2017) of a particular species in amorphous ice, one can monitor, in an isothermal experiment, the time for a particular species to percolate in an amorphous ice of a defined thickness (Mispelaer et al. 2013). These experiments can be used to benchmark

Molecular Dynamics calculations of this diffusion coefficient (Ghesquière et al. 2015), which can be done using GROMACS and a simulated annealing procedure to create a realistic model of low-density amorphous ice. Measuring the temperature dependence of the diffusion coefficient enables the derivation, from an Arrhenius law, of the activation energy for diffusion, E_d (kJ mol^{-1}), as well as the diffusion pre-exponential factor.

Both calculations and experiments (Jenniskens and Blake 1994; Ghesquière et al. 2015, 2018) show that the water ice substrate itself plays an important role in the diffusion of the molecules and therefore, since the kinetic system is in the diffusion-limited regime, in the overall reactivity. Diffusion is enhanced by the mesoscopic and macroscopic structural changes of the ice (Smith et al. 1997). As a consequence, the overall reactivity of reaction (10.1) in amorphous ice is intimately linked to the sequential structural changes (Hill et al. 2016) of a porous amorphous ice transforming into a crystalline ice; all processes—the rotational diffusion, the pore collapse, the possible glass transition, the crystallisation (Ghesquière et al. 2018)—are involved. This reaction-diffusion driven by structural change enables the general reaction (10.1) to occur even when the reactants are diluted in ice in a A:B:H_2O mixture, as shown in Fig. 10.1C, although at a higher temperature than for a binary mixture A:B, as seen in Fig. 10.1B.

10.5 Discussion

Recent laboratory work sheds light on the purely thermal reactions occurring in interstellar ice analogues and reveals the close connection between reaction, diffusion and phase changes. We can conceptually separate two extreme cases of reactivity depending on the availability of reactants. In the first case, both reactants are highly abundant and do no need to move to react since they are initially located directly adjacent to one another. Neutron beam scattering experiments show that one molecule has on average 4.2 nearest neighbors in ASW (Bowron et al. 2006; Finney 2002). Thus, a large fraction of the molecules can react without diffusing—at mild temperatures for open-shell molecules (radicals) or at warmer temperature for closed-shell molecules, which are by far the most abundant (H_2O, NH_3, H_2CO, CO_2, etc). The second case concerns low abundance reactants, whether they are closed- or open-shell molecules. In this case, the overall reactivity is determined by their long-range translational diffusion, which is intimately linked to the major structural changes occurring in metastable amorphous ice before its crystallisation. In both cases, purely thermal reactions occur at lower temperatures than the water ice substrate desorption. Their products can either (1) desorb before or during the water ice mantle desorption (volatile species) and enhance the molecular complexity of the gas-phase, or (2) desorb at higher temperature (refractory species) and thus be integrated into the organic residue, which will be later incorporated into planets and comets. Laboratory studies on ice analogues have been very helpful in understanding the chemical significance and determining the kinetic mechanism of

purely thermal reactions. These reactions are most likely widespread in the ISM and planetary systems as they do not depend on extra non-thermal energy inputs such as UV photons, electrons or cosmic rays.

Acknowledgements This work was supported by the Programme National 'Physique et Chimie du Milieu Interstellaire' (PCMI) of CNRS/INSU with INC/INP co-funded by CEA and CNES.

References

Bacmann, A., Taquet, V., Faure, A., Kahane, C., Ceccarelli, C.: Astron. Astrophys. **541**, L12 (2012)
Baratta, G.A., Leto, G., Palumbo, M.E.: Astron. Astrophys. **384**, 343 (2002)
Bernstein, M.P., Dworkin, J.P., Sandford, S.A., Cooper, G.W., Allamandola, L.J.: Nature, **416**, 401 (2002)
Bossa, J.B., Theule, P., Duvernay, F., Chiavassa, T.: Astrophys. J. **707**, 1524 (2009)
Bowron, D.T., Finney, J.L., Hallbrucker, A., Kohl, I., Loerting, T., Mayer, E., Soper, A.K.: J. Chem. Phys. **125**, 194502 (2006)
Delsemme, A.H.: J. Phys. Chem. **87**, 4214 (1983)
Chen, Y.-J., Ciaravella, A., Muñoz Caro, G.M., et al.: Astrophys. J. **778**, 162 (2013)
Ciaravella, A., Muñoz Caro, G., Jiménez Escobar, A., et al.: Astrophys. J. Lett. **722**, L45 (2010)
Ciaravella, A., Jiménez-Escobar, A., Muñoz Caro, G.M., et al.: Astrophys. J. Lett. **746**, L1 (2012)
Cooke, I.R., Öberg, K.I., Fayolle, E.C., Peeler, Z., Bergner, J.B.: (2017). arXiv:1711.09967
Cottin, H., Gazeau, M.C., Benilan, Y., Raulin, F.: Astrophys. J. **556**, 417 (2001)
Cronin, J.R., Pizzarello, S.: Adv. Space Res. **3**, 5 (1983)
Dartois, E.: Space Sci. Rev. **119**, 293 (2005)
Elsila, J.E., Glavin, D.P., Dworkin, J.P.: Meteorit. Planet. Sci. **44**, 1323 (2009)
Ehrenfreund, P., Charnley, S.B.: Ann. Rev. Astron. Astrophys. **38**, 427 (2000)
Finney, J.L., Hallbrucker, A., Kohl, I., Soper, A.K., Bowron, D.T.: Phys. Rev. Lett. **88**, 225503 (2002)
Frisch, M.J., Trucks, G.W., Schlegel, H.B., Scuseria, G.E., et al.: Gaussian 16, Revision A.03, 2016. Gaussian Inc. Wallingford, CT
Ghesquière, P., Mineva, T., Talbi, D., et al.: Phys. Chem. Chem. Phys. **17**, 11455 (2015)
Ghesquière, P., Noble, J.A., Ivlev, A., Theulé, P.: Astron. Astrophys. **614**, A107 (2018). https://doi.org/10.1051/0004-6361/201732288
Goesmann, F., Rosenbauer, H., Bredehöft, J.H., et al.: Science **349**(6247), aab0689 (2015)
Gudipati, M.S., Abou Mrad, N., Blum, J., et al.: Space Sci. Rev. **197**, 101 (2015)
Herbst, E., van Dishoeck, E.F.: Ann. Rev. Astron. Astrophys. **47**, 427 (2009)
Hill, R.C., Mitterdorfer, C., Youngs, T.G.A., Bowron, D.T., Fraser, H.J., Loerting, Th.: Phys. Rev. Lett. **116**(21), 215501 (2016)
Jenniskens, P., Blake, D.F.: Science **265**, 753 (1994)
Lafosse, A., Bertin, M., Hoffman, A., Azria, R.: Surf. Sci. **603**, 1873 (2009)
Livingston, F.E., Smith, J.A., George, S.M.: J. Phys. Chem. A **106**, 6309 (2002)
Mispelaer, F., Theulé, P., Aouididi, H., et al.: Astron. Astrophys. **555**, A13 (2013)
Müller, H.S.P., Schlöder, F., Stutzki, J., Winnewisser, G.: J. Mol. Struct. **742**, 215 (2005)
Muñoz Caro, G.M., Meierhenrich, U.J., Schutte, W.A., et al.: Nature **416**, 403 (2002)
Noble, J.A., Theule, P., Duvernay, F., et al.: Phys. Chem. Chem. Phys. **16**, 23604 (2014)
Smith, R.S., Huang, C., Kay, B.D.: J. Phys. Chem. B **101**, 6123 (1997)
Postberg, F., Khawaja, N.A., Kempf, S., et al.: Lunar Planet. Sci. Conf. **48**, 1401 (2017)
Theulé, P., Duvernay, F., Danger, G., et al.: Adv. Space Res. **52**, 1567 (2013)
van Dishoeck, E.F.: Faraday Discuss. **168**, 9 (2014)
Varotsos, C.A., Zellner, R.: Atmos. Chem. Phys. **10**, 3099 (2010)

Part IV
Dust Grains and Plasmas

Chapter 11
Spectroscopy of Interstellar Carbonaceous Dust

Víctor J. Herrero, Belén Maté, Germán Molpeceres, Miguel Jiménez-Redondo, and Isabel Tanarro

Abstract Carbonaceous grains make a large part of cosmic dust and contain a significant fraction of the carbon available in the interstellar medium (ISM). Observational evidence for the presence of carbonaceous grains comes mostly from IR absorption spectra. The most intense IR absorption is the 3.4 μm band which is ubiquitous in the diffuse ISM and is also present in other galaxies. It is attributed to CH stretching vibrations of CH_2 and CH_3 groups; weaker absorptions at 6.85 and 7.27 μm are due to aliphatic bendings, and a broad, weak absorption between 6 and 6.4 μm is assigned to C=C stretching. These observations, together with laboratory work on dust analogs, point to amorphous hydrogenated carbon (abbreviated a-C:H or HAC), as the most likely carrier of these IR bands, and thus as the predominant component of carbonaceous grains; however, the H/C ratio and the proportion of sp^2 and sp^3 carbon atoms are presently debated. Emission IR bands at 3.3, 6.2, 7.7, 8.6 and 11.2 μm are also seen at many places in the ISM. They have been associated with stretching and bending vibrations of aromatic material and are often referred to as aromatic IR bands (AIB). They are mostly attributed to polycyclic aromatic hydrocarbons (PAHs). Refinements to the original PAH hypothesis including the presence of heteroatoms, aliphatic chains or non-planar defective π domains have been introduced to account for the presence of aliphatic emissions and for the observed band shapes. It is conjectured that the PAHs or PAHs-related molecules responsible for the IR emissions are related with the a-C:H structures responsible for dust absorption either as formation precursors or as destruction products. IR spectroscopy provides also clues on grain evolution. It is generally assumed that carbonaceous grains are formed as nanoparticles in the outflows of carbon-rich AGB stars and evolve from this point. When they reach the diffuse ISM, the grains are subjected to H atom bombardment, which leads to the

V. J. Herrero (✉) · B. Maté · G. Molpeceres · I. Tanarro
Instituto de Estructura de la Materia, IEM-CSIC, Madrid, Spain
e-mail: v.herrero@csic.es

M. Jiménez-Redondo
Centro de Física da Universidade do Minho, Braga, Portugal

G. M. Muñoz Caro, R. Escribano (eds.), *Laboratory Astrophysics*,
Astrophysics and Space Science Library 451,
https://doi.org/10.1007/978-3-319-90020-9_11

formation of aliphatic structures, and to UV photon and cosmic ray irradiation that destroy aliphatic structures and lead to graphitization. A core/mantel structure is often assumed for the grains in the diffuse ISM, but models differ on whether the aliphatic chains responsible for the 3.4 μm band are located in the core or in the mantle and present day observations cannot decide on that point. In dense clouds the 3.4 μm band disappears. It is believed that the aliphatic carriers of this band are destroyed somewhere in the transition from the diffuse to the dense ISM, since in the interior of dense clouds UV and cosmic ray fluxes are too weak.

11.1 Introduction

Carbon is the fourth element by order of abundance in the Universe and it is the first of the light elements that is exclusively formed in the interior of stars (Henning and Salama 1998). The electronic structure of carbon allows the formation of hybridized orbitals which offer multiple bonding possibilities. As a consequence, carbon is the element with the richest chemistry, a chemistry that leads ultimately to the origin of life.

In the last stages of star evolution most of carbon and oxygen react to form CO and, in C-rich Asymptotic Giant Branch (AGB) stars, the remaining carbon atoms give rise to SiC, to a wealth of organic compounds, and to hydrogenated carbonaceous solids. It is generally assumed that the primary carbonaceous material is formed as nanometer sized particles via gas-phase condensations in the circumstellar envelope (Henning and Salama 1998; Fonfría et al. 2008). The particles are then injected into the interstellar medium (ISM). The composition of these interstellar (IS) solids is deduced mostly from infrared (IR) absorptions and emissions observed in different astrophysical environments. Laboratory work on analogs of IS carbonaceous matter is needed in general to interpret the observations (Jäger et al. 2011; Dartois et al. 2014). Although crystalline phases like nanodiamonds or fullerenes (Jäger et al. 2011; Dartois et al. 2014) have been identified in the ISM, most of the solid carbon is probably locked in some kind of hydrogenated amorphous carbon (abbreviated as a-C:H or HAC) (Dartois et al. 2007; Chiar et al. 2013; Jones et al. 2013, 2014).

Carbonaceous grains are among the most abundant cosmic dust components. These grains, injected into the ISM, can influence the heating rate of gas and provide a site for heterogeneous chemistry, allowing the formation of molecules and, specifically of H_2. The size and chemical composition of carbonaceous grains change markedly as they evolve through the ISM. In dense clouds they can reach μm size and get covered by ice layers; from there, they can grow to macroscopic sizes in the protoplanetary disk resulting from the cloud collapse leading to star formation. Solids formed by mixtures of carbon and hydrogen can be very complex. The size of the polyaromatic units and the proportion of aromatic to aliphatic structures predominant in dust grains are presently a matter of debate (Dartois et al. 2007; Chiar et al. 2013; Jones et al. 2013, 2014). The amount of oxygen or other heteroatoms incorporated in interstellar carbonaceous dust is not known with

precision, but it appears to be low (Pendleton and Allamandola 2002; Dartois et al. 2004). In the diffuse ISM, sputtering and grain shattering can erode and fragment the grains, leading to a release of organic molecules. It is believed that large polycyclic aromatic hydrocarbons (PAHs) are related to the material in carbonaceous dust, both as condensation precursor and as products of grain disintegration.

In this chapter we review available spectroscopic evidence on IS carbonaceous dust, mostly from observations in the infrared, as well as information on the structure and evolution of dust particles and related species gained from laboratory experiments on dust analogs.

11.2 Spectral Features of Interstellar Carbonaceous Matter

There are several spectral features in astronomical observations that are usually attributed to some sort of carbonaceous matter, other than small gas-phase molecules. In some cases the assignment is based on solid evidence, in other cases only speculations can be made about the nature of the carriers. These features include (Kwok 2016): The 220 nm bump, the diffuse interstellar bands, the extended red emission, the aliphatic absorption bands, and the IR emission bands. These spectral signals are strong and ubiquitous, which suggests that the carriers are composed of common and abundant elements with carbon and hydrogen as main candidates. Some of them are also observed in high redshift galaxies, indicating that the feature carriers were already present in the early Universe.

The 220 nm bump in the ultraviolet (UV) extinction curve was first detected in 1965 (Stecher 1965). The peak wavelength is fairly constant at 217.5 nm, but the width can vary between 36 and 77 nm. The band has been attributed to some form of carbonaceous matter including hydrogenated fullerenes and polycrystalline graphite. Small graphite particles or a hydrogen-poor a-C:H seem today the most likely candidates (Mennella et al. 1998; Gadallah et al. 2011).

The diffuse interstellar bands (DIB) have been known for almost a century and still constitute a mystery. More than 500 DIBs have been observed, virtually always in absorption, between the UV and the IR. It is generally assumed that they are due to electronic transitions of C-containing molecules in the gas phase, like PAHs or fullerenes. Rydberg states of hydrogen have also been suggested, but except for two lines of C^{+}_{60} (Campbell et al. 2015) no clear unambiguous assignments have been possible thus far.

The extended red emission (ERE) is common in reflection nebulae like the Red Rectangle, where it was first observed about 35 years ago (Schmidt et al. 1980). It has also been detected in other environments like planetary nebulae and the diffuse interstellar medium. It is attributed to photoluminescence, most likely from a semiconductor with a non-zero band gap. Silicon nanoparticles, fullerenes, nanodiamonds and a-C:H have been advanced as carrier candidates.

The absorption band at 3.4 μm was observed in 1980 in a source toward the galactic center (Wickramasinghe and Allen 1981) and was soon associated with stretching motions of aliphatic methyl and methylene groups (Duley and Williams

1983). Smaller absorption features at 6.85 and 7.24 μm corresponding to bending modes of the same groups have also been found. The 3.4 μm band is common in the diffuse medium and in protoplanetary nebulae. It has also been observed in external galaxies, but it is not seen in dense clouds. At present the mentioned aliphatic absorptions are almost unanimously attributed to a-C:H.

IR emission features were observed since the 1970's (Russell et al. 1977) and were initially dubbed Unidentified IR emission (UIE) bands. Nowadays observed IR emission bands span the range from 3 to 20 μm and are currently assigned to vibrations of mostly aromatic groups, with some aliphatic contributions. The emission features are always associated with a strong emission continuum and are seen in very different radiation environments like HII regions, planetary and protoplanetary nebulae and reflection nebulae. Several candidates have been suggested as possible carriers, including PAH molecules, a-C:H, soot, kerogen, coal, and mixtures of aromatic and aliphatic organic nanoparticles. Among all these, the PAH hypothesis (Léger and Puget 1984; Allamandola et al. 1985; Peeters 2011) is to date the most popular explanation.

In the following we will concentrate on the mid-IR absorption and emission bands and will comment on the properties of their likely carriers, and on the implications for models of dust evolution.

11.3 IR Absorptions: a-C:H

The 3.4 μm absorption band is the strongest known diffuse interstellar feature, and is easily accessible from ground-based telescopes. It is attributed mostly to aliphatic CH stretching vibrations. The band has substructures associated with symmetric and antisymmetric stretching modes of the CH_3 and CH_2 groups. Toward its high frequency end, close to 3.3 μm, a small shoulder or a wing due to aromatic CH stretching can sometimes be observed. Observations from space missions (ISO, Spitzer) also provided data from the 5–8 μm region. In this spectral range, peaks at 6.85 and 7.27 μm, corresponding to bending modes of CH_3 and CH_2, have been found. There is also a broad absorption, between 6 and 6.4 μm, assigned to the aromatic or olefinic C=C stretching mode. Observations of the weaker aliphatic features, and especially of the aromatic absorption, are however rare.

A variety of experimental techniques has been used to produce laboratory analogs to the carriers of the absorption bands. These techniques include laser ablation or pyrolysis of carbon-containing precursors (Jäger et al. 2008), plasma deposition (Jäger et al. 2008; Maté et al. 2014), combustion (Pino et al. 2008) or low temperature photolysis of hydrocarbons (Dartois et al. 2005). A thorough discussion on the suitability of various types of laboratory candidates can be found in Pendleton and Allamandola (2002). All the laboratory analogs of IS carbon dust have disordered structures with variable mixtures of aromatic and aliphatic groups. Among them, a-C:H leads to the best agreement with the observations. This good agreement is illustrated in Fig. 11.1.

The denomination "hydrogenated amorphous carbon" refers to a wide group of carbonaceous materials with variously hybridized carbon atoms and different

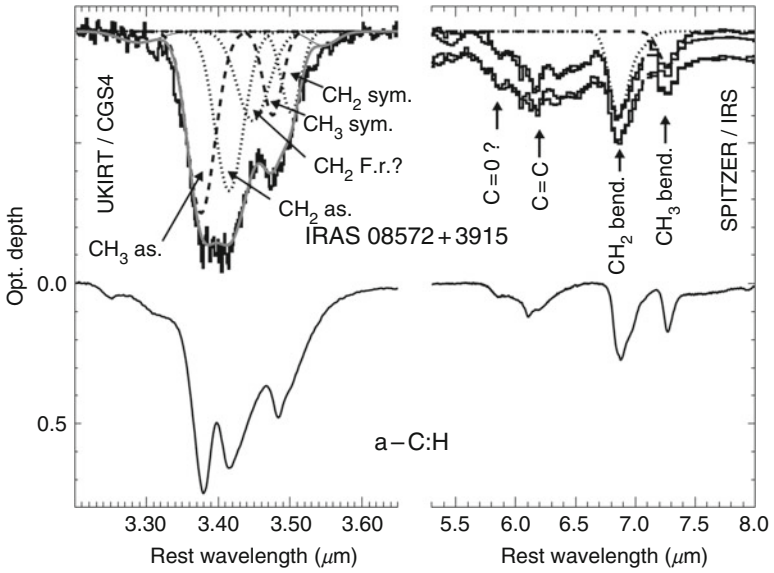

Fig. 11.1 Comparison of observed dust absorptions in an IR galaxy with the spectrum of laboratory generated a-C:H. Taken from Dartois et al. (2007)

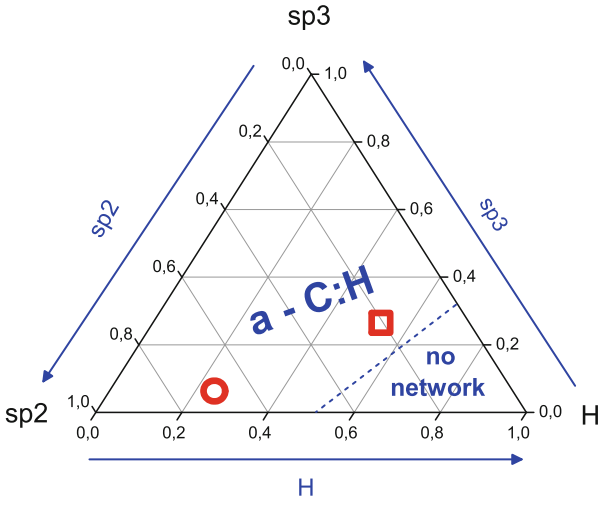

Fig. 11.2 Ternary diagram for C/H solids. Symbols: Competing models for the average composition of carbonaceous dust in the diffuse interstellar medium. Circle, from Chiar et al. (2013). Square, from Dartois et al. (2005) (see text)

C/H ratios. They represent three dimensional structures, with a tendency to cluster, made of aromatic islands of variable sizes linked by aliphatic chains with possible olefinic contributions (Robertson 1986). Figure 11.2 shows the approximate location

of a-C:H in a ternary diagram describing the C/H ratio and the C hybridization states in a variety of solids containing carbon and hydrogen. The adoption of this diagram implies that all atoms in a-C:H are sp^3 carbon, sp^2 carbon, or hydrogen. The possible contribution of sp carbon atoms, unusual in this type of material, is tacitly neglected. Graphite is located at the lower left vertex of the diagram and diamond at the upper vertex. For historical reasons, in the literature on material science, the term a-C:H is often interchanged with "diamond like amorphous carbon", a solid with a relatively high proportion of sp^3 carbon (Robertson 2002). In the astrophysical bibliography the term is more flexible and includes also aromatic-rich, H-poor material, sometimes referred to as amorphous carbon (a-C) (Jones et al. 2013, 2014), that would occupy a region close to the graphite vertex.

Solids made of a-C:H are semiconductors. Their band-gap, E_g, and their electronic $\pi-\pi^*$ transitions, that take place between 190 and 270 nm, are largely determined by the size of the aromatic units. Irradiation of a-C:H samples with UV photons leads to dehydrogenation and graphitization, which results in a decrease of E_g and in changes in the UV–Vis spectra. After long UV irradiation, Gadallah et al. (2011) produced highly graphitic a-C:H samples that exhibited a bump at 220 nm in their electronic absorption. The authors of this work pointed to a-C:H as a likely carrier of this feature in the ISM (see above). However, with this assignment there are inconsistencies between the observed absorptions and the estimated amount of carbon available for IS dust formation.

The predominant structure of the a-C:H material in the dust grains of the diffuse ISM is at present a matter of debate between two competing models. The first of these models assumes that a-C:H in the ISM is relatively hydrogen-rich, composed by small aromatic islands linked by aliphatic chains (Dartois et al. 2005; Kwok and Zhang 2013). The second model assumes that a-C:H is much more graphitic, with large polyaromatic sheets terminated by short aliphatic endings (Chiar et al. 2013; Steglich et al. 2013). Estimates of the sp^2/sp^3 proportion and of the H/C ratio of IS dust from the observed IR spectra have been attempted through sub-band profile decompositions like the one shown in Fig. 11.1. However, this procedure should be taken with care. Estimates of the a-C:H composition based just on IR data might be unreliable (Jacob and Möller 1993), because the band strengths of the individual modes are poorly known for the disordered solid structures constituting a-C:H. In particular, a large uncertainty is attached to the weak absorption features of the aromatic C=C and C–H stretching transitions that are used to estimate the sp^2 fraction in the solid network. Additional information is needed to constrain the likely structures (Dartois et al. 2007, 2005). Recent studies by our group combining IR spectra with theoretical DFT calculations (Molpeceres et al. 2017) and reflectivity measurements (Peláez et al. 2018) suggest that a-C:H compositions derived only from IR spectra are biased toward polyaromatic structures. Our studies favor the dust model with a significant aliphatic component.

11.4 IR Emission: PAHs?

Emission bands at 3.3, 6.2, 7.7, 8.6 and 11.2 μm are ubiquitously observed in the ISM. They have been associated with stretching and bending vibrations of aromatic material and are often referred to as aromatic IR bands (AIB). The assignment of these bands can be seen in Table 11.1. Many possible candidates were suggested as possible band carriers (see above), but solid particles were mostly discarded in favor of polycyclic aromatic hydrocarbons (the so called PAH hypothesis (Léger and Puget 1984; Allamandola et al. 1985; Peeters 2011 and references therein)). The main argument against solid particles is that the AIB are observed in reflection nebulae with a color temperature of ≈1000 K independent of the distance to the illuminating star. In these comparatively cold environments classical dust grains are too cold to emit in the mid IR. In contrast, PAHs can reach temperatures of about 1000 K upon absorption of a single UV photon and then relax, mainly through IR emission causing the AIBs. Besides the main AIB bands, aliphatic transitions at 3.4, 6.85 and 7.27 μm and further unidentified bands in the 15–20 μm range were also found in emission. Figure 11.3 shows emission spectra from different sources.

Table 11.1 Summary of the main mid-IR features of hydrocarbon matter observed in the ISM. Band assignments can be found in Dartois et al. (2007), Chiar et al. (2013) and Hudgins and Allamandola (1999)

Band center (approx)	Type of compound	Observation	Assignment
3.3 μm/3040 cm^{-1}	Aromatic/olefinic	Absorption/emission	CH stretch
3.38 μm/2962 cm^{-1}	Aliphatic	Absorption/emission	CH_3 asym. strtech
3.41 μm/2923 cm^{-1}	Aliphatic	Absorption/emission	CH_2 sym. stretch
3.48 μm/2877 cm^{-1}	Aliphatic	Absorption/emission	CH_3 sym. stretch
3.52 μm/2840 cm^{-1}	Aliphatic	Absorption/emission	CH_2 sym. bend
6–6.4 μm/1666–1562	Aromatic/olefinic	Absorption/emission	sp^2 C=C stretch
6.81 μm/1457 cm^{-1}	Aliphatic	Absorption/emission	CH_2 def. + CH_3 asym. bend
7.27 μm/1374 cm^{-1}	Aliphatic	Absorption/emission	CH_3 sym. bend
7.7 μm/1299 cm^{-1}	Aromatic	Emission	sp^2 C–C stretch
8.6 μm/1162 cm^{-1}	Aromatic	Emission	sp^2 C=C–H in plane bend
11.3 μm/885 cm^{-1}	Aromatic	Emission	sp^2 C=C–H out of plane bending "solo"[a]
12.1 μm/826 cm^{-1}	Aromatic	Emission	sp^2 C=C–H out of plane bending "duo"[a]
12.4 μm/806	Aromatic	Emission	sp^2 C=C–H out of plane bending "trio"[a]
13.3 μm/752 cm^{-1}	Aromatic	Emission	sp^2 C=C–H out of plane bending "quarto"[a]

[a]Solo, duo, trio and quarto refer to the number of exposed benzene ring sides (Hudgins and Allamandola 1999)

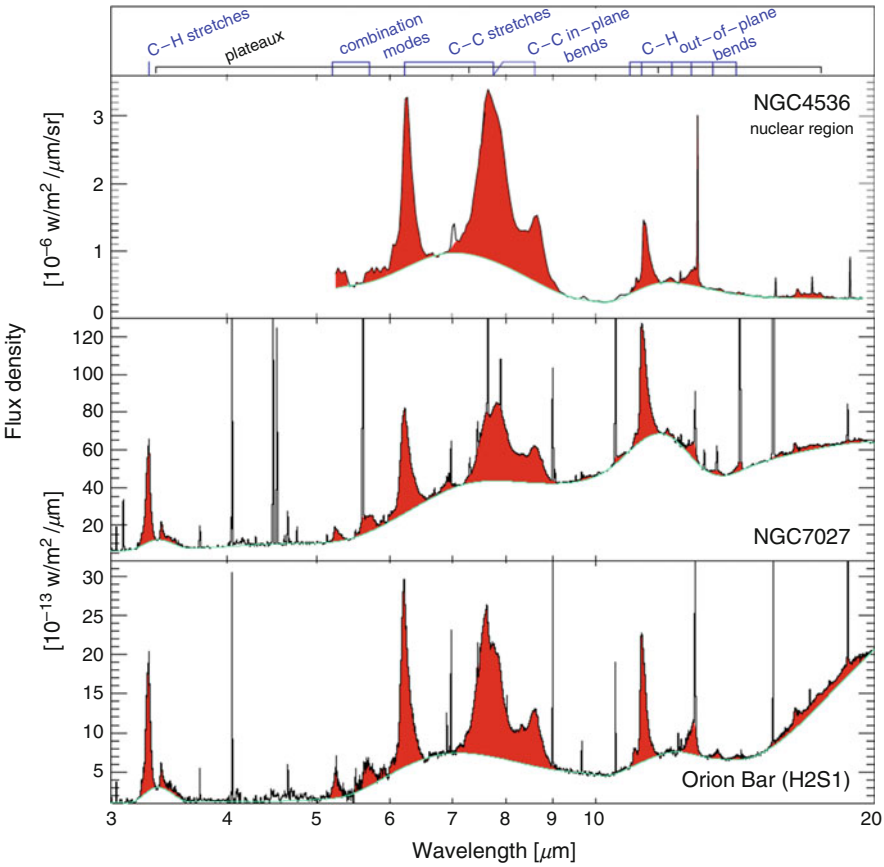

Fig. 11.3 IR emission bands toward different sources (taken from Peeters (2011))

The emission bands are often accompanied by broad emission plateaus at 6–9, 10–15, and 15–20 μm. These plateaus have been variously attributed to the same PAHs spectrum (Peeters 2011) or to superpositions of in-plane and out of plane bending modes emitted by a mixture of aliphatic side groups attached to aromatic rings (Kwok 2016). It has been also suggested that the 15–20 μm plateau might be due to CCC in and out of plane bending of aromatic rings (Kwok 2016).

The relative intensities and profiles of the PAH bands vary from source to source and the PAH model has been refined over the years to account for the observations. Band profile modifications are especially prominent for the 7.7 μm transition complex. The sources are classified into A, B and C depending on the position of the band maximum, which can vary between 7.6 μm (class A) and 8.2 μm (class C). It is generally assumed that band profile variations originate in a chemical modification of the PAHs. Various PAH related species have been contemplated as possibilities, some of them incorporating heteroatoms or aliphatic chains (see refs.

in Peeters 2011). Strictly speaking, these species would not be PAHs. In a recent publication, Gaulé and Díaz Leines (2017), using DFT calculations, show that the spectral patterns in AIBs, and specifically the elusive bands in the 6–9 μm range, arise naturally when structures with non planar defective π domains, and not just flat PAHs, are considered as band carriers.

At present, mixtures of different PAHs, both neutral and ionic, as well as PAH clusters are included in the model and they can successfully reproduce the observed emissions in various astronomical environments (Joblin et al. 2008; Rosenberg et al. 2014). IR spectra, both experimental and theoretical, of the different PAHs are available from the literature and can be found at databases (e. g. http://www.astrochem.org/pahdb/; http://astrochemistry.oa-cagliari.inaf.it/database/). The PAH hypothesis has been criticized because an artificial mixture of PAH structures, sizes and ionization states must be used to account for the broad emission features, and because no individual PAH molecule has ever been detected in the ISM (Kwok and Zhang 2013). As an alternative to PAHs, small nanoparticles, made up of a mixture of aromatic and aliphatic structures, are suggested in Kwok and Zhang (2013) as carriers of the emission bands. This hyothesis has also been contested (Rosenberg et al. 2014) because it lacks a model for the emission mechanism.

A summary of the main observed IR absorption and emission features related to carbonaceous dust, together with their assignment, is given in Table 11.1. Note that the listed band center positions are only approximate, since they do not correspond to individual molecules, but rather to functional groups of materials with complex structures. The band assignments are also approximate, since for this type of substances there is a substantial degree of mode mixing, especially for the longer wavelengths.

An interesting issue, as yet without a clear answer, is the possible relationship between the carriers of the predominantly aliphatic absorption bands, and the predominantly aromatic emission features. Strictly speaking it is not known whether the carriers of the emission and absorption bands are two different materials coexisting in the diffuse ISM, or different evolutionary phases of the same material. As we shall see in the next section, current models of dust evolution assume that they are related.

11.5 Evolution of Interstellar Carbonaceous Dust

In the last section we provide a global view of the transformations of carbonaceous grains in their journey through the ISM and discuss the recent dust evolution models of Chiar et al. (2013) and of Jones et al. (2013, 2014).

Carbonaceous solids appear for the first time in the last phase of evolution of C-rich AGB stars. Spectral energy distributions and IR molecular absorption spectra show that dust is formed in the inner shell of the star when the temperature drops to about 1000 K (Chiar et al. 2013). Laboratory experiments show that this is a favorable temperature for the conversion of acetylene into large PAH molecules and

then into soot (Frenklach and Feigelson 1989). The highly aromatic carbon stardust is then ejected to the ISM. The absence of the aliphatic 3.4 feature in observations towards AGB stars suggests that aromatic structures are indeed predominant in the original stardust (Chiar et al. 2013).

In the ISM, the generated stardust particles are subjected to UV and cosmic ray irradiation and can interact with H atoms. Laboratory experiments show that the exposure of an aromatic solid to a flux of H atoms leads to the formation of aliphatic CH_2 and CH_3 groups (Mennella et al. 2002). On the other hand, interaction with UV photons (Mennella et al. 2001; Gadallah et al. 2012; Alata et al. 2014) and cosmic rays (Jäger et al. 2008; Alata et al. 2014; Mennella et al. 2003) destroy the aliphatic structures and increase graphitization. The decay of the 3.4 μm band under the effects of high energy ions or electrons, used to simulate the effects of cosmic rays, is shown in Fig. 11.4. With the data derived from all these experiments, the effects of H atoms should prevail over UV photons and cosmic rays, and should lead to the formation of an aliphatic mantle on the aromatic grains (Chiar et al. 2013). The aliphatic structures thus formed would be the carriers of the aliphatic absorption features observed in the diffuse ISM.

The 3.4 μm band is not observed in dense molecular clouds, indicating that at some point, the destructive effects of UV photons or CRs must prevail over hydrogenation. Hydrogenation is certainly expected to stop in dense clouds due to the H atom recombination to H_2 molecules and to the formation of ice mantles on the dust grain surfaces. However, the interior of dense clouds is also shrouded from

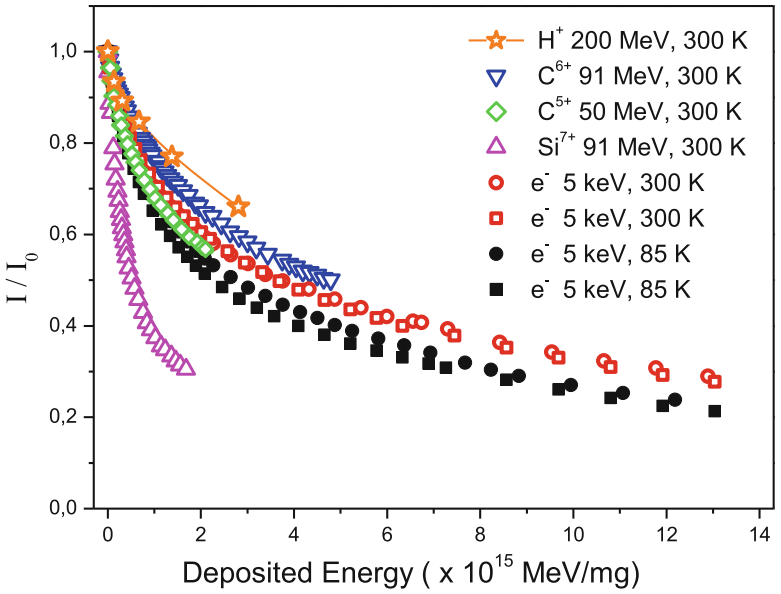

Fig. 11.4 Decay of the 3.4 μm band intensity under ion and electron bombardment. Ion data from Godard et al. (2011), electron data from Maté et al. (2016)

the galactic UV field and the aforementioned experimental measurements show that neither CRs nor the secondary UV field, produced in dense clouds through the CR excitation of fluorescent transitions in molecular hydrogen, should have a great effect on the 3.4 μm band carriers (Godard et al. 2011; Mennella et al. 2003; Maté et al. 2016).

The most likely environment for the destruction of the aliphatic carbon structures is thus the transition region between diffuse and molecular clouds, but the details of the destruction mechanism are not known, and the models of Chiar et al. (2013) and Jones et al. (2013, 2014) differ markedly at this point (see below). Chiar et al. (2013) assume that the aliphatic mantles of dust particles are destroyed somewhere in the translucent cloud phase, for extinction values up to $A_v \approx 3$, which marks the approximate start of ice mantle formation. In the region close to $A_v = 3$, the external (galactic) UV field would not be totally attenuated (Chiar et al. 2013) and would prevail over hydrogenation.

The model of Jones et al. (2013, 2014) advances a comprehensive explanation of the cycling of C in dust. These authors point at the current inconsistency between the timescales assumed for stardust injection into the ISM ($\approx 10^3$ Myr) and for destruction in interstellar shocks ($\approx 10^2$ Myr), and propose a mechanism of grain accretion in dense phases of the ISM as an additional grain growth mechanism. In their model, different grain families are contemplated, namely a population of small, predominantly aromatic, C-grains and another group of large grains with a large aliphatic component, responsible for the 3.4 μm absorption. The model provides a good semiquantitative description of many dust properties, like the 220 nm bump and some IR emissions associated with the small, aromatic-rich grains, and also of the 3.4 μm absorption caused by the larger, aliphatic-rich particles. Contrary to Chiar et al. (2013), Jones et al. (2013, 2014) assume that mostly aliphatic structures can be formed at an early stage of grain evolution, and that H incorporation into the grains is not very efficient in the diffuse ISM. Consequently, in stark contrast to Chiar et al. (2013) they propose that photoprocessing prevails over hydrogenation in diffuse clouds, and leads to the formation of an aromatic mantle on an aliphatic core shielded from UV radiation in large grains. Present experimental evidence cannot decide whether the aliphatic structures, responsible for the 3.4 μm absorption, are in the core (Jones et al. 2013, 2014) or in the mantle (Chiar et al. 2013) of the grains. According to Jones et al. (2013, 2014), in the denser transition region, for $A_v \approx 0.1$–2, accretion of C and H would lead to grain growth through the formation of an aliphatic mantle. The ulterior fate of the aliphatic structures in the grains is not discussed by the authors, but efficient destruction mechanisms must be assumed if the model is to be consistent with the disappearance of the 3.4 μm absorption band in dense clouds. Further work is needed to clarify this issue as well as the discrepancies on the core-mantle structure of grains in the diffuse ISM provided by the two models. Both models (Chiar et al. 2013; Jones et al. 2013, 2014) assume that carbonaceous grains, especially the smallest ones, can be destroyed by energetic photons or shattered in strong shocks, releasing PAH molecules into the ISM. Thus, they establish a relationship between the likely carriers of absorption and emission bands.

Acknowledgements The authors acknowledge funding by the Spanish MINECO under grants AYA2015-71975-REDT (Polvo Cósmico) FIS2013-48087-C2-1P, FIS2016-77726-C3-1P, CSD2009-00038 (Astromol) and by the European Union under grant ERC-2013-Syg 610256 (Nanocosmos).

References

Alata, I., et al.: Astron. Astrophys. **569**, A119 (2014)
Allamandola, L.J., Tielens, A.G.G.M., Barker, J.R.: Astrophys. J. **290**, L25 (1985)
Campbell, E.K., et al.: Nature. **523**, 322 (2015)
Chiar, J.E., et al.: Astrophys. J. **770**, 1 (2013)
Dartois, E., et al.: Astron. Astrophys. **423**, 549 (2004)
Dartois, E., et al.: Astron. Astrophys. **432**, 895 (2005)
Dartois, E., et al.: Astron. Astrophys. **463**, 635 (2007)
Dartois, E., et al.: Geochim J. **48**, 511 (2014)
Duley, W.W., Williams, D.A.: Mon. Not. R. Astron. Soc. **205**, 67 (1983)
Fonfría, P.J., et al.: Astrophys. J. **673**, 445 (2008)
Frenklach, M., Feigelson, E.D.: Astrophys. J. **341**, 372 (1989)
Gadallah, K.A.K., et al.: Astron. Astrophys. **528**, A56 (2011)
Gadallah, K.A.K., et al.: Astron. Astrophys. **544**, A107 (2012)
Gaulé, H.A., Diáz Leines, G.: Phys. Rev. Lett. **119**, 171102 (2017)
Godard, M., et al.: Astrophys. J. **529**, A146 (2011)
Henning, T., Salama, F.: Science. **282**, 2204 (1998)
Hudgins, D.M., Allamandola, M.J.: Astrophys. J. **516**, l41 (1999)
Jacob, W., Möller, W.: Appl. Phys. Lett. **63**, 1771 (1993)
Jäger, C., et al.: Astrophys. J. **689**, 249 (2008)
Jäger, C., et al.: In: Joblin, C., Tielens, A.G.G.M. (eds.) PAHs and the Universe EAS publication series, vol. 46, p. 293 (2011)
Joblin, C., et al.: Astron. Astrophys. **490**, 189 (2008)
Jones, A.P., et al.: Astron. Astrophys. **558**, A62 (2013)
Jones, A.P., et al.: Faraday Discuss. **168**, 313 (2014)
Kwok, S.: Astron. Astrophys. Rev. **24**, 8 (2016)
Kwok, S., Zhang, Y.: Astrophys. J. **771**, 5 (2013)
Léger, A., Puget, J.L.: Astron. Astrophys. **137**, L5 (1984)
Maté, B., et al.: Faraday Discuss. **168**, 267 (2014)
Maté, B., et al.: Astrophys. J. **831**, 51 (2016)
Mennella, V., et al.: Astrophys. J. Lett. **507**, L177 (1998)
Mennella, V., et al.: Astron. Astrophys. **367**, 355 (2001)
Mennella, V., et al.: Astrophys. J. **559**, 531 (2002)
Mennella, V., et al.: Astrophys. J. **587**, 727 (2003)
Molpeceres, G., Timón, V., Jiménez-Redondo, M., Escribano, R., Maté, B., Tanarro, I., Herrero, V.J.: Phys. Chem. Chem. Phys. **19**, 1352 (2017)
Peeters, E.: In: Joblin, C., Tielens, A.G.G.M. (eds.) PAHs and the Universe EAS publication series, vol. 13, p. 27 (2011)
Peláez, R.J., Maté, B., Tanarro, I., Molpeceres, G., Jiménez-Redondo, M., Timón, V., Escribano, R., Herrero, V.J.: Plasma Sources Sci. Technol. **27**, 035007 (2018)
Pendleton, Y.J., Allamandola, L.: Astrophys. J. Suppl. Ser. **138**, 75 (2002)
Pino, T., et al.: Astron. Astrophys. **489**, 665 (2008)
Robertson, J.: Adv. Phys. **35**, 317 (1986)
Robertson, J.: Mat. Sci. Eng. **37**, 129 (2002)
Rosenberg, M.J.F., et al.: Astron. Astrophys. **566**, L4 (2014)

Russell, R.W., Soifer, B.T., Willner, S.P.: Astrophys. J. **217**, L149 (1977)
Schmidt, G.D., et al.: Astrophys. J. Lett. **239**, L133 (1980)
Stecher, T.P.: Astrophys. J. **142**, 1682 (1965)
Steglich, M., et al.: Astrophys. J. Suppl. Ser. **208**, 26 (2013)
Wickramasinghe, D.T., Allen, D.A.: Nature. **287**, 518 (1981)

Chapter 12
Light Scattered by Cosmic Dust at Visible Wavelengths

Jesús Escobar-Cerezo, Olga Muñoz, and Fernando Moreno

Abstract The present chapter is focused on studying the polarimetric response of the scattered light by an ensemble of irregular dust particles. This is done by measuring the so-called scattering matrix which depends on physical parameters of the sample as the shape, the size distribution and the complex refractive index. This has proven to be a powerful diagnostic tool in the past, and has been proposed as a promising method to study exoplanetary atmospheres. In this chapter, the methodology of these measurements is explained through the presentation of an optical laboratory, its theoretical background, the calibration procedures and some applied examples.

Irregular cosmic dust grains play an important role in the radiative balance of planetary and cometary atmospheres in the Solar System. Light scattering properties of spherical particles can be computed from Lorenz-Mie theory. However, an exact solution for realistic polydispersions of irregular dust grains is extremely difficult if possible at all. Therefore, an experimental study of the scattering behaviour of irregular dust particles that are candidates to be present in different atmospheres is of main importance in order to interpret space- and ground-based observations.

In this chapter we present the COsmic DUst LABoratory developed at the Instituto de Astrofísica de Andalucía, CSIC (IAA-CODULAB) (Muñoz et al. 2010). The IAA-CODULAB is devoted to experimentally obtaining the angle dependence of the scattering matrices of clouds of small cosmic dust particles. We are especially interested in mineral dust particles that are candidates for being present in planetary and cometary atmospheres of the Solar System (olivines, pyroxenes, calcite, carbon, etc).

First, we present a theoretical background on the scattering matrix for non-spherical particles. This section is followed by a description of the experimental

J. Escobar-Cerezo (✉) · O. Muñoz · F. Moreno
Instituto de Astrofísica de Andalucía, IAA-CSIC, Granada, Spain
e-mail: jescobar@iaa.es

G. M. Muñoz Caro, R. Escribano (eds.), *Laboratory Astrophysics*,
Astrophysics and Space Science Library 451,
https://doi.org/10.1007/978-3-319-90020-9_12

apparatus. The chapter continues with a section about the tests performed to validate the experimental results. At the end of the chapter experimental results and conclusions from that measurements are presented.

It is not the purpose of this chapter to fully describe the electromagnetic scattering phenomenon from an exact mathematical framework. In this chapter we study the scattering produced by particles of the order and larger than the wavelength. As we study these processes from a macroscopic point of view, we work with some restrictions that are thoroughly used and justified in the literature of light scattering (see e.g. van de Hulst 1957; Mishchenko et al. 2000, 2002; Hovenier et al. 2004; Mishchenko 2014). These are:

- We only consider elastic scattering, i.e. the frequency of the scattered light is the same as that of the incident light. Inelastic scattering phenomena as Raman and Brillouin scattering or fluorescence are not considered (Hovenier et al. 2004; Mishchenko et al. 2002).
- We study scattering only in the far-field zone, where the propagation of the scattered wave is away from the particle, the electric vector vibrates in the plane perpendicular to the propagation direction, and the scattered field amplitude decreases inversely with distance from the particle. Furthermore, if the subject of study is a cluster of particles, the far-field zone is further than any linear dimension of the cluster (Mishchenko et al. 2002).
- Particles forming a cloud are considered as independent scatterers. The scattered field by each particle is the composition of the reactions to the external field and the secondary fields scattered by the surrounding particles. If the number of particles is sufficiently small and their relative distances sufficiently large, the contribution of these secondary waves is negligible compared to the external field. The total scattered field can be computed by the sum of the fields generated by the individual response of each particle to the incident field. This is known as single-scattering approximation (Mishchenko et al. 2002).
- Connected with the previous restriction, the assumption of independent scattering means that there is no systematic relation between the phases of all the waves present in the system (scattered and external). The phase differences may change completely when the particles are slightly altered (in position or orientation). The net effect is that for all practical purposes the scattered intensities by the ensemble of particles must be added without regard to phase. The scattering is considered incoherent (van de Hulst 1957). In the forward direction, at nearly zero angle, no scattering in the ordinary sense can be observed.

12.1 Polarization Parameters and Scattering Matrix

One of the first parameters that appears when studying the electromagnetic radiation is the specific intensity I (or simply, the intensity). The radiant energy $\mathrm{d}E$ depends on the intensity I as follows (Hovenier et al. 2004):

$$\mathrm{d}E = I\mathrm{d}\nu\mathrm{d}\sigma\mathrm{d}\Omega\mathrm{d}t, \tag{12.1}$$

where $d\nu$ defines the frequency interval $\nu \rightarrow \nu + d\nu$, $d\sigma$ is the surface area traversed by the energy perpendicular to the propagation direction of I, $d\Omega$ the solid angle element that confines the directions studied and dt the time interval. The SI units of the intensity are $W\,Hz^{-1}\,m^{-2}\,sr^{-1}$.

A beam of light is not only characterized by its intensity. In 1852, sir George Stokes introduced the so-called Stokes parameters, which represent exactly the polarization state and intensity of a beam of light propagating in certain a direction. It has to be taken into account that these parameters are, in most cases, used in a relative sense, i.e. compared to another Stokes parameters either of the same beam or from another beam (Hovenier et al. 2004). These are named I, Q, U and V. I represents the intensity, Q and U characterize the linear polarization, and V the circular polarization. They are related in general by the equation (Mishchenko et al. 2002):

$$I^2 \geq Q^2 + U^2 + V^2, \tag{12.2}$$

where equality holds when the beam of light is fully polarized. In the case of unpolarized light (also called natural light) $Q = U = V = 0$. In all other situations the light is called partially polarized.

Fluxes rather than intensities are considered in studies of single light scattering by small particles (Hovenier et al. 2004). We can define a flux vector $\pi\mathbf{\Phi} = \pi\{\Phi_1, \Phi_2, \Phi_3, \Phi_4\}$ where $\pi\Phi_1$ is the net flux, and Φ_2, Φ_3 and Φ_4 describe the polarization state of the beam of light in correspondence to the Stokes parameters Q, U and V. The net flux $\pi\Phi_1$ depends on I, and is described as the amount of energy flowing at a point of study in all directions per unit of frequency interval, of surface area, and of time. It is represented by the equation:

$$\pi\Phi_1 = \int d\Omega I \cos\epsilon, \tag{12.3}$$

where the term $\cos\epsilon$ is the correction for the projected surface area in the case that the propagation direction of I is not perpendicular to the surface $d\sigma$ of Eq. (12.1). The net flux has SI units of $W\,Hz^{-1}m^{-2}$.

The scattering matrix $\mathbf{F}$ characterizes the polarimetric response of an ensemble of particles under incident electromagnetic radiation. In what follows, we assume that the particles are not optically active. The scattering matrix relates for each scattering direction the flux vector of the incident light, $\pi\mathbf{\Phi}_{inc}(\lambda, \theta)$, to the flux vector of the scattered light, $\pi\mathbf{\Phi}_{sca}(\lambda, \theta)$. The scattering matrix elements F_{ij} are dimensionless, and they depend on particle's physical properties as size, shape, and refractive index, as well on the wavelength of the incident light. The most general form of a scattering matrix is:

$$\begin{pmatrix} F_{11} & F_{12} & F_{13} & F_{14} \\ F_{21} & F_{22} & F_{23} & F_{24} \\ F_{31} & F_{32} & F_{33} & F_{34} \\ F_{41} & F_{42} & F_{43} & F_{44} \end{pmatrix}, \tag{12.4}$$

where we have sixteen elements. If we suppose that the particles are randomly oriented, certain relationships are given between them (see e.g. Hovenier et al. 2004, Section 2.4.1):

$$\frac{F_{21}(\theta)}{F_{11}(\theta)} = \frac{F_{12}(\theta)}{F_{11}(\theta)}, \tag{12.5}$$

$$\frac{F_{31}(\theta)}{F_{11}(\theta)} = \frac{-F_{13}(\theta)}{F_{11}(\theta)}, \tag{12.6}$$

$$\frac{F_{41}(\theta)}{F_{11}(\theta)} = \frac{F_{14}(\theta)}{F_{11}(\theta)}, \tag{12.7}$$

$$\frac{F_{32}(\theta)}{F_{11}(\theta)} = \frac{-F_{23}(\theta)}{F_{11}(\theta)}, \tag{12.8}$$

$$\frac{F_{42}(\theta)}{F_{11}(\theta)} = \frac{F_{24}(\theta)}{F_{11}(\theta)}, \tag{12.9}$$

$$\frac{F_{43}(\theta)}{F_{11}(\theta)} = \frac{-F_{34}(\theta)}{F_{11}(\theta)}, \tag{12.10}$$

which reduces the complexity to ten independent elements in the scattering matrix. In the case of randomly oriented particles, all scattering planes are equivalent, and the scattering direction is fully described by the scattering angle θ, which is the angle defined by the directions of the incident and scattered beams. Furthermore, if the studied sample consists of particles and their mirror particles in equal numbers, then $F_{13}(\theta)$, $F_{14}(\theta)$, $F_{23}(\theta)$, and $F_{24}(\theta)$ are identically zero for all scattering angles (van de Hulst 1957). Under these conditions of randomly oriented particles and equal amounts of mirror particles, the governing equation relating the flux vectors of the incident and scattered beams can be written as:

$$\mathbf{\Phi}_{sca}(\lambda, \theta) = \frac{\lambda^2}{4\pi^2 D^2} \begin{pmatrix} F_{11} & F_{12} & 0 & 0 \\ F_{12} & F_{22} & 0 & 0 \\ 0 & 0 & F_{33} & F_{34} \\ 0 & 0 & -F_{34} & F_{44} \end{pmatrix} \mathbf{\Phi}_{inc}(\lambda, \theta), \tag{12.11}$$

where only six independent elements in the scattering matrix remain. The first elements of the column vectors are fluxes divided by π, and the other elements describe the state of polarization by means of the Stokes parameters; λ is the wavelength, and D is the distance between the detector and the sample.

The $F_{11}(\theta)$ element describes the angular distribution of scattered light by the sample. It is important to remark that the measured values of $F_{11}(\theta)$ for the aerosol samples in the laboratory setup presented in Sect. 12.2 (Muñoz et al. 2010, 2012)

are arbitrarily normalized so that they are equal to 1 at θ=30°. The function $F_{11}(\theta)$, normalized in this way, is proportional to the flux of the scattered light for unpolarized incident light and called the phase function or scattering function throughout this chapter.

The $-F_{12}(\theta)/F_{11}(\theta)$ ratio is equivalent to the degree of linear polarization for unpolarized incident light. The degree of linear polarization can be defined through the Stokes parameters as:

$$P_L = -\frac{\sqrt{Q_{sca}^2 + U_{sca}^2}}{I_{sca}}, \tag{12.12}$$

but if the incident light is unpolarized, i.e. $U_{inc} = Q_{inc} = V_{inc} = 0$, then Eq. (12.12) simplifies to $-Q_{sca}/I_{sca}$. Also, if measurements are performed at different wavelengths, we can obtain information about the polarization color. This can be described as the difference between the $-F_{12}(\theta)/F_{11}(\theta)$ ratios at two different wavelengths. An example of this feature is presented in Sect. 12.4.

The $F_{22}(\theta)/F_{11}(\theta)$, $F_{33}(\theta)/F_{11}(\theta)$ and $F_{44}(\theta)/F_{11}(\theta)$ ratios can be used as indicators of the non-sphericity of the particle. The Lorenz-Mie theory of light scattering by homogeneous isotropic spheres states that the identities $F_{22}(\theta) \equiv F_{11}(\theta)$ and $F_{33}(\theta) \equiv F_{44}(\theta)$ must be fulfilled. Moreover, the linear and circular backscattering depolarization ratios, δ_L and δ_C respectively, are defined as (see e.g. Mishchenko et al. 2002)

$$\delta_L = \frac{F_{11}(\pi) - F_{22}(\pi)}{F_{11}(\pi) + F_{22}(\pi)}, \tag{12.13}$$

$$\delta_C = \frac{F_{11}(\pi) + F_{44}(\pi)}{F_{11}(\pi) - F_{44}(\pi)}, \tag{12.14}$$

and are related for macroscopically isotropic and mirror-symmetric particles:

$$\delta_C = \frac{2\delta_L}{1 - \delta_L}, \tag{12.15}$$

These coefficients are useful in e.g. the lidar backscatter depolarization technique (LBDT). As these ratios must vanish for spherical particles, the detection of a non-zero ratio is indicative of irregular particles.

12.2 Laboratory Apparatus

In Fig. 12.1 we show the IAA Cosmic Dust Laboratory (IAA-CODULAB) located at the Instituto de Astrofísica de Andalucía. The design is based in the Dutch instrument developed in the group of Prof. J.W. Hovenier at the Free University

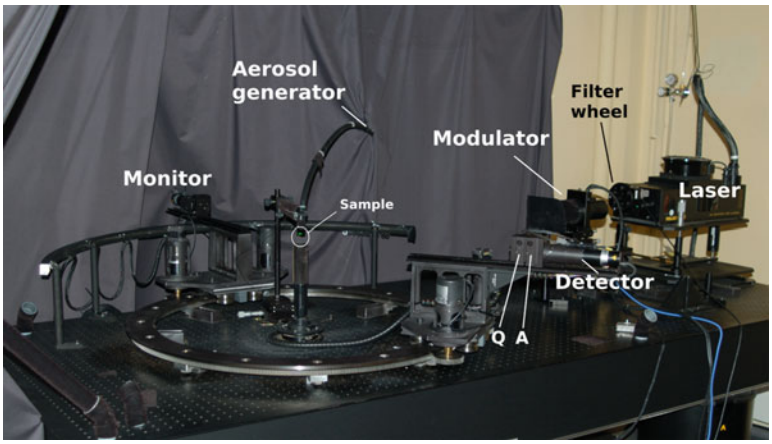

Fig. 12.1 IAA Cosmic Dust Laboratory. The neutral filters are located in a filter wheel between the laser and the modulator. The integrated polarizer is coupled to the modulator. The quarter-wave plate (Q) and the analyzer (A) can be placed in the detector. In the center of the image the dust sample from the nebulizer can be seen as a bright dot. Two photomultipliers gather the signal: the detector which moves from 3° to 177° of scattering angle, and the monitor which is located in a fixed position to correct for fluctuations of dust density in the scattering volume. The sample comes out of the aerosol generator in the center of the apparatus

(Amsterdam) (Hovenier 2000; Volten et al. 2001) following the methodology described by Hunt and Huffman (1973).

A scheme of the setup is displayed in Fig. 12.2. The light source is a tunable Ar-Kr laser, in which the emission wavelength values can be set to 483, 488, 520, 568, or 647 nm. Our measurements are usually presented only for 488, 520, and 647 nm as these wavelength values are far enough from each other to produce differences in the scattering matrix elements. The light beam goes through an integrated polarizer (P) and an electro-optic modulator (M), which are present in all the optical configurations. The beam reaches the scattering volume, usually a dust sample coming from an aerosol generator, or a cloud of water droplets produced by a nebulizer. This design avoids the use of a container for the sample whose walls would potentially distort the scattered field or limit the angular range. The aerosol generator works as follows: a powder sample is loaded and compacted into a cylindrical reservoir; a piston pushes the powder onto a rotating brush at an adjustable speed; an air stream carries the aerosol particles of the brush through a tube to a nozzle above the scattering volume. A schematic picture of the aerosol generator is presented in Fig. 12.3. The light is then scattered by the sample in all directions, reaching two photomultipliers which are placed on a one-meter radius goniometer ring. One of these photomultipliers acts as a detector, which can be moved along the ring from 3° scattering angle (nearly forward scattering) to 177° scattering angle (nearly backward scattering). The other photomultiplier is in a fixed position and works as a monitor to correct for possible fluctuations of the dust flux

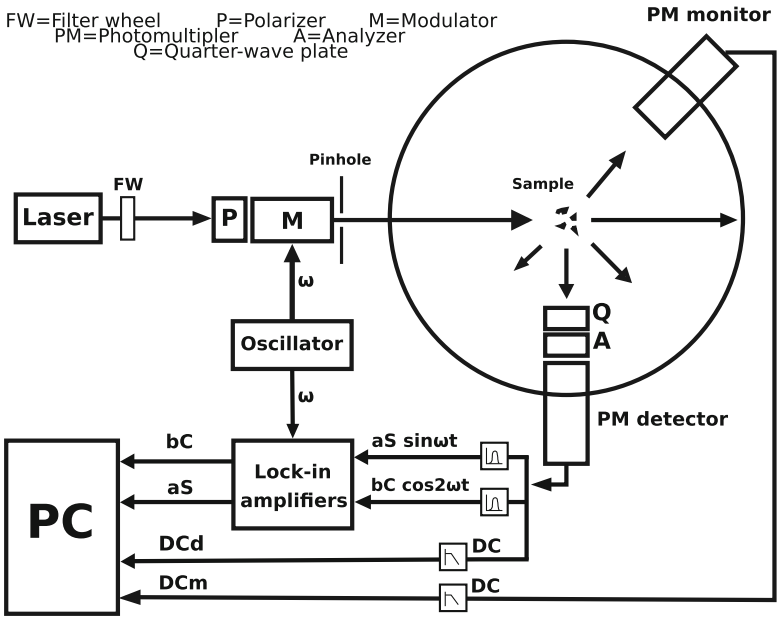

Fig. 12.2 Experimental laboratory scheme from Fig. 12.1 (Muñoz et al. 2010)

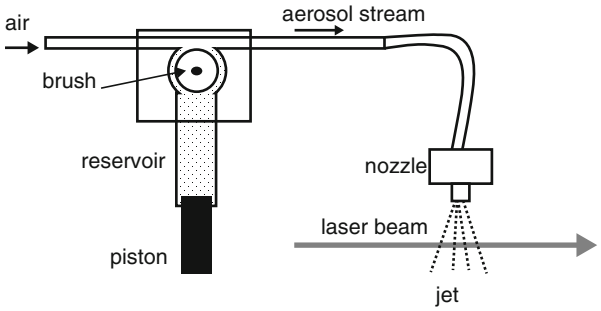

Fig. 12.3 Schematic picture of the aerosol generator. The dust sample in the reservoir is pushed onto the rotating brush by a piston at certain speed. An air stream carries the particles through a tube until a nozzle, which is placed above the laser path (Muñoz et al. 2011)

in the jet stream. Two optical elements can be placed in front of the detector, both optional depending on the optical configuration studied: a second polarizer acting as an analyzer (A), and a quarter-wave plate (Q). Along with these elements, a filter wheel (FW) is placed between the laser and the integrated polarizer (P), and a beam-stop is used to absorb the unscattered part of the incident beam.

The scattered flux vector of the light $\pi\mathbf{\Phi}_{sca}(\lambda,\theta)$ can be computed from the incident flux vector $\pi\mathbf{\Phi}_{inc}(\lambda,\theta)$ through the equation:

$$\mathbf{\Phi}_{sca}(\lambda,\theta) = c_1\mathbf{A}_{\gamma_A}\mathbf{Q}_{\gamma_Q}\mathbf{F}(\theta)\mathbf{M}_{\gamma_M}\mathbf{P}_{\gamma_P}\mathbf{\Phi}_{inc}(\lambda,\theta) \tag{12.16}$$

where **A**, **Q**, **M**, and **P** are the 4 × 4 Mueller matrices of the analyzer, the quarter-wave plate, the modulator, and the polarizer, respectively. The orientation angles γ_A, γ_Q, γ_M, and γ_P of the corresponding optical elements are the angles between their optical axes and the scattering plane, measured counter-clockwise from the scattering plane when looking in the direction of propagation of light. These matrices have the form:

$$\mathbf{A}_\gamma = \mathbf{P}_\gamma = \frac{1}{2}\begin{pmatrix} 1 & C & S & 0 \\ C & C^2 & SC & 0 \\ S & SC & S^2 & 0 \\ 0 & 0 & 0 & 0 \end{pmatrix}, \tag{12.17}$$

$$\mathbf{Q}_\gamma = \begin{pmatrix} 1 & 0 & 0 & 0 \\ 0 & C^2 & SC & -S \\ 0 & SC & S^2 & C \\ 0 & S & -C & 0 \end{pmatrix}, \tag{12.18}$$

where $C = \cos 2\gamma$ and $S = \sin 2\gamma$. However, the electro-optic modulator has a more complex Mueller matrix. It consists of a birefringent crystal whose birefringence is set by an electric field. The parallel and perpendicular components of light emerge from this element with a certain phase shift depending on the electric field applied. If the voltage over the crystal is varied sinusoidally in time, the induced phase shift ϕ varies in the same way. This modulation, in combination with the lock-in amplifiers, increases the accuracy of the measurements and allows to determine several scattering matrix elements simultaneously. In order for this to happen, both electro-optic modulator and lock-in amplifiers must be synchronized through an oscillator. The phase shift is described by the formula:

$$\phi = \phi_c + \phi_0 \sin \omega t, \tag{12.19}$$

where ϕ_c is a constant phase shift owing to the intrinsic birefringence of the modulator crystal, ϕ_0 is the amplitude of the oscillating field and ω is the angular frequency applied to the field. Both ϕ_c and ϕ_0 depend on the wavelength, and must be calibrated when the laser device is tuned to a certain wavelength. ϕ_c is the phase shift produced by the modulator when no voltage is applied, so it must be corrected by the V_{DC} voltage. ϕ_0 is adjusted by the V_{AC} voltage as discussed below.

The Mueller matrix of the electro-optic modulator with an orientation γ_M between the scattering plane and its principal axis is:

$$\mathbf{M}_{\gamma_M}(\phi) = \begin{pmatrix} 1 & 0 & 0 & 0 \\ 0 & C^2 + S^2 \cos\phi & SC(1-\cos\phi) & -S\sin\phi \\ 0 & SC(1-\cos\phi) & S^2 + C^2\cos\phi & C\sin\phi \\ 0 & S\sin\phi & -C\sin\phi & \cos\phi \end{pmatrix}, \tag{12.20}$$

where ϕ is the phase shift from Eq. (12.19). We can decompose $\sin\phi$ and $\cos\phi$ in terms of their harmonics through the Fourier series of Bessel functions of the first kind:

$$\sin\phi = \sin(\phi_0 \sin\omega t) = 2\sum_{k=1}^{\infty} J_{2k-1}(\phi_0)\sin(2k-1)\omega t \tag{12.21}$$

$$\cos\phi = \cos(\phi_0 \sin\omega t) = J_0(\phi_0) + 2\sum_{l=1}^{\infty} J_{2l}(\phi_0)\cos(2l)\omega t \tag{12.22}$$

It is convenient to adjust the modulation voltage V_{AC} so that $J_0(\phi_0) = 0$, i.e. ϕ_0=2.40483 rad. Considering the terms of frequency 2ω or smaller only, the scattered intensity can be written as:

$$\mathbf{\Phi}_{sca}(\lambda,\theta) = c[DC(\theta) + 2J_1(\phi_m)S(\theta)\sin\omega t + 2J_2(\phi_m)C(\theta)\cos 2\omega t], \tag{12.23}$$

where the coefficients $DC(\theta)$, $S(\theta)$ and $C(\theta)$ contain information about the scattering matrix elements, $2J_1(\phi_m)$=1.0383 and $2J_2(\phi_m)$=0.8635 (Muñoz et al. 2010), and c is a constant that depends on the measuring conditions. By using lock-in detection the $\sin\omega t$ and $\cos 2\omega t$ components can be separated from the total detected signal. This electronic configuration allows us to split the signal into $cDC(\theta)$, $c2J_1S(\theta)$ and $c2J_2C(\theta)$. The $c2J_1S(\theta)$ and $c2J_2C(\theta)$ signals are divided by $cDC(\theta)$, so the constant c vanishes. Thus, we can obtain all the scattering matrix elements with a handful of optical arrangements. Table 12.1 provides the results of different optical configurations on each channel.

As an example, if we select configuration 1 in Table 12.1, we obtain:

$$\mathbf{I}_{sca} = \mathbf{F}(\theta)\cdot\mathbf{M}_{0^\circ}\cdot\mathbf{P}_{45^\circ}\mathbf{I}_{in} = \left(\frac{I_{in}+U_{in}}{2}\right)\begin{bmatrix} F_{11} - F_{14}\sin\phi + F_{13}\cos\phi \\ F_{21} - F_{24}\sin\phi + F_{23}\cos\phi \\ F_{31} - F_{34}\sin\phi + F_{33}\cos\phi \\ F_{41} - F_{44}\sin\phi + F_{43}\cos\phi \end{bmatrix} \tag{12.24}$$

Table 12.1 Optical configurations and scattering elements retrieved from the three channels *DC(θ)*, *S(θ)* and *C(θ)* (Muñoz et al. 2010)

Configuration	$\gamma_P(deg)$	$\gamma_M(deg)$	$\gamma_Q(deg)$	$\gamma_A(deg)$	DC(θ)	S(θ)	C(θ)
1	45	0	–	–	F_{11}	$-F_{14}$	F_{13}
2	45	0	–	45	$F_{11}+F_{31}$	$-F_{14}-F_{34}$	$F_{13}+F_{33}$
3	45	0	0	45	$F_{11}+F_{41}$	$-F_{14}-F_{44}$	$F_{13}+F_{43}$
4	0	−45	–	–	F_{11}	$-F_{14}$	F_{12}
5	0	−45	–	0	$F_{11}+F_{21}$	$-F_{14}-F_{24}$	$F_{12}+F_{22}$

The detector only measures the intensity, i.e., the first component of the Stokes vector, $F_{11} - F_{14} \sin\phi + F_{13} \cos\phi$ in the previous equation. The information carried by each channel is F_{11} for the "DC channel", $-F_{14}$ in the "ω channel" ($S(\theta)$ coefficient in Eq. (12.23)) and F_{13} in the "2ω channel" ($C(\theta)$ in the same equation).

12.3 Test Measurements

Owing to the complexity of the instrumental setup, many different tests must be performed to ensure the validity of the measurements. Among this, the correct alignment of the optical setup and the electronics must be tested, along with the fulfillment of the single scattering conditions and the absence of particle agglomeration. Also, the so-called Cloude coherence matrix test should be verified in order to mathematically validate the experimental data (Hovenier and van der Mee 2000).

12.3.1 Water Droplets and Alignment Simulation

To test the optics alignment and electronics of our setup, we perform measurements of the scattering matrix of water droplets and these are compared with a Lorenz-Mie simulations for homogeneous spherical water droplets generated by a nebulizer. Since the size distribution of these water droplets is not known a priori, for the Lorenz-Mie computations a log-normal distribution of spheres is assumed with a refractive index typical for water at visible wavelengths $\mathrm{m}_{water} = 1.33 + i0.0$. The log-normal distribution is characterized by the parameters σ_g and r_g, defined as

$$ln(r_g) = \int_0^\infty ln(rn(r))\mathrm{d}r, \tag{12.25}$$

$$\sigma_g^2 = \int_0^\infty (ln(r) - ln(r_g))^2 n(r)\mathrm{d}r, \tag{12.26}$$

where r is the sphere radius, $n(r)\,dr$ is the fraction of spheres between r and $r+dr$ per unit volume. These parameters are then fitted so that the differences between experimental and theoretical values of the $F_{11}(\theta)$ element and $-F_{12}(\theta)/F_{11}(\theta)$ ratio are minimal. The same procedure is applied at the three studied wavelengths (488, 520, and 647 nm).

In Fig. 12.4 we present a comparison between the experimental measurements for water droplets at 520 nm wavelength and a Lorenz-Mie simulation for homogeneous spheres with a refractive index of m=$1.33 + i0$ and the averaged values for the size distribution obtained from the best fits for the six studied functions, which are equal to r_g=0.68 µm and σ_g=1.76.

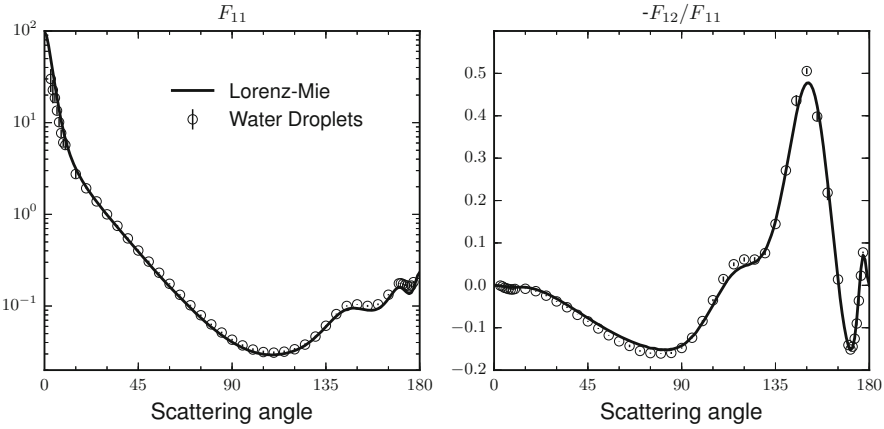

Fig. 12.4 Comparison between the experimental $F_{11}(\theta)$ element and $-F_{12}(\theta)/F_{11}(\theta)$ ratio for water droplets at 520 nm wavelength and a Lorenz-Mie simulation for spheres with a refractive index of $m_{water} = 1.33 + i0$, r_g=0.68 μm and σ_g=1.76

If the Lorenz-Mie simulation and the experimental scattering matrix for water droplets do not match, the differences must be due to systematic errors in the orientation of the principal axis of the optical elements. To locate which optical element could be causing the observed differences, we have developed a computational simulator of the optical train in our experiment based on the report of Kiphardt (1993). This code sequentially simulates errors in the orientation angle γ on each Mueller matrix of the optical elements. Then computes the Eq. (12.16), using as scattering matrix $\mathbf{F}(\theta)$ the results of a Lorenz-Mie simulation for homogeneous water spheres. Depending on the optical configuration (Table 12.1) the output result of the equation can be predicted (as in Eq. (12.24)). The output scattering matrix elements from the code (affected by the misalignment) are plotted against the expected results from the scattering matrix used as test (computed values from the Lorenz-Mie simulation considered as correct), and the misalignment effects are seen as differences between these two datasets. The study of different misalignment combinations on different optical elements gives us an idea of the origin of the problem. The affected element is then realigned accordingly, the experimental matrix is measured again, and the test is performed one more time. As an example, in Figs. 12.5 and 12.6 we present the results of the simulations when errors in the alignment of the optical axis are present in the polarizer, P, and the modulator, M, respectively. The log-normal parameters for the simulated water spheres are r_g=0.75 μm and $\sigma_g = 0.205$, and λ=632.8 nm. Each column corresponds to a channel of information (as described in Eq. (12.23)), and each row corresponds to an optical configuration. In both figures the error values introduced are 4°, 8°, 12° and 16° counter-clockwise. In Fig. 12.7, the same errors that appear in Figs. 12.5 and 12.6 are applied simultaneously to the polarizer and the modulator. It is interesting to note in that figure that certain combinations of misalignments can compensate their effects, as seen in the central column, where no deviation is observed. This makes

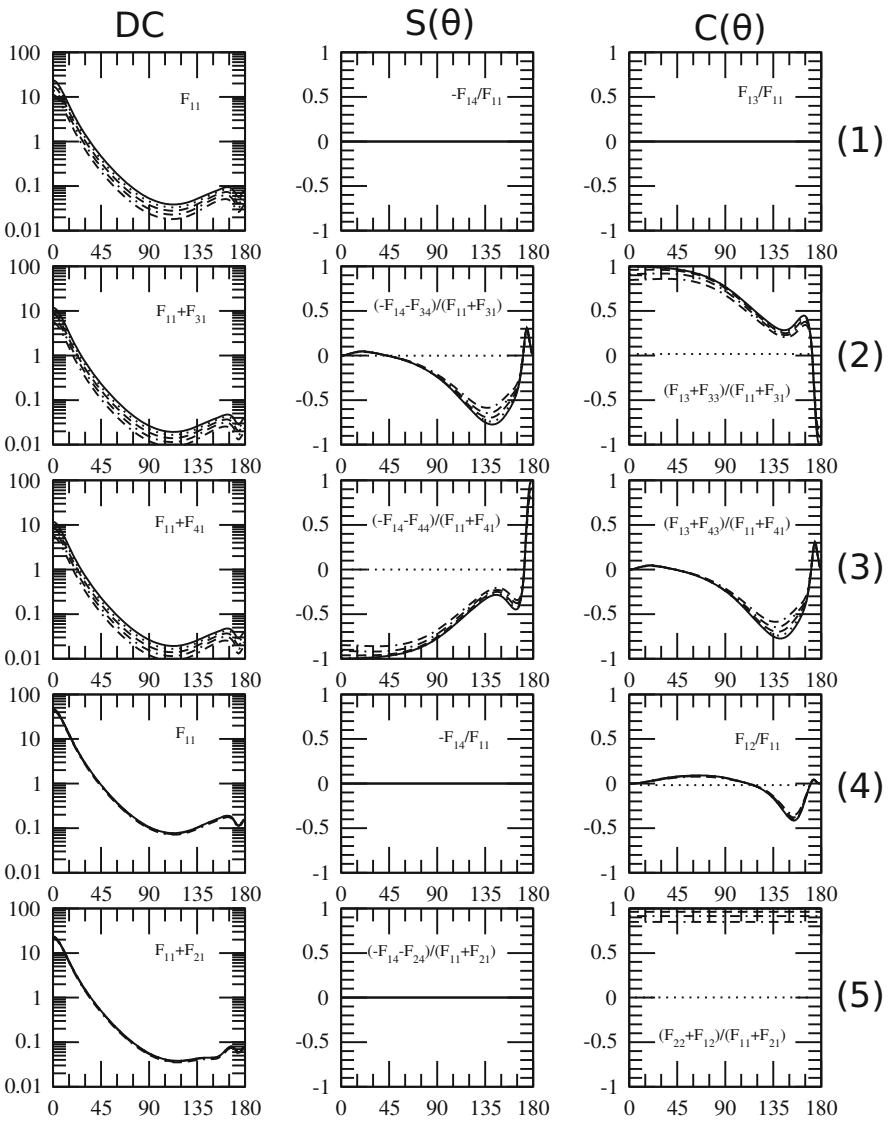

Fig. 12.5 Results of the simulation when the orientation angle of the polarizer is not correctly aligned. The angle errors introduced (counter-clockwise) in degrees are 4 (dotted line), 8 (dashed line), 12 (dot-dashed line) and 16 (dot-dash-dash line). The columns correspond to the channels DC, $S(\theta)$ and $C(\theta)$, and each row corresponds to an optic configuration as shown in Table 12.1

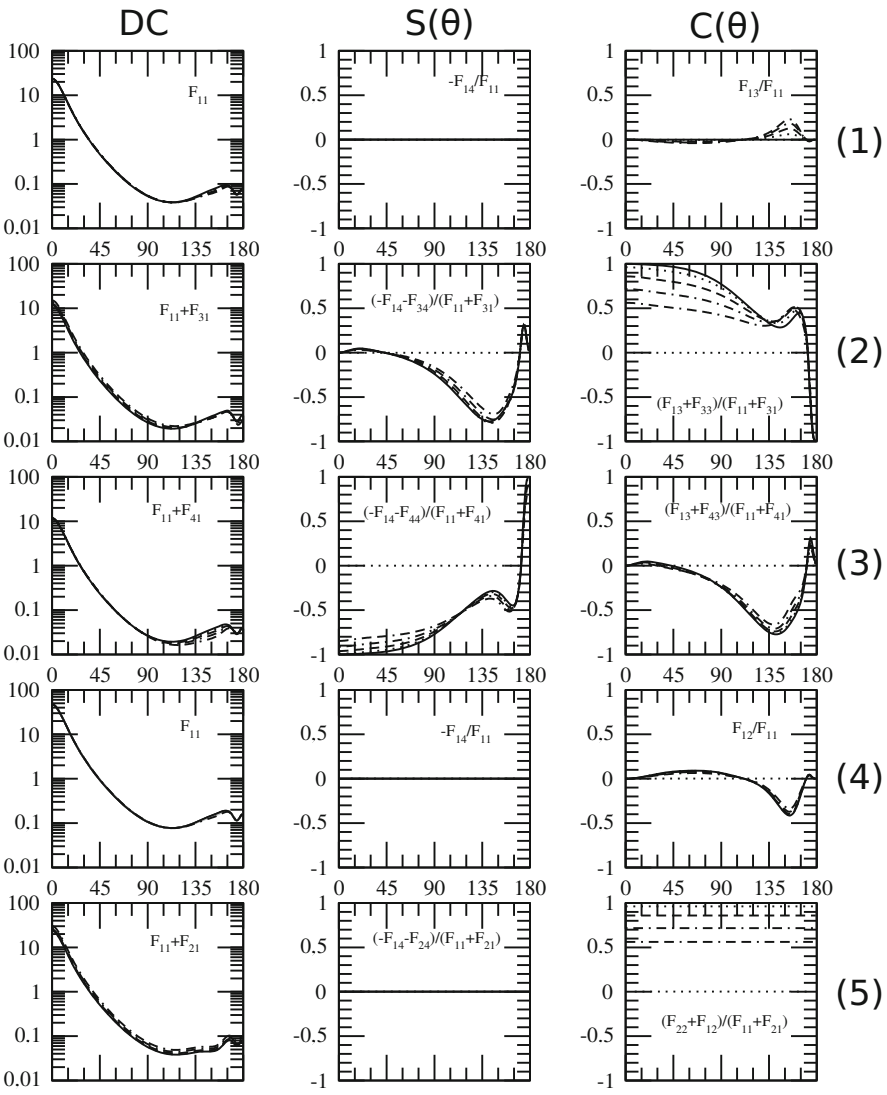

Fig. 12.6 As Fig. 12.5 but the errors are applied to the modulator

uneasy the detection of the cause of these problems. Because of this, it is important to measure and simulate the whole scattering matrix at several wavelengths.

12.3.2 Single Scattering Condition

As stated in the restrictions presented at the beginning of the chapter, the single-scattering condition must be met. The number of particles interacting with the laser

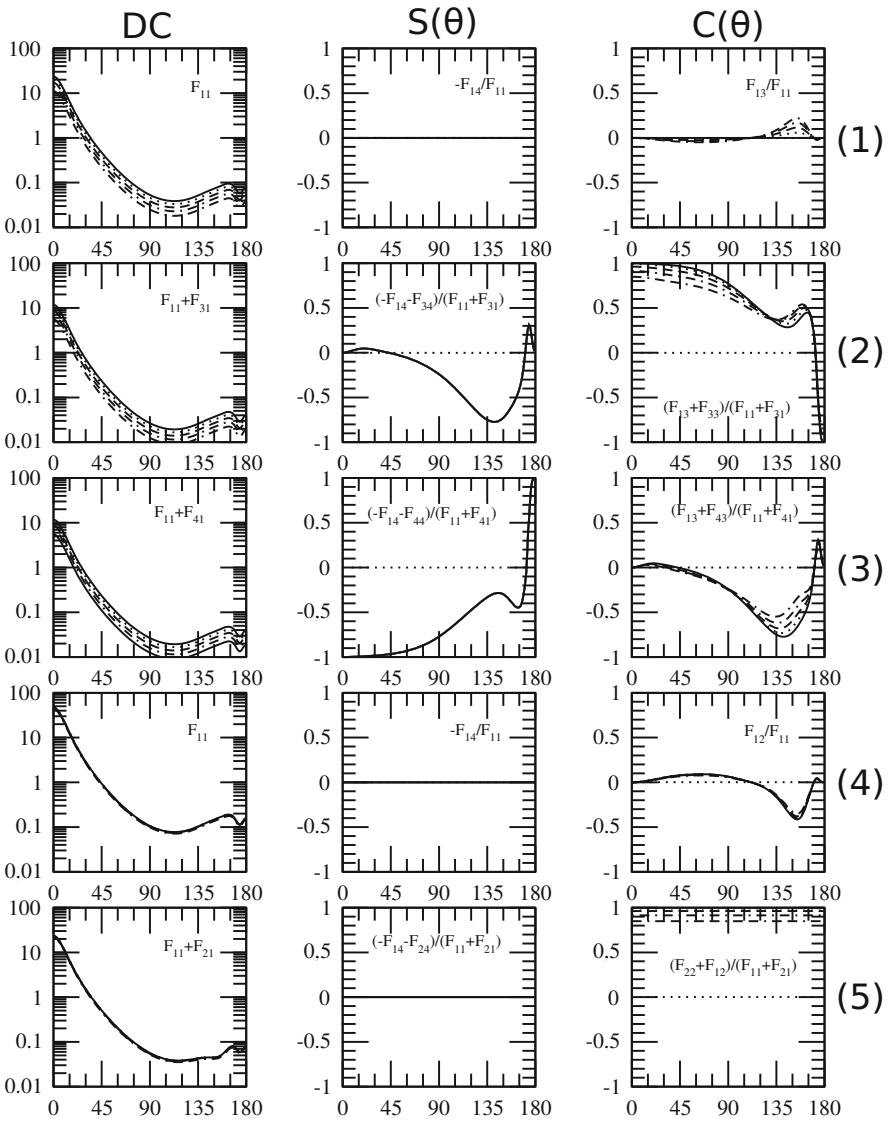

Fig. 12.7 As Figs. 12.5 and 12.6, but equal errors are introduced in both optical elements (counter-clockwise)

during a measurement must be large enough to be representative of the sample, but not so much that multiple scattering may start playing a role.

To test if the single scattering condition is fulfilled in the laboratory, flux measurements with the detector in a fixed position can be made as suggested by Hovenier et al. (2003). Under single scattering conditions, the signal detected must vary linearly with the number density of particles. In the laboratory setup explained

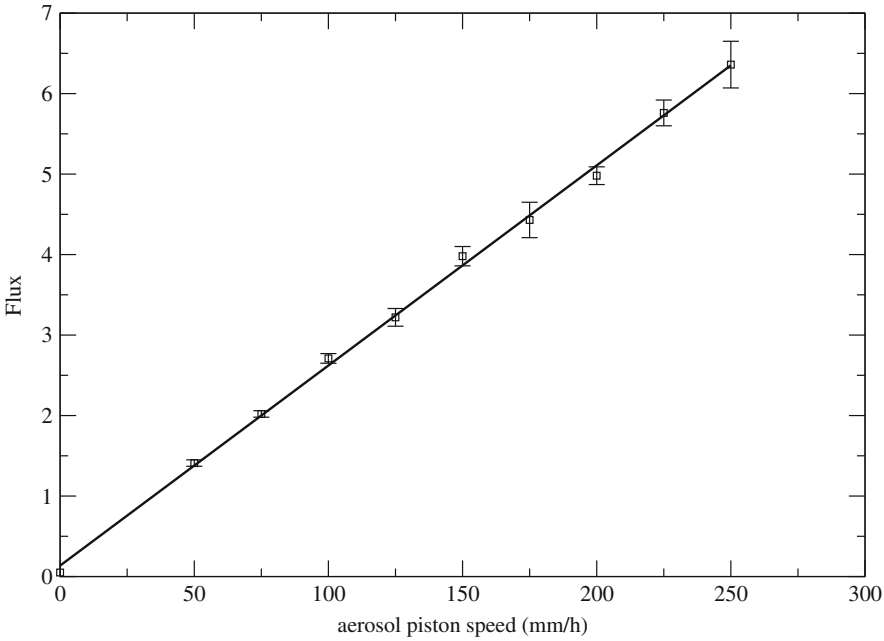

Fig. 12.8 Flux of scattered light (in arbitrary units) versus piston speed for white clay particles. The detector is fixed at a scattering angle of 10° (Muñoz et al. 2011)

in Sect. 12.2, the amount of particles in the scattering volume is controlled by the piston's speed of the aerosol generator. In Fig. 12.8 a test is presented for white clay particles with the detector fixed at a scattering angle of 10°. In this laboratory setup the typical speed used is in the range from 40 to 100 mm/h, depending on the physical properties of the sample and on the wavelength. As it can be seen in the figure, the speed values span from 50 to 250 mm/h, where even at this high value the trend is still linear. The results presented in Fig. 12.8 confirm that the measurements are carried out in single-scattering conditions.

12.3.3 Particle Aggregation

One reasonable question about the laboratory setup is if the aerosol generator changes the shape/size of the sample studied, either by breaking the particles into smaller ones or by inducing some agglomeration. To test this, Field Emission Scanning Electron Microscope (FESEM) images are taken from the sample from the jet stream after it comes out from the aerosol generator. These are compared with images taken from unprocessed sample extracted directly from the container. As it can be seen in Fig. 12.9, there are no substantial changes between the left panel (sample from the container) and the right panel (sample after it passes through

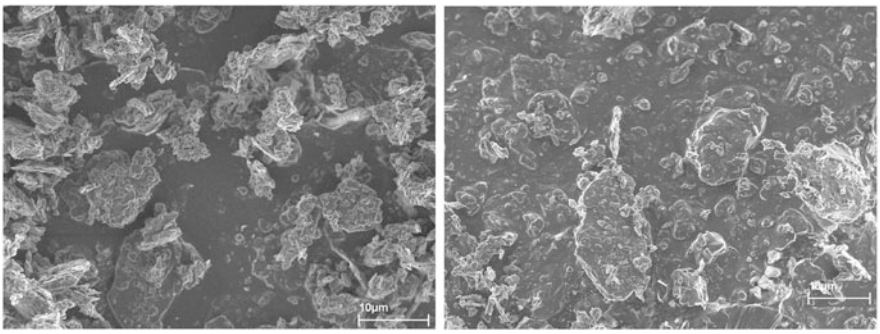

Fig. 12.9 Field emission scanning electron microscope images of white clay particles. The left panel shows the particles before passing through the aerosol generator. The right panel is the sample gathered in the scattering volume where interacts with the laser, after passing the aerosol generator

the aerosol generator). The particles show same general structure and surface roughness, which indicates that no damage has occurred to the shapes. Also we can notice very small particles adhered to the surfaces of larger particles, probably due to electrostatic force. This results prove that the sample maintains its size and shape properties through the aerosol generator.

12.3.4 Cloude Coherency Matrix Test

One final test can be performed to check whether the measured scattering matrix is actually a phase matrix representative of a collection of particles. The scattering matrix **F** must be a sum of pure Mueller matrices. To check this, several type of tests have been proposed (see Hovenier and van der Mee 2000, and references therein). Among these, the Cloude coherency matrix test has been thoroughly used as validity test for measured scattering matrices over the past three decades. The coherency matrix **T** is computed from **F** through linear transformations (Hovenier et al. 2004). This matrix **T** is always Hermitian, so its eigenvalues are real. If all four of these eigenvalues are non-negative and at least one of them is positive, then **F** is a sum of pure Mueller matrices, and the test is fulfilled.

12.4 Measurements with Clouds of Small Cosmic Dust Particles: Applications

From laboratory measurements we have been able to recognize some general trends in the scattering behavior of ensembles of realistic samples of cosmic dust particles. As an example, in Fig. 12.10, we compare the measured scattering matrix elements

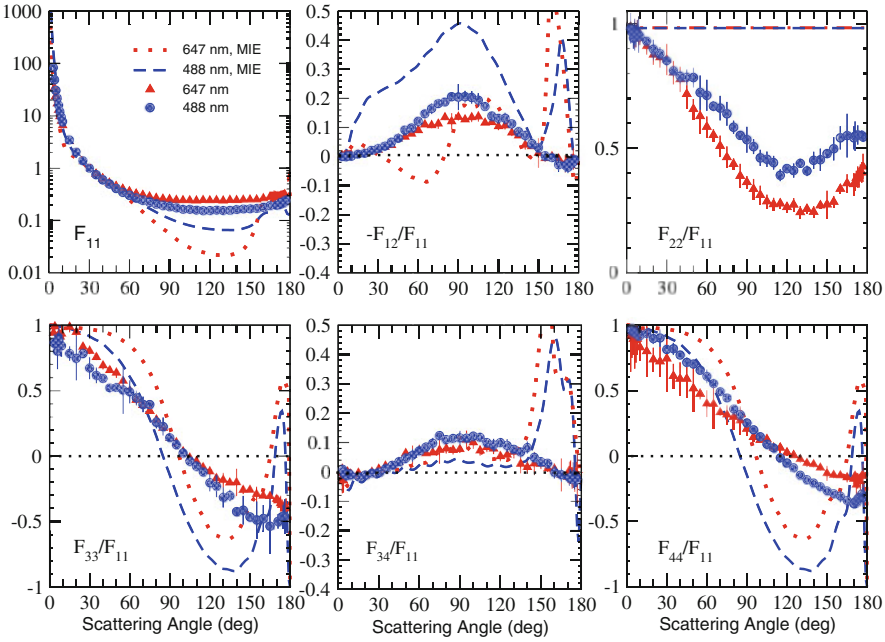

Fig. 12.10 Measured scattering matrix elements as functions of the scattering angle at 488 nm (circles) and 647 nm (triangles) for the JSC Mars-1 Martian dust analog sample. Dashed and dotted lines correspond to Lorenz-Mie calculations for spheres at 488 and 647 nm, respectively. For the Lorenz-Mie calculations we have used the same size distribution and refractive index as the JSC Mars-1 sample (Dabrowska et al. 2015)

as functions of the scattering angle of a Martian dust analog labeled as JSC Mars-1, where JSC stands for Johnson Space Center. The JSC sample consists of the <1 mm size fraction of a palagonitic tephra (glassy volcanic ash altered at low temperatures). The measurements have been performed at the IAA-CODULAB at 488 and 647 nm (Dabrowska et al. 2015). The experimental data are presented together with Lorenz-Mie calculations at the corresponding wavelengths. For the Lorenz-Mie calculations we employ the number size distribution and estimated refractive index of the JSC Mars-1 sample. In particular, $m(448\,\text{nm}) = 1.52 + i0.01$ and $m(647\,\text{nm}) = 1.50 + i0.01$ (Clancy et al. 1995). Tables with the measured scattering matrices and size distribution of the JSC Mars-1 sample are freely available at the Amsterdam-Granada Light scattering Database (www.iaa.es/scattering) under the request of citation of the paper in which data were published (Dabrowska et al. 2015) and Muñoz et al. (2012).

As it is shown in Fig. 12.10, the scattering pattern for spherical particles cannot be used to reproduce the behavior of natural, irregularly-shaped dust particles. In particular, the relative differences between calculated and experimental phase functions ($F_{11}(\theta)$ element) are strong at side-scattering and remarkable at back-scattering angles. Moreover, the measured degree of linear polarization for

incident unpolarized light shows positive values at nearly all scattering angles with a maximum in the 90–100° region and a negative branch at backward direction. This is a typical behavior for irregular mineral dust as shown in e.g. Muñoz et al. (2004) and many examples at the Amsterdam-Granada Light scattering Database (www.iaa.es/scattering). In contrast, the calculated $-F_{12}(\theta)/F_{11}(\theta)$ produces a considerable overestimation at nearly all scattering angles at 488 nm whereas it produces an underestimation in the forward lobe at 647 nm when comparing with the experimental data. Moreover, the $F_{22}(\theta)/F_{11}(\theta)$ is equal to 1 at all scattering angles for spherical particles while the measured results for the JSC Mars-1 dust analog strongly deviate from 1 at nearly all measured scattering angles. Significant differences between calculated and measured values are also found for the other elements of the scattering matrix. Similar differences are found for many other irregular cosmic dust samples, showing that Lorenz-Mie theory can often give bad results.

The experimental data can also be used in a direct manner, e.g. by comparison with astronomical observations of light scattered in single scattering conditions. Further, experimental scattering matrices are used to check the validity of computational techniques devoted to simulate the scattering behavior of realistic polydisperse irregular particles e.g. Moreno et al. (2004), Dubovik et al. (2006), and Nousiainen (2009). An interesting example is related to Martian dust. The scattering function at a certain wavelength of Martian dust particles has been often derived by using the semi-empirical theory for nonspherical particles developed by Pollack and Cuzzi (1980). The efforts have been focused on the use of more sophisticated model particles, namely cylinders, to calculate the phase function of Martian dust particles (Wolff et al. 2006). Even so, as pointed out by Wolff et al. (2010), the calculated phase functions for a size distribution of cylinders produce a considerable overestimation of the phase function near back-scattering direction when comparing with observations of Martian dust. However, that overestimation is not observed when the phase function of natural dust particles is experimentally obtained in the laboratory (Muñoz et al. 2012). As presented in Fig. 12.11, the experimental phase function for a basalt sample shows an excellent agreement with the observations from Wolff et al. (2010). In contrast, none of the computed phase functions (Lorenz-Mie for spheres or cylinders) reproduce the observations for Mars.

Further, based in our experimental data, spectropolarimetry appears to be a powerful diagnostic tool for inferring the composition of Martian dust. In Fig. 12.12, we present the measured degree of linear polarization for basalt and the JSC Mars-1 samples. The measurements have been performed at 488 and 647 nm. The basalt sample, whose refractive index shows a nearly flat wavelength dependence in the visible, presents a red polarization color (the maximum of the $-F_{12}(\theta)/F_{11}(\theta)$ shows higher values at 647 nm than at 488 nm). In contrast, the JSC Mars-1 that presents a significantly higher imaginary part of the refractive index at 488 nm than at 647 nm, shows a blue polarization color. Thus, the polarization color is directly dependent on the refractive index of the particles showing a red polarization color those particles with a flat dependence of the imaginary part of the refractive index at visible wavelengths and blue polarization color if it is significantly higher at blue than at red wavelengths.

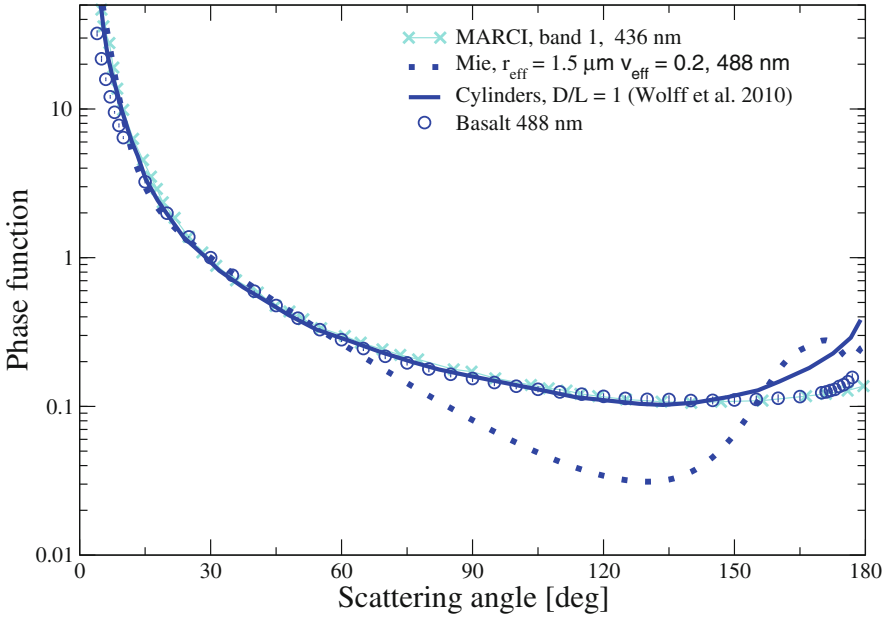

Fig. 12.11 Pseudo emission phase function from MARCI band 1 (Wolff et al. 2010) at 436 nm (crosses). We also present the calculated phase functions for spheres (dotted line) and cylinders (solid line) together with our measurements for a Martian dust analog, basalt, at 488 nm (circles) from Dabrowska et al. (2015)

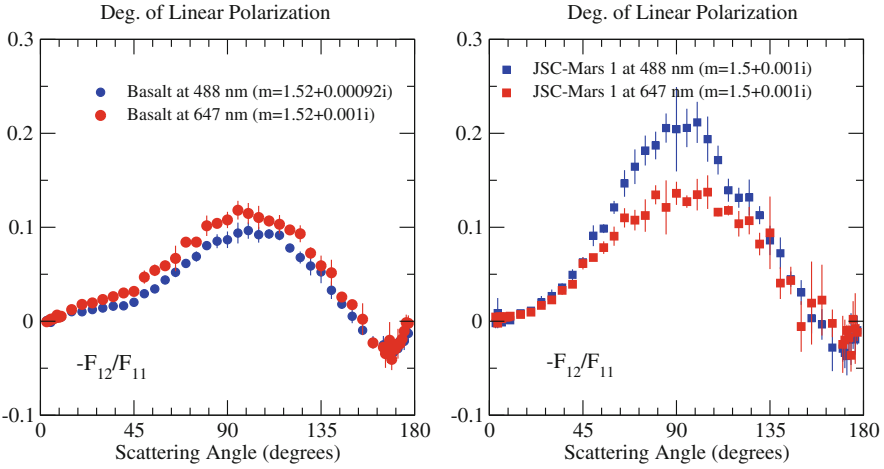

Fig. 12.12 Measured degree of linear polarization as function of the scattering angle at 488 nm (blue symbols) and 647 nm (red symbols). The left panel correspond to a basalt sample and the right panel to the JSC Mars-1 sample

References

Clancy, R.T., Lee, S.W., Gladstone, G.R., McMillan, W.W., Rousch, T.: A new model for Mars atmospheric dust based upon analysis of ultraviolet through infrared observations from Mariner 9, Viking, and PHOBOS. J. Geophys. Res. **100**, 5251–5263 (1995). https://doi.org/10.1029/94JE01885

Dabrowska, D.D., Muñoz, O., Moreno, F., Ramos, J.L., Martínez-Frías, J., Wurm, G.: Scattering matrices of martian dust analogs at 488 nm and 647 nm. Icarus **250**, 83–94 (2015)

Dubovik, O., Sinyuk, A., Lapyonok, T., Holben, B.N., Mishchenko, M., Yang, P., Eck, T.F., Volten, H., Mu noz, O., Veihelmann, B., van der Zande, W.J., Leon, J.-F., Sorokin, M., Slutsker, I.: Application of spheroid models to account for aerosol particle nonsphericity in remote sensing of desert dust. J. Geophys. Res. Atmos. **111**, D11208 (2006). https://doi.org/10.1029/2005JD006619

Hovenier, J.W.: Measuring scattering matrices of small particles at optical wavelengths. In: Mishchenko, M.I., Hovenier, J.W., Travis, L.D. (eds.) Light Scattering by Nonspherical Particles, 1st edn. chap. 12, pp. 355–365. Academic, New York (2000)

Hovenier, J.W., van der Mee, C.: Relationships for matrices describing scattering by small particles. In: Mishchenko, M.I., Hovenier, J.W., Travis, L.D. (eds.) Light Scattering by Nonspherical Particles, 1st edn., chap. 3, pp. 61–89. Academic, New York (2000)

Hovenier, J.W., Volten, H., Muñoz, O., van der Zande, W.J., Waters, L.B.: Laboratory study of scattering matrices for randomly oriented particles: potentials, problems, and perspectives. J. Quant. Spectrosc. Radiat. Transf. **79**, 741 (2003)

Hovenier, J.W., Van Der Mee, C., Domke, H. (eds.): Transfer of Polarized Light in Planetary Atmospheres: Basic Concepts and Practical Methods. Astrophysics and Space Science Library, vol. 318. Springer, New York (2004)

Hunt, A.J., Huffman, D.R.: A new polarization-modulated light scattering instrument. Rev. Sci. Instrum. **44**, 1753–1762 (1973)

Kiphardt, M.M. (ed.): Experimental determination of scattering matrices of ice crystals. Graduation Report (1993)

Mishchenko, M.I.: Electromagnetic Scattering by Particles and Particle Groups. Cambridge University Press, New York (2014)

Mishchenko, M.I., Hovenier, J.W., Travis, L.D.: Light Scattering by Nonspherical Particles: Theory, Measurements, and Applications. IOP Science, New York (2000)

Mishchenko, M.I., Travis, L.D., Lacis, A.A.: Scattering, Absorption, and Emission of Light by Small Particles. Cambridge University Press, Cambridge (2002)

Moreno, F., Lara, L.M., Muñoz, O., López-Moreno, J.J., Molina, A.: Dust in Comet 67P/Churyumov-Gerasimenko. Astrophys. J. **613**, 1263–1269 (2004). https://doi.org/10.1086/423268

Muñoz, O., Volten, H., Hovenier, J.W., Veihelmann, B., van der Zande, W.J., Waters, L.B.F.M., Rose, W.I.: Scattering matrices of volcanic ash particles of Mount St. Helens, Redoubt, and Mount Spurr Volcanoes. J. Geophys. Res. Atmos. **109**, D16201 (2004). https://doi.org/10.1029/2004JD004684

Muñoz, O., Moreno, F., Guirado, D., Ramos, J.L., López, A., Girela, F., Jerónimo, J.M., Costillo, L.P., Bustamante, I.: Experimental determination of scattering matrices of dust particles at visible wavelengths: the IAA light scattering apparatus. J. Quant. Spectrosc. Radiat. Transf. **111**, 187–196 (2010)

Muñoz, O., Moreno, F., Guirado, D., Ramos, J.L., Volten, H., Hovenier, J.W.: The IAA cosmic dust laboratory: experimental scattering matrices of clay particles. Icarus **211**, 894–900 (2011)

Muñoz, O., Moreno, F., Guirado, D., Dabrowska, D.D., Volten, H., Hovenier, J.W., The Amsterdam-Granada light scattering database. J. Quant. Spectrosc. Radiat. Transf. **113**, 565–574 (2012)

Nousiainen, T.: Optical modeling of mineral dust particles: a review. J. Quant. Spectrosc. Radiat. Transf. **110**, 1261–1279 (2009)

Pollack, J.B., Cuzzi, J.N.: Scattering by nonspherical particles of size comparable to wavelength - a new semi-empirical theory and its application to tropospheric aerosols. J. Atmos. Sci. **37**, 868–881 (1980). https://doi.org/10.1175/1520-0469(1980)037\T1\textless0868:SBNPOS\T1\textgreater2.0.CO;2

van de Hulst H. C.: Light Scattering by Small Particles. Wiley, New York (1957)

Volten, H., Muñoz, O., Rol, E., de Haan, J.F., Vassen, W., Hovenier, J.W., Muinonen, K., T.: Scattering matrices of mineral aerosol particles at 441.6 nm and 632.8 nm. J. Geophys. Res. **106**, 17375–17402 (2001). https://doi.org/10.1029/2001JD900068

Wolff, M.J., Smith, M.D., Clancy, R.T., Spanovich, N., Whitney, B.A., Lemmon, M.T., Bandfeld, J.L., Banfeld, D., Ghosh, A., Landis, G., Christensen, P.R., Bell, J.F., Squyres, S.W.: Constraints on dust aerosols from the Mars Exploration Rovers using MGS overflights and Mini-TES. J. Geophys. Res. Planets **111**, E12S17 (2006). https://doi.org/10.1029/2006JE002786

Wolff, M. J., Todd Clancy, R., Goguen, J.D., Malin, M.C., Cantor, B.A.: Ultraviolet dust aerosol properties as observed by MARCI. Icarus **208**, 143–155 (2010). https://doi.org/10.1016/j.icarus.2010.01.010

Chapter 13
Infrared Spectroscopy of Ions of Astrophysical Interest

José-Luis Doménech

Abstract Molecular ions are key species in the chemistry of the interstellar medium (ISM). Given the low temperatures and number densities typically occurring in the ISM, one of the few available mechanisms to form more complex molecules is through barrierless exothermic reactions, as it is the case for many ion-molecule reactions. Ions are highly reactive species but they can be formed efficiently in the ISM by cosmic-ray or ultraviolet ionization and can survive for relatively long times due to the few collisions they suffer. On earth, molecular ions are "exotic" species much more difficult to produce in appreciable quantities. Electrical discharges in low pressure gases form cold plasmas which can be used to produce molecular ions in abundances high enough to enable their spectroscopic study.

13.1 Introduction: Spectroscopy, Astrophysics, Chemistry and Plasmas All Stirred

The light coming from space, wether it reaches our eyes or the detectors in the most sophisticated telescopes, is the only way to gather knowledge about the "vastly, hugely, mind-bogglingly big" (Adams 1979) space surrounding our solar system. Just the closest planets or asteroids can be reached by probes capable of performing in situ analysis. The rest of the Universe can only be investigated analyzing the quantity and distribution of the light emitted, scattered or absorbed by the zoo of astronomical environments in our galaxy and beyond. Surpassing imaging and photometry, spectroscopy at all wavelengths is the most powerful tool to gain insight about the chemical composition and the physical conditions out there, and it is not surprising that astronomy and spectroscopy have walked hand in hand since the development of the latter in the early nineteenth century.

J.-L. Doménech (✉)
Molecular Physics Department, Instituto de Estructura de la Materia (IEM-CSIC), Madrid, Spain
e-mail: jl.domenech@csic.es

G. M. Muñoz Caro, R. Escribano (eds.), *Laboratory Astrophysics*,
Astrophysics and Space Science Library 451,
https://doi.org/10.1007/978-3-319-90020-9_13

For more than one hundred years astronomical spectroscopy was mostly devoted to the analysis of stars, comets, nebulae and galaxies, all of them bright sources in the visible region of the spectrum, and atomic spectroscopy was the tool to gather information about the composing elements and their excitation or ionization state. It was not until (roughly) the beginning of the twentieth century that it became increasingly evident that the interstellar medium was not empty, and that, furthermore, that harsh environment did not contain only atoms and their ions, but also chemically bonded species. Until then, it was generally assumed that any molecule would be dissociated, the constituent atoms would lose their valence electrons and the formation of a new bond would be impossible. Eddington (1926) suggested that the opacity of interstellar clouds could be explained by the presence of molecules shielded from the radiation field, and the discovery of absorption lines of CH, CN and CH^+ against bright visible stars in the period 1937–1941 proved the existence of molecules in interstellar space (see e.g. Herzberg 1980 for a recollection of these early discoveries). Twenty years later a new diatomic molecule, the radical OH, was identified by its radio emission (Weinreb et al. 1963), and a few years afterwards the first polyatomic, ammonia (NH_3, by Cheung et al. 1968), also by its microwave emission.

To make a really long story short, the development of astronomical spectroscopy techniques, most notably, radioastronomy, brought up the science of molecular astrophysics, a.k.a astrochemistry. Up to today, around 200 molecules (including closed-shell neutrals, radicals, cations and anions), with up to 60 atoms, have been identified in space, revealing that there is a rich chemistry up there that has to be understood. Updated lists of identified molecules in the interstellar and circumstellar medium, together with bibliographic references, can be found in the web page maintained by D. E. Woon (www.astrochimist.org) or in the Cologne Database for Molecular Spectroscopy (Müller et al. 2001, 2005) at www.astro.uni-koeln.de/cdms/molecules. More descriptive accounts have been written over the years, e.g. Menten and Wyrowski (2011) and Kroto (1981).

The classification or description of the different environments of the ISM is well beyond the scope of this chapter and of the abilities of the author, and readers are referred to the reviews by Snow and McCall (2006) and Snow and Bierbaum (2008) or to many books on molecular astrophysics.

There is no single model of chemistry in space. Different processes prevail in different environments, and, moreover, astronomical observations are not always able to resolve a "pure" environment. Rather, the same line of sight intercepts different regions. The ISM is heterogeneous, with more diffuse regions permeated by UV radiation, and cold dusty regions shaded from UV but exposed to cosmic rays, with globular or filamentary structures with different densities, temperatures and dust content. However, most models for chemical reactions in the ISM, share two common basic premises: (1) given the low densities in the ISM, collisions are binary, and (2) dust grain surfaces are key elements by providing an energy release path for binary encounters (recall that a binary collision cannot result in a bond between the colliders unless there is a way to release part of the kinetic energy of the colliding pair, either a third body or the emission of a photon). The first

attempts to model gas phase chemistry in dark clouds (e.g. Watson 1973; Herbst and Klemperer 1973; Black et al. 1978) already relied on ion-molecule reactions as an important mechanism to form new molecules, as these reactions are typically exothermic and barrierless. The role of dust grains in the formation of the most abundant molecule, H_2, was discussed by Hollenbach and Salpeter (1971) and for a variety of other molecules by Tielens and Hagen (1982).

Most of the molecules identified in space have been found in dense clouds, where the central role in initiating the chemistry is played by the ion H_3^+, which, in turn, is formed upon ionization of H_2 by cosmic rays followed by a collision with another H_2 molecule:

$$H_2^+ + H_2 \rightarrow H_3^+ + H. \tag{13.1}$$

The proton affinity of H_2 is rather low, and H_3^+ acts as a proton donor to almost any other molecule or atom upon collision, in a reaction of the type

$$X + H_3^+ \rightarrow XH^+ + H_2. \tag{13.2}$$

(Only the proton affinities of He, Ne, Ar, N, and O_2 are smaller than that of the abundant H_2, and then the previous reaction does not proceed.) In general, the species XH^+ is much more reactive than X, initiating a chain of reactions forming more complex molecules. In particular the reaction $H_3^+ + CO \rightarrow HCO^+ + H_2$ produces the most abundant ion in dense clouds, HCO^+, which was the second molecular ion to be detected in space and the first to be detected by its rotational emission. In fact it took several years before it was detected in the laboratory, definitely sanctioning the ion-molecule mechanism. Since then, many other cations have been detected: N_2H^+, HCS^+, $HOCO^+$, HOC^+, NO^+, $HCNH^+$, H_3O^+, SO^+, CO^+, HC_3NH^+, H_3^+, H_2COH^+, CF^+, H_2O^+, OH^+, H_2Cl^+, HCl^+, SH^+, C_3H^+, C_{60}^+, NH_4^+, ArH^+, H_2NCO^+, NO^+, $NCCNH^+$ and NS^+. As it can be seen, many of them can be considered protonated forms of neutral molecules. It is worth noting that, although astronomers had considered some processes through which anions might form in interstellar clouds and circumstellar envelopes, it was not until the detection in 2006 of a rotational line emission from C_6H^- that their role in astrochemistry was vindicated (Millar et al. 2017). Anions identified up to now are C_nN^- ($n = 1, 3, 5$) and C_nH^- ($n = 4, 6, 8$).

In order to assign any spectral feature in an astronomical observation to a particular spectroscopic transition of a particular molecule, the frequency of that transitions must be accurately known. In other words, laboratory spectroscopy has to provide the transition frequencies, and, if possible, also the Einstein coefficients, in order to interpret astronomical spectra. It is quite safe to state that no identification of any species in space is secure if there is not reliable laboratory support for it.

The infrared study of ions in the laboratory requires to have a column density of ions in the observation volume high enough to allow for their detection. This is not an easy task. In the ISM the densities are so low ($\sim 10^4\,cm^{-3}$ in a typical dense

cloud, or $10^2\,\mathrm{cm}^{-3}$ in a diffuse cloud) that collisions take place very rarely and the reactive molecular ions can survive for a long time. Under the best laboratory conditions, it is exceedingly difficult to achieve a vacuum of $\sim 10^{-12}$ mbar (roughly $10^4\,\mathrm{cm}^{-3}$) and obviously the optical path is negligible, compared to that in an interstellar cloud, forcing us to devise ways to generate molecular ions in much more abundant quantities to produce detectable absorptions or emissions. Cold plasmas formed in low pressure electrical discharges ("glow discharges") are one of those environments.

A very general definition of a plasma is *an electrically quasi-neutral gas formed by neutral and charged particles that exhibits a collective behaviour*. Usually, the negative charged particles are mostly electrons, and cations maintain the electrical neutrality of the system. In a simple scheme, plasmas can be classified into *thermal* plasmas and *cold* plasmas. Thermal plasmas usually happen at high pressure ($\sim$1 bar) and they exhibit local thermal equilibrium (LTE) between the different types of particles (electrons, ions and neutrals), all possessing quite a high energy content (10^2–10^4 eV). Examples are flames, arcing, lightning or fusion plasmas. Cold plasmas lack LTE, with electrons having a much higher temperature (1–10 eV or 10^4–10^5 K) than the positive ions, that are at nearly the same temperature than the neutrals (or the bulk of the system). Examples are the ionosphere, the aurorae, or glow discharges. The *degree of ionization* (the ratio of the number density of ions to the sum of the number densities of ions and neutrals) in a glow discharge is rather low, 10^{-4}–10^{-6}, meaning that only a small fraction of the neutral species becomes ionized.

Glow discharges are luminous electrical discharges which glow due to the emission from electronically excited states. Very succinctly, the very few free electrons in a low pressure gas (produced by natural radioactivity or cosmic rays) are accelerated by the electric field between the electrodes and gain kinetic energy. Upon collision with neutral particles, owing to the huge mass difference, little kinetic energy is transferred, but the neutrals can be ionized releasing new electrons that start a sort of chain reaction, called *Townsend's avalanche*. The heavier ions and the neutrals accelerated by collisions with the ions, can strike the surface of the cathode releasing *secondary electrons*, and it is actually this secondary electrons emission that sustains the discharge. For the purposes of this introduction, lets suffice to say that this type of glowing plasma is a highly reactive medium with translationally cold ions and molecules. Depending on the geometry of the discharge, and the type and position of the electrodes, the plasma can exhibit a complex pattern of bright and dark regions determined by electron-gas interactions (see Fig. 13.1). Also for the purposes of this description, two luminous regions are the most relevant, the *negative glow* and the *positive column* (see e.g. Piel 2010 or Fridman 2008 for detailed descriptions of the anatomy of a glow discharge). The negative glow resides close to the cathode, the electric field is close to zero and it is the region with the highest ion density. The positive column occupies a region near the anode and has a weak axial field. In a typical Crookes-type discharge, by increasing the distance between electrodes, the positive column can occupy most of

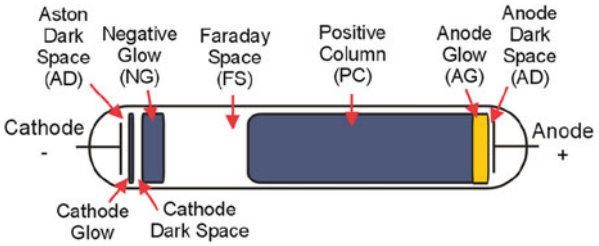

Fig. 13.1 A diagram showing the different glowing regions in the gas that appear when a high DC voltage is applied between the electrodes of a Crookes tube. http://en.wikipedia.org/wiki/User:Iantresman (https://commons.wikimedia.org/wiki/File:Electric_glow_discharge_schematic.png), "Electric glow discharge schematic", https://creativecommons.org/licenses/by/2.5/legalcode

the volume, while the reverse can make it disappear. Other important types of glow discharges, besides the DC discussed above, are radio frequency discharges and microwave discharges. Energy is coupled into the system capacitively or inductively at frequencies of 13.56 or 2450 MHz typically.[1] Although they have some useful properties in the formation of ions and radicals, they have been less widely used than DC discharges for the study of astrophysical ions.

It has already been stated that rotational spectroscopy has been instrumental in our knowledge about the molecular universe, but, of course, it is not the only tool. In particular, high resolution IR spectroscopy, accessing transitions among vibration-rotation levels, has some unique characteristics that are of benefit in this field. First, all polyatomic molecules, regardless of their permanent electric dipole moment, have IR absorption spectra. Only homonuclear diatomics escape, and not all of them, since, e.g. H_2 can be detected by its quadrupole transitions. Some very important interstellar molecules have no permanent dipole moment, and have been detected by its IR spectrum: H_3^+, CH_4, SiH_4, C_2H_2, C_3, to name a few. For the particular case of ions, some of them, like H_3^+ do not have bound electronic excited states, and no vis–UV spectrum. Second, for the same reflector size, the higher frequency of the radiation allows for higher spatial resolution. Also, different sources and objects can be studied: the infrared region of the spectrum is particularly valuable for investigating cool thermal sources (i.e. temperatures less than a few thousand K) as well as any astronomical sources that are highly extinguished by foreground dust. Finally, the analysis of vibration-rotation bands provide the energy levels of the upper and lower vibrational states, which, indirectly, allows us to compute the frequencies of the rotational transitions (see Sects. 13.3.2 and 13.3.3). Because of their large rotational constants, many light protonated ions have widely spaced rotational lines, and, often, only one or two can be measured with the same

[1]There is nothing magical about these particular frequencies. They are within bands assigned by the International Telecommunication Union for Industrial, Scientific and Medical (ISM!) purposes, other than radiocommunications.

instrument, both in the lab and in radiotelescopes. In the IR domain, the same setup can cover wide spectral regions. Although, generally speaking, instrumental resolution and frequency accuracy are higher in the radiofrequency domain, both laboratory and astronomical instrumentation in the IR are becoming more and more refined, and the rotational frequencies derived from IR spectra are accurate enough to efficiently guide both astronomical and laboratory searches.

13.2 Experimental Techniques

In this section I intend to cover some practical aspects of laboratory astrochemistry experiments related to the IR spectroscopy of molecular ions. It is not possible to make a unique classification of experimental methods, since the ion production techniques, the infrared sources available, and the methods used to increase the sensitivity can mingle in almost any possible combination. Therefore I will try to give a broad overview that serves to illustrate all significant aspects of the experiments.

As far as the production of ions goes, glow discharges have played a prominent role, using both the positive column and the negative glow regions of the discharge. The field of IR spectroscopy of molecular ions was born when Takeshi Oka at the University of Chicago recorded the vibration-rotation spectrum of the very fundamental H_3^+. The ion was produced in the positive column of a discharge in pure hydrogen, cooled by liquid nitrogen, and he employed direct laser absorption spectroscopy to detect the spectrum (Oka 1980).[2] He estimated a density of H_3^+ ions $n \simeq 3 \times 10^{10}\,\mathrm{cm}^{-3}$, or equivalently, 1 μbar partial pressure in a 1 mbar H_2 buffer. Note that this is probably one of the cleanest (i.e. with less interfering species) discharges that can be made in the laboratory with molecular ions present, so it illustrates the sensitivity and selectivity that are necessary to detect ions by IR absorption in more complex mixtures. Since the blooming of IR spectroscopy of ions in the 1980s a variety of techniques have been developed in order to increase the sensitivity for these weak signals and also the selectivity to discriminate them from those coming from the much more abundant neutral precursor and/or reaction products.

[2]Other authors had made significant contributions before and should also be mentioned: Wing et al. (1976) and Carrington and Softley (1983) developed the Doppler-tuned ion-beam infrared spectroscopy technique, in which the transitions of the ions were brought into resonance with a fixed-frequency laser using electric fields and the Doppler effect. Saykally and Evenson (1979) used the Laser Magnetic Resonance technique (LMR), in which far-IR transitions of paramagnetic species (such as HBr^+ in that work) were brought into resonance by tuning the transitions with an electric field using the Zeeman effect. In both types of experiments CO_2 and CO lasers were used. These are fixed frequency lasers, emitting in the IR, that can only be tuned line-by-line, thus making the techniques applicable only to a few molecules with resonances close to the laser lines. The success of Oka in recording the IR spectrum of the ν_2 band of H_3^+ was partly due to a high resolution broadly tunable IR source, a difference frequency spectrometer (Pine 1974, 1976) continuously tunable from 2400 to 4500 cm^{-1}.

A known hurdle of direct absorption (more properly, transmission) measurements of weak transitions is the fact that the detector receives a large background of IR radiation (produced by the source and also coming from the environment), and the signal is a tiny decrease in the photon flux that has to be detected against this strong background. Modulation techniques have been extensively used to increase both selectivity and sensitivity, shifting the detection band to higher frequencies, where the signal can be effectively filtered out from the unwanted background or from absorption signals of other neutral species. *Phase-sensitive detection* (a.k.a. *lock-in* detection) is profusely used to retrieve the signal at the modulation frequency (or some multiple).

13.2.1 Velocity Modulation

The experiment by Oka on H_3^+ used a DC discharge, and only frequency modulation of the IR radiation was used to increase the sensitivity. This got rid of the IR environmental radiation and of that of the discharge itself in the detection, but any species absorbing in the frequency scan would had been detected as well. Fortunately, the dominant species in this discharge is H_2, that has very few populated rotational levels and no vibration dipole absorption, so it did not cause major interferences, but this discharge is certainly the exception and not the rule.

Gudeman et al. (1983) used the Doppler shift of the transitions of ions due to the drift velocity induced by the electric field of the positive column to develop the technique of *velocity modulation*, and detected the ν_1 band of HCO^+. By applying an AC discharge current, rather than a DC one, the ions are accelerated towards one of the electrodes in one half period of the discharge, and to the other one in the next half period. Neutral particles are not affected. In this way, when the IR source is tuned across a transition of the ion, the transmitted intensity is modulated at the frequency of the discharge (typically in the tens of kHz regime), since the symmetric oscillating electric field Doppler-shifts the absorption frequency of the ionic vibration-rotation transition in and out of resonance with the infrared radiation. The suppression of signals from the much more abundant neutral species was 20–30 dB. The technique of velocity modulation was extensively used by numerous groups in combination with different tunable IR sources: difference frequency spectrometers, color-center lasers, lead-salt diode lasers and, more recently, quantum-cascade lasers and optical parametric oscillators (OPO). The review by Stephenson and Saykally (2005) provides a good overview of the technique and of many significative achievements. Let's mention here only two caveats: (1) In principle, light should travel in only one direction for the method to work, thus making a multipass arrangement difficult (there are tricks to overcome this limitation, and some will be shown below), and (2) any asymmetry between the electric field in the two halves of the discharge plasma translates into an offset of the measured frequency. In any case, together with the availability of narrow-linewidth broadly-tunable IR lasers, velocity modulation was a cornerstone in the

spectroscopy of molecular ions. Probably the most notable contributions were those from the groups of R. Saykally (Berkeley, USA), T. Oka (Chicago, USA) and P.B. Davies (Cambridge, UK).

13.2.2 Concentration Modulation

An alternative approach to identifying absorptions due to molecular ions makes use of their rather short lifetimes compared to neutral species. Typically, a large hollow cathode electrode arrangement with the anode external and perpendicular to the tube at its midpoint is used. When the discharge is established (through a hole cut in the cathode wall), a negative glow region fills most of the space inside the cathode, thus taking advantage of the fact that ion production is enhanced in the negative glow as compared to the positive column. By pulsing a DC discharge (again at rates of some kHz) the ion production is also modulated, following the discharge cycle. This type of discharge cell works as a rectifier, i.e. only when the copper tube is at negative potential respect to the outer electrode the plasma can ignite (Foster and McKellar 1984). The ion concentration follows that of the electrons in the discharge, swinging from zero to whatever small value it reaches. Precursor gases and stable products do not follow the discharge current so rapidly, and produce a signal with much smaller "contrast". Nevertheless, the discrimination between ion signals and those of stable molecules is poorer than in the velocity modulation scheme. That said, some advantages must also be noted: rotational and translational temperatures are generally lower than in positive column discharges (very close to that of the cathode wall), ion production is enhanced, a multipass arrangement is easily implemented and the electric field in the axial direction is negligible. This is particularly relevant for the precise measurement of transition frequencies, as mentioned in the previous subsection. Also, from the astrophysical point of view, hollow cathode discharges are more effective in producing protonated ions, such as many of those mentioned in the preceding section, through the mechanism of Eq. (13.2). Positive column discharges are more effective in producing radicals and excited states. The work of T. Amano at NRC (Ottawa, Canada) and the group of Hirota at the IMS (Okazaki, Japan) is particularly relevant in this context, the former using a difference frequency laser, and the latter using lead-salt diode lasers as IR sources.

13.2.3 Magnetic Field Modulation

While developing techniques for the study of molecular ions in the mm and sub-mm wave regions, De Lucia and Herbst (1983) observed a dramatic 10 to 100-fold increase in the signal coming from ions when a longitudinal magnetic field was applied to a glow discharge. Building upon those observations, Kawaguchi

et al. (1985) found that the signal intensity of ions was decreased by an order of magnitude by applying a magnetic field of about 100 G to a hollow cathode discharge. In this way they devised another way to discriminate absorptions produced by ions from those produced by closed-shell neutrals, that would not be affected by the magnetic field. Actually the magnetic field effect in the hollow cathode discharge is different than in the common (two opposite electrodes) glow discharge. In the former, it seems that the loss of energy by the electrons in the magnetic field decreases the yield of impact ionization, while in the latter it is the confinement of the electrons and the decrease of electron-wall collisions the cause of the higher ion production rate (together with an enlargement of the negative glow region). Magnetic field modulation is another poweful method to imprint a modulation on only the absorption signal due to ions. However, it has been more widely used together with discharge current modulation to tag the lines as coming from ions or neutrals by observing their different behaviour under a static magnetic field (which is typically 50–200 G).

13.2.4 Supersonic Expansions

Supersonic expansions are a well-known method to obtain rotationally cold molecules, facilitating the interpretation of complex spectra thanks to concentration of population in fewer levels and the intensity of the spectrum in fewer lines. An electric discharge in the nozzle extends these benefits to the study of ions and other transient molecules. Several groups have developed this type of systems, again, in conjunction with a tunable IR laser source. The spectrometer developed by the group of D. Nesbitt at JILA (Boulder, USA) used a difference frequency spectrometer (Davis et al. 2001), while that developed at NRC (Ottawa, Canada) used also a diode laser, depending on the frequency region (Yunjie et al. 1995). In both of them, the discharge across the nozzle was pulsed, so the concentration modulation technique was used to further increase the sensitivity. More recently, the group of H. Linnartz (Leiden, The Netherlands) has set up a slit discharge expansion using a cw OPO as the IR source and with *Cavity Ring-Down* detection (Zhao et al. 2013; Verbraak et al. 2007). The B. McCall group (Urbana, USA) has setup a similar system, but with a pinhole nozzle in this case (Crabtree et al. 2010; Talicska et al. 2016).

Cavity Ring-Down (CRD) Spectroscopy

As this technique is possibly not so well-known to some readers, I will take a short detour just to highlight its most relevant aspects. A much better treatment can be found in e.g. Berden and Engeln (2009). A ring-down cavity is basically an optical resonator formed by two highly reflective mirrors. When a pulse of laser light is coupled into the cavity, at each round-trip, a small fraction escapes, and the envelope of the outgoing pulses intensity follows an exponential decay. If a cw laser

is coupled into the cavity, and is suddenly switched off, the light leak-out intensity follows an exponential decay. It can be shown that the time constant τ of those decays can be expressed as

$$\tau = \frac{L}{c(1 - R - \alpha l)} \tag{13.3}$$

where L is the optical length of the cavity, c the speed of light, R the averaged reflectivity of the two mirrors and αl the absorbance for a sample present in the cavity with absorption coefficient α and length l. As it is immediately seen from Eq. (13.3) the absorption coefficient can be determined independently of the laser power, since it only depends on the decay time constant, and not on its amplitude. This immunity to source noise is one of the beauties of CRD, the other one being the high optical absorption paths achieved because of the high reflectivity mirrors. Effective pathlengths 10^4–10^5 times larger than the separation between mirrors can easily be achieved. These characteristics have made CRD a very sensitive detection technique for weakly absorbing species such as ions formed in discharges.

13.2.5 NICE-OHVMS

Noise Immune Cavity Enhanced Optical Heterodyne Velocity Modulation Spectroscopy (NICE-OHVMS) is a sensitive spectroscopic technique specific to molecular ions that is being developed at the University of Illinois. NICE-OHVMS combines three separate techniques, each of them being a powerful tool. The *noise immunity* comes from the locking scheme of the laser frequency to an optical cavity, which was originally developed for metrology purposes (Drever et al. 1983). Two sidebands are imposed on the laser central frequency by frequency modulation (i.e. *heterodyning*), with the spacing between them set to an integer multiple of the free spectral range of the cavity. In this way the carrier and the two sidebands are coupled in and out of the cavity simultaneously and a fast photodiode measures the beat signals among them. Because the two sidebands have the same intensity when no absorbers are present within the cavity and are 180° out of phase with one another, the positive and negative RF beat signals created by the sideband frequencies beating against the carrier frequency cancel each other out, giving a zero-background. As the laser is scanned across a resonance of a molecule in the cavity, one of the sidebands is absorbed more than the other one, giving an imbalance between the two beats that can be used to derive a spectroscopic signature. *Cavity enhancement* extends the interaction pathlength of the light through the absorber, while frequency modulation encodes the detected signal at radio frequencies to minimize the $1/f$ noise. If the centre frequency of the laser and the two sidebands match exactly the cavity modes, any noise in the laser-cavity lock is the same for the carrier and both sidebands, so the demodulated signal is unaffected. The optical cavity also results in a large power enhancement through the absorber which can saturate molecular transitions.

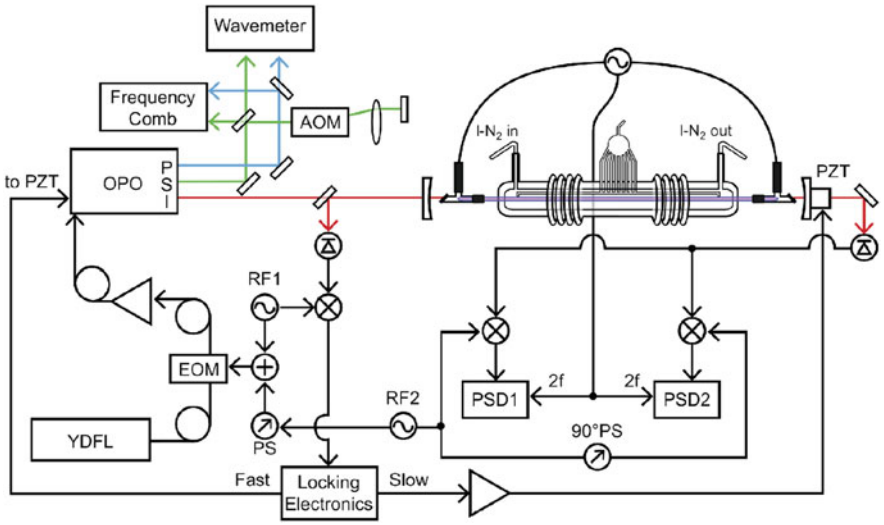

Fig. 13.2 A diagram of the NICE-OHVMS instrument. PZT: Piezo Transducer, EOM: Electro-Optic Modulator, PS: Phase Shifter, PSD: Phase Sensitive Detector, RF: Radio Frequency Oscillator, OPO: Optical Parametric Oscillator, P: Pump, S: Signal, I: Idler, YDFL: Ytterbium Doped Fiber Laser. A YDFL is fiber coupled to an EOM where locking and heterodyne sidebands are placed on the laser. The laser is then amplified in a fiber amplifier and sent to an OPO. The OPO creates the signal and idler beams. The pump and signal are used for frequency measurements, and the idler in the mid-IR is used for spectroscopy. The back reflection detector is used for Pound-Drever-Hall locking, and the signal from the transmission detector is sent to rf mixers for heterodyne processing. The output of the mixers is sent to PSDs to process the velocity modulation signal. The output is then recorded as the spectrum. Reprinted from Hodges et al. (2013), with the permission of AIP Publishing

The Lamb dips in the spectra, due to saturation, are free from Doppler broadening, and can be fit with high precision. The use of an optical frequency comb as an accurate frequency reference allows transitions to be recorded with MHz/sub-MHz uncertainty. In many cases, these represent a two order of magnitude improvement on the transition frequency measurement. Finally *velocity modulation* makes the detection specific to ions. This is not a simple setup! I refer the readers to the papers of the group for a rigorous description (e.g. Hodges et al. 2013 and references therein). Figure 13.2 shows a schematic of this experiment.

13.2.6 Action Spectroscopy in Cryogenic Ion Traps

By action spectroscopy I mean techniques in which the spectroscopic signal does not come from the observation of the light, but of some chemical change, like the rate of production of a given species, which is altered by the interaction of light

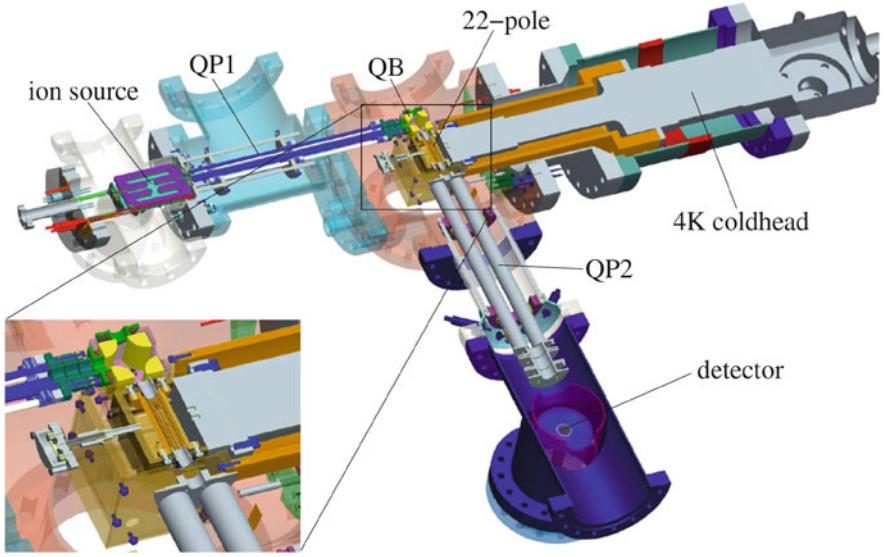

Fig. 13.3 Setup of the Cologne-built 4 K ion trap machine COLTRAP. It comprises an ion storage source, a first quadrupole mass selector (QP1), an electrostatic quadrupole bender (QB), the 22-pole ion trap mounted on a 4 K coldhead, the second quadrupole mass selector (QP2) and finally a Daly-type ion detector. While both end flanges (close to QB and detector) can be used for laser access, the flange closer to the 22-pole trap is especially suited for attaching a THz radiation source or a molecular beam which can traverse the trap. Reprinted by permission from Springer Nature, Applied Physics B: Lasers and Optics, COLTRAP: a 22-pole ion trapping machine for spectroscopy at 4 K, Asvany et al. ©2013

with the parent ion.[3] Ion traps are multipolar arrangements (four poles being the simplest, and 22-pole being a common one) in which a rapid change (at MHz rate, hence the term *rf-trap*) of the potential applied to the electrodes, maintains ions trapped in an effective radial potential well from which it cannot escape (Gerlich 1995). Electrostatic potentials "open" or "close" the longitudinal ports of the trap. In the frame of IR and rotational spectroscopy of ions these experiments are led by S. Schlemmer's group at the University of Cologne. Only a couple of techniques will be briefly described here: the laser induced reaction method (LIR) and the state-dependent attachment of He atoms to ions.

The experiment is depicted in Fig. 13.3. It begins with the electron impact ionization of the precursors in a storage chamber, followed by the production of other ions and products by collisions. The target ions are mass-filtered and

[3]I have already mentioned the problem of detecting small fluctuations in the photon flux received by a detector, especially if the background is strong. Moreover, the quantum efficiency of detectors for low energy photons (like those in the IR or microwave energy range) is rather low. On the contrary, ion-counting techniques are extremely well developed, and even a single ion can be counted.

extracted from the mixture of other products formed in the ion source, and are directed to the trap, where they are kept for times ∼1 s. Inside the trap, held at cryogenic temperatures, the ions thermalize with a buffer gas and can interact with the radiation and with some carefully chosen "reactant". In the LIR method, one seeks a reaction which has an activation barrier lower than the energy of the photons from radiation source. The reaction product (a different ion) is only formed if the parent ion has absorbed a photon and has gained enough energy to overcome the barrier. By mass selecting again the trap products, it is possible to count the number of product ions as a function of the frequency of the source, and, in so doing, obtain an absorption spectrum of the parent ion (e.g. Asvany 2005; Schlemmer et al. 2002). This method can be applied not only to IR transitions, but also to purely rotational transitions, although the higher energy of IR photons favours the first. However, if combined with a THz source in a double resonance experiment rotational spectroscopy can also be performed. The second method uses the state selective attachment of helium to the cold stored molecular ions as action spectroscopic probe [*Light Induced Inhibition of Complex Growth, or LIICG* (Asvany et al. 2014)]. When the ions are admitted to the trap, a pulse of He is injected, and He_nX^+ complexes form (X^+ is the parent ion). The rate of attachment of He atoms to X^+ depends on the internal excitation state of the latter, so, if X^+ has absorbed a photon, less He_nX^+ form in a given time. By mass selecting one of these complexes and counting them after each trapping cycle as a function of the source frequency, the absorption spectrum of X^+ can be obtained. This method is of more general applicability, working for rotational, ro-vibrational and even electronic spectroscopy. One recent example is the accurate measurement of rotational and vibrational transitions of the fundamental CH^+ ion (Doménech et al. 2018). The power of these methods resides mainly in their high selectivity. Ions can be selectively admitted to and extracted from the trap, so, in principle, the signals are free from interference from the potpourri of species present in the ion source or the trap. The infrared source in the laboratories at Cologne is an OPO, whose frequency is accurately measured by using a frequency comb. This is similar to the setup at Urbana, and a new small detour will be taken here to briefly describe its workings.

OPO's and Frequency Combs

An Optical Parametric Oscillator (OPO) is a non-linear optical device that splits an input laser wave (the *pump* beam) with frequency ω_p into two different output waves: the *signal beam* with frequency ω_s and the *idler* beam, with frequency ω_i. Conservation of energy holds ($\omega_p = \omega_s + \omega_i$), as well as that of momentum ($\mathbf{k_p} = \mathbf{k_s} + \mathbf{k_p}$, where the $\mathbf{k}$'s are the corresponding wavevectors). The OPO's used for IR generation usually contain a $LiNbO_3$ crystal inside a cavity which is resonant for one of the signal or idler waves. Tuning is achieved by either changing the pump frequency or the phase matching condition (the momentum conservation relation above) by changing the refraction indexes of the waves (usually by temperature

tuning of the crystal) or a combination of both. IR powers of ∼1 W can be achieved, with very narrow linewidth (below 100 kHz) in the 2.2–4.6 μm mid-IR region. As with any narrowband radiation source, it is necessary to measure its frequency with an accuracy as high as required for the experiment. Optical frequency combs have become one of the best standards for optical metrology. A modelocked femtosecond laser puts out a train of short pulses at a very well defined repetition rate. The frequency spectrum corresponding to this time behaviour is a "frequency comb", i.e., a set of very narrow lines precisely spaced by the inverse of the repetition rate. Since this frequency is in the ∼100 MHz range, very accurate time references (traceable to the Cs-clock standard) can be used to control the frequency spacing of the comb tooths. The principle behind using a frequency comb to measure an unknown laser frequency is the measurement of the beat frequency between the unknown laser and that of a comb tooth which is a multiple of the comb spacing. (There is a potential issue due to the so called "carrier envelope offset" that has to be addressed, but I will not get into that.) As already mentioned, accurate frequency measurement in the MHz domain is a nearly trivial task, so the frequency of the unknown laser can be determined with sub-MHz precision just by knowing the frequency of the comb tooth, and the beat-note frequency. Of course there is a load of subtleties and nuances that I have overlooked in this short description. The point of this paragraph is to stress that IR frequencies can now be measured with accuracies approaching those of microwave rotational spectroscopies (see e.g. Asvany et al. 2012).

13.3 Case Studies

In this section I show two examples of the interplay between laboratory spectroscopy of ions and astrophysics, that illustrate and emphasize the role of high resolution infrared spectroscopy in the growing field of Laboratory Astrophysics. I have chosen two studies where the spectroscopic experiments have been performed in the laboratory of IR laser spectroscopy at the Molelcular Physics Department of IEM-CSIC, in close collaboration with astronomers and other Molecular-Physics groups.

13.3.1 The Experimental Setup at IEM

The setup consists of a difference frequency laser spectrometer, coupled to a hollow cathode discharge with concentration modulation. The difference frequency spectrometer follows the design by Pine (1976), with some improvements. Briefly, frequency-tunable IR radiation is generated by mixing the output of an Ar^+ laser with that of a tunable ring dye laser in a periodically poled $LiNbO_3$ crystal contained in a temperature-controlled oven (30–200 °C). The Ar^+ laser is locked to the $^{127}I_2$

a_3 hyperfine component of the $B - X$ P(13) 43–0 transition[4] with an in-house built polarization spectroscopy setup. The laser frequency has a residual frequency jitter <1 MHz and similar long-term stability. The tunable single mode ring dye laser is also frequency stabilized, with commercial stabilization electronics (residual jitter <2 MHz). Its wavelength is measured with a high accuracy commercial wavemeter (High Finesse WSU10, with stated accuracy of 10 MHz (3σ)), calibrated with the stabilized Ar^+ laser. The IR frequency is calculated at each data point as the difference in frequency between that of the precisely known Ar^+ laser frequency and the instantaneous wavemeter reading, and is therefore limited by the wavemeter accuracy. The wavelength coverage is $\sim$2.2–5.3 μm, with $\sim$2 MHz linewidth and $\sim$1 mW power. The IR beam is amplitude modulated at $\sim$15 kHz, and is split into two fractions, one directed towards the discharge reactor and an InSb detector and the other directly to a reference detector. A home-made autobalanced amplifier (designed after Lindsay 2002) is used to subtract the laser amplitude noise from the signal.

The hollow cathode reactor follows the design of Foster and McKellar (1984) (actually the blueprints were graciously given to us by Bob McKellar), albeit some modifications have also been introduced along the development of our experiments. The cathode is an 80 cm long copper tube, 50 mm diameter, surrounded with copper tubing coils for cooling. The anode is a stainless steel piece placed external and perpendicular to the cathode at its midpoint, and the discharge is established through a hole cut in the cathode wall. A piece of quartz tubing helps to prevent the discharge from spilling over to the outside of the cathode. Typical discharge conditions are 500 V between electrodes and 300 mA current. The reactor is enclosed in a glass tube with a vacuum insulation jacket, with the sides closed by flanges that hold the windows for coupling the IR radiation, and gold coated spherical mirrors in a White-type multipass arrangement (White 1942). It is possible to achieve $\sim$32 m optical absorption path inside the discharge. The discharge is modulated at $\sim$10 kHz by passing the driving current through a rectifier bridge, therefore it is a DC-pulsed discharge. The system is evacuated down to $\sim 10^{-3}$ mbar prior to the introduction of the precursors, whose flows are adjusted by mass flow controllers. Typical discharge pressures are 1–0.1 mbar.

The detection is made with a lock-in amplifier referenced to the sum of the modulation frequencies of the IR beam amplitude and of the discharge current, the input to the lock-in being the output of the autobalanced amplifier. The goal of the double-modulation scheme is to detect only changes of the IR intensity that are due to changes in the transmission of the reactor. With this arrangement, neither the emission from the discharge, nor IR background fluctuations in the laboratory introduce drifts in the baseline. IR scans are typically made at a 0.01 cm^{-1}/s speed, and the use of the wavemeter eases the task of averaging many scans, in order to increase the signal to noise ratio.

A schematic of the setup is depicted in Fig. 13.4.

[4]Known to $\sim$0.1 MHz accuracy (Quinn 2003).

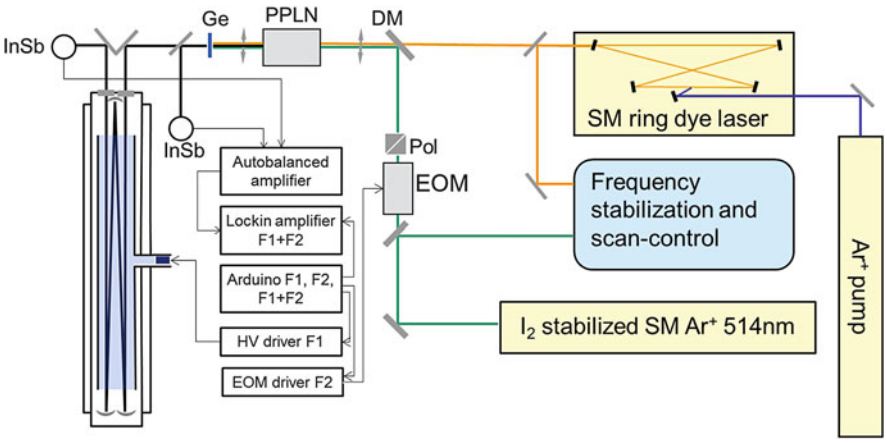

Fig. 13.4 Schematic of the main components of the high resolution infrared spectrometer coupled to a hollow cathode reactor at IEM-CSIC. SM means single-mode. EOM: electrooptic modulator. Pol: polarizing beam-splitter. DM: dicroic mirror. PPLN: periodically poled $LiNbO_3$ crystal. Ge: Germanium filter. InSb: liquid nitrogen cooled indium antimonide detectors. The frequency stabilization and scan control box comprises the optics and electronics for the SM Ar^+ laser frequency lock, the stabilization of the ring dye laser, and the wavemeter. The main components of the double modulation rig are also shown

13.3.2 A New Molecule Identified in Space: NH_3D^+

Two of the most abundant nitrogen-bearing molecules in the ISM are N_2 and NH_3, which models predict to be present in many different astrophysical media. Diazenylium (N_2H^+) and ammonium (NH_4^+), the protonated ions of N_2 and NH_3, can provide crucial information for the understanding of interstellar chemistry involving nitrogen. Since N_2 is nonpolar it cannot be detected by radioastronomy, but N_2H^+, usually taken as a tracer of N_2, has been detected in numerous sources. NH_4^+ is a key precursor of NH_3 and other nitrogen bearing molecules, potentially pre-biotic. Indeed, NH_3 and its deuterated isotopologues have also been detected in numerous sources. Chemical models predict rather high abundances of NH_4^+, since the proton affinity of NH_3 is very high, and once it is formed, it remains stable against further collisions with the abundant H_2. Unfortunately, NH_4^+ has tetrahedral symmetry, hence no permanent electric dipole moment and no rotational spectrum, making it unsuitable for astronomical searches. Its deuterated variants (d_1 to d_3), on the contrary, do possess small permanent dipole moments, and could be candidates for an astronomical identification. The only laboratory spectroscopic information on NH_3D^+, until recently, was an IR spectrum taken by Nakanaga and Amano (1986) of the ν_4 band with a difference frequency laser spectrometer and a hollow cathode discharge. From the analysis of that spectrum they could provide an estimation of the lower rotational transitions of this molecule, namely the 1_0–0_0 transition, at 262,807 MHz with a standard deviation $\sigma = 3$ MHz. It turns out that

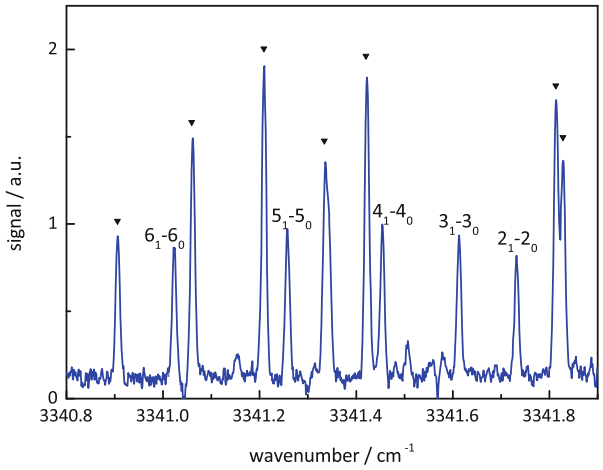

Fig. 13.5 Portion of the ν_4 band of NH_3D^+ near the band center. The labeled lines belong to the $(J, K' = 1) \leftarrow (J, K'' = 0)$ progression. Lines marked with a triangle belong to NH_4^+. Adapted from Doménech et al. (2013), ©American Astronomical Society

one of the strongest unidentified lines in a line survey of Orion-IRc2 (Tercero et al. 2010, 2011) lies at 262816.7 MHz, slightly above the 3σ confidence interval derived from the IR spectrum. Since the linewidth of this line was similar to that of NH_2D also observed in the same survey, there were chemical arguments to support the presence of NH_4^+ and, given the proximity of the frequency to the one derived from the laboratory measurement, the possibility of the unknown line being a rotational transition of NH_3D^+ was quite promising, so a more specific investigation was initiated. Astronomers made new observations towards the cold prestellar core B1-bS, where almost all isotopologues of ammonia and diazenylium had already been identified, and, as a result, a narrow feature was detected at the expected frequency. However, in order to claim a detection, more accurate laboratory data were also necessary. At that time, no laboratory rotational spectrum of NH_3D^+ was available, and even some concurrent dedicated efforts at JPL were unsuccessful, so the ν_4 band of deuterated ammonium was measured again at IEM, with better absolute frequency calibration and more lines than those reported previously. An example of some of the measured lines is shown in Fig. 13.5. The derived rotational frequency was 262,817 MHz with a standard deviation $\sigma = 2$ MHz, in excellent agreement with the astronomical observations, therefore securing the assignment of the observed features in Orion IRc2 and B1-bS to the 1_0–0_0 rotational transition of NH_3D^+ (Cernicharo et al. 2013; Doménech et al. 2013).[5]

This study beautifully illustrates the interplay between laboratory spectroscopy and astrophysics and the benefit that can be obtained from the development of

[5]Some years later, the rotational transition was accurately measured in Cologne, obtaining a value 262816.904 with $\sigma = 15$ kHz (Stoffels et al. 2016).

Laboratory Astrophysics. It also demonstrates the capability of high resolution infrared spectroscopy to provide pure rotation frequencies with accuracies high enough to guide both laboratory and radioastronomical searches.

13.3.3 The High Resolution Spectrum of SiH^+

Only about twelve out of the nearly 200 molecules identified in the ISM contain silicon. Surprisingly, only in three of them Si is bound to the most abundant element, hydrogen (these are silane SiH_4, methyl-silane CH_3SiH_3 and sylil-cyanide SiH_3CN.) The hydrides SiH (silylidyne) and SiH^+ (silylidynium) have only been identified in the photosphere of the sun (SiH also in the envelopes of some cold stars). Although these simple hydrides should be among the first species to form out of the bare atoms or ions, the models do not predict a high abundance: in cold clouds most Si is supposed to be depleted onto dust grains and SiO is the most abundant gas phase Si-containing species, therefore the reaction $H_3^+ + Si \rightarrow SiH^+ + H_2$, although exothermic, would not be very efficient. In diffuse environments where Si could be ionized, the reaction $Si^+ + H_2 \rightarrow SiH^+$ is quite slow, since it is highly endothermic (by $\sim$14,200 K). However, it is worth noting that the chemically similar CH^+ is much more abundant in the diffuse medium than it is predicted by models, and the same is true for SH^+. In both cases there is a formation barrier, albeit smaller than that for SiH^+, and a warm chemistry with vibrationally excited H_2, shocks and turbulence is invoked to overcome the energy barrier and interpret the observed abundances. Furthermore, the spectroscopic information on SiH^+ was surprisingly scarce, with no accurate measurements or predictions of its rotational frequencies. In view of all the above considerations, the effort of undertaking a careful measurement of those frequencies seemed advantageous.

The $v = 1 - 0$ fundamental vibration of SiH^+ was recorded at IEM with the difference-frequency laser spectrometer coupled to the hollow cathode discharge system. A mixture of SiH_4 in He was used as precursor. Finally, a total of 23 lines were measured, from P(11) to R(11), spanning the range 1902–2236 cm^{-1} (see Fig. 13.6 for two examples). Besides providing a much more accurate and complete set of infrared frequencies than previously available, it allowed for an accurate prediction of the $J = 1$–0 rotational transition. The predicted value was 453057.7 MHz with $\sigma = 0.5$ MHz. The fundamental rotational transition of SiH^+ was then measured in the Cologne laboratories using the rotational state dependence of the attachment of He atoms to cations obtaining a value of 453056.3632 MHz, $\sigma = 0.4$ kHz, within just 1.3 MHz of the IR prediction. A more detailed account of this work is given in Doménech et al. (2017).

The Herschel Space Observatory (Pilbratt et al. 2010) produced huge amounts of information on interstellar hydrides in its lifetime (2009–2013). Unfortunately, the frequency of the $J = 1 - 0$ transition of SiH^+ was outside its frequency coverage. Since there are no other current far-IR satellite missions, observations with radiotelescopes from ground could be an alternative: ALMA (Atacama Large

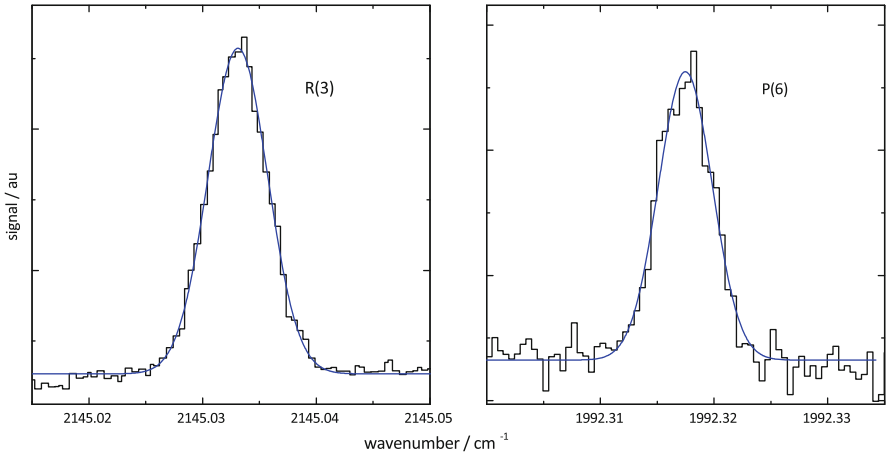

Fig. 13.6 Two examples of detected lines of SiH^+ and their Gaussian fits. Both lines are the result of averaging 100 scans (total 1000 s integration time). Adapted from Doménech et al. (2017), ©American Astronomical Society

Millimiter Array) or APEX (Atacama Pathfinder EXperiment), are both in very dry sites and above 5000 m altitude, and both cover that frequency. Unfortunately a telluric water vapor line lies very close by, and atmospheric transmission under average weather conditions (1 mm precipitable water vapor) drops to ∼15%. Yet another alternative is to use high resolution infrared telescopes from ground: iSHELL (an IR spectrograph for NASA Infrared Telescope Facility on Maunakea) or CRIRES+[6] (at the Very Large Telescope facilities of Cerro Paranal) have high resolution and cover the vibration rotation band.

The accurate frequencies determined in this work enable the search for this fundamental ion in space. The lines of sight would be those of the diffuse medium, shock regions, or supernova ejecta against bright IR sources.

13.4 Final Remarks

Infrared astronomy is a very active field, more so with the excitement aroused by the almost daily discovery of new exoplanets. The James Webb Space Telescope carries two infrared spectrometers onboard, and several ground-based facilities offer (or will offer soon) high sensitivities and spectral resolutions of $R \simeq 100{,}000$. Accurate laboratory measurements in the IR regions will help maximize the scientific return of these efforts. Furthermore, since the end of the successful Herschel mission, infrared astronomy from the ground is one of the few alternatives to continue the study of light hydrides, as it is the case of many protonated ions. Infrared laboratory

[6]Expected to be in operation in 2019.

spectroscopy is an enabling tool not only for those direct IR observations but also for observations in the radio or mm-wave domains. The new interferometric facilities such as ALMA, or NOEMA as well as laboratory rotational spectroscopy will also benefit from accurate IR data, since good predictions can spare very long searching times, both at the telescopes and in the lab.

Acknowledgements The work carried out at the laboratories of the Molecular Physics Department of IEM- CSIC has been partially funded by Spanish MINECO through grants CSD2009-00038 (Consolider Astromol project), FIS2012-38175, FIS2013-408087-C2-1P and FIS2016-77726-C3-1P. Additional partial support has been received from the European Research Council through the Synergy Grant ERC-2013-SyG-610256 NANOCOSMOS. Dr. O. Asvany and the support for a research stay at the University of Cologne by the Deutsche Forschungsgemeinschaft via SFB 956 project B2 are most gratefully acknowledged.

References

Adams, D.: The Hitchhicker's Guide to the Galaxy. Pan Books, London (1979)

Asvany, O.: Understanding the infrared spectrum of bare CH_5^+. Science **309**(5738), 1219–1222 (2005). https://doi.org/10.1126/science.1113729

Asvany, O., Krieg, J., Schlemmer, S.: Frequency comb assisted mid-infrared spectroscopy of cold molecular ions. Rev. Sci. Instrum. **83**(9), 093110 (2012). https://doi.org/10.1063/1.4753930

Asvany, O., Brünken, S., Kluge, L., Schlemmer, S.: COLTRAP: a 22-pole ion trapping machine for spectroscopy at 4 K. Appl. Phys. B **114**(1–2), 203–211 (2014). https://doi.org/10.1007/s00340-013-5684-y

Berden, G., Engeln, R. (eds.): (2009) Cavity Ring-Down Spectroscopy: Techniques and Applications. Wiley, Chichester. https://doi.org/10.1002/9781444308259

Black, J.H., Hartquist, T.W., Dalgarno, A.: Models of interstellar clouds. II - the Zeta Persei cloud. Astrophys. J. **224**, 448 (1978). https://doi.org/10.1086/156392

Carrington, A., Softley, T.P.: High-resolution infrared spectroscopy of molecular ions. In: Miller, T.A., Bondybey, V.E. (eds.) Molecular Ions: Spectroscopy, Structure and Chemistry, pp. 49–72. North-Holland, Amsterdam (1983)

Cernicharo, J., Tercero, B., Fuente, A., Domenech, J.L., Cueto, M., Carrasco, E., Herrero, V.J., Tanarro, I., Marcelino, N., Roueff, E., Gerin, M., Pearson, J.: Detection of the ammonium ion in space. Astrophys. J. **771**(1), L10 (2013). https://doi.org/10.1088/2041-8205/771/1/L10

Cheung, A.C., Rank, D.M., Townes, C.H., Thornton, D.D., Welch, W.J.: Detection of NH_3 molecules in the interstellar medium by their microwave emission. Phys. Rev. Lett. **21**(25), 1701–1705 (1968). https://doi.org/10.1103/PhysRevLett.21.1701

Crabtree, K.N., Kauffman, C.A., McCall, B.J.: Note: A modular and robust continuous supersonic expansion discharge source. Rev. Sci. Instrum. **81**(8), 086103 (2010). https://doi.org/10.1063/1.3478019

Davis, S., Fárnk, M., Uy, D., Nesbitt, D.J.: Concentration modulation spectroscopy with a pulsed slit supersonic discharge expansion source. Chem. Phys. Lett. **344**(1-2), 23–30 (2001). https://doi.org/10.1016/S0009-2614(01)00746-1

De Lucia, F.C., Herbst, E.: The production of large concentrations of molecular ions in the lengthened negative glow region of a discharge. J. Chem. Phys. **78**(5), 2312 (1983). https://doi.org/10.1063/1.445004

Doménech, J.L., Cueto, M., Herrero, V.J., Tanarro, I., Tercero, B., Fuente, A., Cernicharo, J.: Improved determination of the $1_0 - 0_0$ rotational frequency of NH_3D^+ from the high-resolution spectrum of the ν_4 infrared band. Astrophys. J. **771**(1), L11 (2013). https://doi.org/10.1088/2041-8205/771/1/L11

Doménech, J.L., Schlemmer, S., Asvany, O.: Accurate frequency determination of vibration-rotation and rotational transitions of SiH^+. Astrophys. J. **849**(1), 60 (2017). https://doi.org/10.3847/1538-4357/aa8fca

Doménech, J.L., Jusko, P., Schlemmer, S., Asvany, O.: The First laboratory detection of vibration-rotation transitions of $^{12}CH^+$ and $^{13}CH^+$ and improved measurement of their rotational transition frequencies. Astrophys. J. **857**, 61 (2018). https://doi.org/10.3847/1538-4357/aab36a

Drever, R.W.P., Hall, J.L., Kowalski, F.V., Hough, J., Ford, G.M., Munley, A.J., Ward, H.: Laser phase and frequency stabilization using an optical resonator. Appl. Phys. B Photophysics. Laser Chem. **31**(2), 97–105 (1983). https://doi.org/10.1007/BF00702605

Eddington, A.S.: Bakerian lecture. Diffuse matter in interstellar space. Proc. R. Soc. London Ser. A Contain. Pap. Math. Phys. Character **A111**, 424–456 (1926)

Foster, S.C., McKellar, A.R.W.: The ν_3 fundamental bands of HN_2^+, DN_2^+, and DCO^+. J. Chem. Phys. **81**(8), 3424–3428 (1984). https://doi.org/10.1063/1.448066

Fridman, A.: Plasma Chemistry. Cambridge University Press, Cambridge (2008). https://doi.org/10.1017/CBO9780511546075

Gerlich, D.: Ion-neutral collisions in a 22-pole trap at very low energies. Phys. Scr. **T59**, 256–263 (1995). https://doi.org/10.1088/0031-8949/1995/T59/035

Gudeman, C.S., Begemann, M.H., Pfaff, J., Saykally, R.J.: Velocity-modulated infrared laser spectroscopy of molecular ions: the ν_1 band of HCO^+. Phys. Rev. Lett. **50**(10), 727–731 (1983). https://doi.org/10.1103/PhysRevLett.50.727

Herbst, E., Klemperer, W.: The formation and depletion of molecules in dense interstellar clouds. Astrophys. J. **185**, 505 (1973). https://doi.org/10.1086/152436

Herzberg, G.: The interplay of molecular spectroscopy and astronomy. Highlights Astron. **5**, 3–26 (1980). https://doi.org/10.1017/S1539299600003725

Hodges, J.N., Perry, A.J., Jenkins, P.A., Siller, B.M., McCall, B.J.: High-precision and high-accuracy rovibrational spectroscopy of molecular ions. J. Chem. Phys. **139**(16):164201 (2013). https://doi.org/10.1063/1.4825251

Hollenbach, D., Salpeter, E.E.: Surface recombination of hydrogen molecules. Astrophys. J. **163**, 155 (1971). https://doi.org/10.1086/150754

Kawaguchi, K., Yamada, C., Saito, S., Hirota, E.: Magnetic field modulated infrared laser spectroscopy of molecular ions: the ν_2 band of HCO^+. J. Chem. Phys. **82**(4), 1750 (1985). https://doi.org/10.1063/1.448407

Kroto, H.W.: The spectra of interstellar molecules. Int. Rev. Phys. Chem. **1**(3), 309–376 (1981). https://doi.org/10.1080/01442358109353324

Lindsay, C.M.: Highly-sensitive and efficient infrared spectroscopy of molecular ions. PhD thesis, Chicago (2002)

Menten, K.M., Wyrowski, F.: Molecules detected in interstellar space. In: Yamada, K., Winnewisser, G. (eds.) Interstellar Molecules, pp. 27–42. Springer, Berlin (2011). https://doi.org/10.1007/978-3-642-16268-8_2

Millar, T.J., Walsh, C., Field, T.A.: Negative ions in space. Chem. Rev. **117**(3), 1765–1795 (2017). https://doi.org/10.1021/acs.chemrev.6b00480

Müller, H.S., Schlöder, F., Stutzki, J., Winnewisser, G.: The Cologne Database for Molecular Spectroscopy, CDMS: a useful tool for astronomers and spectroscopists. J Mol Struct 742(1–3):215–227 (2005). https://doi.org/10.1016/j.molstruc.2005.01.027

Müller, H.S.P., Thorwirth, S., Roth, D.A., Winnewisser, G.: The Cologne Database for Molecular Spectroscopy, CDMS. Astron. Astrophys. **370**(3), L49–L52 (2001). https://doi.org/10.1051/0004-6361:20010367

Nakanaga, T., Amano, T.: Difference-frequency laser spectroscopy of the ν_4 fundamental band of NH_3D^+. Can. J. Phys. **64**, 1356–1358 (1986)

Oka, T.: Observation of the infrared spectrum of H_3^+. Phys. Rev. Lett. **45**(7), 531 (1980)

Piel, A.: Plasma Physics. Springer, Berlin (2010). https://doi.org/10.1007/978-3-642-10491-6

Pilbratt, G.L., Riedinger, J.R., Passvogel, T., Crone, G., Doyle, D., Gageur, U., Heras, A.M., Jewell, C., Metcalfe, L., Ott, S., Schmidt, M.: Herschel space observatory. Astron. Astrophys. **518**, L1 (2010). https://doi.org/10.1051/0004-6361/201014759

Pine, A.S.: Doppler-limited molecular spectroscopy by difference-frequency mixing. J. Opt. Soc. Am. **64**(12), 1683–1690 (1974)

Pine, A.S.: High-resolution methane ν_3-band spectra using a stabilized tunable difference-frequency laser system. J. Opt. Soc. Am. **66**(2), 97–108 (1976)

Quinn, T.J.: Practical realization of the definition of the metre, including recommended radiations of other optical frequency standards (2001). Metrologia **40**, 103–133 (2003)

Saykally, R.J., Evenson, K.M.: Observation of pure rotational transitions in the HBr^+ molecular ion by laser magnetic resonance. Phys. Rev. Lett. **43**(7), 515–518 (1979). https://doi.org/10.1103/PhysRevLett.43.515

Schlemmer, S., Lescop, E., von Richthofen, J., Gerlich, D., Smith, M.A.: Laser induced reactions in a 22-pole ion trap: $C_2H_2^+ + h\nu_3 + H_2 \rightarrow C_2H_3^+ + H$. J. Chem. Phys. **117**(5), 2068–2075 (2002). https://doi.org/10.1063/1.1487373

Snow, T.P., Bierbaum, V.M.: Ion chemistry in the interstellar medium. Annu. Rev. Anal. Chem. **1**:229–59 (2008). https://doi.org/10.1146/annurev.anchem.1.031207.112907

Snow, T.P., McCall, B.J.: Diffuse atomic and molecular clouds. Annu. Rev. Astron. Astrophys. **44**(1), 367–414 (2006). https://doi.org/10.1146/annurev.astro.43.072103.150624

Stephenson, S.K., Saykally, R.J.: Velocity modulation spectroscopy of ions. Chem. Rev. **105**(9), 3220–3234 (2005). https://doi.org/10.1021/cr040100d

Stoffels, A., Kluge, L., Schlemmer, S., Brünken, S.: Laboratory rotational ground state transitions of NH_3D^+ and CF^+. Astron. Astrophys. **56**, 1–7 (2016). https://doi.org/10.1051/0004-6361/201629101

Talicska, C.N., Porambo, M.W., Perry, A.J., McCall, B.J.: Mid-infrared concentration-modulated noise-immune cavity-enhanced optical heterodyne molecular spectroscopy of a continuous supersonic expansion discharge source. Rev. Sci. Instrum. **87**(6), 063111 (2016). https://doi.org/10.1063/1.4953652

Tercero, B., Cernicharo, J., Pardo, J.R., Goicoechea, J.R.: A line confusion limited millimeter survey of Orion KL I. Sulfur carbon chains. Astron. Astrophys. **517**, A96 (2010). https://doi.org/10.1051/0004-6361/200913501

Tercero, B., Vincent, L., Cernicharo, J., Viti, S., Marcelino, N.: A line-confusion limited millimeter survey of Orion KL. Astron. Astrophys. **528**, A26 (2011). https://doi.org/10.1051/0004-6361/201015837

Tielens, A.G.G.M., Hagen, W.: Model calculations of the molecular composition of interstellar grain mantles. Astron. Astrophys. 114:245–260 (1982). https://doi.org/1982A&A...114..245T

Verbraak, H., Ngai, A., Persijn, S., Harren, F., Linnartz, H.: Mid-infrared continuous wave cavity ring down spectroscopy of molecular ions using an optical parametric oscillator. Chem. Phys. Lett. **442**(1–3), 145–149 (2007). https://doi.org/10.1016/j.cplett.2007.05.051

Watson, W.D.: The rate of formation of interstellar molecules by ion-molecule reactions. Astrophys. J. **183**, L17 (1973). https://doi.org/10.1086/181242

Weinreb, S., Barett, A.H., Meeks, M.L., Henry, J.C.: Radio observations of OH in the interstellar medium. Nature **200**(4909), 829–831 (1963). https://doi.org/10.1038/200829a0

White, J.U.: Long optical paths of large aperture. J. Opt. Soc. Am. **32**(5), 285 (1942). https://doi.org/10.1364/JOSA.32.000285

Wing, W.H., Ruff, G.A., Lamb, W.E., Spezeski, J.J.: Observation of the infrared spectrum of the hydrogen molecular ion HD^+. Phys. Rev. Lett. **36**(25), 1488–1491 (1976). https://doi.org/10.1103/PhysRevLett.36.1488

Yunjie, X., Fukushima, M., Amano, T., McKellar, A.: Infrared absorption spectroscopy of molecular ions in a corona-discharge slit expansion. Chem. Phys. Lett. **242**(1–2), 126–131 (1995). https://doi.org/10.1016/0009-2614(95)00720-O

Zhao, D., Guss, J., Walsh, A.J., Linnartz, H.: Mid-infrared continuous wave cavity ring-down spectroscopy of a pulsed hydrocarbon plasma. Chem. Phys. Lett. **565**, 132–137 (2013). https://doi.org/10.1016/j.cplett.2013.02.025

Part V
Astrophysical Models

Chapter 14
Interstellar Chemical Models

Marcelino Agúndez

Abstract Interstellar clouds are harsh environments exposed to a energetic radiation, where the survival of molecules does not seem favorable. However, molecules are found in many different types of interstellar clouds. The study of molecules has a twofold interest. On the one hand, they serve as excellent tools to characterize the physical conditions prevailing in the clouds, and on the other, knowing how molecules are synthesized and why different environments host different types of molecules allows to understand the chemical evolution that matter experiences along the process in which stars and planets form. For this latter purpose, chemical models are an essential tool. This chapter provides the fundaments to build a chemical model of an interstellar cloud, describes which are the basic physical and chemical data needed to feed the model, and briefly discuss how these models assist in the interpretation of astronomical observations of molecules.

14.1 Introduction

It is nowadays well established that molecules are an important component in many different astronomical environments, that they can be used as efficient diagnostic tools of the physical and chemical state of such regions, and that—with about 200 different molecules discovered to date—chemical complexity can be developed in the outer space, with potential implications for the appearance of life. Scientists have wondered how molecules are synthesized in situ in harsh environments where, a priori, the survival of molecules does not seem favorable, and in this way, Astrochemistry and the development of chemical models have come to aid in the search for answers to these questions (see, e.g., Herbst and Yates 2013).

The aim of this chapter is to provide an introduction on how chemical models are constructed, which are the key physical and chemical data needed to feed them,

M. Agúndez (✉)
Instituto de Física Fundamental, CSIC, Madrid, Spain
e-mail: marcelino.agundez@csic.es

G. M. Muñoz Caro, R. Escribano (eds.), *Laboratory Astrophysics*,
Astrophysics and Space Science Library 451,
https://doi.org/10.1007/978-3-319-90020-9_14

and how models assist in the interpretation of astronomical observations. Although the basics behind the chemical models to be described can be applied to different types of astronomical sources, such as interstellar clouds, circumstellar envelopes, or planetary atmospheres, this chapter focuses on the theoretical description of interstellar chemistry. Section 14.2 presents the basic equations that enter into a chemical model, Sects. 14.3 and 14.4 describe the main gas-phase and grain-surface processes and their associated parameters, Sect. 14.5 discusses some types of chemical models developed for specific classes of interstellar regions, and finally, in Sect. 14.6 some concluding remarks are presented.

14.2 Construction of a Chemical Model

The low densities and temperatures prevailing in most interstellar regions make their chemical composition to be completely out of thermochemical equilibrium. That is, the composition is by no means determined by the minimum of the Gibbs energy of the system, but by chemical kinetics. This fact is key for the way interstellar chemistry works. First, *time* is a key quantity, i.e., the chemical composition may evolve with time and the current composition of a certain interstellar region is the consequence of the chemical evolution from a given initial time to the current age of that region. Therefore, to theoretically describe the chemical evolution the composition at the initial time must be known. In the practice, however, this is an important handicap of chemical models since the definition of the time zero and the knowledge of the composition at that time are not straightforward. Second, the chemical evolution of matter is the result of the competition between the rates at which the different physical and chemical processes take place.

The key equations behind a chemical kinetics model are differential equations that describe the variation of the abundance of each species i with time. This variation is given by the rate at which the species i is produced by any physical or chemical process minus the rate at which this species is destroyed by any process, i.e.

$$\frac{dn_i}{dt} = \sum_{j,k} k_{jk} n_j n_k - n_i \sum_l k_{il} n_l + \left(\sum_m K_m n_m - K_i n_i \right) + \left[R_i^{des} n_i^{s,desorbable} - R_i^{ads} n_i \right] \tag{14.1}$$

$$\frac{dn_i^s}{dt} = \left\{ \sum_{j,k} k_{jk}^s n_j^s n_k^s - n_i^s \sum_l k_{il}^s n_l^s \right\} + \left[R_i^{ads} n_i - R_i^{des} n_i^{s,desorbable} \right] \tag{14.2}$$

where n and n^s stand for the abundances of the different species (i, j, k, l, m, n) in the gas phase and on the surface of dust grains, respectively. These abundances are usually expressed as volume densities, i.e., number of particles per cubic centimeter,

following the cgs system of units. The quantities n^s are a convenient way to express abundances on grain surfaces from a mathematical point of view, although they are not very intuitive. The abundance of a species i on grain surfaces, ${n_i}^s$, can be expressed as ${n_i}^s = {N_i}^s \times n_d$, where ${N_i}^s$ is the number of particles of species i on the surface of an average dust grain and n_d is the volume density of dust particles. There is a subtle aspect to take into account about desorption, which is that not all ice particles can efficiently desorb but only those in the top monolayers. This fact makes necessary to introduce the quantity ${n_i}^{s,desorbable}$, which is the volume density of particles of species i in the top desorbable monolayers. This quantity is simply equal to ${n_i}^s$ when these layers are not fully occupied and to ${n_i}^s$ corrected by the fraction of ice particles in the top desorbable monolayers otherwise (see, e.g., Aikawa et al. 1996; Woitke et al. 2009; Cuppen et al. 2017).

The first two terms in Eq. (14.1) describe the formation and destruction of species i by bimolecular gas-phase chemical reactions, and thus, in these two terms, k_{jk} represents the rate coefficients of reactions between species j and k that produce i, while k_{il} stands for the rate coefficients of reactions in which species i reacts with other reagent l. Both k_{jk} and k_{il} have cgs units of $\mathrm{cm^3\ s^{-1}}$. The terms in parentheses in Eq. (14.1) describe the formation and destruction of species i by processes that follow a first-order kinetics, with rate coefficients K_m and K_i, respectively, both of which have cgs units of $\mathrm{s^{-1}}$. The coefficient K_i takes into account all unimolecular processes of destruction of species i, which in the interstellar medium are mainly ionization or dissociation induced by cosmic rays or ultraviolet photons. Apart from unimolecular and bimolecular processes, termolecular reactions, i.e., those in which the reactive collision takes place between three bodies—the third one is chemically inert but carries out the excess of energy of the reaction—are a priori possible, although the low volume densities prevailing in the interstellar medium prevent these processes from being efficient, and are not included in Eqs. (14.1) and (14.2).

If a gas phase species i can be efficiently adsorbed onto dust grains, where it may experience some chemical transformations, then it is necessary to include the terms in square brackets in Eq. (14.1) and it is also necessary to describe the variation of the abundances of the ice species, n^s, with time according to Eq. (14.2). The terms in square brackets in Eqs. (14.1) and (14.2) describe the adsorption (desorption) of a species i on (from) the surface of dust grains. The kinetics of adsorption is regulated by the rate coefficient ${R_i}^{ads}$ (with units of $\mathrm{s^{-1}}$), which depends on the abundance and size of dust grains. The kinetics of desorption is described by the rate coefficient ${R_i}^{des}$ (with units of $\mathrm{s^{-1}}$), which results from the sum of the contributions of different desorption mechanisms. As long as chemical reactions can take place on the surface of dust grains, the chemical composition of the ice mantle can change and so the abundances of the adsorbed species. The kinetics of these grain-surface reactions is described by a formalism rather similar to that used to describe the kinetics of gas-phase chemical processes (Hasegawa et al. 1992). In this case, ${k_{jk}}^s$ stands for the rate coefficients of formation of the ice species i through reactions between ice species j and k, and ${k_{il}}^s$ represents the rate coefficients of grain-surface reactions that deplete the ice species i. Both ${k_{jk}}^s$ and ${k_{il}}^s$ have cgs units of $\mathrm{cm^3\ s^{-1}}$. This "rate-equation approach" has been widely used to deal with grain surface chemistry because it

can be easily implemented in chemical models including a large number of species. This approach however lacks a proper description of grain surface chemistry at a microscopic level. Simulations using a stochastic treatment of the kinetics on a grain surface have come to assist here (e.g., Cuppen et al. 2013), although they are computationally expensive and still cannot be used to simultaneously model the chemistry of many species.

Once the main processes of chemical transformation have been identified and their rate coefficients are known or can be estimated, it is possible to write an equation with the source and sink terms for each gas-phase and ice species and build the full system of equations for all species included in the model. Usually, chemical models of interstellar clouds involve hundreds of species, which are linked by thousands of physical and chemical processes. The system of equations can be solved either at steady state or as a function of time. In the first case, the left-side terms in Eqs. (14.1) and (14.2) are set to zero and we are left with a system of algebraic equations. In this case we do not need to care about the initial conditions. In the time-dependent case, we have a system of ordinary differential equations (ODE), which can be solved as a function of time starting from some initial conditions, i.e., some initial abundance for every gas-phase and ice species considered in the model. The rate coefficients of these processes depend on parameters such as the gas kinetic temperature (e.g., for bimolecular gas-phase chemical reactions), the dust temperature (e.g., in the case of grain-surface chemical reactions), or the intensity and energy distribution of energetic radiation fields (e.g., in the case of ionizations and dissociations induced by ultraviolet photons). The chemical model thus has to be fed with some physical knowledge of the region to be studied. In a time-dependent chemical model, the abundances of all species are computed as a function of time under fixed or varying physical conditions. The former case is known as "pseudo time-dependent chemical model" and is a good approximation when the chemistry occurs on timescales shorter than those associated to the physical evolution of the interstellar region. If this is not the case, then the time-dependence of the gas and dust temperature, volume density, and strength of ultraviolet radiation must be taken into account.

14.3 Processes in the Gas Phase

14.3.1 Interactions with Energetic Radiation

Interstellar gas-phase species can be exposed to energetic radiation (ultraviolet, X-rays, γ-rays, cosmic-rays) of different degrees of intensity, and thus can interact with this energetic radiation suffering chemical transformations such as ionization and molecular dissociation. Here we concentrate on cosmic rays and ultraviolet photons, both of which are important drivers of the chemistry in the interstellar medium.

Cosmic rays are present allover our Galaxy—probably arising from supernovae remnants—and thus permeate the interstellar medium, being able to penetrate large columns of interstellar matter and ionize atoms and molecules in places where ultraviolet photons are not able to penetrate. For astrochemical purposes, the cosmic-ray flux is quantified through the ionization rate of H_2 molecules, ζ_{H2} (with units of s^{-1}), which is the integral of the product of the ionization cross section of H_2 by the cosmic-ray flux integrated over the energy spectrum of cosmic rays (see, e.g., Padovani et al. 2009). In the local interstellar medium, ζ_{H2} takes values in the range (1–5) $\times$ 10^{-17} s^{-1} (Dalgarno 2006). The ionization rates of species other than H_2 are usually expressed in terms of ζ_{H2} through a scaling factor, which can be found in astrochemical databases.

The ionization of H_2 by cosmic rays results in high energetic electrons, which lose energy through collisions with the gas, exciting H_2 molecules to high-energy electronic states. The desexcitation of H_2 molecules produces a cascade of ultraviolet photons, which can further ionize and dissociate species other than H_2. This source of secondary ultraviolet photons induced by cosmic rays, known as Prasad-Tarafdar mechanism, has an ionizing power $\sim$1000 times greater than the direct ionization by cosmic rays, and is of particular importance in the interior of cold dense clouds, where external ultraviolet photons cannot penetrate due to the large extinction (Gredel et al. 1989).

The interstellar medium is exposed to an ultraviolet radiation field originated by the emission of ambient hot stars (Draine 1978). Interstellar molecules are efficiently photoionized and photodissociated by ultraviolet photons with wavelengths from 91.2 nm (this is the ionization threshold of H, which corresponds to 13.6 eV, and shorter-wavelength photons are efficiently absorbed by interstellar atomic hydrogen) to 200–300 nm (longer-wavelength photons have little ionizing and dissociating power). The photoionization and photodissociation rates of a given species i is given by the integral of the relevant cross section over the spectral shape of the ultraviolet radiation field:

$$K_i = \int_{91.2\ nm}^{\lambda_i} 4\pi\, J\,(\lambda)\, \sigma_i\,(\lambda)\, d\lambda \tag{14.3}$$

where the integral extends from 91.2 nm up to a wavelength λ_i that depends on each species i, $J(\lambda)$ is the mean specific intensity (with units of photon cm^{-2} s^{-1} nm^{-1} sr^{-1}) of the radiation field, which can be the interstellar radiation field, the secondary radiation field induced by cosmic rays, or any other, e.g., arising from nearby hot stars. The ionization/dissociation cross section $\sigma_i(\lambda)$ is expressed in cgs units of cm^{-2}. Because of the energy cutoff of the interstellar ultraviolet radiation field at 13.6 eV, a given species with an ionization potential IP_i can only be ionized by interstellar ultraviolet photons with energies in the range IP_i –13.6 eV. If the ionization potential is above 13.6 eV, that species cannot be ionized by interstellar ultraviolet photons. As concerns photodissociation of interstellar molecules, the cross section is delimited at the high-energy edge by the cutoff at 13.6 eV and at the low-energy edge by the dissociation energy of the molecule. The

shape of the photodissociation cross section depends on the type of mechanism that dominates the photodissociation process, which can occur through discrete lines or a continuum (van Dishoeck 1988).

Computing a photorate using Eq. (14.3) requires the knowledge of the ultraviolet radiation field, which may involve radiative transfer calculations. For the standard interstellar medium it is usual to parameterize photorates as a function of the visual extinction. The visual extinction, A_V, is a measure of the attenuation of radiation at optical wavelengths (in the V band centered at 550 nm) by a column density of interstellar material (essentially due to dust absorption and scattering), and is measured in magnitudes. A visual extinction of 1 magnitude implies that the intensity in the V band decreases by a factor of ∼2.5, according to the definition of a magnitude in astronomy. In the local interstellar medium, A_V is proportional to the column density of H nuclei according to $A_V = N_H/1.87 \times 10^{21}$ cm^{-2} (Bohlin et al. 1978), and photorates can be expressed as:

$$K_i = \alpha_i \exp(-\gamma_i A_V) \tag{14.4}$$

where α_i (with units of s^{-1}) is the photorate of species i under the unattenuated interstellar radiation field of Draine (1978) and γ_i is a parameter used to take into account the increased dust extinction at ultraviolet wavelengths compared to the V band.

14.3.2 Gas-phase Chemical Reactions

Bimolecular gas-phase chemical reactions are one of the most important drivers of chemical complexity in the interstellar medium. In most interstellar regions the gas kinetic temperature is low and thus only exothermic reactions without important activation barriers play an important role. In warm regions where temperatures reach some hundreds of degrees Kelvin, endothermic reactions and reactions with moderate activation barriers may become important as well. In general, the rate coefficients of gas-phase chemical reactions depend on temperature, and this dependence is usually expressed through a modified Arrhenius equation:

$$k = \alpha T^{\beta} \exp\left(-\frac{\gamma}{T}\right) \tag{14.5}$$

where T is the gas kinetic temperature and α, β, and γ are three empirical parameters: α has cgs units of cm^3 s^{-1}, β is a dimensionless exponent, and γ is usually interpreted in terms on an endothermicity or activation barrier and is expressed in K. Although most molecules identified in the interstellar medium are neutral, ions play an important role in interstellar chemistry. Thus, gas-phase chemical reactions between neutral species as well as those involving ions are

both important and necessary to build a realistic chemical model of any interstellar region.

The kinetics of a bimolecular gas-phase reaction between an ion and a neutral species is relatively simple. If such a reaction is exothermic, then it is usually rapid, even at very low temperatures. If the neutral species is non-polar, long-range capture theories indicate that the rate coefficient is independent of temperature and given by the Langevin expression:

$$k_L = 2\pi e\left(\alpha/\mu\right)^{1/2} = 2.3420 \times 10^{-9} cm^3 s^{-1} \sqrt{\alpha\left[\text{Å}^3\right]/\mu\,[amu]} \qquad (14.6)$$

where e is the electric charge of the ion, α is the polarizability of the neutral species, and μ is the reduced mass of the reactants. For a single charged ion, as is usually the case in interstellar chemistry, the Langevin rate coefficient is given by the expression at the right side of Eq. (14.6). Most molecules of astrophysical interest have polarizabilities around 1 Å^3 and reduced masses are usually a few atomic mass units (amu), so that rate coefficients are typically around 10^{-9} cm^3 s^{-1}. In the case of polar neutral species, the kinetic behavior becomes more complex because the potential describing the interaction depends on the orientation of the dipole moment and thus it is no longer isotropic. In this case, rate coefficients usually show a negative temperature-dependence (i.e., the lower the temperature the faster the reaction is) in a way that can be theoretically described according to classical trajectory calculations. A commonly used expression is the Su-Chesnavich one (see details in Wakelam et al. 2010). Measurements of rate coefficients of ion–neutral reactions have shown that the kinetics of most such reactions can be well described by long-range capture theories. This fact is extremely important because, in the absence of experimental data, it permits to predict to a fair degree of accuracy the rate coefficients of ion–neutral reactions.

In the case of reactions between neutral species, if both reactants are stable species, i.e., both are closed-shell electronic molecules, reactions tend to have large activation barriers, and thus negligible rate coefficients at low temperatures, so that they can be neglected for interstellar chemistry. Exothermic reactions in which at least one of the reactants is a radical may or not occur fast at low temperatures. Unlike in the case of ion–neutral reactions, here it is difficult to anticipate theoretically whether or not the reaction has an activation barrier, and experiments are needed. There is a vast experimental literature on the kinetics of neutral–neutral reactions, although most measurements have been done at room (and higher) temperature for reactions of interest in areas such as combustion chemistry or Earth atmospheric chemistry. In the last years, thanks to development of the CRESU (*Cinétique de Réaction en Ecoulement Supersonique Uniforme*) technique, great efforts have been carried out to measure rate coefficients of neutral–neutral reactions of astrophysical interest at very low temperatures (Smith 2006). The emerging paradigm is that many more exothermic neutral–neutral reactions than previously thought are very rapid ($\sim 10^{-10}$ cm^3 s^{-1}) at low temperatures, and even

some of them experience spectacular enhancements in their reactivity when the temperature decreases from 300 K to 10 K. Moreover, recent experiments have put on the table that reactions with moderately small activation barriers can still be very rapid at very low temperatures, presumably due to quantum tunneling or roaming effects (Shannon et al. 2013; Zanchet et al. 2018).

Apart from ion–neutral and neutral–neutral reactions, there are other types of bimolecular gas-phase chemical reactions that are also important in interstellar chemistry. Among them, we have dissociative recombination of positive molecular ions and electrons, which are usually very fast. From a theoretical point of view the rate coefficient of these reactions should be around 10^{-7} cm^3 s^{-1} (Bates 1950), something that has been verified experimentally. Moreover, the rate coefficient tends to increase with the size of the molecular ion, and there is a more or less marked dependence with temperature of the type $k \propto T^{-n}$ (where n takes values in the range 0–2), i.e., the rate coefficient increases with decreasing temperature. Another type of reactions of interest for interstellar chemistry is radiative association, in which two species form an activated complex that can decay to a stable state through radiative emission. These reactions are usually slow, although in certain cases, in particular when ions of a certain size are involved, they can be fast enough to compete with other types of reactions (Gerlich and Horning 1992).

14.4 Processes Involving Dust Grains

Dust grains, which are ubiquitous in the interstellar medium, are active agents in regulating the chemical state of clouds. These tiny particles provide a reservoir where gas-phase material can be deposited in the form of ices. These ices can experience chemical transformations through reactions taking place on the surface of grains, and later on this chemically processed material can be injected back into the gas phase.

14.4.1 Gas-grain Exchange: Adsorption and Desorption

The adsorption of a gas-phase particle i onto the surface of a dust grain particle occurs through collisions between these two particles with a rate (with units of s^{-1}) given by:

$$R_i^{ads} = S_i v_i \langle \sigma_d n_d \rangle \tag{14.7}$$

where S_i is the sticking efficiency of species i, in the absence of better constraints it is usually assumed to be 1 for most species, and v_i is the thermal velocity of the gas species i, which can be evaluated as $\sqrt{3k_B T/m_i}$, where k_B is the Boltzmann constant, T is the gas kinetic temperature, and m_i is the mass of species i. The

term $\langle \sigma_d n_d \rangle$ in Eq. (14.7) is the product of the geometric cross section and the volume density of dust particles averaged over the grain size distribution, which in the interstellar medium is given by the power law $n(a) \propto a^{-3.5}$, where $n(a)$ is the number of grains of radius a (Mathis et al. 1977).

Species that have been adsorbed on dust grains forming ice mantles can return to the gas phase via a variety of mechanisms, such as thermal desorption, photodesorption, or cosmic-ray induced desorption. Thermal desorption depends on the dust temperature T_d and the binding energy of adsorption of each species i ($E_{D,i}$). The thermal desorption rate, in units of s^{-1}, of an adsorbed species i is given by

$$R_i^{des,th} = \nu_{0,i} \exp\left(-E_{D,i}/T_d\right) \tag{14.8}$$

where $E_{D,i}$ is expressed in units of K, $\nu_{0,i}$ is the characteristic vibration frequency of the adsorbed species i, which can be evaluated as $\sqrt{2 n_s k_B E_{D,i}/\pi^2 m_i}$, where n_s is the surface density of sites, typically $\sim 1.5 \times 10^{15}$ cm^{-2} (see Hasegawa et al. 1992). Thus, the fundamental parameters needed to describe the kinetics of thermal desorption in the interstellar medium are the binding energies $E_{D,i}$, which can be measured using temperature programmed desorption (TPD) experiments. There are, however, some issues concerning the applicability of the laboratory data to model the chemistry of interstellar clouds. For example, different results may be obtained depending on whether sublimation occurs at the sub-monolayer or multilayer regime, or depending on the nature of the substrate (e.g., binding energies tend to be higher if the substrate is water ice instead of silicates; e.g., Noble et al. 2012).

The absorption of ultraviolet photons (emitted by nearby stars, from the ambient interstellar radiation field, or generated through the Prasad–Tarafdar mechanism) by icy dust grains can induce desorption of molecules on the ice surface. In regions where dust is too cold to allow for thermal desorption, photodesorption can provide an efficient way to bring molecules to the gas phase. The photodesorption rate, in units of s^{-1}, of an adsorbed species i is given by

$$R_i^{des,ph} = Y_i F_{UV} \frac{\langle \sigma_d n_d \rangle}{4 \langle \sigma_d n_d \rangle n_s N_l} \tag{14.9}$$

where Y_i is the yield of molecules desorbed per incident photon, F_{UV} is the ultraviolet flux (in units of photon cm^{-2} s^{-1}), and molecules are assumed to desorb only from the top N_l monolayers. Experimental work using isotopic markers (Bertin et al. 2012, 2013) and molecular dynamics calculations (Andersson and van Dishoeck 2008) indicate that molecules desorb efficiently from the two (or even three) top monolayers. Experiments carried out to study the photodesorption of pure ices or binary ice mixtures suggest that the main underlying mechanism is the so-called indirect desorption induced by electronic transition (DIET). This mechanism involves absorption of ultraviolet photons in the ~5 top monolayers and electronic excitation of the absorbing molecules, followed by energy redistribution

to neighboring molecules, which can then break their intermolecular bonds and be ejected into the gas phase. This mechanism dominates over direct photodesorption of the absorbing molecule (see, e.g., Muñoz Caro et al. 2010; Bertin et al. 2012, 2013). If these electronic transitions are dissociative the situation complicates because, in addition to the redistribution of the excess energy to neighboring molecules, the fragments may desorb directly, recombine in the ice surface and then desorb, or diffuse through the ice and recombine with other species to form new molecules. These new molecules may immediately desorb due to the exothermicity of the recombination reaction (see chemical desorption below) and/or desorb later on upon absorption of new incoming photons (Fillion et al. 2014; Martín-Doménech et al. 2016). Photodesorption processes are described in more detail in Chap. 9.

The impact of cosmic rays on icy dust grains can induce desorption of adsorbed molecules. The energy deposited on dust grains upon impact of relativistic heavy nuclei of Fe results in a local heating that induces the thermal desorption of the ice molecules present in the heated region. According to Hasegawa and Herbst (1993), the desorption rate induced by cosmic rays, in units of s^{-1}, of a species i is given by

$$R_i^{des,CR} = 3.16 \times 10^{-19} R_i^{des,th}(70\ K) \tag{14.10}$$

where the numerical factor stands for the fraction of time spent by a grain in the vicinity of a temperature of 70 K, which is reached by the grain at the expense of the energy deposited upon impact of a relativistic Fe nucleus in the formalism of Hasegawa and Herbst (1993). The term $R_i^{des,th}$ (70 K) is the thermal desorption rate of species i at 70 K, as given by Eq. (14.8).

The desorption mechanisms described above are not able to explain the presence of certain molecules in the interior of cold dense clouds. In these regions, temperatures are very low and thermal desorption is suppressed, interstellar ultraviolet photons cannot penetrate and photodesorption is restricted to the weak Prasad–Tarafdar radiation field, and the efficiency of cosmic-ray induced desorption remains low. Alternative desorption mechanisms have thus been invoked. One of them is chemidesorption (Garrod et al. 2007; Minissale et al. 2016), in which the energy released when an exothermic reaction takes place on the grain surface is in part used to inject the reaction products into the gas phase.

14.4.2 Grain-surface Chemical Reactions

In most chemical models of interstellar clouds, grain-surface reactions are assumed to occur through the Langmuir–Hinshelwood mechanism, in which two species undergo diffusion until finding one another and reacting. The kinetics of such a grain-surface chemical reaction between two species i and l can be expressed in terms of a rate coefficient $k_{il}{}^{s}$, with cgs units of $cm^3\ s^{-1}$, in an analogous way to gas-phase bimolecular reactions (see details in Hasegawa et al. 1992). This rate

coefficient can be expressed as

$$k_{il}^{s} = \frac{\kappa_{il}\left(R_i^{diff} + R_l^{diff}\right)}{n_d} \tag{14.11}$$

where R_i^{diff} and R_l^{diff} are the diffusion rates of species i and l, respectively, on the grain surface. For a given species i the diffusion rate, in units of s^{-1}, is given by

$$R_i^{diff} = \frac{1}{N_s}\upsilon_{0,i}\exp\left(-E_{b,i}/T_d\right) \tag{14.12}$$

where N_s is the number of adsorption sites on the surface of a grain, typically $\sim 10^6$ for dust grains of 0.1 μm, and $E_{b,i}$ is the potential energy barrier between adjacent surface potential energy wells, usually $E_{b,i} \sim 0.3\ E_{D,i}$. The parameter κ_{il} in Eq. (14.11) is the probability for the reaction to happen upon an encounter between species i and l, which is unity for exothermic reactions without activation barrier. If an activation barrier is present, the reaction can proceed via quantum tunneling, with $\kappa_{il} < 1$ (see Hasegawa et al. 1992).

14.5 Chemical Models of Different Types of Interstellar Clouds

Depending on the type of interstellar cloud (basically on the temperature, density of particles, intensity of ultraviolet radiation, and initial conditions and evolutionary history), different processes dominate the chemical composition of the gas and dust.

First, we have diffuse interstellar clouds (see Snow and McCall 2006), with typical densities of 100–1000 cm^{-3}, temperatures of 30–100 K, and low extinction values ($A_V \sim 0.2$–1). The results of a time-dependent pure gas-phase chemical model of a typical diffuse cloud ($n_H = 500\ cm^{-3}$, $T = 50$ K, and $A_V = 1$) are depicted in Fig. 14.1. It is seen that the degree of ionization is high (the fractional abundance of electrons is $\sim 10^{-4}$) as a result of the exposition to ultraviolet radiation, and most molecules are simple (diatomic and triatomic), with a certain importance of some exotic ions. A known failure of this model is the underestimation of the abundance of CH^+ by 2–3 orders of magnitude. The chemistry of diffuse clouds is largely driven by ultraviolet photons arising from the ambient radiation field. In this sense, these regions are photon-dominated regions (PDRs), although the term is usually reserved for the edges of denser clouds located close to hot stars, and thus exposed to a far more intense ultraviolet field than in standard diffuse clouds. The Orion Bar and Horsehead Nebulae are good examples of such regions, where the higher densities and stronger ultraviolet radiation fields drive a faster and richer chemistry. Models aiming to describe the chemistry and physics of PDRs have been specifically developed (Hollenbach and Tielens 1997). These models couple processes driving chemical transformations to radiative and collisional processes driving the thermal

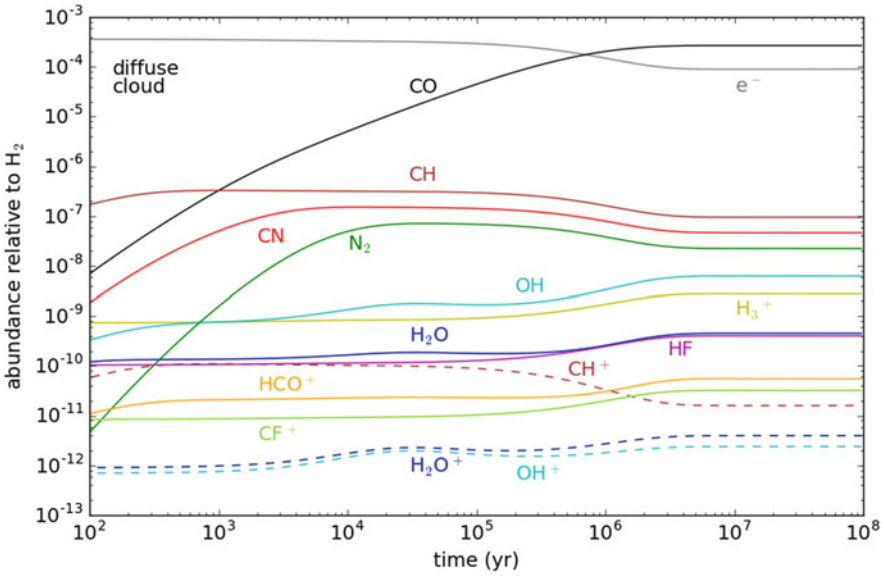

Fig. 14.1 Molecular abundances calculated as a function of time for a diffuse cloud using a pure gas-phase chemical model (the chemical network employed is UMIST 2012; McElroy et al. 2013) with typical physical conditions ($n_H = 500$ cm^{-3}, $T = 50$ K, and $A_V = 1$). The calculated abundance of CH^+ is severely underestimated with respect to the values derived from observations (see text)

balance, and solve them at different depths (or A_V) from the edge to the internal regions of the cloud. Since in this case the system of equations becomes more complicated, only the solution at steady state (i.e., not as a function of time) is computed. This is a known handicap of these models. Whether or not the steady state assumption is good enough in PDRs is yet to be evaluated.

The interiors of cold dense clouds have densities significantly higher (10^4–10^5 cm^{-3}) than those of diffuse clouds, very low temperatures (~10 K), and large extinction values ($A_V > 10$). In these regions the chemistry is driven by cosmic rays (see Agúndez and Wakelam 2013). Figure 14.2 shows the abundances of some molecules as a function of time as calculated with a pure gas-phase chemical model of a typical cold dense cloud ($n_H = 2 \times 10^4$ cm^{-3}, $T = 10$ K, and $A_V = 30$). In this case the degree of ionization remains relatively low (the fractional abundance of electrons is $\sim 10^{-8}$) and the absence of intense ultraviolet radiation allows gas-phase chemical reactions to develop a richer molecular complexity than in diffuse clouds. Pure gas-phase chemical models have known failures to correctly estimate the abundances of some molecules (dashed lines in Fig. 14.2). The abundance of CH_3OH is severely underestimated by models and the abundances of O_2 and H_2O are much higher than observed. In the case of H_2O, the disagreement can be explained by the lack of adsorption processes in the model, since water is probably in the form of ice on dust grains at the low temperatures of cold dense clouds.

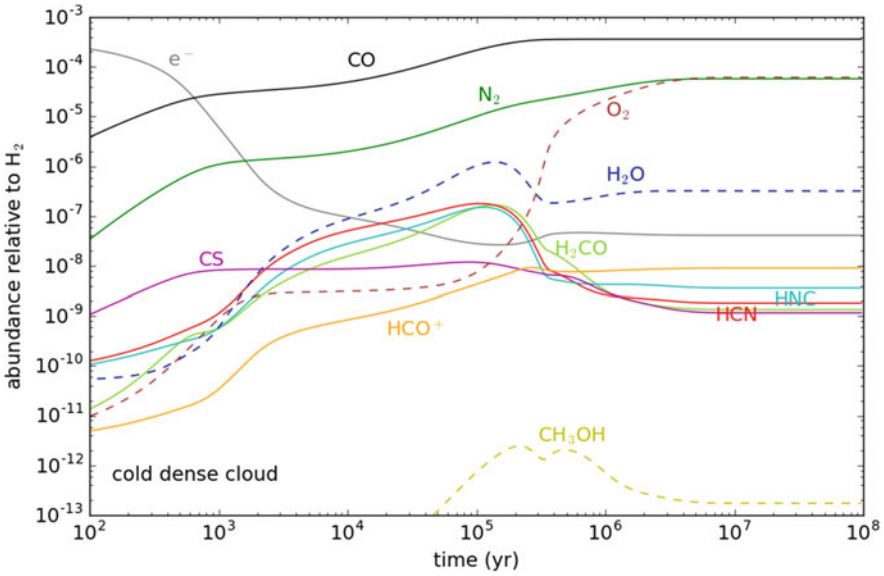

Fig. 14.2 Abundances of assorted molecules calculated as a function of time for a cold dense cloud using a pure gas-phase chemical model (the chemical network employed is UMIST 2012; McElroy et al. 2013) with typical physical conditions ($n_H = 2 \times 10^4$ cm^{-3}, $T = 10$ K, and $A_V = 30$; see Agúndez and Wakelam 2013). The calculated abundances of H_2O, O_2, and CH_3OH are in severe disagreement with observations (see text)

In more advanced evolutionary stages, when protostars are born at the cores of dense clouds (the so-called hot cores), the chemical composition experiences drastic changes. The switch on of the protostar at the core center injects energy into the cloud and heats up the gas and dust. Densities in hot cores are somewhat higher ($\sim 10^6$ cm^{-3}) than in cold cores as a result of the more advanced stage of gravitational collapse of the cloud, and temperatures are much higher (some hundreds of degrees Kelvin) as a result of the heating produced by the protostar. These high temperatures make ice mantles to desorb thermally and activate endothermic gas-phase reactions, leading to a rich chemistry with many complex organic molecules being formed (Herbst and van Dishoeck 2009). Chemical models aiming to describe such regions must therefore account for grain-surface chemical processes and gas-grain exchange processes.

14.6 Concluding Remarks

A wide variety of molecules are present in the interstellar medium. Moreover, each type of interstellar region has its own chemical signature, that is, contains a specific type of chemistry and a very concrete type of molecules. Chemical models are

needed to interpret observations of interstellar molecules and to understand the underlying physical and chemical processes that give rise to the chemical differentiation present in different types of interstellar clouds. For that purpose, laboratory and theoretical data of gas-phase and grain-surface processes are essential.

References

Agúndez, M., Wakelam, V.: Chem. Rev. **113**, 8710 (2013)
Aikawa, Y., Miyama, S.M., Nakano, T., Umebayashi, T.: Astrophys. J. **467**, 684 (1996)
Andersson, S., van Dishoeck, E.F.: Astron. Astrophys. **491**, 907 (2008)
Bates, D.R.: Phys. Rev. **78**, 492 (1950)
Bertin, M., Fayolle, E.C., Romanzin, C., et al.: Phys. Chem. Chem. Phys. **14**, 9929 (2012)
Bertin, M., Fayolle, E.C., Romanzin, C., et al.: Astrophys. J. **779**, 120 (2013)
Bohlin, R.C., Savage, B.D., Drake, J.F.: Astrophys. J. **224**, 132 (1978)
Cuppen, H.M., Karssemeijer, L.J., Lamberts, T.: Chem. Rev. **113**, 8840 (2013)
Cuppen, H.M., Walsh, C., Lamberts, T., et al.: Space Sci. Rev. **212**, 1 (2017)
Dalgarno, A.: Proc. Natl. Acad. Sci. U.S.A. **103**, 12269 (2006)
Draine, B.T.: Astrophys. J. Suppl. Ser. **36**, 595 (1978)
Fillion, J.-H., Fayolle, E.C., Michaut, X., et al.: Faraday Discuss. **168**, 533 (2014)
Garrod, R.T., Wakelam, V., Herbst, E.: Astron. Astrophys. **467**, 1103 (2007)
Gerlich, D., Horning, S.: Chem. Rev. **92**, 1509 (1992)
Gredel, R., Lepp, S., Dalgarno, A., Herbst, E.: Astrophys. J. **347**, 289 (1989)
Hasegawa, T.I., Herbst, E.: Mon. Not. R. Astron. Soc. **261**, 83 (1993)
Hasegawa, T.I., Herbst, E., Leung, C.M.: Astrophys. J. Suppl. Ser. **82**, 167 (1992)
Herbst, E., van Dishoeck, E.F.: Annu. Rev. Astron. Astrophys. **47**, 427 (2009)
Herbst, E., Yates Jr., J.T.: Chem. Rev. **113**, 8707 (2013)
Hollenbach, D.J., Tielens, A.G.G.M.: Annu. Rev. Astron. Astrophys. **35**, 179 (1997)
Martín-Doménech, R., Muñoz Caro, G.M., Cruz-Díaz, G.A.: Astron. Astrophys. **589**, A107 (2016)
Mathis, J.S., Rumpl, W., Nordsieck, K.H.: Astrophys. J. **217**, 425 (1977)
McElroy, D., Walsh, C., Markwick, A.J., et al.: Astron. Astrophys. **550**, A36 (2013)
Minissale, M., Dulieu, F., Cazaux, S., Hocuk, S.: Astron. Astrophys. **585**, A24 (2016)
Muñoz Caro, G.M., Jiménez-Escobar, A., Martín-Gago, J.A., et al.: Astron. Astrophys. **552**, A108 (2010)
Noble, J.A., Congiu, E., Dulieu, F., Fraser, H.J.: Mon. Not. R. Astron. Soc. **421**, 768 (2012)
Padovani, M., Galli, D., Glassgold, A.E.: Astron. Astrophys. **501**, 619 (2009)
Shannon, R.J., Blitz, M.A., Goddard, A., et al.: Nat. Chem. **5**, 745 (2013)
Smith, I.W.M.: Angew. Chem. Int. Ed. **45**, 2842 (2006)
Snow, T.P., McCall, B.J.: Annu. Rev. Astron. Astrophys. **44**, 367 (2006)
van Dishoeck, E.F.: In: Millar, T.J., Williams, D.A. (eds.) Rate Coefficients in Astrochemistry, p. 49. Kluwer Academic, Dordrecht (1988)
Wakelam, V., Smith, I.W.M., Herbst, E., et al.: Space Sci. Rev. **156**, 13 (2010)
Woitke, P., Kamp, I., Thi, W.-F.: Astron. Astrophys. **501**, 383 (2009)
Zanchet, A., del Mazo, P., Aguado, A., et al.: Phys. Chem. Chem. Phys. **20**, 8 (2018) https://doi.org/10.1039/c7cp05307j

Index

G. M. Muñoz Caro, R. Escribano (eds.), *Laboratory Astrophysics*,
Astrophysics and Space Science Library 451,
https://doi.org/10.1007/978-3-319-90020-9